

Antiproton-Proton Annihilation
in Flight into $K^+K^-\pi^0$

Dissertation der Fakultät für Physik
der Ludwig-Maximilians-Universität
München

vorgelegt von
Ismail Uman
aus Istanbul, Türkei

11 Januar 2001

1. Gutachter: Prof. Dr. M. A. Faessler
 2. Gutachter: Prof. Dr. A. Staude
- Tag der mündlichen Prüfung: 20 Juli 2001

*Seht die Sterne, die da lehren
Wie man soll den Meister ehren
Jeder folgt nach Newtons Plan
Ewig schweigend seiner Bahn.*

ALBERT EINSTEIN, 1942

Abstract

The antiproton-proton annihilation into $K^+K^-\pi^0$ was studied at 900 and 1642 MeV/c with the Crystal Barrel detector at LEAR. The Dalitz plots are analyzed using a partial wave formalism that integrates over production angle. In the f/θ region around $1.7\text{ GeV}/c^2$ the K^+K^- system shows structure containing at least two resonances, in addition to the vector resonance $\rho/\phi(1700)$: one tensor at $1620\text{ MeV}/c^2$ ($\Gamma = 280\text{ MeV}/c$), which is possibly the first radial excitation of the well-known $a_2(1320)$, and one state at $1770\text{ MeV}/c^2$ ($\Gamma = 110\text{ MeV}/c$) with spin 0 (slightly preferred) or 2. The rate of the latter is similar to that observed for the $f_0(1500)$. A scalar with these properties would complete the mixing scheme of the low-lying 0^{++} states.

Contents

1	Introduction	1
1.1	The Quantumchromodynamics	1
1.2	Ordinary Mesons	2
1.3	Glueballs	5
1.3.1	Theoretical Predictions	5
1.3.2	Glueball Decays	6
1.4	The Scalar Mesons	6
1.4.1	The $f_0(1500)$	8
1.4.2	The $f_j(1710)$	9
1.5	The Physics Goals of the Present Analysis	10
2	The Crystal-Barrel Experiment at LEAR	12
2.1	The Production of Antiprotons	12
2.2	The Crystal-Barrel Detector	12
2.3	The Silicon-Vertex Detector	14
2.4	The Jet-Drift Chamber	15
2.5	The Electromagnetic Calorimeter	15
2.6	Data Acquisition and the Trigger System	18
2.7	The Calibration and Event Reconstruction	19
2.7.1	JDC calibration	19
2.7.2	Z -calibration	19
2.7.3	$\rho\phi$ -calibration	20
2.7.4	dE/dx calibration	20
2.7.5	Electromagnetic calorimeter calibration	20
2.7.6	Photon reconstruction	21
2.7.7	Track reconstruction	23
2.7.8	Photon energy correction functions	24
2.7.9	Electrical wire length scaling	26
3	Data Selection and Kinematic Fit	28
3.1	Preselection	28
3.2	Selection	32
3.3	Constrained Fit	36
3.4	Application on $K^+K^-\pi^0$ Final States	38
3.5	Monte Carlo Simulation	44

4	The Presentation of the Data and the Dalitz Plot	46
4.1	Dalitz Plot	46
4.2	Dalitz Plot at 900 MeV/c	49
4.3	Dalitz Plot at 1642 MeV/c	50
4.4	Acceptance Corrected Dalitz Plots	55
5	The Partial Wave Analysis	60
5.1	The Transition Amplitude	60
5.2	Selection Rules	62
5.3	The Canonical Formalism	66
5.4	The Fitting Procedure	68
5.5	χ^2 Test with Equal Binning Content	70
5.6	Description of the Fitting Program	73
6	Results of the Analysis	74
6.1	Basic Fit at 900 MeV/c	74
6.2	Improved Fit at 900 MeV/c	79
6.3	Additional Spin Tests	95
6.4	Best Fit at 900 MeV/c	97
6.5	Basic Fit at 1642 MeV/c	106
6.6	Improved Fit at 1642 MeV/c	110
6.7	Best Fit at 1642 MeV/c	116
7	Conclusion	126
7.1	Observed Resonances	126
7.2	Interpretation of the Results	126
A	Probability Density Function for the Reaction $\bar{p}p \rightarrow K^+K^-\pi^0$ at 900 and at 1642 MeV/c	129

List of Figures

1.1	Lightest meson nonets	4
1.2	Proton-antiproton annihilation	7
1.3	Radiative J/ψ decay	7
1.4	Central Production	7
1.5	Scalar nonets	9
1.6	Invariant K^+K^- mass distributions	11
2.1	CERN-Antiproton Complex	13
2.2	The Crystal-Barrel Detector	13
2.3	Overall layout of the beam counters and liquid hydrogen target	14
2.4	The Silicon-Vertex Detektor	16
2.5	The Jet-Drift Chamber	16
2.6	Cross section of the electromagnetic calorimeter	17
2.7	Cross section of a CsI(Tl)-module	17
2.8	Photon Energy Correction Functions	25
2.9	Electrical wire length scaling	27
3.1	Type 13 event in the rz view of the JDC with energy towers	30
3.2	E_1/E_9	31
3.3	Vertex distribution along the z-axis	31
3.4	Invariant mass of the $\gamma\gamma$ distribution at a incoming antiproton momentum of 900 MeV/c	32
3.5	Total energy and momentum distributions	33
3.6	Total momentum vs. total energy	34
3.7	Window cuts on energy/momentum at 900 MeV/c and at 1642 MeV/c	35
3.8	Confidence level distribution at 900 MeV/c and at 1642 MeV/c	39
3.9	Pulls at 900 MeV/c with no corrections	41
3.10	Pulls at 900 MeV/c	42
3.11	The differential energy losses versus the momentum of the charged mesons at 900 MeV/c	43
3.12	Monte Carlo vertex distribution along the z-axis	44
4.1	Scheme of the Dalitz plot of $K^+K^-\pi^0$ states at 900 MeV/c	48
4.2	Scheme of the asymmetric Dalitz plot of $K^+K^-\pi^0$ states at 900 MeV/c	48

4.3	Scheme of Dalitz plot of $K^+K^-\pi^0$ states at 900 MeV/c and at 1642 MeV/c	50
4.4	Dalitz plot of $K^+K^-\pi^0$ states at 900 MeV/c	51
4.5	Dalitz plot and the projections of $K^+K^-\pi^0$ states at 900 MeV/c	52
4.6	Polar production angles of the $K^\pm\pi^0$ isobars at 900 MeV/c and at ~ 890 MeV	53
4.7	Acceptance corrected polar production angles of the $K^\pm\pi^0$ isobars at 900 MeV/c and at ~ 890 MeV	54
4.8	Dalitz plot of $K^+K^-\pi^0$ states at 1642 MeV/c	56
4.9	Dalitz plot and the projections of $K^+K^-\pi^0$ states at 1642 MeV/c	57
4.10	Dalitz plot of $K^+K^-\pi^0$ Monte Carlo events at 900 MeV/c	58
4.11	Dalitz plot of $K^+K^-\pi^0$ Monte Carlo events at 1642 MeV/c	58
4.12	Acceptance corrected Dalitz plots and the K^+K^- projections	59
5.1	Gottfried-Jackson reference system	60
5.2	Partial wave annihilation cross sections	63
5.3	Angles used in the canonical formalism	66
5.4	Dalitz plot at 900 MeV/c binned with equal content of data	71
5.5	Dalitz plot at 1642 MeV/c binned with equal content of data	72
6.1	Fitted polar production angles of the $K^\pm\pi^0$ isobars	76
6.2	Basic fit of the Dalitz plot at 900 MeV/c	77
6.3	Basic fit: projections of the Dalitz plot at 900 MeV/c	78
6.4	Improved fit with a tensor at 1650 MeV	80
6.5	Improved fit with a tensor at 1650 MeV (K^+K^- projection)	81
6.6	Improved fit with a tensor at 1650 MeV and the $f'_2(1525)$ (K^+K^- projection)	82
6.7	Improved fit with a tensor at 1650 MeV, the $f'_2(1525)$ and the $a_2(1320)$	83
6.8	Improved fit with a tensor at 1650 MeV, the $f'_2(1525)$ and the $a_2(1320)$ (K^+K^- projection)	84
6.9	Fitted mass and width of the $K^{*\pm}(892)$	87
6.10	Fitted mass of the $\phi(1020)$	88
6.11	Fitted mass and width of the $f_2(1275)$	89
6.12	Fitted mass and width of the $a_2(1320)$	90
6.13	Fitted mass and width of the $f_0(1500)$	91
6.14	Fitted mass and width of the $f'_2(1525)$	92
6.15	Improved fit: mass and width of the $X_J(1680)$ if $J = 1$	93
6.16	Improved fit: mass and width of the $X_J(1670)$ if $J = 2$	94
6.17	Fit with the channels (1)-(5), (7),(8) excluding the $f_0(1500)$	96
6.18	Best fit at 900 MeV/c (K^+K^- projection)	100
6.19	Best fit at 900 MeV/c	101
6.20	Best fit at 900 MeV/c (projections)	102
6.21	Best fit: mass and width of the $(a/f)_2(1620)$ if $J = 2$	103
6.22	Best fit: mass and width of the $(\phi/\rho)_1(1680)$	104

6.23	Best fit: mass and width of the $X_J(1680)$ if $J = 0, 1, 2$	105
6.24	Fitted polar production angles of the $K^\pm\pi^0$ isobars	107
6.25	Basic fit of the Dalitz plot at 1642 MeV/c	108
6.26	Basic fit: projections of the Dalitz plot at 1642 MeV/c	109
6.27	Improved fit (projections) including the $f'_2(1525)$	112
6.28	Improved fit: mass and width of the $X_J(1740)$ if $J = 0, 2$	113
6.29	Improved fit including the $f'_2(1525)$, $X_0(1740, 190)$ and the $X_2(1930, 110)$	114
6.30	Improved fit (projections) including the $f'_2(1525)$, $X_0(1740, 190)$ and the $X_2(1930, 110)$	115
6.31	Best fit: mass and width of the $X_J(1620)$ if $J = 0, 2$	118
6.32	Best fit: mass and width of the $X_J(1680)$ if $J = 1$	119
6.33	Best fit: mass and width of the $X_J(1770)$ if $J = 0, 2$	120
6.34	Best fit: mass and width of the $(f/a)_0(1770)$	121
6.35	Best fit: mass and width of the $X_J(1930)$ if $J = 0, 2, 4$	122
6.36	Best fit: mass and width of the $(f/a)_2(19300)$	123
6.37	Best fit including the channels (1)-(6),(8)-(12)	124
6.38	Best fit including the channels (1)-(6),(8)-(12) (projections)	125
7.1	Possible mixing scheme for the low-lying scalar isoscalar mesons .	128
7.2	Suggested trajectories of M^2 v. radial quantum number for 2^+ states	128

List of Tables

1.1	Quark quantum numbers and their masses	4
2.1	Main trigger conditions used in the runs during Oct-Dec, 1996 . .	18
3.1	Selection of $K^+K^-\pi^0$ events	40
3.2	Widths of the pulls	45
3.3	Selection of $K^+K^-\pi^0$ MC events	45
5.1	Initial states of the $\bar{p}p$ system up to $J = 3$	63
5.2	Selection rules for the production of K^+K^- resonances up to $J_{\bar{p}p} = 3$.	65
5.3	Selection rules for the production of $K^\pm\pi^0$ resonances up to $J_{\bar{p}p} = 3$.	65
6.1	Log-likelihood changes for crossing interferences	75
6.2	Log-likelihood changes including $X_J(1650)$ with $J = 0, 1, 2, 3$. . .	79
6.3	Log-likelihood changes including the $f'_2(1525)$ and the $a_2(1320)$. .	79
6.4	Log-likelihood changes including the $a_0(1450)$	85
6.5	Log-likelihood changes including $X_J(1650)$ with $J = 0, 1, 2, 3$ after the optimization of the production angles	85
6.6	Improved fit at 900 MeV/c: fitted masses and widths.	86
6.7	Fit at 900 MeV/c without the $f_0(1500)$: fitted masses and width of the $X_J(1650)$ for $J = 0, 1, 2$	95
6.8	Additional spin tests	95
6.9	Best fit at 900 MeV/c: comparison including and excluding the $(a/f)_2$ or the $(\phi/\rho)_1$	98
6.10	Best fit at 900 MeV/c: fitted masses and width of the $(a/f)_2(1620)$, $(\phi/\rho)_1(1680)$	98
6.11	Best fit: contributions at 900 MeV/c	99
6.12	Basic interferences at 1642 MeV/c	110
6.13	Additional interferences at 1642 MeV/c	110
6.14	Optimization of the $X_J(1750)$, $X_J(1930)$ for $J = 0, 2$	111
6.15	Improved fit at 1642 MeV/c: fitted masses and widths.	111
6.16	Best fit at 1642 MeV/c: comparison including and excluding the $(a/f)_2$ or the $(\phi/\rho)_1$ or the X_0	116
6.17	Spin test and mass/width scanning including all channels at 1642 MeV/c	117
6.18	Best fit: contributions at 1642 MeV/c	117

Chapter 1

Introduction

1.1 The Quantumchromodynamics

After the discovery of the neutron by Chadwick in 1932, a better comprehension of the forces acting on the nuclear scale and a new definition of the fundamental or elementary particles was needed. With the proton and the electron, considered as basic constituent of the matter, and the electromagnetic interaction it was possible to describe only extra-nuclear processes. In addition to the electromagnetic force and to gravity, which plays a negligible role in particle physics, two new forces were postulated: the weak interaction (Fermi 1934) to explain the slow process of the β -decay of the nuclei, and the strong interaction (Yukawa 1935) to describe the short range force between neutron and proton in the atomic nucleus.

When the pion with a mass of $\sim 150MeV$ was discovered (1947) it was assigned to be the quantum of the field in the same way as the photon was assigned to be the quantum of the electromagnetic field. However, the advent of high energy accelerators in the '50s and in the '60s revealed that the nuclear force was more complicated. A "jungle" of other particles was observed: besides more than 20 relatively stable particles with a mean live longer than 10^{-10} s, more than hundred extremely short lived particles ($< 10^{-21}$ s), called "resonances", were found. Similar structures or regularities were found in the nuclear spectra. The pion now had to be considered as ground state of these resonances.

A relativistic formulation of the quantum theory for the strong interaction, called quantum chromodynamics (QCD), was carried out (Fritzsch 1971, Gross 1973, Weinberg 1973) in analogy to the successful theory of quantum electrodynamics (QED).

In the QCD, new particles, called quarks, are combined in different ways to form hadrons. Three quarks build the baryons $\equiv q_1q_2q_3$ and a quark-antiquark pair form a meson $q_1\bar{q}_2$.

Quark and anti-quark have spin 1/2, so are fermions with baryon quantum number 1/3 and -1/3 respectively, charge $\pm 1/3|e|$ and $\pm 2/3|e|$. They occur in several varieties or "flavours" and are labeled u,d,s,c,b,t, which stands for up, down, strange, charm, bottom, top, respectively.

The quark hypothesis was already put forward in 1964 by Gell-Mann and by

Zweig, using the local symmetry of the SU(3)-special unitary group theory to develop multiplets out of three flavours. With only the three lightest quarks u, d and s it was possible to describe 10 baryon states of lower mass and of spin parity $J^P = \frac{3}{2}^+$ (baryon decuplet) and the baryon octet $J^P = \frac{1}{2}^+$: the proton (uud) and the neutron (udd) are the lightest states.

For mesons, restricting ourselves again to three flavours, we expect nonets. With the spin parallel we get triplet states, the vector mesons with $J=1$, and with spins anti parallel singlet states of $J=0$, the pseudoscalar mesons: here the pion is the lightest state ($u\bar{d}$).

An additional property of the quarks, the "colour charge" play the same role for the strong interaction as the electric charge for the electromagnetic interaction. A quark can carry any of three colours ("red, blue, green"). This additional degree of freedom was needed to save the Pauli principle: in the lowest mass spin- $\frac{3}{2}$ baryons with three equal quarks, if we assume the quarks to be in a spatial symmetric ground state ($l = 0$), the spin $J^P = \frac{3}{2}$ is obtained with all the spins parallel (eg.: $\Delta^{++} = u \uparrow u \uparrow u \uparrow$). Without the colour, this means to have symmetry of the three-quark wave function in flavour, spin and space, against the principle that two or more fermions cannot exist in the same quantum state. The colour charges account for the binding of the quarks: differently coloured quarks attract each other, in the same way as opposite electrical charges, so that the neutron and the proton can be considered as clusters of three quarks with different colours, mutually attracting.

As in the electromagnetic interaction where a "gauge" boson with spin 1, the photon, acts on the spin- $\frac{1}{2}$ protons and electrons, in QCD the transmission occurs through the spin-1 'gluons', acting on spin- $\frac{1}{2}$ quarks, with the difference that the gluons can, as the quarks, carry colour themselves. This means that gluons can also attract each other, in addition to interacting with quarks, and explains empirically the short range of the strong interaction compared to the electromagnetic interaction, where photons are free to stream out over a long distance. This property leads not only to the confinement of the colour, but also to the existence of a new form of matter like *glueballs* [1], states of two or three gluons, and *hybrids* (eg.: $q\bar{q}g$).

The possibility to identify glueballs or gluonic mesons, mainly depends on our understanding of the conventional meson spectroscopy and the classification of the quark-antiquark mesons in terms of nonets. Evidence of hybrids are based on the identification of structures with "exotic" quantum numbers not allowed for $q\bar{q}$ objects (eg.: $J^{PC} = 0^{--}, 0^{+-}, 1^{-+}, 2^{+-}, \dots$).

1.2 Ordinary Mesons

The total spin S equals 0 (singlet state) or S equals 1 (triplet state), of a $q\bar{q}$ state couples with the orbital angular momentum L , with a resulting total angular momentum J .

In the spectroscopic notation we write $n^{2S+1}L_J$ where n is the radial quan-

tum number and with S, P, D, \dots for $L = 0, 1, 2, \dots$ the letters S, P, D, \dots are used following a tradition of atomic physics. Fermion and antifermion have opposite parities so that P equals $(-1)^{L+1}$. Quark-antiquark pairs $q_i\bar{q}_i$ are also eigenstates of the C -parity with $C = (-1)^{L+S}$. For the ground state, $L = 0$, the pseudoscalars have $J^{PC} = 0^{-+}$, while for the vectors $J^{PC} = 1^{--}$. The small mass difference between the u and d quarks, like in the case of the proton and the neutron, leads to consider them as members of an isospin doublet ($I = 1/2$) with the z -component $I_z = 1/2$ for u and $I_z = -1/2$ for d, while the s,c,b,t quarks with heavier mass are assigned to be isospin singlets (s. Tab. 1.1)¹.

With u,d and s quarks, mesons are grouped together, according to SU(3), into an octet and a singlet:

$$\mathbf{3} \otimes \bar{\mathbf{3}} = \mathbf{8} \oplus \mathbf{1}$$

The quark-model assignments for the lowest-lying pseudoscalar and vector meson nonets

$$\begin{aligned} 1^1S_0 : & \quad \pi(140), \eta(547), \eta'(958), K(495) \\ 1^3S_1 : & \quad \rho(770), \omega(782), \phi(1020), K^*(892) \end{aligned}$$

are represented in the Fig. 1.1. The $s\bar{s}$ isoscalar heavier states are partially mixed with the $n\bar{n}$; here the symbol n means non-strange combinations of u,d quarks:

$$n\bar{n} = (u\bar{u} + d\bar{d})/\sqrt{2}$$

The mixing angle θ_P relates the physical states η and η' to the octet ($\eta_8 = (u\bar{u} + d\bar{d} - 2s\bar{s})/\sqrt{6}$) and singlet ($\eta_1 = (u\bar{u} + d\bar{d} + 2s\bar{s})/\sqrt{3}$) states:

$$\begin{aligned} \eta &= \eta_8 \cos\theta_P - \eta_1 \sin\theta_P \\ \eta' &= \eta_8 \sin\theta_P + \eta_1 \cos\theta_P \end{aligned}$$

Using the Gell-Mann-Okubo ($mass$)² formula for mesons

$$m_8^2 = \frac{1}{3}(4m_K^2 - m_\pi^2)$$

and considering that η and η' are orthogonal one gets

$$tg^2\theta = \frac{m_8^2 - m_\eta^2}{m_{\eta'}^2 - m_8^2}$$

and $\theta_P = -10^\circ$ [2].

If we apply this procedure for the vectors and insert the measured masses of the correspondent physical states ($\eta \rightarrow \phi$, $\eta' \rightarrow \omega$, $\pi \rightarrow \rho$ and $K \rightarrow K$), we get

¹The mass here is that of constituent quarks as opposed to free quarks

Quark	Symbol	I_z	S	C	B	T	Q/e	$M[MeV/c^2]$
up	u	-1/2	0	0	0	0	+2/3	300 ± 100
down	d	+1/2	0	0	0	0	-1/3	300 ± 100
strange	s	0	-1	0	0	0	-1/3	450 ± 100
charm	c	0	0	1	0	0	+2/3	~ 1500
bottom	b	0	0	0	-1	0	-1/3	~ 5000
top	t	0	0	0	0	1	+2/3	~ 170000

Table 1.1: Quark quantum numbers and their masses. I_z = z-component of the isospin, S = strangeness, C = Charmness, B = Bottomness, T = Topness, Q = Charge, M = Constituent mass.

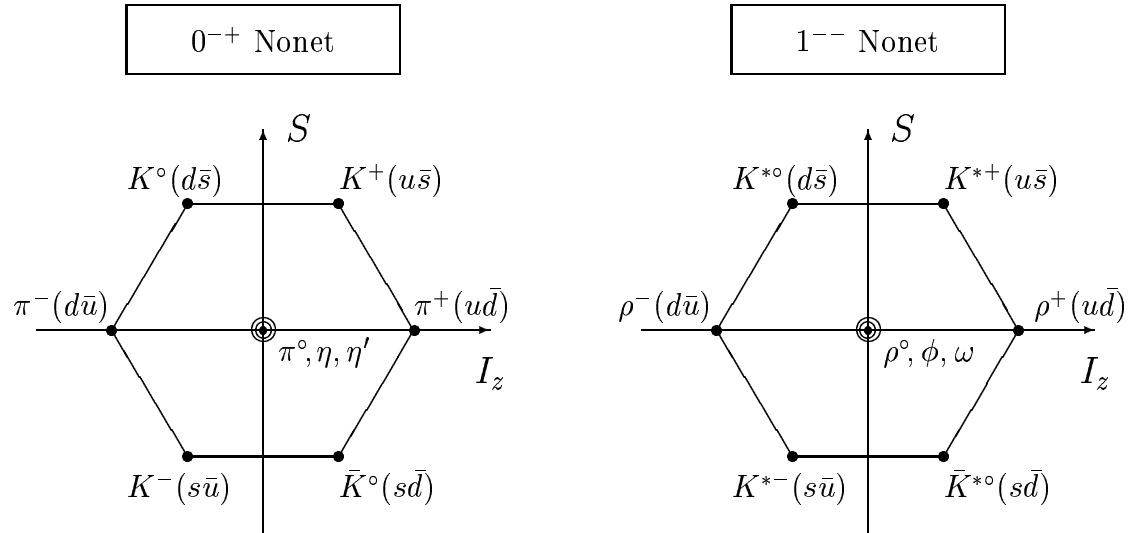


Figure 1.1: Representation of the lowest-lying meson states with their respective quark assignments. Left the pseudoscalar mesons ($J^{PC} = 0^{-+}$), right the vector mesons ($J^{PC} = 1^{--}$).

$\theta_V = -39^\circ$, which is close to the "ideal" mixing $\theta_V \simeq -35^\circ$, $\sin\theta_V = 1/\sqrt{3}$: for the case of ideal mixing the ϕ would be composed only of $s\bar{s}$ and the ω of $n\bar{n}$.

$$\begin{aligned}\phi &= s\bar{s}, \\ \omega &= (u\bar{u} + d\bar{d})/\sqrt{2}\end{aligned}$$

The first *radial excitation* (i.e.: radial quantum number $n = 2$) of the vector mesons is represented by the nonet consisting of:

$$2^3S_1 : \rho(1450), \omega(1420), \phi(1680), K_1^*(1410)$$

The quark assignment, for the observed resonances, becomes increasingly difficult at higher masses where many states overlap. For example, the identification of the vector nonet of the $q_1\bar{q}_2$ -states with relative angular momentum $L = 2$ with observed mesons is still open:

$$1^3D_1 : \rho(1700), \omega(1620), \phi(?), K_1^*(1680)$$

A complete *tensor* ($J^{PC} = 2^{++}$) nonet is the

$$1^3P_2 : a_2(1320), f_2(1270), f_2'(1525), K_2^*(1430)$$

Particular interest in this work is given to the lowest *scalar* mesons ($J^{PC} = 0^{++}, 1^3P_0$), whose identification is the most difficult and controversial in meson spectroscopy: candidates of this group are the $I = 1$ state $a_0(980)$ and the $a_0(1450)$, for $I = 0$ the $f_0(980)$, $f_0(400 - 1200)$ and $f_0(1370)$. The $f_0(1500)$ and the $f_j(1710)$, if $J = 0$, cannot easily find a place in this nonet and are considered, in view of theoretical predictions, to be candidates of a gluonic meson or *non- $q\bar{q}$* state.

In addition, in the pseudoscalar sector two isoscalar peaks were observed at masses range of ~ 1410 and 1470 MeV with different decay properties: one of these can be the first radial excitation of the η' so that the corresponding nonet could be composed as follows:

$$2^1S_0 : \pi(1300), \eta(1295), \eta'(1440), K(1460)$$

The decay of the upper η peak with a mass ~ 1470 into $K^*\bar{K}$, and the mass degeneracy of the $\pi(1300)$, $\eta(1295)$ suggest that ideal mixing occurs and the state at 1470 MeV can be the $s\bar{s}$, while the lowest peak at ~ 1410 MeV can be considered as a mixture of a gluonium with $\bar{q}q$ [3] or a bound state of gluinos according to the some SUSY models [5]. However the existence of three pseudoscalars in this mass range still needs confirmation.

1.3 Glueballs

1.3.1 Theoretical Predictions

The first attempt to construct a relativistic model for gluons was based on the so called *bag model* [7]. The correct description of high energy inelastic lepton

scattering, where the quarks were considered as asymptotically free light particles inside the hadron, was used as a guide. Quarks were confined within a radius of ~ 1 fm, and imposing the boundary condition, the bag forces the quarks into eigenstates with specific values. The mass of the hadron is then a function of the energy of these confined quarks.

In the same model glueballs were constructed inserting massless spin-1 gluons in a spherical bag of a size comparable to that of the bag filled with quarks. According to this assumption one expects that the lightest glueballs will have a mass around 1 GeV, and in order of increasing mass one should have the quantum numbers

$$J^{PC} = 0^{++}, 2^{++}, 0^{-+}, 2^{-+}$$

Other models like the *QCD Sum Rules* [8] and the *Flux tube model* [9] predict as well the lightest glueball to be a scalar 0^{++} with a mass of 1.5 GeV.

Particular attention has to be given to the latest results of the *Lattice gauge theories* [10], [11]. The lightest "ideal" glueball (i.e.: quenched approximation) is predicted again to have $J^{PC} = 0^{++}$ with a mass of 1.55 ± 0.05 GeV [10] or 1.74 ± 0.07 GeV [11].

The predicted next state is a tensor (2^{++}) glueball with a mass of 2.27 ± 0.1 GeV [10] or 2.36 ± 0.13 GeV [11].

1.3.2 Glueball Decays

The main property of a glueball is that it has no flavour and is electrically neutral. So we expect that it has no preferred decay to a particular quark flavour or charge. Glueballs are flavour singlets and should decay like an isoscalar flavour singlet. Sexton *et al.*[12] estimated a 0^{++} glueball width to all pseudoscalar pairs of 108 ± 29 MeV, and a phase space normalized branching fraction

$$\Gamma(G \rightarrow \pi\pi : K\bar{K} : \eta\eta : \eta\eta' : \eta'\eta') / (\text{phasespace}) = 3 : 4 : 1 : 0 : 1.$$

There are three mechanism, which are believed to be particularly suited for glueball production:

- (1) Proton-antiproton annihilation where the available energy can be transferred to gluons in the 1-2 GeV range (see fig. 1.2).
- (2) Radiative decay of a heavy meson like $J/\psi \rightarrow \gamma + G$. (fig. 1.3).
- (3) Double pomeron exchange at very high energies, where the gluons surrounding each proton fuse to form mesons in the central region away from beam and target: $pp \rightarrow pGp$ (fig. 1.4).

Since gluons do not have an electrical charge, glueball production should be suppressed in $\gamma\gamma$ collision.

1.4 The Scalar Mesons

Besides the $I = 1/2$ states ($K_0^*(1430)$), the identification of the other members of the scalar meson nonet is controversial. Problems are due to the close masses

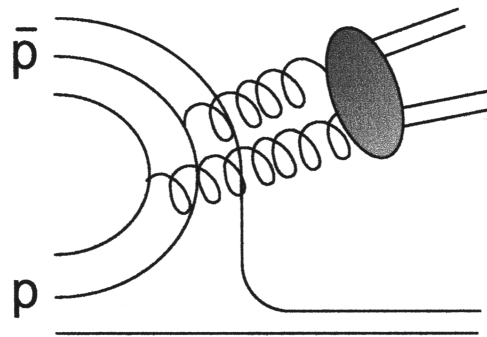


Figure 1.2: Proton-antiproton annihilation.

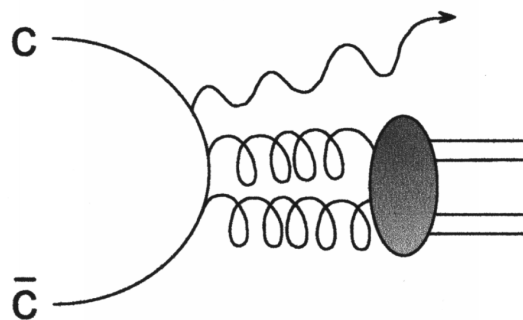
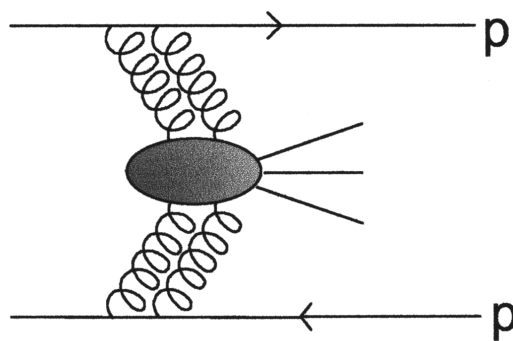
Figure 1.3: Radiative J/ψ decay.

Figure 1.4: Central production via gluons in hadron interaction.

and large widths of the $I = 0, 1$ states. The first possible configuration taken into consideration was [2] (see fig. 1.5),

$$1^3P_0 : a_0(980), f_0(980), f_0(1370), K_0^*(1430).$$

The observation of other 0^{++} resonances ($a_0(1450)$ [13], [14], $f_0(1500)$ [15], [14], $f_j(1710)$ [28]) makes other configurations possible, if the $f_j(1710)$ has spin 0:

$$1^3P_0 : a_0(1450), f_0(1370), f_0(1720), K_0^*(1430).$$

There are additional indications that the $a_0(980)$ and the $f_0(980)$ cannot be considered as members of the $q\bar{q}$ scalar nonet. Weinstein and Isgur studied a $qq\bar{q}\bar{q}$ non-relativistic potential model using a four-particle Schroedinger equation [18]. They conclude that such bound states do not exist with the exception of two weak 0^{++} states with $I=0,1$, with a meson-meson structure similar to the one of the deuteron. The mass degeneracy of the $a_0(980)$ and the $f_0(980)$, just below $K\bar{K}$ threshold and their decay to $K\bar{K}$ suggest to identify these states as bound $K\bar{K}$ systems.

1.4.1 The $f_0(1500)$

The Crystal Barrel collaboration at CERN has performed a systematical analysis of $\bar{p}p$ annihilation into neutral final states involving π , K , η , and η' .

The $f_0(1500)$ state was seen decaying into $\pi^0\pi$, $K\bar{K}$, $\eta\eta$ and $\eta\eta'$, and 4π [19] [20] [22] [21]. The following branching ratios for the production and decay of the $f_0(1500)$ were determined:

$$B[\bar{p}p \rightarrow f_0(1500)\pi^0, f_0(1500) \rightarrow \pi^0\pi^0] = (12.7 \pm 3.3) \times 10^{-4}$$

$$B[\bar{p}p \rightarrow f_0(1500)\pi^0, f_0(1500) \rightarrow \eta\eta] = (6.0 \pm 1.7) \times 10^{-4}$$

$$B[\bar{p}p \rightarrow f_0(1500)\pi^0, f_0(1500) \rightarrow \eta\eta'] = (1.6 \pm 0.4) \times 10^{-4}$$

and [23] [22]:

$$B[\bar{p}p \rightarrow f_0(1500)\pi^0, f_0(1500) \rightarrow K_L K_L] = (1.13 \pm 0.09) \times 10^{-4}.$$

Amsler and Close [24] tested the SU(3) flavour symmetry breaking and meson form factors on the well known 2^{++} nonet. Following this model Godfrey and Napolitano [4] derived, the following relative decay rates, corrected for two-body phase space ("invariant couplings"), of the $f_0(1500)$ to different pairs of pseudoscalar mesons

$$B(f_0(1500) \rightarrow \pi\pi : KK : \eta\eta : \eta\eta') = 5.1 \pm 2.0 : 0.71 \pm 0.21 \equiv 1 : 1.3 \pm 0.5$$

where all the charge combination of $\pi\pi$ (KK) are accounted for by multiplying the branching ratio by 3 (4).

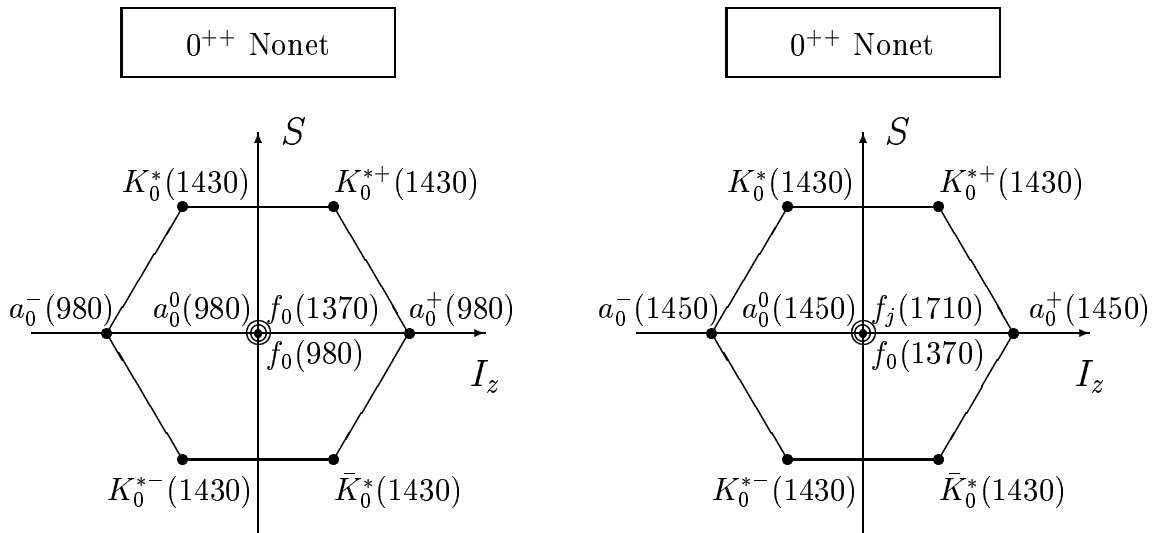


Figure 1.5: Different hypothetical configurations of the lowest-lying scalar nonet states ($J^{PC} = 0^{++}$).

The $f_0(1500) \rightarrow K\bar{K}$ is inconsistent with an $s\bar{s}$ member of a nonet. This led Amsler and Close to consider it as a candidate for the scalar glueball. However, if it is a pure glueball, one should expect the coupling 3:4:1:0 while the decay to $K\bar{K}$ is strongly suppressed with respect to $\pi\pi$. It is however consistent with a $n\bar{n}$ meson.

Using first order perturbation theory, Amsler and Close [24], argue that this problem is related to a further scalar state $f'_0(1500-1800)$ which couples strongly to $K\bar{K}$, $\eta\eta$, $\eta\eta'$. The decay properties of the $f_0(1500)$ are compatible with a ground state glueball mixed with the nearby $n\bar{n}$ and $s\bar{s}$ states of the 0^{++} nonet.

According to this picture and assuming that the $f_0(1370)$ is the $n\bar{n}$ member an $s\bar{s}$ state in the 1500-1800 mass region was needed. A possible candidate is the $f_j(1710)$, even though this state can be also identified as the lowest-lying scalar glueball [11].

1.4.2 The $f_j(1710)$

The $f_j(1710)$ has been seen first by the Crystal Ball collaboration in $J/\psi \rightarrow \gamma\eta\eta$ and was called θ . The analysis preferred a 2^{++} over 0^{++} , and it was considered the prima candidate for a glueball, because the 2^{++} ground state of the tensor nonet was already identified.

Particularly interesting was the fact that a tensor, at 1713 MeV, was observed by the WA76 collaboration [25] in the K^+K^+ mass distribution of the central production $pp \rightarrow p_f(K^+K^-)p_s$ at 300 GeV/c and not in the two photon collision [27] (see fig. 1.6): this showed that $f_j(1710)$ had characteristics to be a glueball state. The $f'_2(1525)$ and the $f_j(1710)$ are evident in both the radiative decay [29] and in central production, while in the $\gamma\gamma$ collision around 1.5-1.8 GeV there is

only one enhancement that can be attributed to the $f'_2(1525)$.

Successively other experiments (MARK III) gave contradicting results on the spin of this resonance. A reanalysis of the data from this experiment in $J/\psi \rightarrow \gamma(\pi^+\pi^-\pi^+\pi^-)$ [28] resolved two resonances, a 2^{++} at 1640 MeV and a 0^{++} at 1750 MeV.

The BES collaboration [29] found a scalar at 1781 MeV and a tensor with a mass of 1696 MeV.

Very recently the PDG lists the $f_j(1710)$ with $j = 0$ at a mass of 1715 ± 7 MeV and a width of 125 ± 12 MeV. The controversy on the spin it is mainly resolved by a recent re-analysis of the centrally produced WA76/WA102 K^+K^- final state which shows evidence for peaks in the S-wave at ~ 1505 and at ~ 1710 MeV [30]. In the previous attempt the angular distribution in the 1.5 and 1.7 GeV mass intervals were studied [25]. The two regions were found to be similar and they concluded that the signal at 1.7 GeV was two two because they assumed that the signal at 1.5 GeV was due to the $f'_2(1525)$. However in a recent WA102 analysis [31] showed that the $f_0(1500)$ had a large component in the 1.5 GeV region.

An analysis of the Crystal Barrel data revealed [32] a clear peak in the $\eta\eta$ invariant mass in the $\bar{p}p \rightarrow \pi^0\eta\eta$ reactions at \bar{p} momentum from 600 to 1200 MeV/c. It has a mass of 1770 MeV and a scalar was preferred, but its existence was not confirmed at higher momentum [33].

1.5 The Physics Goals of the Present Analysis

The present work investigates antiproton-proton annihilation into $K^+K^-\pi$ final states at an initial \bar{p} momentum of 900 MeV/c and 1642 MeV/c

$$\bar{p}p \rightarrow K^+K^-\pi^0$$

The large amount of data collected with the Crystal Barrel 4π detector allows to perform an appropriate analysis of this charged kaonic channel. On the other hand, the high number of initial states for annihilation in flight requires to develop an appropriate simplification of the partial wave analysis.

It is mandatory to confirm the spin of the $f_0(1710)$ as well as its mass and width. The purpose of this work is to clarify the nature of the $f_0(1500)$ and of the $f_0(1710)$ from the branching ratio in $K\bar{K}$ relative to other channels ($\pi\pi, \eta\eta, \eta\eta'$). Current pictures see each of this resonances as a mixture of a glueball and an $s\bar{s}$ state, so we expect to have important contributions in this channel. The formalism of the partial wave analysis has include any possible interference terms due to $f'_2(1525)$ which can have an effect on the observed intensity.

In the reaction $\bar{p}p \rightarrow K^+K^-\pi^0$ both $I = 0, 1$ K^+K^- states are allowed. This complicate the analysis. In order to determine the contribution of the I=0 (eg. $f_2(1270)$) and of the I=1 counterpart of the corresponding nonet (eg. $a_2(1320)$) a high resolution is required. To improve the resolution a cross-check of the calibration constant of the detector that were used for annihilation at rest will be performed.

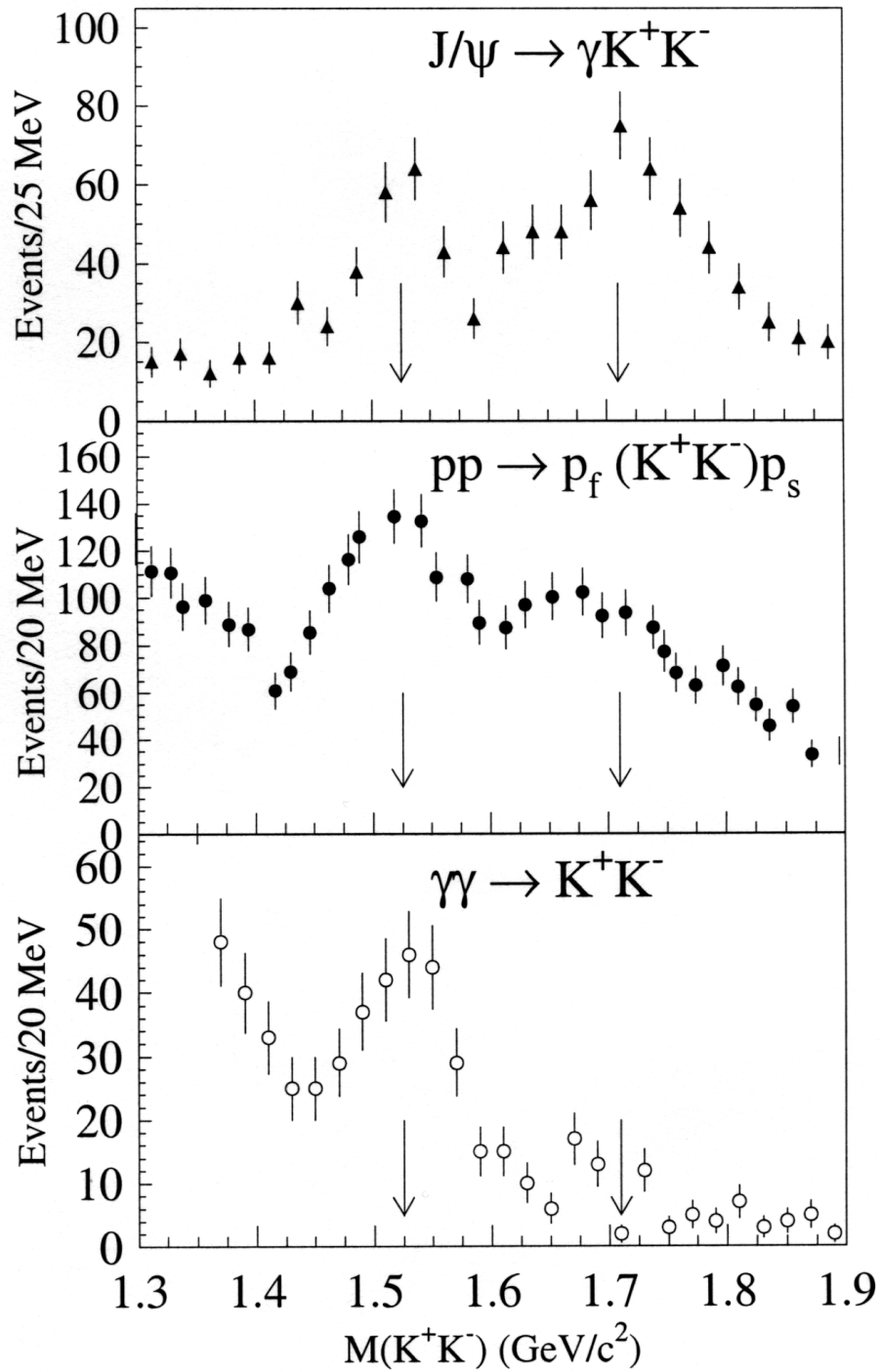


Figure 1.6: [4] Invariant K^+K^- mass distributions in different reactions: $J/\psi \rightarrow \gamma(K^+K^-)$ [29], $pp \rightarrow p_f(K^+K^-)p_s$ [26] and $\gamma\gamma \rightarrow K^+K^-$ [27]. The arrow indicates 1525 MeV and 1710 MeV

Chapter 2

The Crystal-Barrel Experiment at LEAR

2.1 The Production of Antiprotons

The advent of the Low-Energy-Antiproton-Ring facility at CERN, in the south hall of the CERN Proton Synchrotron (PS) (s. Fig. 2.1), enabled the production of intense and extremely pure beams of antiprotons. Antiprotons are extracted from the Antiproton Accumulator (AA) at the nominal momentum of 3.5 GeV/c, decelerated in the PS down to 0.6 GeV/c and injected in the LEAR [34]. Stochastic beam-cooling techniques [35] damp coherent betatron oscillations and permit the compression in phase space before the deceleration cycle in the PS and in the LEAR, without relevant losses of antiprotons.

The LEAR feeds the experimental area with $10^6 \bar{p}/s$ with ultra-slow ejection periods lasting typically 10^3 s. The momentum of the beam is then adjusted between 0.1 and 2 GeV/c, with a dispersion of $\Delta p/p \sim 10^{-4}$ and with an intensity independent of the momentum chosen. The high antiproton rate and a beam splitter permit to feed two out of the four experimental locations. For annihilations in flight the antiproton rate is increased to $3 \times 10^5 \bar{p}/s$ to reach a similar annihilation rate at rest of typically 3000 \bar{p}/s .

2.2 The Crystal-Barrel Detector

The Crystal-Barrel detector was the first low-energy physics universal 4π detector involving the simultaneous efficient detection and high precision measurement of charged mesons and photons [36].

Antiprotons from LEAR enter the apparatus (Fig. 2.2) along the symmetry axis of a solenoidal magnetic field of 1.5 T. Antiprotons at low momenta (0.2 GeV/c) lose energy by ionization and stop in the center of the 44 mm long liquid hydrogen target (Fig. 2.3).

In front of the target a segmented silicon diode antiproton counter is located. It allows also to focus the beam and provides the start signal for valid events.

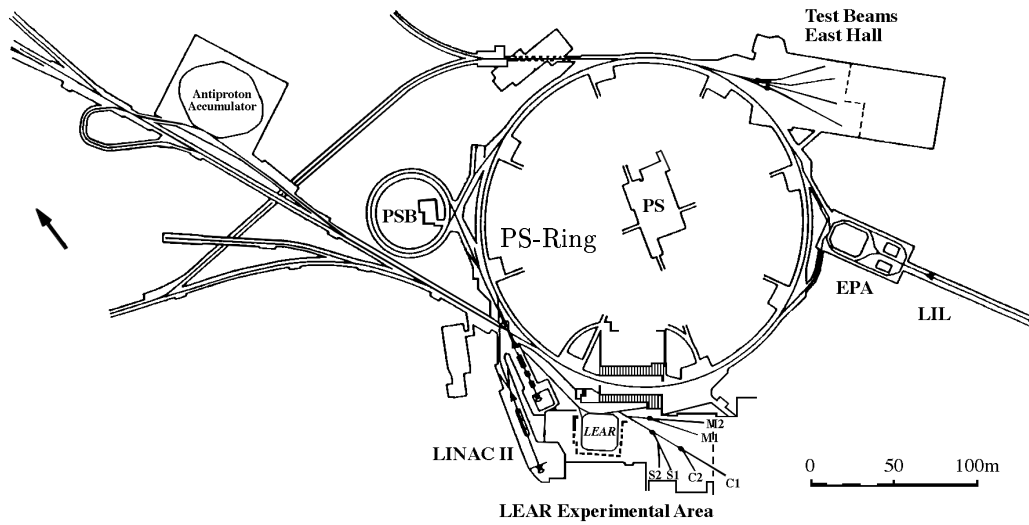


Figure 2.1: The CERN Antiproton Complex. LEAR feeds the experimental area where the Crystal-Barrel-Experiment is located (C2) with antiprotons.

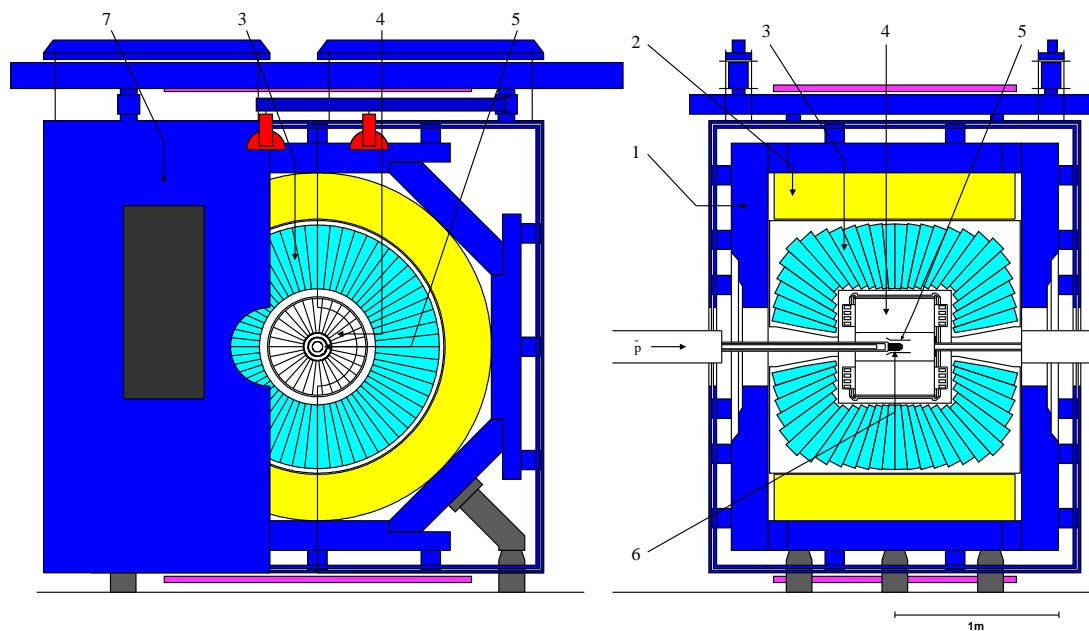


Figure 2.2: Side and front layout of the Crystal-Barrel Detector:
 1 magnet yoke, 2 magnet coils, 3 CsI barrel, 4 jet-drift chamber, 5 silicon-vertex detector, 6 target, 7 one half of the endplate.

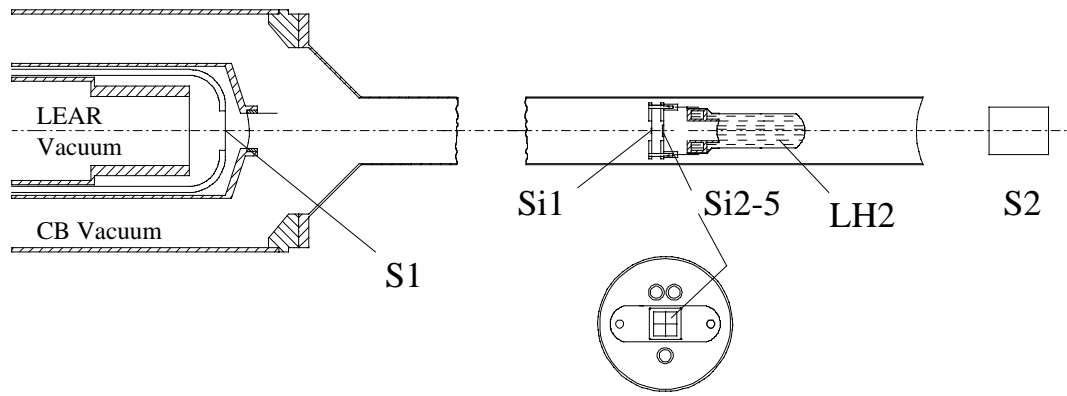


Figure 2.3: Overall layout of the beam counters and liquid hydrogen target. The enlarged scale is a front cut of the segmented silicon counter.

For annihilation at rest the antiproton captured from the H_2 molecule in a high Rydberg level, dissociates the molecule and forms a protonium atom. Annihilation occurs mainly from S-states of the $\bar{p}p$ atom. They are reached by radiative deexcitation or Stark-mixing. [37].

This description is not adequate for annihilation in flight. At higher momentum only a small part of the antiprotons annihilate. The rest transverses the target without interaction. For this reason a second counter is placed behind the target: it gives a veto to the signal of the front-silicon diode. Only a signal of the front counter in correspondence with a missing veto means that an annihilation in flight occurs.

An additional reaction, because of the higher rate of incoming antiprotons in flight, during the opening of the gate circuits can occur. This type of event is named *pile-up*.

2.3 The Silicon-Vertex Detector

After 1994 the inner part of the detector surrounding the target, the proportional wire chamber, was replaced by a silicon microstrip detector [39]. It was constructed to enhance the number of events with secondary vertices from $K_s \rightarrow \pi^+\pi^-$ by means of a special trigger with the jet drift chambers; it also improves the momentum and vertex resolution of the tracks originating within the target (see fig. 2.4).

It consists of 15 overlapping modules of 128 microstrips each. They are positioned at a mean distance of 1.2 cm from the axis and at a distance of only 4 mm from the target. They provide a full azimuthal coverage of the target; in the polar angle the region between 15° and 145° is covered. The backplane signals are used as a fast first level trigger ($0.5 \mu s$), while the preamplified strip-side signal determines the charged particle multiplicity.

2.4 The Jet-Drift Chamber

The cylindrical jet-drift chamber surrounds the silicon vertex detector. It is divided into 30 azimuthal sectors and has 23 radial sense wires (see fig. 2.5). The wires are placed at a distance of 8 mm and are staggered by 0.2 mm. This technique allows to resolve the left-right spatial ambiguity during the reconstruction. The curvature of the track allows a transverse momentum resolution of 2% and 12% at 0.1 and 1.0 GeV/c, respectively. The resolution of the z-coordinates, measured by charge division, is 7-9 mm. Every wire is 399 mm long so that the solid angle covered is 93% of 4π if at least three layers are required for a track fit.

Sectors are separated by a plane containing 45 wires that form the cathode. The voltages on these wires are chosen using the GARFIELD drift chamber simulation program [38] and increase almost linearly with the radius from -4775 V for the inner wires to -2750 V for the outer wires in order to have an approximately homogeneous drift field of 1100 V/cm. Because of the dependence of the electron drift velocity on the gas density and composition, a "slow control" of the gas temperature, atmospheric pressure and gas mixture is performed.

A "slow" gas mixture of 90% CO_2 and 10% of isobutane (C_4H_{10}) is used at ambient pressure at CERN and at a regulated room temperature of $25^\circ C$. A spatial r, ϕ resolution of $100 \mu m$ is reached. The determination of the differential energy losses of the charged tracks allows to distinguish pions from kaons up to a momentum of 500 MeV/c.

2.5 The Electromagnetic Calorimeter

The design of the electromagnetic calorimeter allows a solid angle coverage of 87% of 4π . It consists of a barrel of 1380 crystals, each covering 6° in both polar and azimuthal angle with the exception of the crystals close to the beam axis with a higher azimuthal angular range of 12° (Fig. 2.6).

The CsI thallium doped crystals have similarly high resolution photon detection properties to NaI scintillators but a shorter radiation length ($L_R = 1.86 cm$) and require a smaller volume. They are 30 cm long corresponding to 16.1 radiation lengths (Fig. 2.7). They allow to detect photons over an energy range from 20 MeV to 2000 MeV. To avoid conversion of photons, low-Z material for the supporting structures had to be chosen. Every crystal is covered by a 0.1 mm titanium and is suspended with a minimum load on the inner aluminum wall.

Because of the strong magnetic field the use of conventional photomultiplier tubes is precluded. A single silicon photodiode, placed on the edge of the wavelength shifter, functions normally in a high field. This configuration improves the efficiency; leakage from the rear of the crystal is less than 1% up to photon energies of 2 GeV.

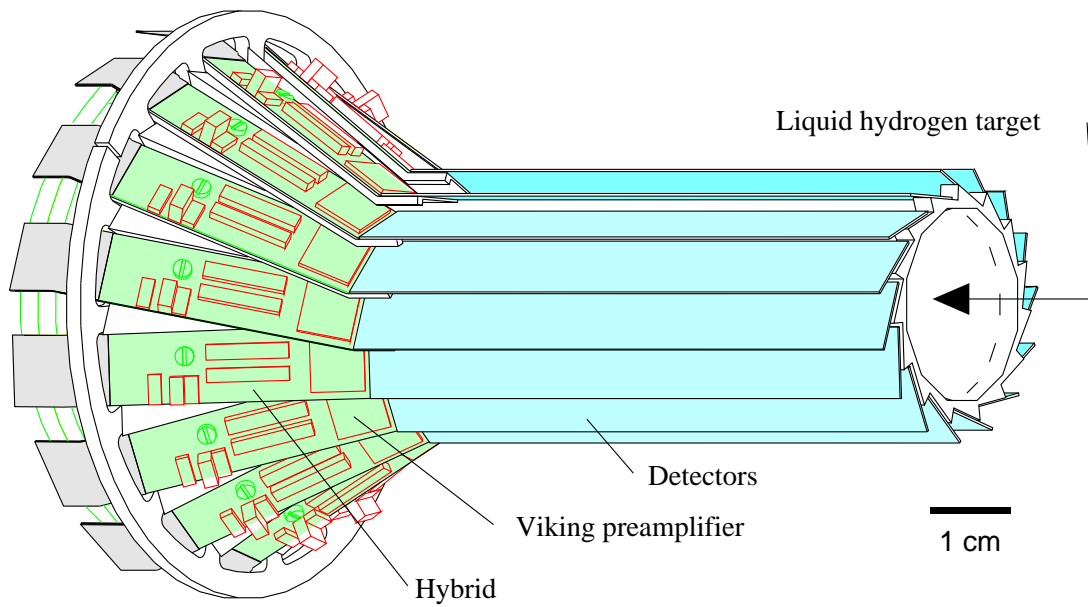


Figure 2.4: The Silicon-Vertex Detector (SVX).

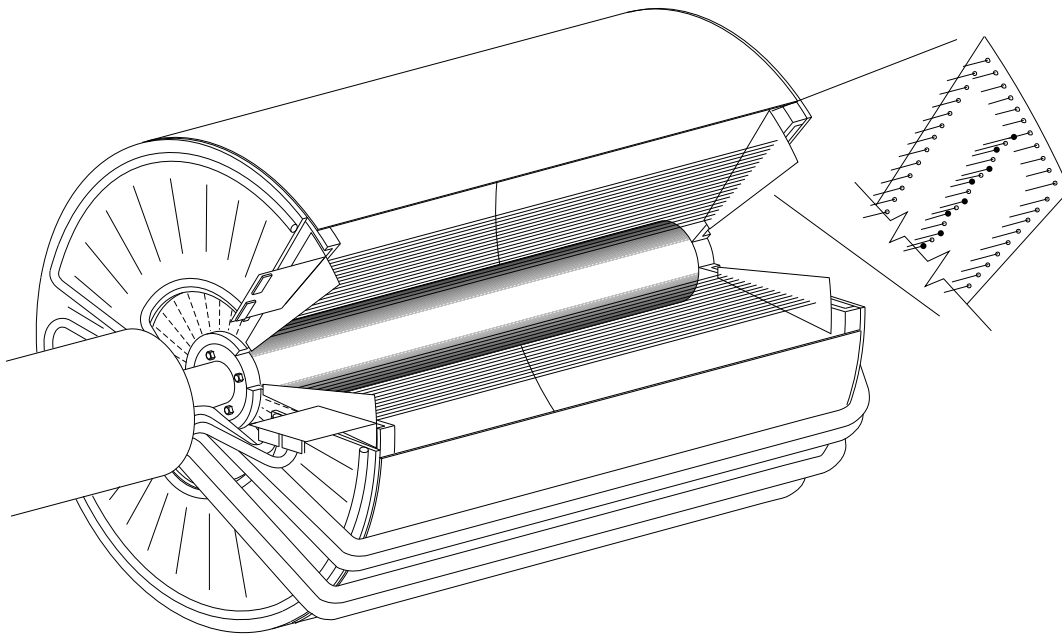


Figure 2.5: The Jet-Drift Chamber. In the expanded picture the staggering is shown exaggerated for clarity.

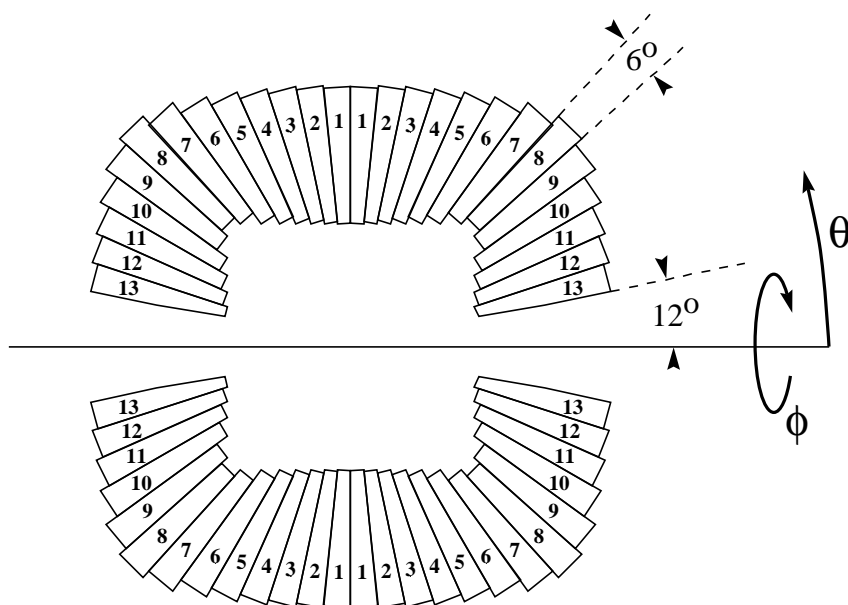


Figure 2.6: Cross section of the electromagnetic calorimeter. The range of the polar angle covered by the 1380 CsI modules is $12^\circ \leq \theta \leq 168^\circ$.

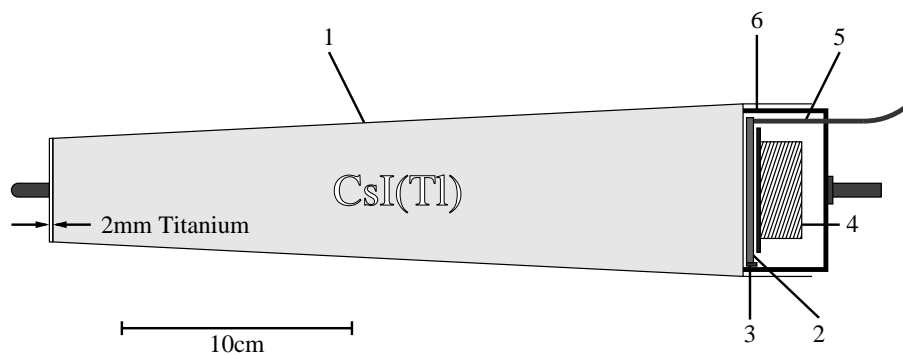


Figure 2.7: Cross section of a CsI(Tl)-module 1: titanium can (0.1 mm thick), 2: wavelength shifter, 3: photodiode, 4: preamplifier, 5: light fiber of the light pulser system, 6: brass cover.

2.6 Data Acquisition and the Trigger System

The global event builder synchronizes the data of each detector and sends the basic information of the accepted event to a μ -VAX for the on-line event analysis. During the monitoring a rapid event reconstruction is performed in order to check the quality of the data for a given trigger condition. The basic information is recorded in ZEBRA [40] data banks. To minimize the effect of the "dead time" during data acquisition, three different trigger levels are defined.

The **level 0** also called "minimum bias" is defined by the start signal of the beam entrance counters (S_1 and $S_{i_{1-5}}$) and, only for annihilation in flight, by the veto scintillator S_2 behind the target. To check the proper operation of the detector parts, during the time when no antiproton beam is present, the source of this trigger can be replaced using additional cosmic ray counters or light pulser.

The **level 1** combines the level 0 trigger with the information on the charged multiplicity that comes independently from the SVX and the JDC. A multiplicity increase in the JDC is defined by a coincidence between different layers.

The **level 2** trigger is a software trigger and uses the information of the CsI crystal to enhance typical final states containing π^0 and η . For this purpose a search for local maxima in the energy deposition of all the crystals, and a corresponding calculation of the photon energies and of the invariant masses of $\pi^0 \rightarrow \gamma\gamma$, $\eta \rightarrow \gamma\gamma$ is performed.

When the required trigger conditions are satisfied, the ZEBRA data bank is filled with the remaining information of the event and all the data are written on DLT tapes.

In the present work the analysis of in flight data, at 900 MeV/c and at 1642 MeV/c of the incoming antiproton into $K^+K^-\pi^0$, means two charged tracks in the final state; this requires trigger level 1 with charged multiplicity two in the JDC (2-prong) and a multiplicity 2,3 in the SVX. Because of the forward Lorentz boost for annihilation in flight a multiplicity increase in the JDC is defined by a hit in the layer 9/10 only.

Examples of the main trigger conditions used for 2-prong or 0-prong data in the Oct-Dec 96 run are illustrated in table 2.1 [41].

Run Time	\bar{p} -momenta (MeV/c)	Trigger name	SVX multiplicity	JDC multiplicity	Events
8.10-14.10 1996	900	2 - <i>Pr.default</i>	2-3	2 in layer 9/10	19.4M
11.10,15-17.10 1996 and 28.10-4.11 1996	900	0 - <i>Pr_nm.900</i>	no SVX	0 in layer 9/10 and 0 in layer 2/3	18M
8-11.11,14-18.11 1996 and 2-8.12 1996	1642	0 - <i>Pr_nm.1642</i>	no SVX	0 in layer 9/10 and 0 in layer 2/3	11.2M
6-9.12 1996	1642	2 - <i>Pr.default</i>	2-3	2 in layer 9/10	12.4M

Table 2.1: Main trigger conditions used in the runs during Oct-Dec, 1996.

No restrictions in the number of clusters in the electromagnetic calorimeter (i.e. the number of photons in the final state) are given for these runs.

2.7 The Calibration and Event Reconstruction

The purpose of the off-line reconstruction is to identify the particles in the final state for each event and to measure, with the best resolution, the corresponding energy/momentum 4-vectors.

A rapid guess of the proper calibration constant is obtained making a reconstruction of a limited number of events in simple final state configurations. This new set of constants that are stored in one file, the *database*, is used in turn to reconstruct a larger sample of events with more complicated topologies.

The reconstruction code is written in Fortran 77 and uses the CMZ management system [42].

2.7.1 JDC calibration

In correspondence of every hit the drift time of the electrons to the closest wire and the preamplified amplitudes A_+ and A_- , measured at the $+z$ and $-z$ end, are correlated to give the exact knowledge of the position of the hit. The distance of the hit from the wire is given by a pair of coordinates in the $\rho\phi$ plane,

$$x(t) = \int_{t_1}^{t_2} v_d dt \quad y(t) = y(x(t)) \quad (2.1)$$

where v_d is the drift velocity of the electrons, t_1 is the time relative to the start of the event defined by the beam entrance counters and t_2 is defined when the measured amplitudes are larger than a given threshold.

2.7.2 Z-calibration

The wires have an electrical resistance. Hence the z -coordinate of the hit is obtained using the charge division

$$z = z_0 + z_l \frac{(A_+ - \alpha A_-)}{(A_+ + \alpha A_-)} \quad (2.2)$$

where

z_0 = center of the signal wire

z_l = electrical wire length

α = correction of the preamplification gain at either end of the wire

A_+, A_- = the two signal amplitudes at the $+z$ and $-z$ end.

In the first step of the z -calibration the proper values of these constants are obtained turning the magnetic field off. In this case the z -coordinates can be fitted with straight lines converging to a common point in the target. The fitting procedure, using the MINUIT minimization program [43] for more than 50000 events, is iterated until a stable set of all calibration constants is obtained. Typical values are: $0.9 < \alpha < 1.1$, $z_0 \sim 0$, $z_l \sim 23.7$ cm.

It is important to notice here that the amplifier input impedance introduces a non linearity near the end of the sense wires. For annihilation in flight the fitted tracks are, because of the Lorentz boost, generally closer to the end of the wire. In this case the electrical wire length needs an additional correction factor.

2.7.3 $\rho\phi$ -calibration

The $\rho\phi$ -calibration is performed by fitting two-body final states $\pi^+\pi^-$ and K^+K^- [44]. Because of energy/momentum conservation the pions and kaons have a momentum of 927.8 MeV/c and 797.9 MeV/c respectively. The two charged tracks can be treated as a single helix, reducing the number of constraints.

Using the GARFIELD simulation program [38], a set of tables of coordinates as a function of the drift times, that in turn depends on the drift velocities, are obtained for different values of atmospheric pressure, gas temperature. During the processing of the data the exact values of the $x(t)$, $y(t)$ coordinates in eq. 2.1 are obtained by interpolating between the drift times of the corresponding tables.

The hits are then processed by using the pattern recognition algorithms. The tracks can be inside one single sector or more. For the latter case, after an initial loose fit in the ρz projections with disconnected segments, the fitting procedure tries to match these segments in the $\rho\phi$ plane with a single circle. A different algorithm that takes the staggering into account to solve the left-right ambiguity is used to solve tracks within one single JDC sector. At the end, the final track is fitted with a helix in the full three-dimensional space. Only events which pass the helix fit with a probability greater than 1% are accepted. An accuracy of $\sigma_p/p = 2.0\%$ on the π momentum is obtained at 927.8 MeV/c.

2.7.4 dE/dx calibration

Between the sum of the amplitudes at either end of the wire and the differential energy loss of the charged particles along a length dx of a driftcell there is a linear dependence

$$\frac{dE}{dx} = c(A_+ + \alpha A_-) \quad (2.3)$$

To determine the 690 different factors for all wires tracks in a minimum ionizing range ($\beta\gamma \approx 4$) are fitted. The correspondence with the expected energy loss calculated with the Bethe-Bloch formula is obtained multiplying the single amplitudes with a global factor.

2.7.5 Electromagnetic calorimeter calibration

The analog signal from each crystal is digitized by two ADC systems. The LeCroy FERA with 2048 channels is used to extend the energy range beyond 400 MeV, while the LeCroy 2282 with 4096 channels is more sensitive at low energies. The

two systems overlap up to 400 MeV. This allows the first system to be calibrated in terms of the second one and to reduce the non-linearities of the FERA system at low energies.

An initial starting point for the calibration of each crystal is performed using the minimum ionizing peak method. A high energy charged particle can traverse the whole length of a crystal losing energy only by electromagnetic interaction. For pions this corresponds to 170 MeV. 10^6 minimum bias events with the magnetic field off provide a high statistical accuracy but has a systematical deviation because the energy deposited by a charged meson has a different pattern respect to a photon.

Another high statistics method for the crystal calibration using no extra beam time is performed histogramming the invariant masses of pairs of photons. A sharp peak at 135 MeV corresponds to the π^0 mass from the decay $\pi^0 \rightarrow \gamma\gamma$.

All-neutral events with a total energy deposit equivalent to twice the proton mass and with only 8 gamma to reduce the combinatorial background are selected. For every hitted crystal a histogram is filled with the mass-squared values of the photon in combination with all other detected photons. The position of the peak, obtained fitting the histogram with a gaussian and a polynomial for the combinatorial background, can be shifted to the correct value changing the pre-calibration constant for that crystal and using the pre-calibrated values for all the others. This process is iterated until a correct π^0 mass is obtained for all crystals and a new set of calibration constants is determined.

2.7.6 Photon reconstruction

During the reconstruction a search for a local maxima inside a cluster of neighboring crystals of energy above 1 MeV is performed.

The associated total energy of all crystals belonging to the same cluster corresponds to the particle energy deposit (PED). If in a cluster more than one local maximum is found, the cluster energy E_{cl} is shared according to

$$E_{PED} = \frac{E_9}{\sum_{i=1}^9 E_i} E_{cl}, \quad (2.4)$$

where E_9 is the energy of the central crystal corresponding to the local maxima and the sum is extended to that crystal and all the other 8 neighbours. In the present work the following cuts on the crystal, cluster, PED and central crystal energies are performed to reduce the number of secondary showers arising from statistical fluctuations or electromagnetic splitoffs :

$$\begin{aligned} E_{crystal} &= 1.MeV \\ E_{cluster} &= 4.MeV \\ E_{PED} &= 10.MeV \\ E_{central} &= 13.MeV \end{aligned} \quad (2.5)$$

In the standard analysis up to 1992 any PED with less than 20 MeV was treated as a splitoff while every PED over 20 MeV was considered as a photon. This was inaccurate because there are splitoff above 20 MeV and photons below 20 MeV.

Charged tracks can also have a PED. These clusters are identified during the global reconstruction matching the PED with the charged tracks. In addition charged tracks can also generate splitoffs, known as hadronic splitoffs.

Two routines were developed to identify electromagnetic and hadronic splitoffs. "Dolby-C" was developed for 0-prong triggered data [45], so it is more specific for finding electromagnetic splitoffs. The procedure is based on the observation of the topological distribution of a pair of PEDS and of the "asymmetry-opening angle plot".

In the calculation of the invariant mass of a π^0 decaying into two photons the angle between the two photons is related to their energy $E_{\gamma 1}$, $E_{\gamma 2}$ according to

$$\begin{aligned} m_{\pi^0}^2 &= 2E_{\gamma 1}E_{\gamma 2}(1 - \cos \psi) \\ &= 4E_{\gamma 1}E_{\gamma 2}\sin^2(\psi/2) \\ &= \frac{1}{2}E^2(1 - A^2)(1 - \cos \psi) \end{aligned} \quad (2.6)$$

where ψ is the angle subtended at the decay vertex in the lab system, $E = E_{\gamma 1} + E_{\gamma 2}$ is the total pion energy and A is the energy decay asymmetry

$$A = \frac{E_{\gamma 1} - E_{\gamma 2}}{E_{\gamma 1} + E_{\gamma 2}} \quad (2.7)$$

For a given E the equation 3.4 is a hyperbola

$$1 - A^2 = \frac{\text{const.}}{(1 - \cos \psi)} \quad (2.8)$$

In the plot of $1 - A^2$ vs $1 - \cos \psi$, Dolby-C interprets the area below the hyperbola corresponding to a pion energy of 940 MeV, that is the maximum energy allowed for pions for annihilation at rest, as being due to a splitoff. Obviously this procedure has a limit for annihilation in flight.

The TAXI logic of the hadronic splitoff recognition is based on purely topological grounds and a new clustering algorithm that defines in a different way the neighborhood of a crystal [46]. This technique extends the possible area of hadronic splitoffs in the neighborhood of a matched PED. In a MC simulation of collinear tracks using the FLUKA[56] shower simulation an agreement with the data is reached asking a minimum energy of the central crystal of 13 MeV. In a split-off removal in $\pi^+\pi^-\gamma\gamma\gamma$ events the TAXI logic works efficiently when it is used in combination with Dolby-C removing PEDS, having the central crystal energy smaller than 13 MeV and/or $E_1/E_9 \geq 0.96$.

In the present work the final state with $\pi^+\pi^-\pi^0$ has a similar and more simple configuration than $\pi^+\pi^-\gamma\gamma\gamma$, and the same procedure during the reconstruction showed a successful result at both initial \bar{p} momenta.

The TAXI logic cannot be applied for final states with more than three mesons. The probability to remove PEDS associated to photons instead of hadronic splitoffs increases with the number of photons.

2.7.7 Track reconstruction

During the initial pattern recognition tracks are fitted in the ρz plane with a straight line and in the $\rho\phi$ plane with a circle. The transversal impulse is given by

$$p_T = qBr, \quad (2.9)$$

where r is the circle radius, B the magnetic field and q is the charge. From the inclination in the ρz plane the longitudinal impulse is obtained

$$p_L = p_T \tan \lambda. \quad (2.10)$$

In the final step the track is fitted in the three-dimensional space with a helix using the following parametrization:

$$\begin{aligned} x_i &= \rho_0 \sin \Psi_0 + r(\cos \beta_i + s \sin \Psi_0) \\ y_i &= -\rho_0 \cos \Psi_0 + r(\sin \beta_i + s \cos \Psi_0) \\ z_i &= z_0 - r \cdot s \cdot \tan \lambda (\beta_i - \Psi_i - s \frac{\pi}{2}) \end{aligned} \quad (2.11)$$

where β_i is the azimuthal angle of the point (x_i, y_i, z_i) relative to the center of the helix. For every track we have 5 free parameters:

$\rho_0 z_0$: ρ, z coordinates of the closest approach of the helix to the origin

Ψ_0 : angle between the tangent to the helix in $\rho_0 z_0$ and the x axis

λ : inclination of the helix in the ρ, z plane

r : radius of the $\rho\phi$ projection of the helix

s : sign of the charge

This procedure has the disadvantage that the vertex is fitted against the constraints of the helix parameter rather than against the JDC/SVX hits. As a result the fitted track can move far from the original hits. In addition the fit program does not take into consideration the eventual charge conservation at the vertex, that is the case of $K^+K^-\pi^0$ and many other channels.

For these reasons a new vertex fitter was developed to fit also events with more than one vertex [48]. If N is the number of tracks the number of parameters is reduced, if $N \geq 2$, from $5N$ to $3 + 3N$ for the location of the vertex and the new helix parameters. The main advantage is that a negative and a positive track are fitted simultaneously.

The new helix parametrization is

$$\begin{aligned}
x(\beta) &= x_v - \frac{\cos\phi_0}{\alpha} + \frac{\cos(\phi_0 - s\beta_i)}{\alpha} \\
y(\beta) &= y_v - \frac{\sin\phi_0}{\alpha} + \frac{\sin(\phi_0 - s\beta_i)}{\alpha} \\
z(\beta) &= z_v + \frac{\tan\lambda}{\alpha}\beta
\end{aligned} \tag{2.12}$$

where (x_v, y_v, z_v) is the position of the vertex

α is the curvature of the track

ϕ_0 the position of the vertex referred to the center of the circle

β is a free parameter that varies from 0 at the vertex to ∞

λ and s here have the same definition as in 2.11

2.7.8 Photon energy correction functions

The sum of the energy E_{PED} of all crystals in a PED is not in general the same as the energy of the photon. The shape of the crystal, the penetration depth, the shower radius and energy leakings introduce non linearities in the calculation of the photon energy.

An estimate of the photon energy E_γ given by the energy of the PED and the position θ of the photon (the crystal configurations are symmetric with respect to the azimuthal angle) is obtained by a comparison of MC studies with experimental data.

The photon energy correction function is defined by

$$PECF = \frac{E_\gamma}{E_{PED}}. \tag{2.13}$$

For annihilation at rest 6 photons were generated using GEANT version 3.1415 [47] and the correction is separated into energy and θ dependent parts.

$$E_{MC} = E_\gamma = PECF \cdot E_{PED} = f(E_{PED})C(\theta)E_{PED} \tag{2.14}$$

By plotting $f(E_{PED})$ against E_{PED} we get the energy correction function and by plotting $C(\theta)$ against E_{PED} we get the correction factors for different crystal types.

On average C is about 1.016. The crystal type 13 with $C = 1.09$ and the crystal type 1 with $C = 1.038$ show the highest energy losses because of the holes and the aluminum plates.

The response of the photon of a fixed energy shows a tail at low energy. The result of the simulation for $f(E_{PED})$, taking the mean position of the response, is a cubic function of E_{PED} up to 250 MeV and a straight line for $E_{PED} > 250$ MeV. This function from Hessey's work [47] is drawn in fig. 2.8.

With these correction functions systematic shifts in the total energy of all neutral events depending on the number of photons in the event were removed.

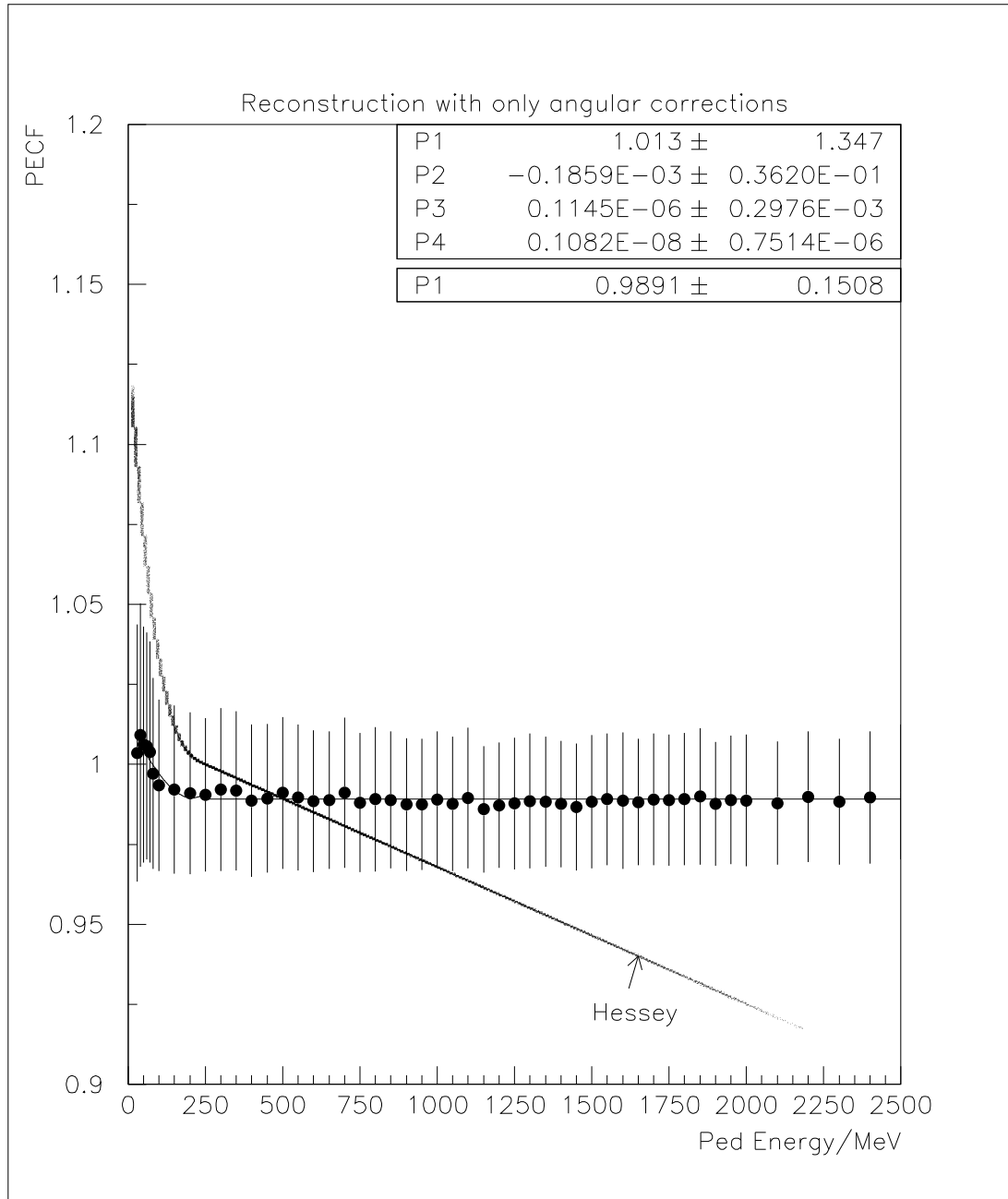


Figure 2.8: Photon Energy Correction Functions [49]. The Hessey correction function is a simulation that consider 6 photons at rest. A simulation of a single photon at higher energies shows a linear response of the crystals.

An extrapolation of the energy correction function to higher photon energies was not satisfactory for annihilation in flight. Several groups of the Crystal-Barrel collaboration found a non-negligible missing momentum, as compared to the antiproton beam from LEAR.

For this reason a new PECF was developed [49]. In this simulation, for simplicity, a single photon is isotropically distributed over a sphere at different energy using the GEANT version 3.21/05.

Assuming that the shower size is independent from the energy of the photon, the crystal correction factors of the previous MC can be used.

The simulation showed a linear behavior of the crystals at high energies (see fig. 2.8). The fitted PECF is again a cubic function of E_{PED} at low energies ($E\gamma < 200$ MeV) and a constant factor (~ 1.0) for $E\gamma > 200$ MeV.

An additional comparison between a MC simulation of $\bar{p}p \rightarrow \eta\pi^0$ at 1642 MeV/c and all-neutral data at 1642 MeV/c showed consistence with a constant factor close to unity for the PECF[49].

The difference between energy/momentum mean values of the simulation and the experimental data are of the order of 0.7%. The reconstructed invariant masses of π^0 , η of 133.8 and of 547.1 MeV respectively are in agreement with the PDG values of 134.97 and 547.3 MeV. The small discrepancy of the π^0 mass can be explained as follows: at high energies the angle ψ of the decaying photons in the lab. frame in eq 3.4 decreases. The two local maxima in one single cluster overlap. As a consequence the reconstructed angle is lower than the effective angle, and from eq. 3.4 it can be seen that the invariant mass is too.

The η has a higher invariant mass and in the allowed energy range the two PEDs are well separated. Therefore, it represents a better check of the calibration compared to the π^0 .

2.7.9 Electrical wire length scaling

As we pointed out before, every charged track produces also a hit in the electromagnetic calorimeter. If the calibration of the JDC and of the barrel is correct, the fitted charged track has to match the local maxima in the crystal.

Assuming that the $\rho\phi$ calibration is correct an analysis of events with charged track in the final state was carried out [50] in order to get the z -scaling in eq. 2.2.

As we can see in fig 2.9 this is equivalent to multiplying $\tan\lambda$ with a constant factor, that means in turn, from eq. 2.10, to scale the longitudinal momentum p_L .

Minimizing the distance between the entry point of the track into the barrel and the matched PED, a scaling factor of 1.06 for z_i is obtained.

An additional check of electrical wire length scaling can be obtained also by histogramming the $\pi^+\pi^-\pi^0$ invariant mass in final states with two tracks and 4 gammas [49]. A peak in the mass region of ~ 780 MeV can be attributed to the reaction $\bar{p}p \rightarrow \omega\pi^0$, $\omega \rightarrow \pi^+\pi^-\pi^0$.

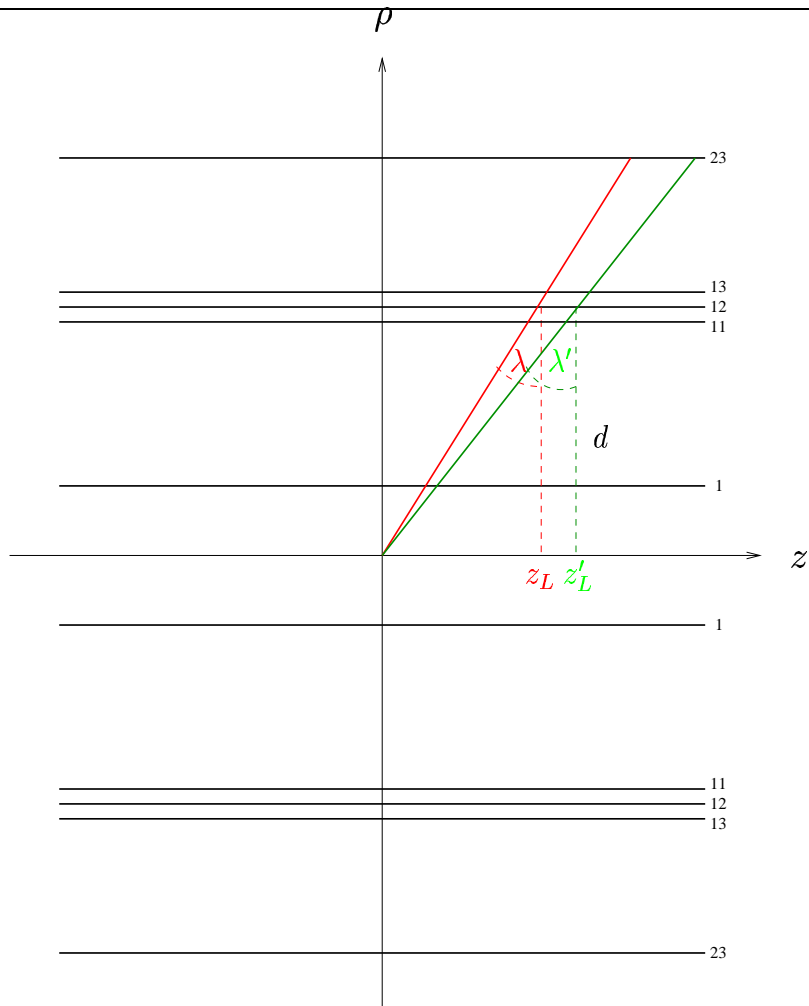


Figure 2.9: Electrical wire length scaling. The correct position z'_L of the hit along the wire is obtained by scaling the position $z = z_l \frac{(A_+ - \alpha A_-)}{(A_+ + \alpha A_-)}$: $\tan \lambda' = \frac{z'_L}{d} = 1.065 \frac{z_L}{d} = 1.065 \cdot \tan \lambda$.

Fitting the peak with a gaussian and a polynomial for the combinatorial background, the optimum of the $\omega(782)$ invariant mass at ~ 780 MeV is obtained in correspondence to an electrical wire length scaling of 1.065, that is in agreement with the previous estimate.

Chapter 3

Data Selection and Kinematic Fit

In this chapter we describe the criteria used to select $K^+K^-\pi^0$ final states from initial 2-prong data at 900 and at 1642 MeV/c recorded in October and December 1996 (see table 2.1).

The standard Crystal Barrel software and the version used for the data reconstruction are:

CBOFF 1.30/13: the "Offline Reconstruction Software" [51]

LOCATER 2.01/14: the "Chamber Reconstruction Software" [52]

BCTRAK 2.04/03: the "Crystal Data Reconstruction Software" [53]

GTRACK 1.37/01: the "Global Tracking Reconstruction Software" [54]

All Monte Carlo events are generated using the

CBGEANT 5.05/10 : the "Monte Carlo Generation Software" [57]

The initial version 4.06/03 [58] based on CERN GEANT 3.15 simulation tool has been modified to improve the speed with a new geometry definition and linked with the upgraded GEANT release 3.21/05 [59].

After an initial selection of all events a constraint fit is performed to improve the quality of the data [60]. It increases the resolution of the detector and allows also to test the hypotheses and the classification of the final states. In addition the kinematic fit is a powerful tool to find systematic errors.

3.1 Preselection

Because of the particular detector geometry, designed originally for annihilation at rest, the efficiency and the acceptance of the apparatus decrease as the initial antiproton momentum increases.

The selection criteria are similar to the one used for annihilation at rest but the conventional definition of "golden track" has to be modified for annihilation in flight in order to increase the acceptance in the forward direction.

Because of the Lorentz boost charged tracks have in average a lower number of hits. For annihilation at rest at least one hit in the first 3 layers and in the last 3 layers and in total, at least 15 JDC hits are required for a golden track. In flight the restriction on the last 3 layers is removed, while the restriction on the first 3 JDC layers is kept and a minimum number of only 10 hits is required. This

is useful to remove those events where additional short tracks are produced in a secondary reaction in the outer part of the detector ("backsplash"). In addition a golden track requires a helix fit with a $\chi^2 \leq 1.5$.

In summary, exactly two golden tracks are required during the initial preselection and their definition is

1. number of JDC hits ≥ 10
2. $\chi^2 \leq 1.5$
3. at least one hit in the first 3 layers

Requiring in addition a total charge equal to zero allows a quick rejection of those events where the left-right ambiguity of a charged track is not resolved correctly.

The spread of the energy of the photons over the neighbouring crystals limits the energy definition of the photons having the central crystal in the peripheral type 13 crystals. In fig. 3.1 an event of this type is displayed.

At 900 MeV/c only $\sim 10\%$ of the events passing the kinematic fit with a confidence level higher than 10% have at least one type 13 PED, so removing these events improves the quality of the data without affecting significantly the statistics (see table 3.1).

The amount of data lost because of the cut on type 13 crystals increases, because of the forward boost, to about $\sim 13.4\%$ at 1642 MeV/c. The lower acceptance in the forward direction at higher momentum and the lower amount of initial data does not permit to apply this cut at 1642 MeV/c.

The cuts on the crystal energies and the splitoff recognition software described in the previous chapter are applied to identify final states with two photons. The electronic noise is causing often a firing crystal with no hits in the neighbouring crystals. The frequency of such events can be estimated from the E_1/E_9 distribution in fig. 3.2.

The "golden gamma" definition is then:

1. no electromagnetic splitoff (Dolby-C)
2. no hadronic splitoff (Taxi)
3. $E_1/E_9 \leq .96$
4. central crystal energy $\geq 13MeV$

Exactly 2 golden gammas with no limits in the number of splitoffs are selected.

As we pointed out in the previous chapter for annihilation in flight the antiproton can annihilate at any point within the target region along the z-axis (see 3.3). The distribution is not flat because of the detector configuration.

When the two fitted tracks converge the coordinates of the vertex are known. In this case the information of the vertex coordinates is transferred for every event to the crystal reconstruction software. The direction cosines of the photons are then calculated with respect to these vertex coordinates improving their corresponding momentum resolution.

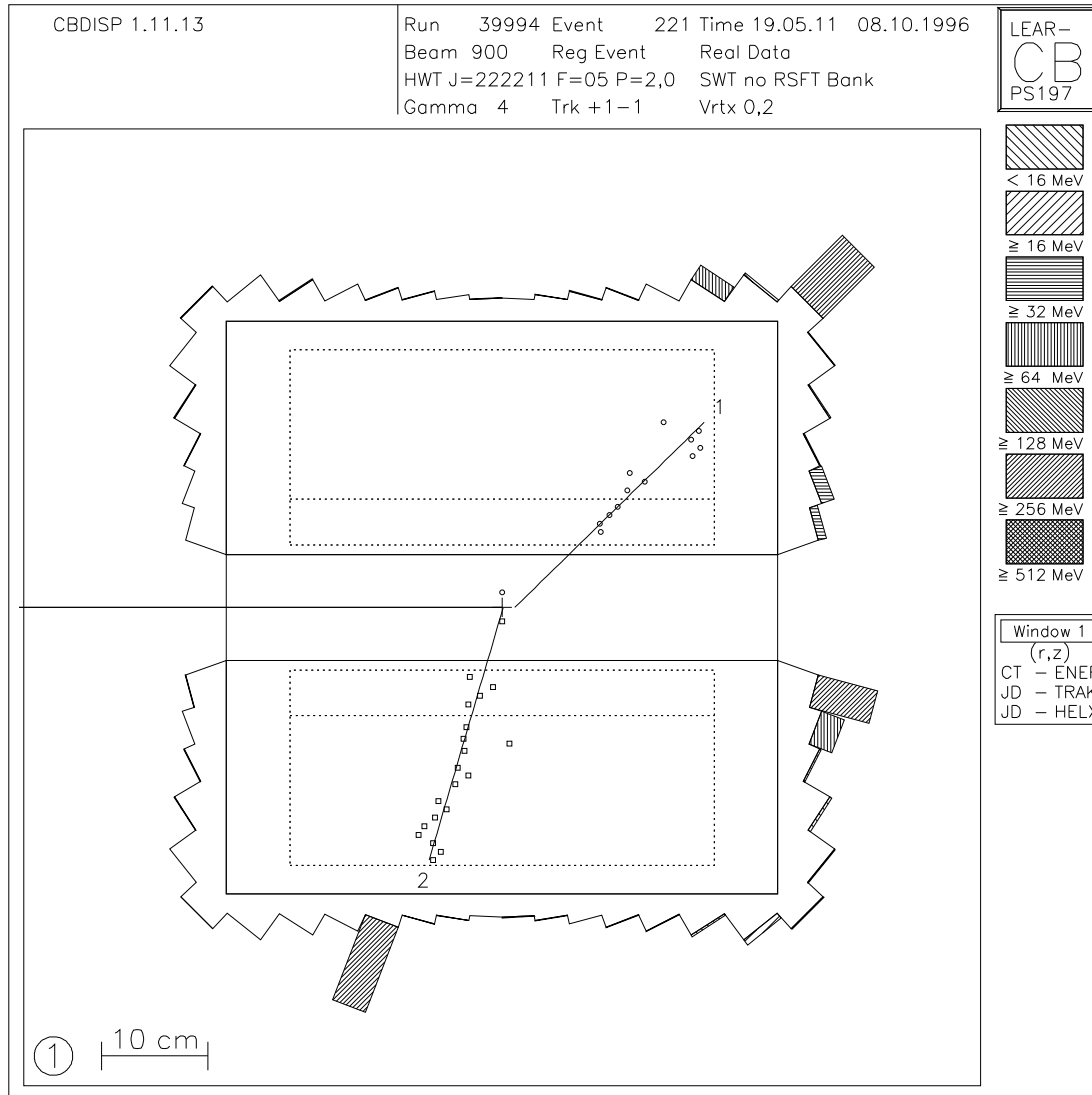


Figure 3.1: Type 13 event in the rz view of the JDC with energy tower. One un-matched photon has the central crystal in a type 13 crystal.

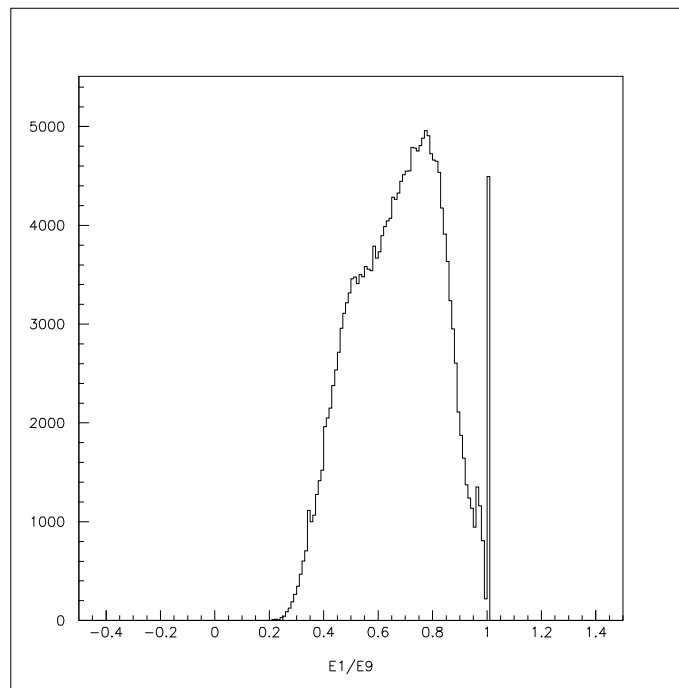


Figure 3.2: E_1/E_9 is the ratio between the central crystal energy and the sum of the energy of this crystal and all the other 8 neighbours.

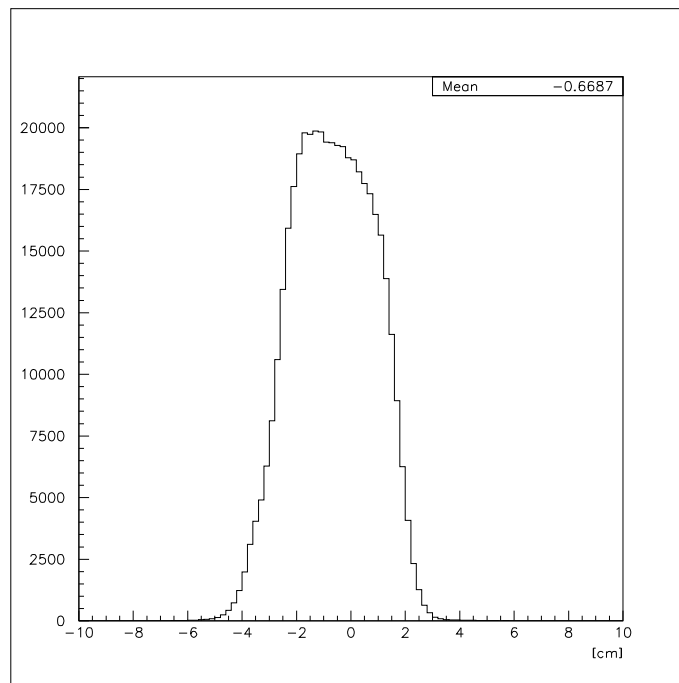


Figure 3.3: Vertex distribution along the z-axis at 900 MeV/c.

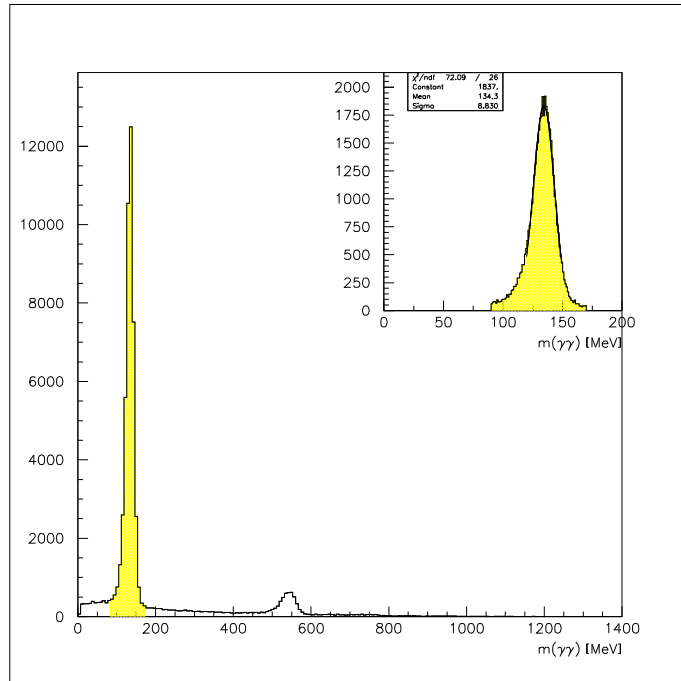


Figure 3.4: Invariant mass of the $\gamma\gamma$ distribution at an incoming antiproton momentum of 900 MeV/c. Two peaks corresponding to the π^0 and to the η are clearly visible.

3.2 Selection

With only two photons only one possible combination of the decay $\pi^0 \rightarrow \gamma_1\gamma_2$ exists. The corresponding invariant mass of the π^0 is

$$m_{\pi^0} = \sqrt{(E_1 + E_2)^2 - |\vec{\mathbf{p}}_1 + \vec{\mathbf{p}}_2|^2} \quad (3.1)$$

where $E_1, \mathbf{p}_1, E_2, \mathbf{p}_2$ are the energy and the momentum of the two photons. A second peak at ~ 547 MeV related to the decay $\eta \rightarrow \gamma\gamma$ is also visible (fig. 3.4).

Finally a broad window cut on energy/momentum is done. The energy and momentum distributions peak at the nominal antiproton beam momentum (LEAR) and the total energy in the laboratory frame (3.5). In the two dimensional plots 3.6 showing the total momentum versus the total energy different enrichment regions that correspond to different final states are visible.

Of these regions, the most populated one corresponds to the final $\pi^+\pi^-\pi^0$ state. The points in the low energy/momentum range can be interpreted as events with one missing photon. The program assumes, by default, that all charged tracks are associated to pions. The $K^+K^-\pi^0$ states, which populate a region close to that of $\pi^+\pi^-\pi^0$, are more evident in the plot where the sum of the energy of the charged mesons is recalculated as a function of the kaon mass $E_K = \sqrt{(m_K)^2 + (\vec{\mathbf{p}}_K)^2}$ (see fig. 3.7).

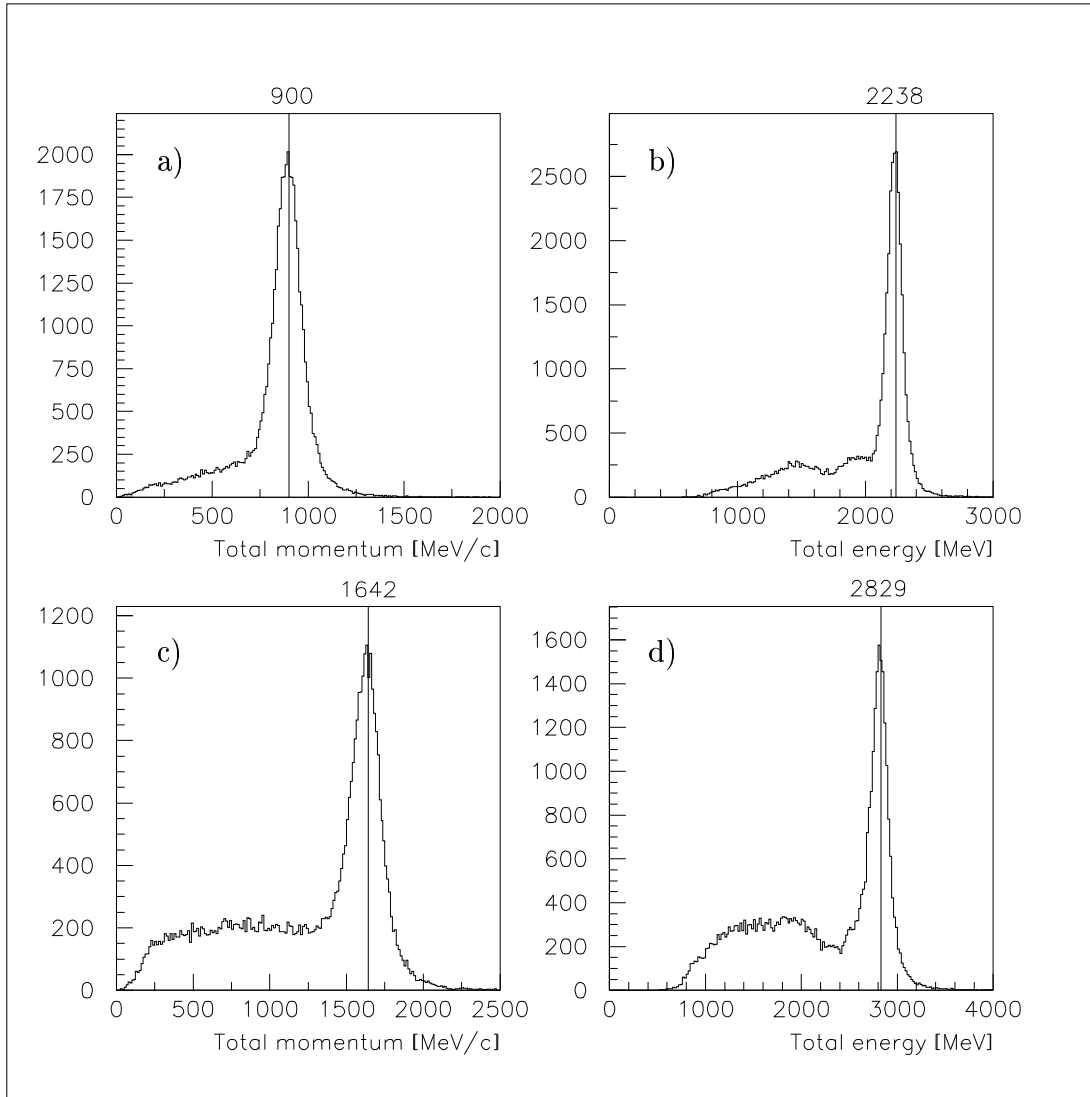


Figure 3.5: Total energy and momentum distributions: a), b) for 900 MeV/c incoming \bar{p} momentum and c), d) for 1642 MeV/c incoming \bar{p} momentum.

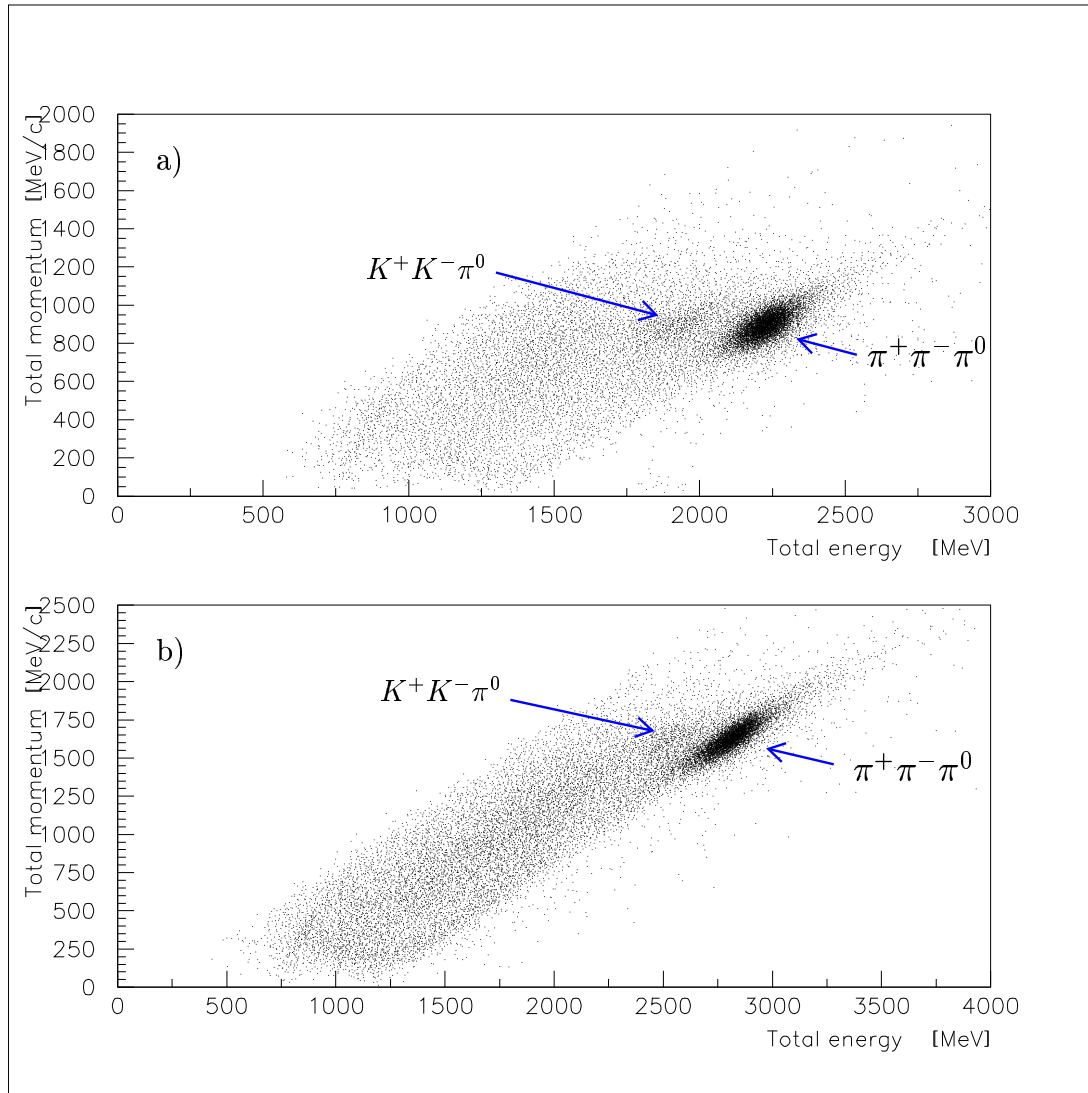


Figure 3.6: Total energy and momentum. Two enrichment regions corresponding to the $K^+K^-\pi^0$ and to $\pi^+\pi^-\pi^0$ final states are visible: a) for 900 MeV/c incoming \bar{p} momentum, and b) for 1642 MeV/c incoming \bar{p} momentum.

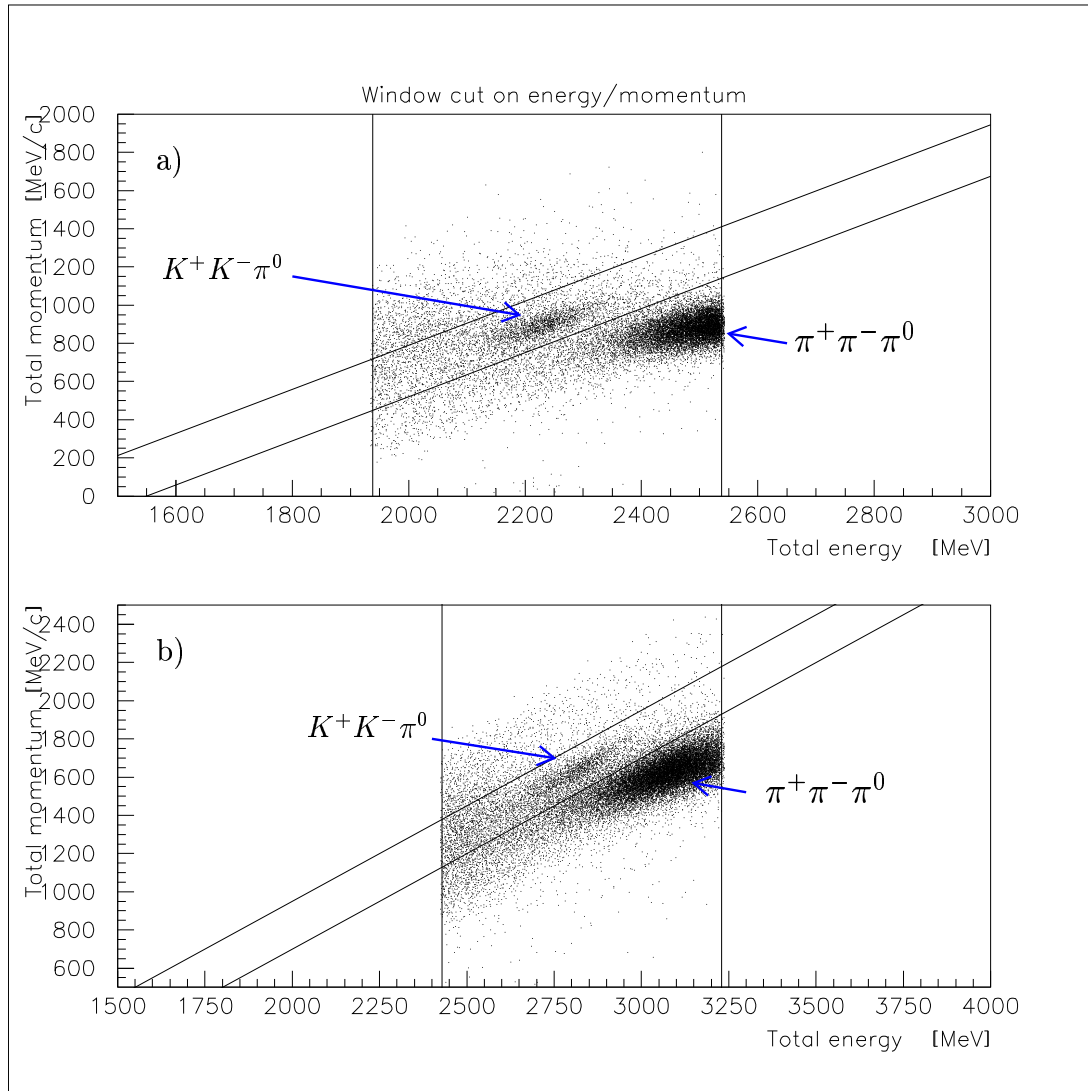


Figure 3.7: Window cuts on energy/momentum at 900 MeV/c and at 1642 MeV/c: a) for 900 MeV/c incoming \bar{p} momentum, b) for 1642 MeV/c incoming \bar{p} momentum.

The following window cuts are then performed in these ranges. At $p_{LAB} = 900 MeV/c$, $E_{LAB} = 2238.4 MeV$:

- $E_{LAB} - 300 MeV < E_{tot} < E_{LAB} + 300 MeV$
- $1.155 \cdot E_{tot} - 1790 MeV < P_{tot} \cdot c < 1.155 \cdot E_{tot} - 1520 MeV$

at $p_{LAB} = 1642 MeV/c$, $E_{LAB} = 2829.4 MeV$:

- $E_{LAB} - 500 MeV < E_{tot} < E_{LAB} + 500 MeV$
- $1.0 \cdot E_{tot} - 1300 MeV < P_{tot} \cdot c < 1.0 \cdot E_{tot} - 1050 MeV$

The full statistics is listed in table 3.1.

3.3 Constrained Fit

The least square method that follows [61] assumes that the measured quantities y_i with $i = 1, \dots, n$ are affected by the errors ϵ_i , which are normally distributed around 0

$$y_i = a_i + \epsilon_i \quad i = 1, \dots, n \quad (3.2)$$

where a_i are the true values. The measured quantities are correlated by the m equations

$$f_k(\mathbf{a}) = 0 \quad k = 1, \dots, m. \quad (3.3)$$

We are interested to know the corrected values η_i of the measured quantities

$$y_i = \eta_i + \epsilon_i \quad i = 1, \dots, n. \quad (3.4)$$

The solution that takes into consideration the errors of the measured quantities and the correlations $f_k(\eta) = 0$ is obtained with the help of the minimum function,

$$\mathbf{M} = \boldsymbol{\epsilon}^T \mathbf{C}_y^{-1} \boldsymbol{\epsilon} \quad (3.5)$$

where C_y is the corresponding covariance matrix of the errors

$$\mathbf{C}_y = \begin{pmatrix} \sigma_1^2 & & \\ & \sigma_2^2 & \\ & & \ddots \\ & & & \sigma_n^2 \end{pmatrix}, \quad \mathbf{C}_y^{-1} = \begin{pmatrix} \frac{1}{\sigma_1^2} & & \\ & \frac{1}{\sigma_2^2} & \\ & & \ddots \\ & & & \frac{1}{\sigma_n^2} \end{pmatrix}. \quad (3.6)$$

To minimize the function 3.5 the method of the Lagrange multipliers α_k with $k = 1, \dots, m$ is used. That is

$$\mathbf{L} = \boldsymbol{\epsilon}^T \mathbf{C}^{-1} \boldsymbol{\epsilon} + 2\boldsymbol{\alpha}^T \mathbf{f}. \quad (3.7)$$

The minimum of L is obtained when

$$\frac{1}{2} \begin{pmatrix} \delta \mathbf{L} \\ \delta \boldsymbol{\eta} \end{pmatrix}^T = 2\mathbf{C}^{-1}\boldsymbol{\epsilon} + 2\mathbf{B}^T\boldsymbol{\alpha} = 0 \quad (3.8)$$

and

$$\frac{1}{2} \begin{pmatrix} \delta \mathbf{L} \\ \delta \boldsymbol{\alpha} \end{pmatrix}^T = \mathbf{f}(\boldsymbol{\eta}) = 0 \quad (3.9)$$

with $B = \frac{\delta \mathbf{f}}{\delta \boldsymbol{\eta}}$. These are n+m equations for the n variables η_i and for m boundary condition f_k . In general the system of eqs. 3.9 are not linear functions of η . With the assumption that the functions f_k within the interval of variability can be approximately considered linear, the system of equations can be solved iteratively.

In relation to the new corrected quantities the shifts p (*pulls*) can be defined

$$p_i = \frac{\epsilon_i}{\sqrt{(C_y)_{ii}}}. \quad (3.10)$$

When the detector is correctly calibrated and the errors are correctly determined, the pulls are normally distributed with widths close to 1 and the minimized quantity M is described by a χ^2 distribution with m degrees of freedom.

Then a probability W that fulfills the hypothesis can be defined [2]

$$W(M) = \int_M^\infty g_m(\chi^2) d\chi^2 \quad (3.11)$$

where g_m is the χ^2 distribution with m degrees of freedom. This probability is called confidence level. It is a flat distribution for the events that correspond to the hypothesis. Those events which do not satisfy the hypothesis, have a big value of M and a small confidence level.

3.4 Application on $K^+K^-\pi^0$ Final States

The variables y_i of eqn. 3.2 in question are for every photon

- ϕ : azimuthal angle of the shower
- θ : polar angle of the shower
- \sqrt{E} : square-root of the shower energy (PED)

and for every charged track

- ψ : the angle of the track in the xy-plane with respect to a fixed direction
- $1/P_{xy}$: inverse of the xy-component of the momentum
- $\tan\lambda$: inclination of the track in the ρz plane.

In addition to the 4 constraints, given by the energy-momentum conservation, conditions given by decay of mesons in the final state may apply: in the case of $K^+K^-\pi^0$ this is the condition that the invariant mass of the $\gamma\gamma$ pair is equal to the pion mass, so in total a 5C fit with 6 + 6 variables is performed.

The error of the energy is given by

$$\frac{\sigma_E}{E} = \frac{2.8\%}{E^{0.25}} \quad (3.12)$$

where σ and E are in GeV.

The errors of θ , ϕ are estimated using a Monte Carlo simulation. The result is a parametrization of the form

$$p_1 + p_2\sqrt{E} + p_3\ln(E) \quad (3.13)$$

where different parameters are given for crystal type 1-11 or 13 and for the case that one PED or more belong to the same cluster [53].

$1/P_{xy}$ is proportional to the curvature of the track, so all quantities regarding the charged tracks have the errors related to the uncertainty in the position of the hits.

Confidence level distributions for both initial momenta are shown in fig. 3.8. A confidence level cut of 10% for the hypothesis $K^+K^-\pi^0$ was applied. At this stage the remaining background of $\pi^+\pi^-\gamma\gamma$ and $\pi^+\pi^-\pi^0$ events is removed requiring a confidence level less than 1% for this hypothesis.

The pulls for the remaining events are shown in fig. 3.9. With the exception of $1/P_{xy}$ and \sqrt{E} all pulls are normally distributed, as expected for a correct calibration. The asymmetric distribution of the \sqrt{E} is connected to the fact that there is a systematic energy loss of a part of events having an electromagnetic splitoff or having only a part of the photon shower detected because of the holes.

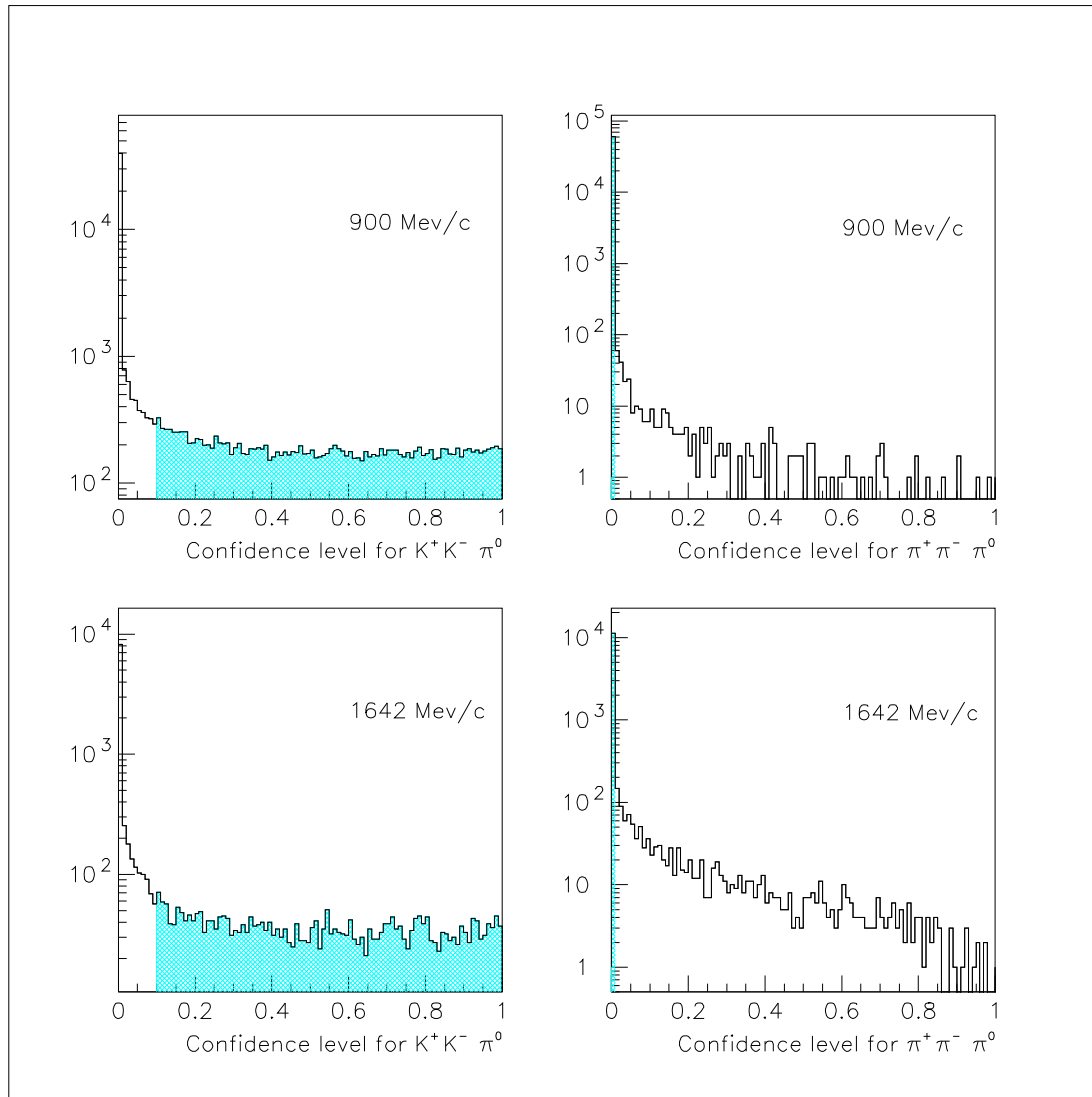


Figure 3.8: Confidence level distribution at 900 MeV/c and at 1642 MeV/c.

Condition	N. of events at 900 MeV/c	N. of events at 1642 MeV/c
2-prong trigger	18808350	12367264
<i>pile-up</i> flag*	3765977	2716764
2 prongs	12625025	7605030
2 long tracks	11620767	6718944
charge conservation	10143845	5483069
2 golden tracks	7105586	3353222
normal convergence	6433000	2875997
2 golden gammas	841534	347763
window cut on pions	573507	198284
soft energy cut	269382	77561
energy-mom. cut	60687	15240
$CL(K^+K^-\pi^0) > 0.1$	16842	4677
$CL(\pi^+\pi^-\gamma\gamma) < 0.01$	16811	4301
$CL(\pi^+\pi^-\pi^0) < 0.01$	16802	4271
no type 13 PED	15036	3700**

Table 3.1: Selection of $K^+K^-\pi^0$ states.

*The pile-up flag indicates that a second \bar{p} entered the target within a time window of 11 μs length. It indicates potential pile-up, but it is not used in the present selection because of the low statistics.

**No cut on events with type 13 PED is done at 1642 MeV/c, all 4271 events were accepted

About $1/P_{xy}$ we note that every charged track according to the eq. 2.9 is inversely proportional to the magnetic field. It is reasonable to assume then that an incorrect value of B can be associated with a systematic error on $1/P_{xy}$. In fact a 1% correction of the magnetic field from 1.5 T to 1.515 T leads to a correct pull of $1/P_{xy}$ and of all the other fitted variables (see fig. 3.10).

In the final sample 15036 and 4271 events respectively pass all the cuts (see table 3.1). No background of $\pi^+\pi^-\pi^0$ events is present as it can be seen in fig 3.11, where the differential energy loss is plotted as a function of the momentum of the charged mesons (Bethe-Bloch formula [2]).

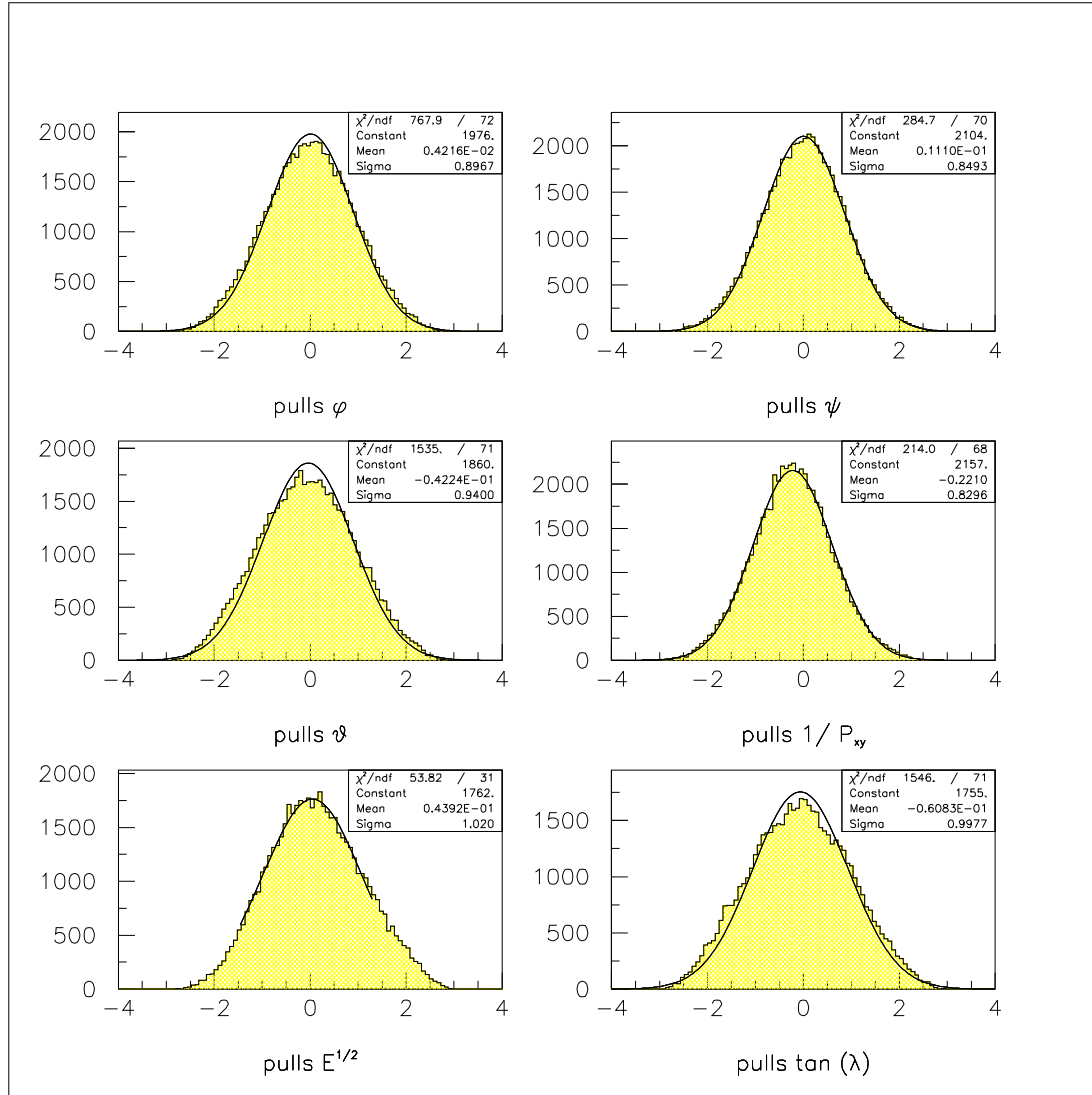


Figure 3.9: Pulls at 900 MeV/c with no corrections. The shift of the mean of $1/P_{xy}$ indicates the presence of a systematic error.

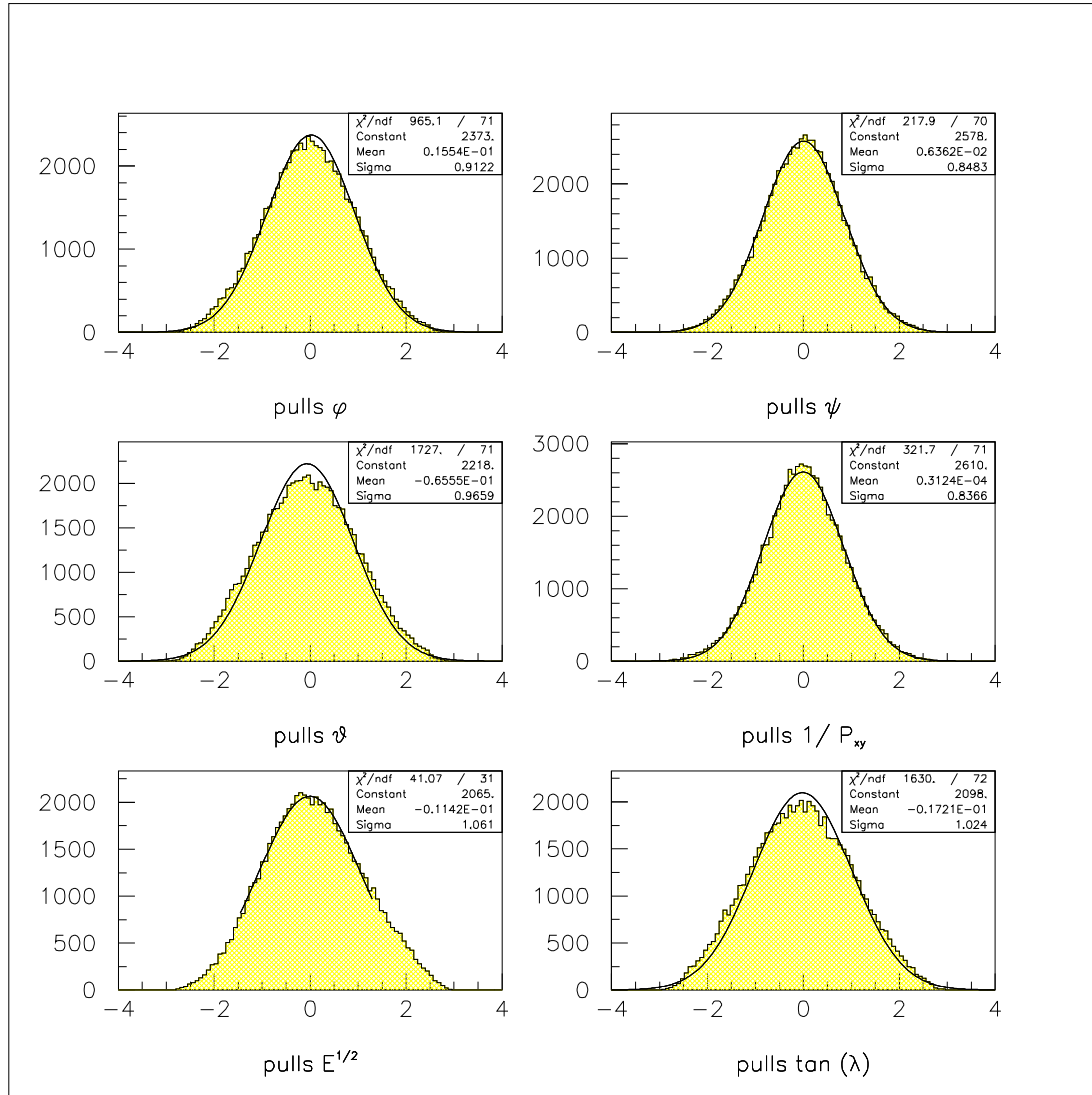


Figure 3.10: Pulls at 900 MeV/c after the 1% correction of the magnetic field.

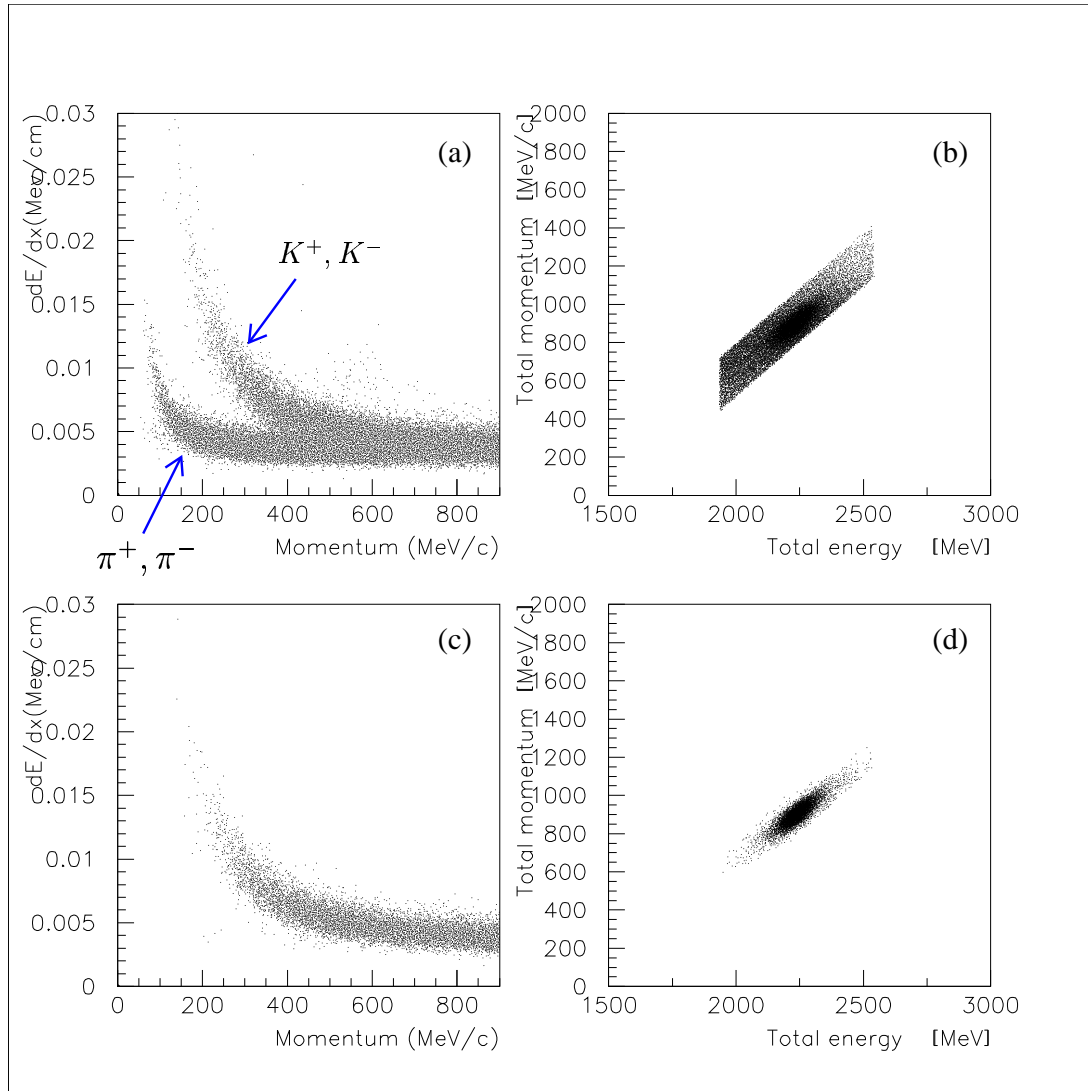


Figure 3.11: The differential energy loss versus the momentum of the charged mesons at 900 MeV/c (first plot (a)) shows that both $K^+K^-\pi^0$ and $\pi^+\pi^-\pi^0$ states are still present after the window cut on energy/momentum (b). $\pi^+\pi^-\pi^0$ final states are removed after a kinematic fit (plots (c),(d)). The values of momentum and energy before kinematic fitting are plotted here.

3.5 Monte Carlo Simulation

The Monte Carlo events were generated using the GEANT simulation program. All relevant secondary processes of $\bar{p}p \rightarrow K^+K^-\pi^0$ with the active and passive parts of the detector are taken into account. These are for photons:

- pair production, Compton scattering, photo-electric effect.

For charged tracks:

- Multiple scattering, ionization, production of δ -electrons, *bremsstrahlung* of charged particles, positron-electron annihilation, muon decay, direct e^+ , e^- production, hadronic interaction.

For the latter process the FLUKA (FLUctuating KAskade) [55] shower simulation has been used. A Crystal Barrel Monte Carlo simulation with charged kaons [56], [57] with a new updated FLUKA release has a more realistic extension to low momenta (below 1 GeV/c) with respect to other standard packages used in high energy physics (eg. GHEISHA).

Furthermore a flat $\bar{p}p$ annihilation z-vertex distribution has been simulated. In addition, as in the real data, the inaccuracy of the position of the target has been also taken into account implementing the code with additional information about the position from a run-dependent database. The resulting shapes of the two distributions 3.3 and 3.12 are similar.

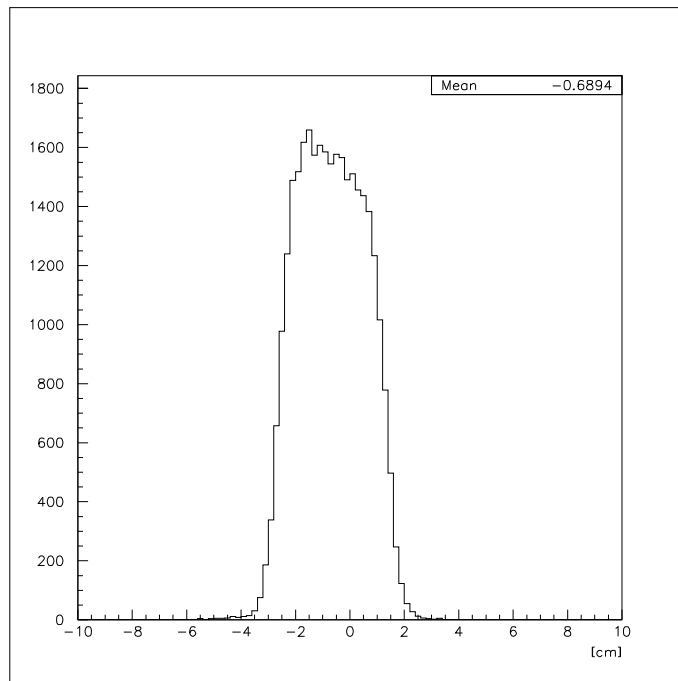


Figure 3.12: Vertex distribution along the z-axis of Monte Carlo events at 900 MeV/c.

During the reconstruction the same selection procedure with the same confidence level cuts defined for experimental data was carried out. In table 3.2 the mean values and the pull width of Monte Carlo simulation and of experimental data are listed. All pulls are correctly centered with values below 10^{-1} . Concerning the widths, the errors on $1/P_{xy}$ and on ψ used in the kinematic fit are overestimated both for Monte Carlo as for experimental data. In table 3.2 their values are listed.

The full statistics is reported in table 3.3 A total number of 1 million and 500K phase-space distributed $K^+K^-\pi^0$ events has been generated at 900 MeV/c and at 1642 MeV/c and an efficiency of 8.2% and of 7.6% respectively is obtained.

	$\langle \phi \rangle$	$\langle \theta \rangle$	$\langle \sqrt{E} \rangle$	$\langle \psi \rangle$	$\langle 1/P_{xy} \rangle$	$\langle \tan\lambda \rangle$
900 MeV/c exp. data	0.015	-0.065	-0.011	0.006	0	-0.017
900 MeV/c MC data	0.005	-0.088	0.051	-0.009	-0.087	-0.047
1642 MeV/c exp. data	0.006	-0.111	0.133	0.005	-0.051	0.002
1642 MeV/c MC data	0.003	0.031	-0.137	-0.013	-0.033	-0.087
	σ_ϕ	σ_θ	$\sigma_{\sqrt{E}}$	σ_ψ	$\sigma_{1/P_{xy}}$	$\sigma_{\tan\lambda}$
900 MeV/c exp. data	0.91	0.97	1.06	0.85	0.84	1.02
900 MeV/c MC data	0.84	0.90	0.95	0.67	0.62	0.87
1642 MeV/c exp. data	0.91	0.95	1.00	0.85	0.84	1.02
1642 MeV/c MC data	0.83	0.92	1.08	0.64	0.58	0.87

Table 3.2: Widths of the pulls

Condition	N. of events at 900 MeV/c	N. of events at 1642 MeV/c
2-prong trigger	1000000	500000
2 prongs	576813	283495
2 long tracks	376035	165449
charge conservation	351843	151071
no type 13*	273121	-
2 golden tracks	214770	110404
normal convergence	201198	103427
2 golden gammas	126363	55629
window cut on pions	114333	50263
soft energy cut	112313	48654
energy-mom. cut	110183	47352
$CL(K^+K^-\pi^0) > 0.1$	81938	38615
$CL(\pi^+\pi^-\gamma\gamma) < 0.01$	81896	37999
$CL(\pi^+\pi^-\pi^0) < 0.01$	81878	37876

Table 3.3: Selection of $K^+K^-\pi^0$ MC events.

*As for experimental data no cut on type 13 events is done at high momenta.

Chapter 4

The Presentation of the Data and the Dalitz Plot

In this chapter we present the $K^+K^-\pi^0$ data. After an overview of the kinematics of a Dalitz plot for a three-body final state the description of the experimental data follows. From the analysis of the Dalitz plot and of the invariant mass spectra we draw the first conclusion about the dominant intermediate states in the $\bar{p}p \rightarrow K^+K^-\pi^0$ reaction.

4.1 Dalitz Plot

Consider the process

$$a + b \rightarrow 1 + 2 + 3 \quad (4.1)$$

where a is the incident particle, b is the target and $1,2,3$ are the resulting particles. The information about the dynamical features, for example the occurrence of a resonance c ,

$$a + b \rightarrow 1 + c, \quad c \rightarrow 2 + 3 \quad (4.2)$$

comes from the observation of the energy spectra of particle 1 in a given direction. In this case the spectra differ from a continuous distribution since this process involves only two particles and the energy of the particle 1 is fixed for a given direction of motion.

More generally speaking much of the information about the properties of the particles, like their spin, coupling strength, etc ... comes from the transition rate per incident flux per target particle or cross section σ . This is given by the product of the square of a matrix element and the density of the final state or phase-space factor ρ_f

$$\sigma \sim \int |M_{if}|^2 d\rho_f \quad (4.3)$$

The Lorentz-Invariant-Phase-Space (LIPS) ρ_f has the form

$$\rho_f = \int \frac{d^3p_1}{2E_1} \frac{d^3p_2}{2E_2} \frac{d^3p_3}{2E_3} \delta(E_{tot} - \sum_{i=1}^3 E_i) \delta^3(\sum_{i=1}^3 p_i) \quad (4.4)$$

where $E_i, p_i, i = 1, \dots, 3$ are the energy and momentum of the particles in the center of mass system (CMS).

The precise form of the transition matrix M_{if} is in general not known and it will be discussed for the reaction $\bar{p}p \rightarrow K^+K^-\pi^0$ in flight in the next chapter.

From the energy-momentum conservation the number of undefined variables is reduced to two so that

$$d\rho_f = const \cdot dE_1 dE_2 \quad (4.5)$$

and the plane E_1, E_2 contains the information about the dynamics of a phase space-distributed event. For a better investigation of the dynamical features the square of the invariant mass m_{12}^2 of the particle 1 and 2 is plotted versus m_{13}^2 . In this two-dimensional plot, called Dalitz plot [62] [63], every event is represented by a point.

The advantage of this representation lies in the fact that phase-space distributed events, where no interaction among the final state particle occurs, are equally distributed within the kinematically allowed limits. Dynamical effects can be recognized directly from the observation of structures in the Dalitz plot, that is from a departure of a uniform density. In fig. 4.1 the Dalitz plot of $K^+K^-\pi^0$ at 0.9 GeV/c that is equivalent to a center of mass energy W of 2.05 GeV, is schematically represented. If the invariant mass $m_{K^-\pi^0}^2$ is plotted against the $m_{K^+K^-}^2$ the Dalitz plot has an asymmetric form (see Fig. 4.2). Vertical bands in the symmetric Dalitz plot indicate the presence of a resonance between particle 1 and 2, that is between K^+ and π^0 and horizontal bands between particles 1 and 3 (K^- and π^0).

The following equation exists between the invariant masses and the total energy in the center of mass system

$$m_{12}^2 + m_{13}^2 + m_{23}^2 = W^2 + m_1^2 + m_2^2 + m_3^2 = C \quad (4.6)$$

so that any resonance between particles 2 and 3 (K^+ and K^-) appears as a diagonal band in the symmetric Dalitz plot of equation

$$m_{12}^2 = (C - m_{23}^2) - m_{13}^2. \quad (4.7)$$

In simple cases, for example in the case of annihilation at rest, the angular distribution of a resonance is directly observable from the density of points in the corresponding bands.

Indeed, if θ is defined as the angle between the direction of the primary particle and the decay product of a resonance in the rest system of the resonance, we have a linear relation

$$m_{13}^2(m_{12}) = \frac{m_{13,min}^2 + m_{13,max}^2}{2} + \frac{m_{13,min}^2 - m_{13,max}^2}{2} \cos\theta. \quad (4.8)$$

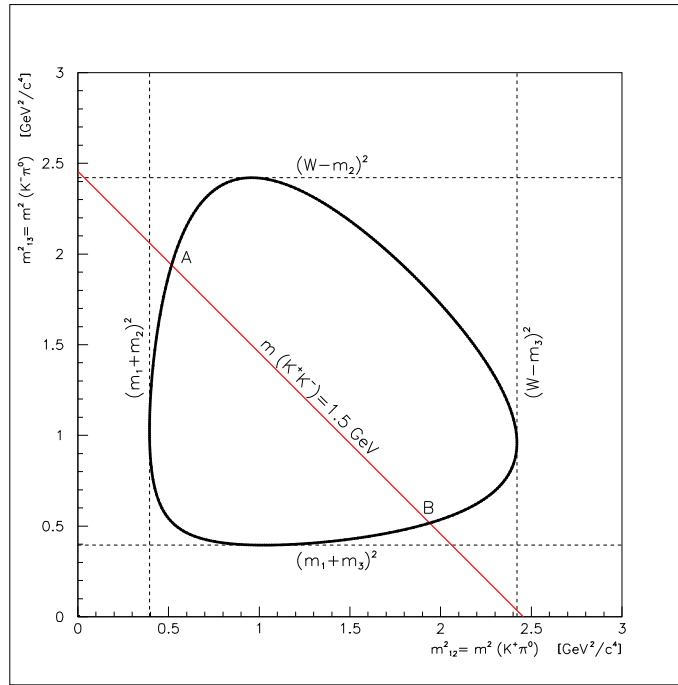


Figure 4.1: Scheme of the Dalitz plot of $K^+K^-\pi^0$ states at 900 MeV/c. A resonance between K^+ and K^- corresponds to a diagonal band.

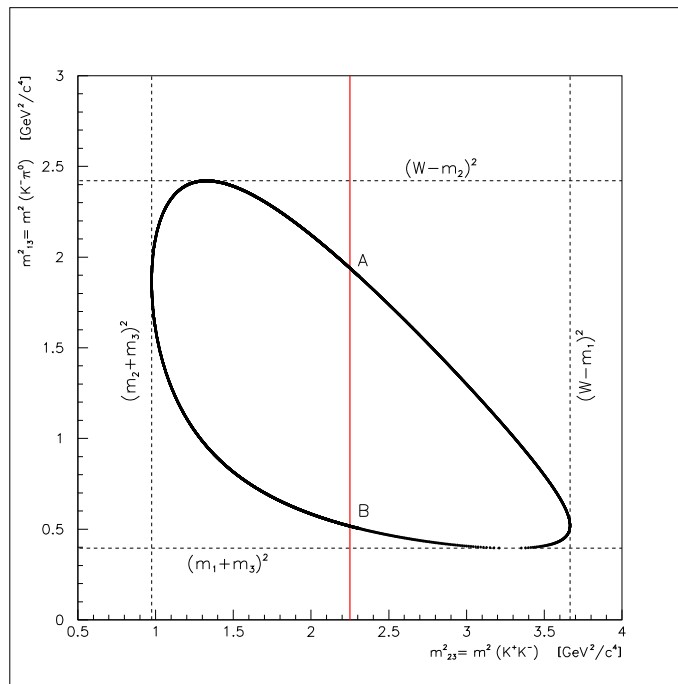


Figure 4.2: Scheme of the asymmetric Dalitz plot of $K^+K^-\pi^0$ states at 900 MeV/c. Here a resonance between K^+ and K^- correspond to a vertical band

The boundaries of the Dalitz plots can be obtained taking in consideration that, for a fixed m_{ik} mass, the maximum and the minimum values of m_{ij} correspond to the configuration in which all three momenta are collinear. The solution is obtained using relativistic kinematics [2]:

$$m_{ij,max}^2 = (E_j + E_i)^2 - (\sqrt{E_i^2 - m_i^2} + \sqrt{E_j^2 - m_j^2})^2 \quad (4.9)$$

$$m_{ij,min}^2 = (E_j + E_i)^2 - (\sqrt{E_i^2 - m_i^2} - \sqrt{E_j^2 - m_j^2})^2 \quad (4.10)$$

where

$$E_j = \frac{s - m_{ik}^2 - m_j^2}{2m_{ik}} \quad (4.11)$$

$$E_i = \frac{m_{ik}^2 + m_i^2 - m_k^2}{2m_{ik}}. \quad (4.12)$$

The coordinates of $A \equiv m_{K^-\pi^0,min}^2$ and $B \equiv m_{K^-\pi^0,max}^2$ in the asymmetric Dalitz plot at a given $m_{K^+K^-}$ mass are calculated with eqs. 4.10, 4.9. The corresponding points A', B' in the symmetric Dalitz plot are calculated using the relation 4.7.

The invariant masses $m_{K^+K^-}^2$ in the asymmetric Dalitz plot lie along the x-axis between

$$m_{K^+K^-,min}^2 = (m_{K^+} + m_{K^-})^2 \quad m_{K^+K^-,max}^2 = (W - m_{\pi^0})^2 \quad (4.13)$$

so that at 900 MeV/c the observation of structures between ~ 1.0 GeV and 1.9 GeV is possible. At an incoming antiproton momentum 1.642 GeV we have an energy in the center of mass of 2.3 GeV and the Dalitz plot is enlarged (see Fig. 4.3). Structures up to a limit of $m_{K^+K^-,max} \sim 2.1$ GeV can be observed.

4.2 Dalitz Plot at 900 MeV/c

The Dalitz plot of the 15036 selected and fitted events at 900 MeV/c is shown in fig 4.4. The most evident structures are relative to vertical and horizontal $K^{*\pm}(892)$ bands. Close to the boundary the narrow diagonal band of the $\phi(1020)$ is visible. Three further enrichment regions are at ~ 1300 MeV, at ~ 1500 and at ~ 1660 MeV. They are likely to be identified with the $f_2(1270)$, the $f_0(1500)$ and the $f_j(1710)$, respectively.

Other possible resonances are the $a_2(1320)$ the $f'_2(1525)$ and the $a_2(1660)$. The identification of these resonances and their separation is not possible by eye and requires a detailed partial wave analysis.

Complications arise in the analysis whenever bands overlap or cross. In particular it can be seen that the $K^{*\pm}(892)$ bands cross the diagonal bands at a $m_{K^+K^-}$ mass of ~ 1760 MeV, which makes the identification of the $f_j(1710)$ difficult.

Other structures are evident in the $K^\pm\pi^0$ projections (see Fig. 4.5).

The $K_0^{*\pm}(1430) \rightarrow K^\pm\pi^0$ is also likely to be present but its broad width of 287 MeV [2] and its proximity to the edge of the phase-space complicates its observation.

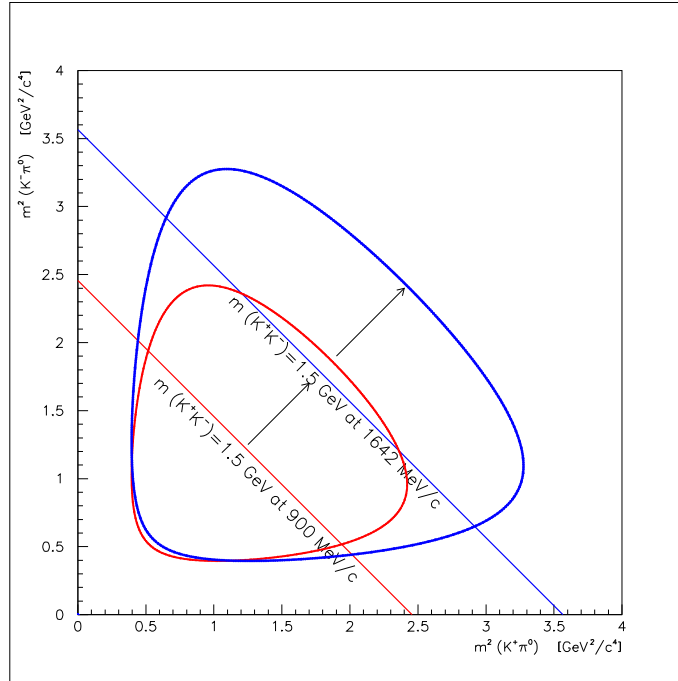


Figure 4.3: Scheme of the Dalitz plot of $K^+K^-\pi^0$ states at 900 MeV/c (red) and at 1642 MeV/c (blue). At higher center of mass energy the Dalitz plot is enlarged and the diagonal K^+K^- bands are shifted

Another visible feature is the asymmetric density of points in the horizontal and vertical $K^{*\pm}(890)$ bands. The same effect is also visible in the $m_{K^\pm\pi^0}$ projections at ~ 890 and at ~ 1430 MeV. The explanation of this asymmetry is related to the physics of the $\bar{p}p \rightarrow K^+K^-\pi^0$ reaction. The $K^+\pi^0$ and the $K^-\pi^0$ resonances are produced at different polar angles. These asymmetries cannot be explained quantitatively by acceptance effects due, for example, to different hadronic interactions of the charged kaons with the detector, but are related to the charged natures of the incident antiproton and the proton target.

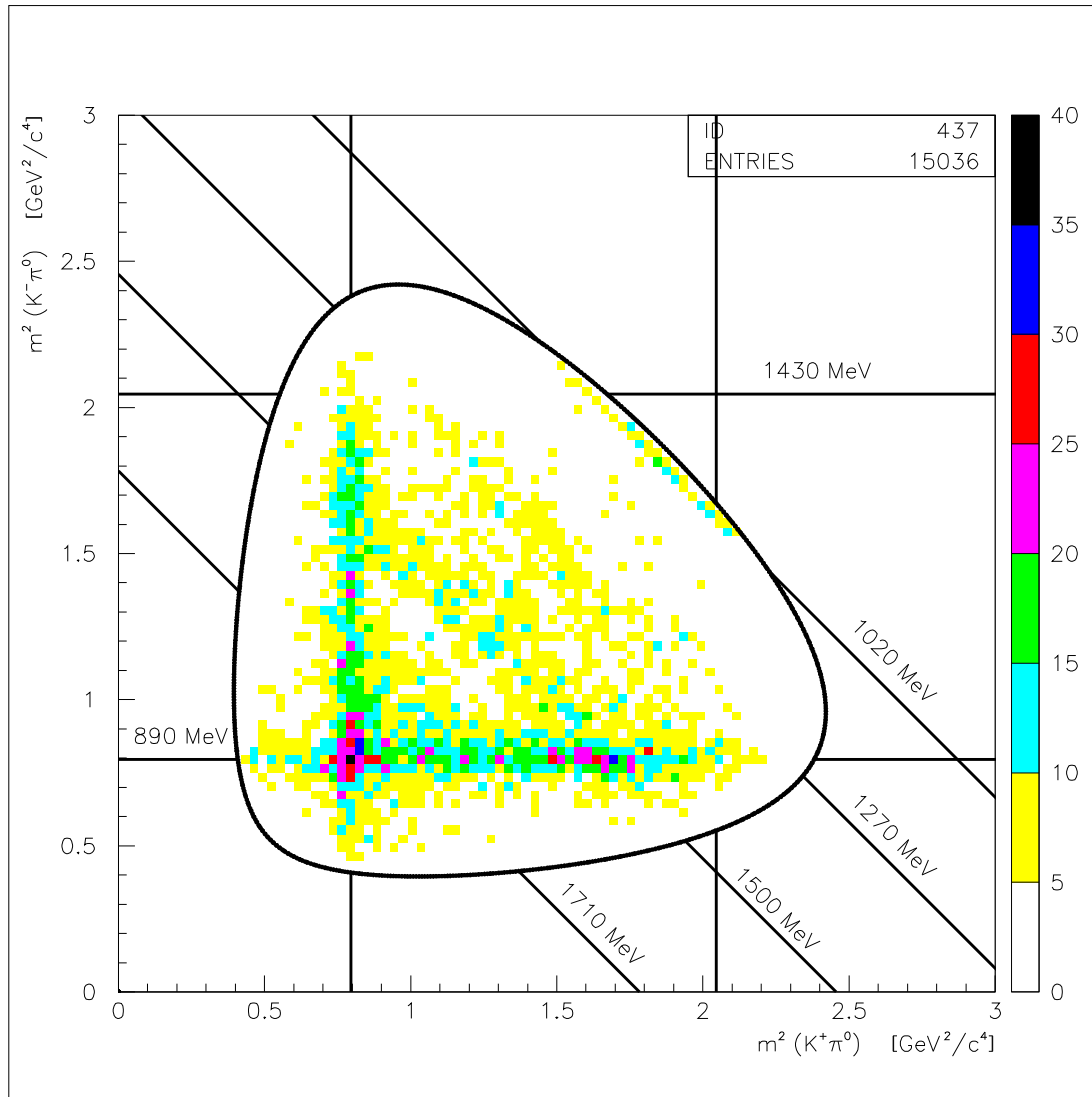
The effect is strong in the backward-forward directions, as can be seen in fig. 4.6 and 4.7 where the ratio between the $K^+\pi^0$ and $K^-\pi^0$ polar production angles, at an invariant mass range close to 890 MeV is shown in the $\bar{p}p$ rest frame.

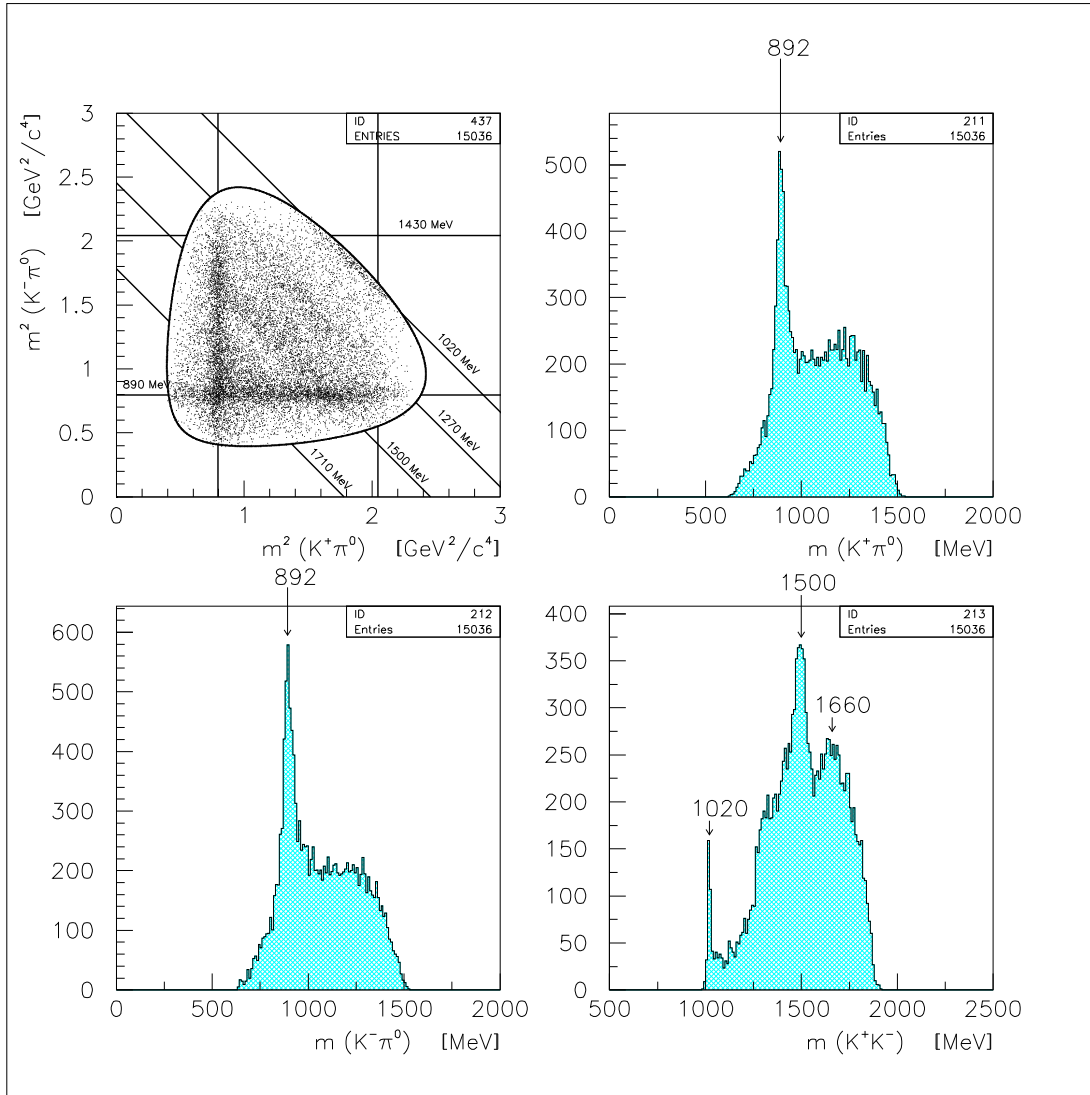
4.3 Dalitz Plot at 1642 MeV/c

At an incoming antiproton momentum of 1.642 GeV/c the main structures close to ~ 1700 are shifted to the center of the Dalitz plot and are well separated from the crossing $K^{*\pm}(890)$ bands (see Fig. 4.8).

Indeed, in this case, the $K^{*\pm}(890)$ crossing occurs on the diagonal bands at a $m_{K^+K^-}$ mass of ~ 2054 MeV.

The data, even if with a lower statistics (~ 4300 events), shows a peak around ~ 1740 MeV, while at 900 MeV/c this was at ~ 1660 , as can be seen from the

Figure 4.4: Dalitz plot of $K^+K^-\pi^0$ states at 900 MeV/c.

Figure 4.5: Dalitz plot and the projections of $K^+K^-\pi^0$ states at 900 MeV/c

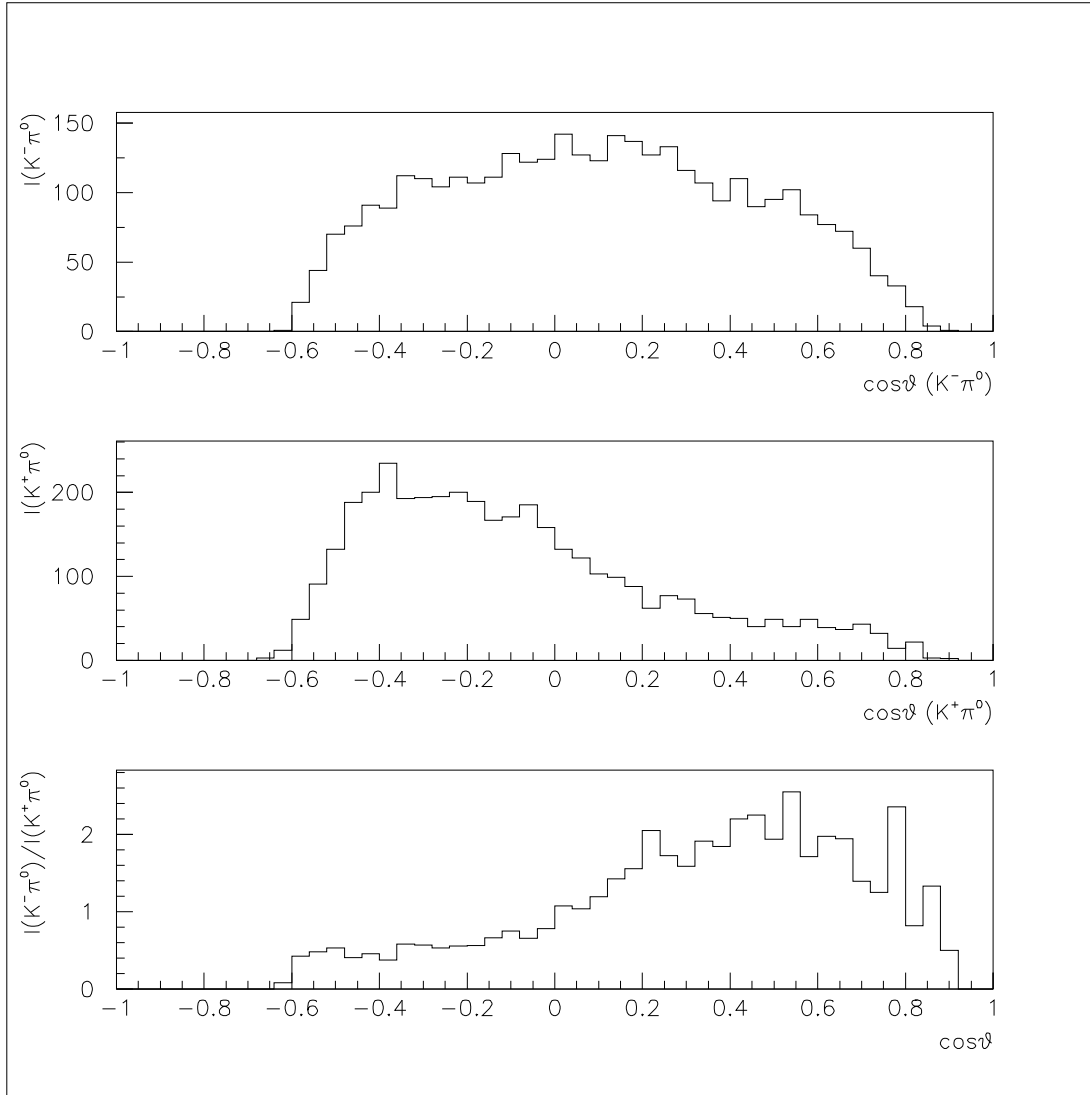


Figure 4.6: Polar production angles of the $K^-\pi^0$ and $K^+\pi^0$ isobars at 900 MeV/c and in a mass range of $840 < m_{K^\pm\pi^0} < 940$ MeV in the $\bar{p}p$ rest frame.

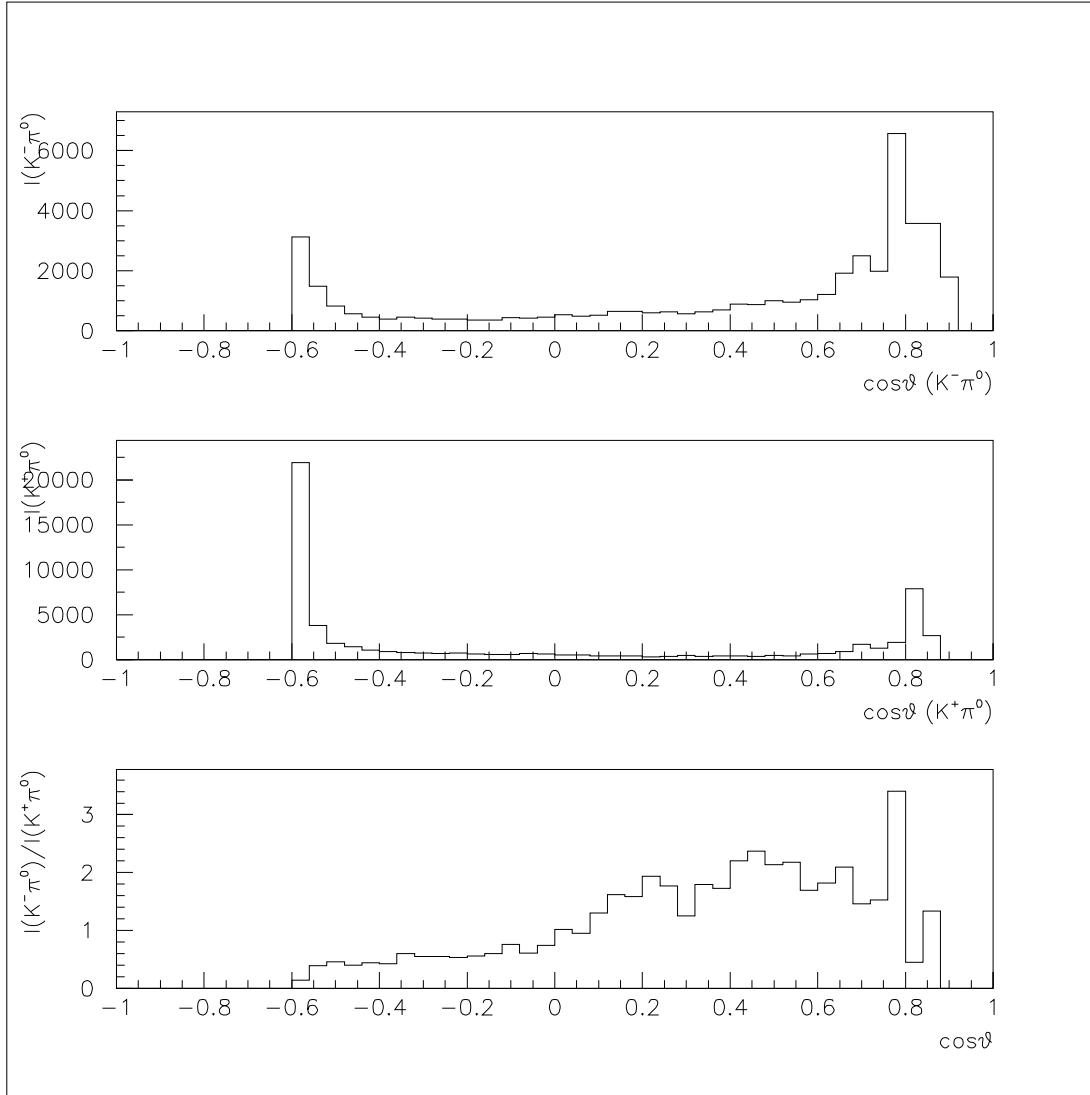


Figure 4.7: Acceptance corrected polar production angles of the $K^-\pi^0$ and $K^+\pi^0$ isobars at 900 MeV/c and in a mass range of $840 < m_{K^\pm\pi^0} < 940$ MeV in the $\bar{p}p$ rest frame.

mass projections fig. 4.5 and fig. 4.9.

This leads to different hypothesis:

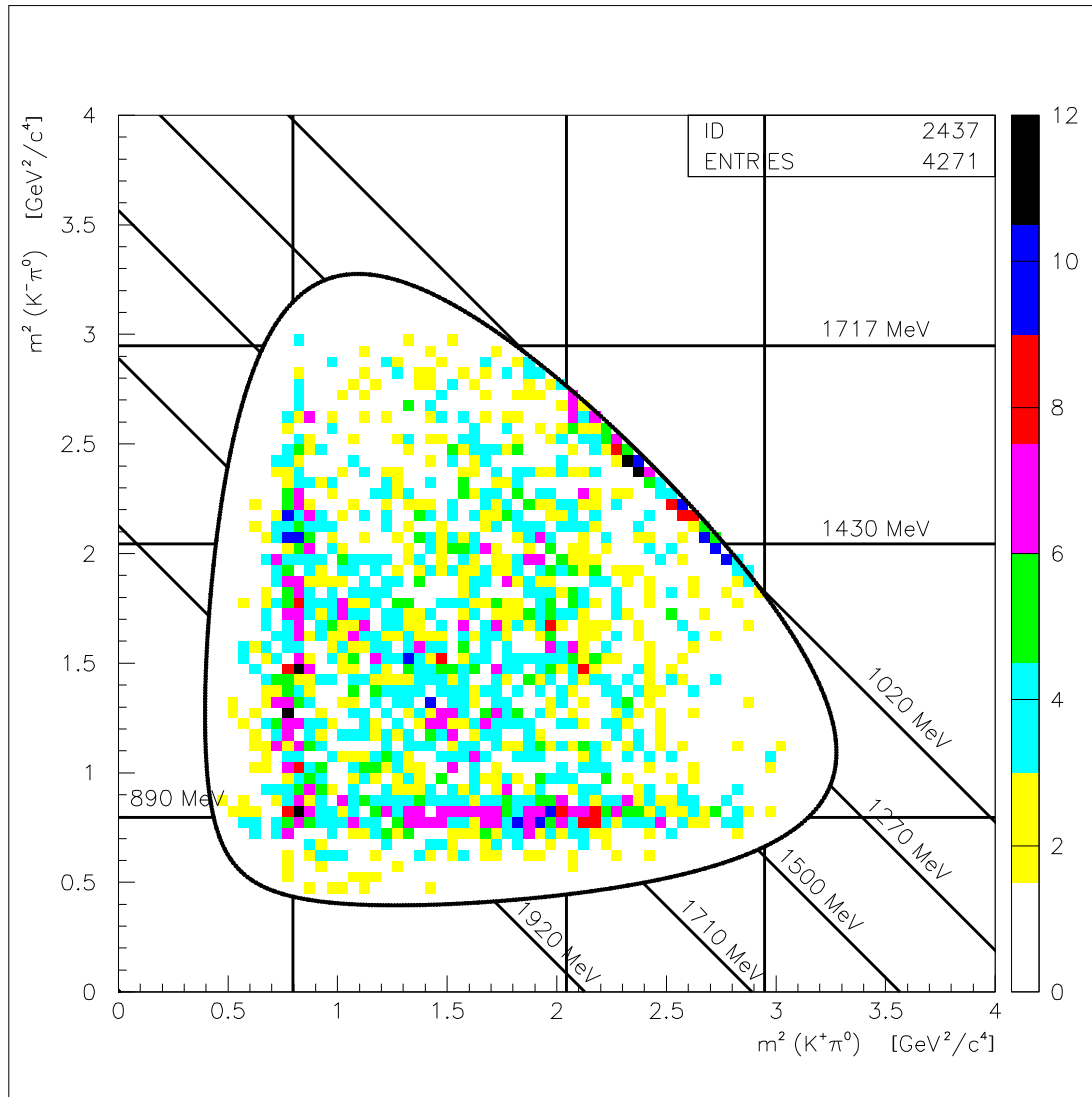
- the structure at ~ 1740 MeV does not appear at 900 MeV/c because it is obscured from the $K^{*\pm}(890)$ crossing. Possible interference or distortion due to the $K^{*\pm}(890)$ shifts the mass to ~ 1660 MeV at 900 MeV/c.
- more than one structure is present in this mass range.

Because of the low statistics it is not possible to separate by eye two resonances in this region. For this purpose, to estimate the masses and widths with a good accuracy and to find the peculiar characteristics like the spin and the coupling strengths, a partial wave analysis is essential.

A weak signal of a resonance close to ~ 1900 MeV can be seen. In addition to the $K^{*\pm}(890)$ and the $K_{0/2}^{*\pm}(1430)$, the $K_1^{*\pm}(1660)$ close to the boundaries of the Dalitz plot, are also likely to be present.

4.4 Acceptance Corrected Dalitz Plots

The Dalitz plots of the Monte Carlo data are shown in figs. 4.10 and 4.11. The departure of the density of points from a uniform population, because of the efficiency and the acceptance of the detector, has the consequence of a depletion of events close to the upper limits of the Dalitz plots. These areas correspond to the maximum value of the invariant masses of the $K^\pm\pi^0$ systems. This configuration arises when the kaons are collinear to the pions and when the pions have the highest energy allowed from energy momentum conservation. In this case the detector is not able to separate the matched PED of the charged track from the photon showers of the pion decay. The effective strength of a resonance with a low K^+K^- mass that is close to the depletion regions can be better appreciated from the acceptance corrected Dalitz plot and the projections (see fig. 4.12). Fortunately the region of higher interest between 1.4 and 1.8 GeV is only marginally affected.

Figure 4.8: Dalitz plot of $K^+K^-\pi^0$ states at 1642 MeV/c.

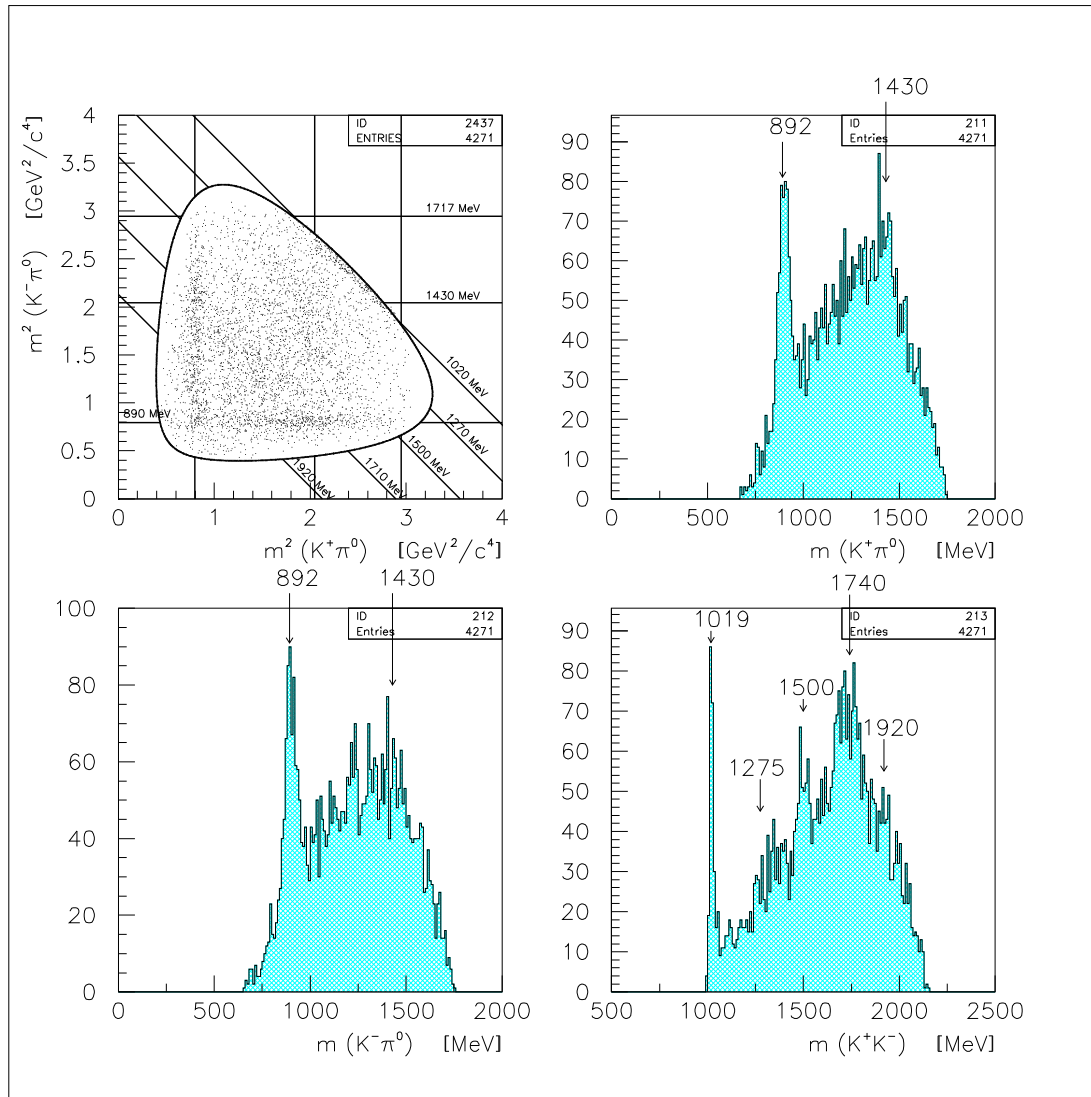


Figure 4.9: Dalitz plot and the projections of $K^+K^-\pi^0$ states at 1642 MeV/c

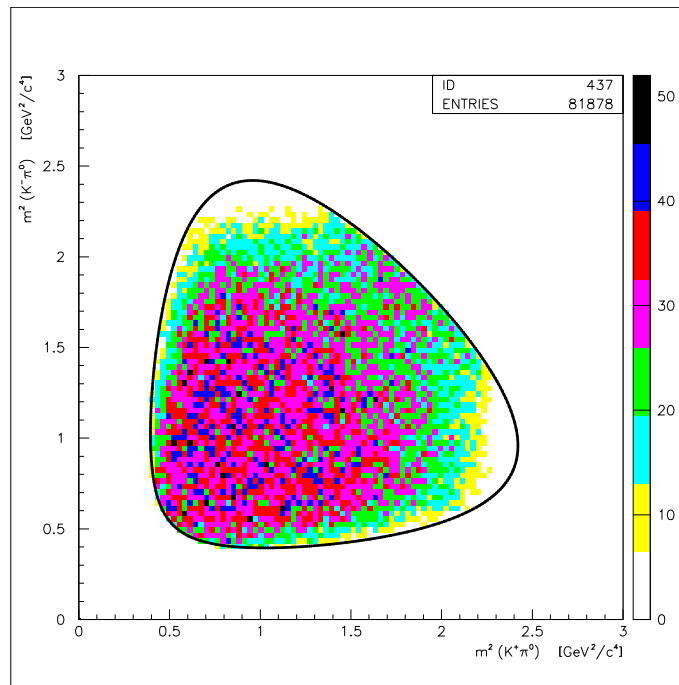


Figure 4.10: Dalitz plot of $K^+K^-\pi^0$ Monte Carlo events at 900 MeV/c.

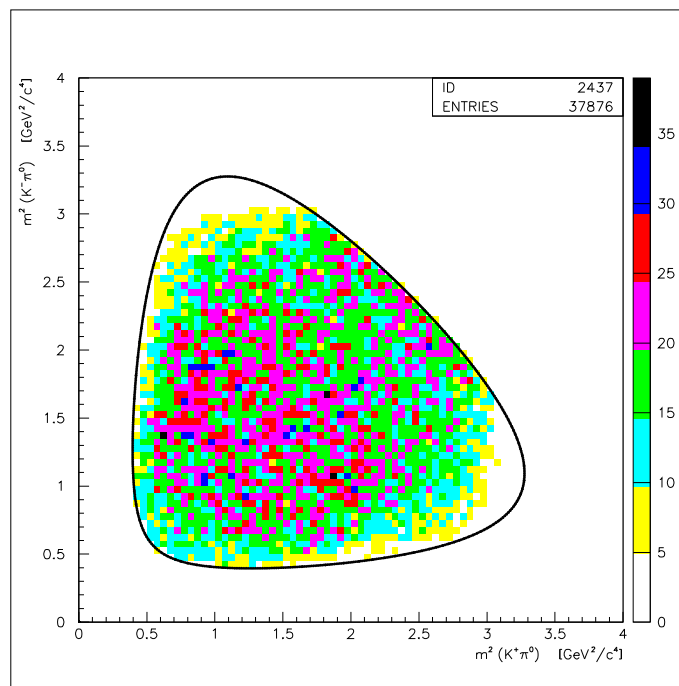


Figure 4.11: Dalitz plot of $K^+K^-\pi^0$ Monte Carlo events at 1642 MeV/c.

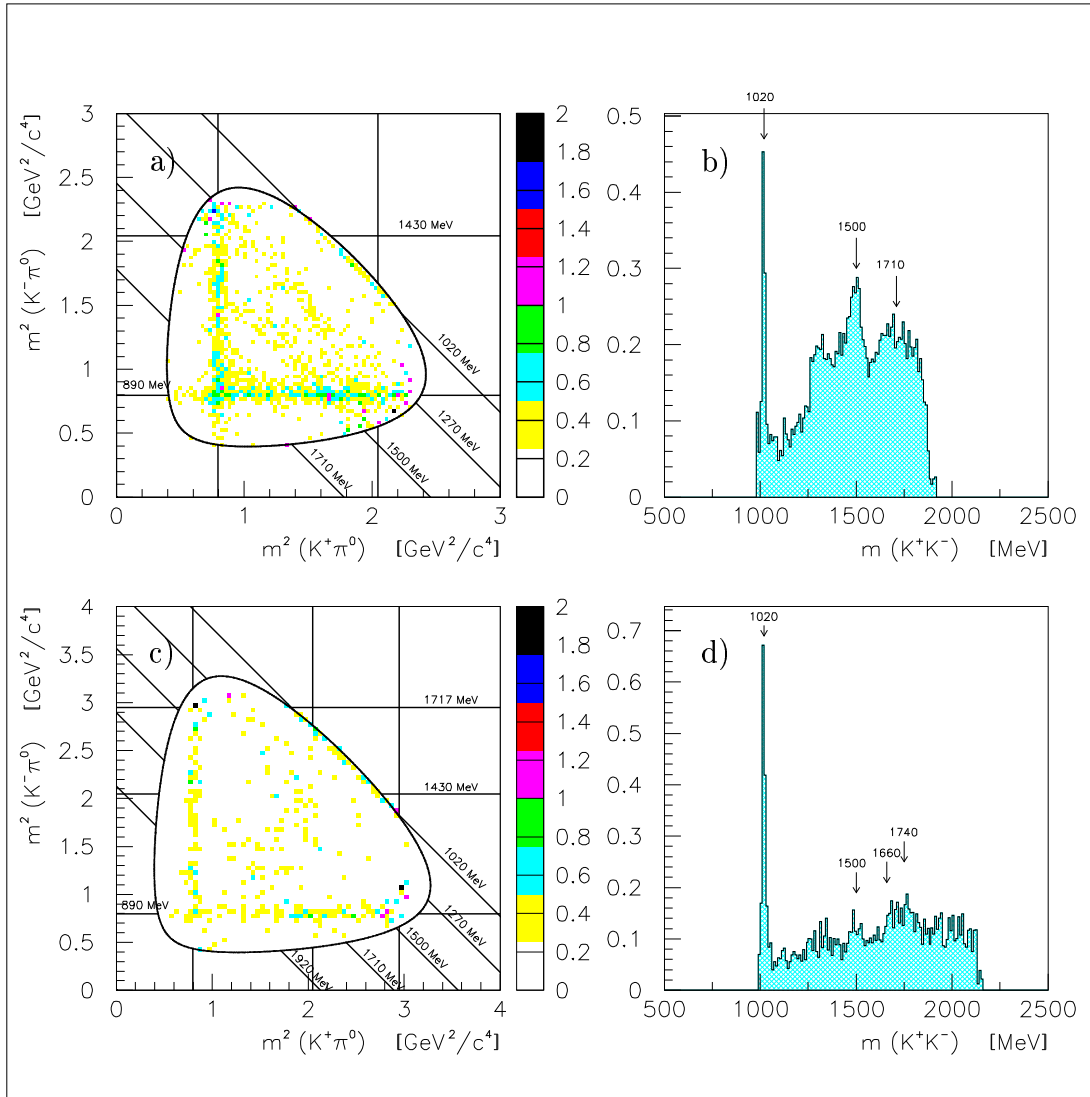


Figure 4.12: Acceptance corrected Dalitz plots and the K^+K^- projections: a), b) for 900 MeV/c incoming \bar{p} momentum, c), d) for 1642 MeV/c incoming \bar{p} momentum.

Chapter 5

The Partial Wave Analysis

In this chapter the form of the transition matrix M_{if} from the initial $\bar{p}p$ states to the final $K^+K^-\pi^0$ states will be discussed in the frame of the isobar model.

The moderate statistics and the high number of initial states in flight require a simplification of the partial wave analysis by averaging over all initial states.

The same method has already been used to analyze the reaction $\bar{p}p \rightarrow 3\pi^0\eta$ at 1200 MeV/c and at 1942 MeV/c [64] and $\bar{p}p \rightarrow \pi^0\pi^0\eta$ [33], [32]. It is described in details for the reaction in $3\pi^0\eta$ in the note [65]. A short review is given in this chapter.

5.1 The Transition Amplitude

In the isobar model the transition to a 3-body final state is described in two steps. In the first step two particles are produced, one is the isobar A and the other is the recoiling meson. In the second step the isobar A decays into two other mesons. The definition of the kinematic quantities is given in the so-called Gottfried-Jackson system [66] (see fig. 5.1), where

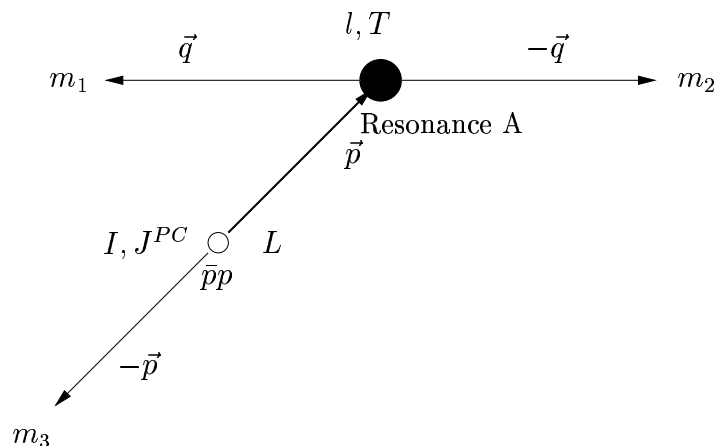


Figure 5.1: Definition of the kinematical quantities in the Gottfried-Jackson reference system.

m_1, m_2, m_3 are the masses of the final state particles,
 \vec{p} is the momentum of the isobar A in the $\bar{p}p$ rest system,
 \vec{q} is the momentum of the mesons from the decay of the isobar in its rest frame,

I, J^{PC} are the isospin, spin and parity of the initial state,

L is the angular momentum between the isobar and the recoiling meson,

l, T are the angular momentum and isospin of the two-meson system.

The final state particles have spin 0 so the angular momentum l is equivalent to the spin s of the two-meson system. According to this model the partial transition amplitude from a specific $\bar{p}p$ states to the final states via a specific intermediate two-meson state can be expressed

$$A_{I,J^{PC},L,l}(\vec{p}, \vec{q}) = b_{I,T,C} Z_{J,L,l}(\vec{p}, \vec{q}) D_L(\vec{p}) F_l(\vec{q}) \quad (5.1)$$

where:

$b_{I,T,C}$ is a isospin-coupling coefficient,

$Z_{J,L,l}(\vec{p}, \vec{q})$ is the spin-parity function,

$F_l(\vec{q})$ is the dynamic function that is given by a relativistic Breit-Wigner amplitude in the present work,

$D_L(\vec{p})$ are the centrifugal barrier factors of the two-meson-meson production with relative angular momentum L . A standard parametrization with the Blatt-Weisskopf damping factors [67] is used. At low momentum $D_L(\vec{p})$ suppresses the amplitude with a factor that is approximately proportional to p^L . The damping factors are included to avoid divergence at high momentum.

We denote with $i(\equiv J^{PC})$ all the possible initial state and with $f(\equiv T, s)$ all possible intermediate states. When n_i intermediate states are produced from the same initial state leading to the same final state their amplitudes must be added coherently. This means the probability density $d_i(X, Y)$ in any point X, Y of the Dalitz plot is given by

$$d_i(X, Y) = \left| \sum_{f=1}^{n_i} a_{if} A_{if}(X, Y) \right|. \quad (5.2)$$

The "production strenghts" a_{if} are in general complex constants and can be written in the form $a_{if} = x_{if} e^{i\phi_{if}}$ with $\phi_{i1} = 0$. The absolute phase disappears with the normalization, so that for the transition via n_i intermediate states coming from one initial state i we get $2n_i - 1$ parameters. The total probability density is obtained adding incoherently all different initial states

$$D(X, Y) = \sum_{i=1}^m d_i(X, Y) = \sum_{i=1}^m \left| \sum_{f=1}^{n_i} a_{if} A_{if}(X, Y) \right| \quad (5.3)$$

where m is the number of initial states. The observed intensity $w(X, Y)$ in any cell or bin of the Dalitz plot is obtained by integrating over the elementary phase-space volumes

$$\begin{aligned}
w(X, Y) &= \int_{dXdY} D(X, Y) dXdY \\
&= \int_{dXdY} \sum_{i=1}^m \left\{ \left(\sum_{f=1}^{n_i} x_{if} e^{i\phi_{if}} A_{if} \right) \left(\sum_{f=1}^{n_i} x_{if} e^{-i\phi_{if}} A_{if}^* \right) \right\} dXdY \quad (5.4)
\end{aligned}$$

Since the production strengths and the relative phases are constant over the phase-space they can be extracted from the integration, and eq. 5.4 can be written in the form

$$\begin{aligned}
w(X, Y) &= \sum_{i=1}^m \left\{ \sum_{f=1}^{n_i} x_{if}^2 |A_{if}|^2 + \right. \\
&\quad \sum_{f=1}^{n_i-1} \sum_{l=f+1}^{n_i} \left[2x_{if}x_{il} \cos(\phi_{if} - \phi_{il}) \int_{dXdY} \Re(A_{if}A_{il}^*) dXdY \right. \\
&\quad \left. \left. - 2x_{if}x_{il} \sin(\phi_{if} - \phi_{il}) \int_{dXdY} \Im(A_{if}A_{il}^*) dXdY \right] \right\} \quad (5.5)
\end{aligned}$$

5.2 Selection Rules

The $\bar{p}p$ annihilation can only occur from states with certain J^{PC} quantum number combinations. The isospin is given by the G-parity of the final state particles and their quantum numbers. The total wave function of the $\bar{p}p$ state can be written combining the orbital wave function with the spin wave function. The spin wave function can be in a singlet ($S = 0$) or in a triplet state ($S = 1$). In the spectroscopic notation we write

$${}^{2S+1}L_J \quad (5.6)$$

where J is the total angular momentum, L is the relative angular momentum with the conventional symbols S, P, D, F, G, H, \dots for $L = 0, 1, 2, 3, 4, 5, \dots$. In the case of annihilation at rest the proton and the antiproton have a relative orbital angular momentum of $L = 0$ with a 10% contribution of $L = 1$. The contribution of the partial waves for annihilation in flight can be estimated in two different ways. In a semi-classical model the maximum value of the orbital angular momentum for a given impact parameter b of 1.6 fm is obtained from

$$\frac{h}{2\pi} \sqrt{L(L+1)} \simeq \vec{p} \times \vec{b} \quad (5.7)$$

where \vec{p} is the antiproton momentum in the $\bar{p}p$ center of mass system.

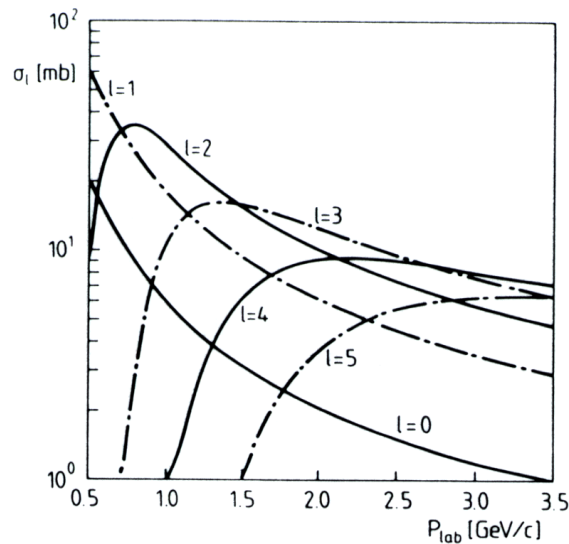


Figure 5.2: Partial wave annihilation cross sections σ_l as a function of lab. momentum for several angular momenta l and for a hadron radius of 0.6 fm [68].

In a statistical model, the so-called two-meson doorway model [68], [70], the cross section of the single partial waves can be derived using equation 5.7 with an impact parameter of 1.6 fm and a hadron radius of $r = 0.6$ fm. The results of this model are represented in fig 5.2, where the contributions of the partial wave annihilation cross section for several angular momenta l are shown as a function of the momentum of the incoming antiproton. From the statistical model, it can be established (see fig 5.2) that, at an antiproton momentum of 900 MeV/c, a high contribution of P and D waves with a non-negligible amount of F and S waves (with approximately equal contributions) has to be considered.

At 1642 MeV/c an upper limit of $L = 5$ is derived. The initial states up to $J = 3$ are listed in table 5.1. The J^{PC} quantum numbers are calculated considering that the parity of the proton-antiproton system is $(-1)^{L+1}$ and the C-parity is $(-1)^{L+S}$.

Total ang. mom. $J_{\bar{p}p}$	Singlets	Triplets
$J = 0$	$0^{-+}({}^1S_0)$	$0^{++}({}^3P_0)$
$J = 1$	$1^{+-}({}^1P_1)$	$1^{++}({}^3P_1), 1^{--}({}^3S_1/{}^3D_1)$
$J = 2$	$2^{-+}({}^1D_2)$	$2^{++}({}^3P_2/{}^3F_2), 2^{--}({}^3D_2)$
$J = 3$	$3^{+-}({}^1F_3)$	$3^{++}({}^3F_3), 3^{--}({}^3D_3)$

Table 5.1: Initial states of the $\bar{p}p$ system up to an estimated upper limit of $J = 3$ at an incoming antiproton momentum of 900 MeV/c. The initial state 3P_0 does not contribute to the production of 3 pseudoscalar mesons by parity and angular momentum conservation.

Selection rules can be applied to reduce the number of partial waves for a given quantum number of the two-meson state. Consider the two possible reaction

types:

- A. $\bar{p}p \rightarrow X\pi^0, X \rightarrow K^+K^-$
 B. $\bar{p}p \rightarrow Y^\pm K^\mp, Y^\pm \rightarrow K^\pm\pi^0$

In the case of a reaction type A, with the isobar $X \rightarrow K^+K^-$, the following rule holds:

$$P_X = (-1)^{l_{K^+K^-}} \quad (5.8)$$

$$C_X = (-1)^{l_{K^+K^-} + S_{K^+K^-}} \quad (5.9)$$

where $l_{K^+K^-}$ is the angular momentum between kaons. $J_{K^\pm} \equiv 0$ so $S_{K^+K^-} = 0$. Hence $C_X = (-1)^{l_{K^+K^-}} = P_X$ and only resonances with the same P and C parity can decay into K^+K^- , i.e. 0^{++} (scalar), 1^{--} (vector), 2^{++} (tensor), 3^{--} , 4^{++} , \dots .

Conservation of parity implies

$$P_{\bar{p}p} = (-1)^{L_{\bar{p}p}+1} = P_X P_{\pi^0} (-1)^{L_{X\pi^0}} \quad (5.10)$$

where P_X is the parity of the isobar and $L_{X\pi^0}$ is the angular momentum between the isobar X and π^0 . The parity of the π^0 is $P_{\pi^0} = -1$. Hence,

$$P_{\bar{p}p} = (-1)^{L_{\bar{p}p}+1} = P_X (-1)^{L_{X\pi^0}+1}. \quad (5.11)$$

In addition conservation of C-parity implies

$$C_{\bar{p}p} = C_X C_{\pi^0} = C_X. \quad (5.12)$$

Finally conservation of the total angular momentum implies

$$\vec{J}_{\bar{p}p} = \vec{J}_X + \vec{J}_{\pi^0} + \vec{l}_{X\pi^0} = \vec{J}_X + \vec{L}_{X\pi^0}. \quad (5.13)$$

Using the selection rules we fill table 5.2 where we list the allowed initial states for different quantum numbers of K^+K^- resonances.

In the case of reaction type B the isobar $Y^\pm \rightarrow K^\pm\pi^0$, like the $K^*(892)$, can be produced from every initial state. For the $K^{*\pm}(892) \rightarrow K^\pm\pi^0$ which has $J^P = 1^-$ parity and angular momentum conservation limits the possible values of the angular momentum L_{YK} between the isobar Y^\pm and the recoiling K^\mp (see table 5.3).

In a simple description of the Dalitz plot at 900 MeV/c at least the following resonances decaying into K^+K^- have to be included: $\phi(1020)$, $f_2(1275)$, $f_0(1500)$, $f_2'(1525)$, $f_j(1710)$. In addition, for $Y^\pm \rightarrow K^\pm\pi^0$ the $K^*(892)$, $K_0^*(1430)$, $K_2^*(1430)$ must be considered.

A rapid calculation to estimate the number of parameters can be performed using tables 5.2, 5.3. Because of the centrifugal barrier effect, high values of the angular momentum are suppressed, particularly for the production of an isobar with a high mass. If upper limits of $L=1$ and $L=2$ for an isobar with a mass $m > 1700\text{MeV}$ and $1400 < m < 1700\text{MeV}$ respectively are taken, a full partial wave analysis requires, keeping the masses and widths of the resonances fixed, the optimization of more than 100 free parameters.

This makes the analysis unsuccessful even at 900 MeV/c where the statistics is considerably higher and the number of initial states is lower in comparison to the data at 1642 MeV/c.

Initial state $J_{\bar{p}p}^{PC}$	$L_{X\pi^0}$ ($J_X^{PC} = 0^{++}$)	$L_{X\pi^0}$ ($J_X^{PC} = 1^{--}$)	$L_{X\pi^0}$ ($J_X^{PC} = 2^{++}$)	$L_{X\pi^0}$ ($J_X^{PC} = 3^{--}$)	$L_{X\pi^0}$ ($J_X^{PC} = 4^{++}$)
0^{-+}	0		2		4
1^{--}		1		3	
1^{+-}		0,2		2,4	
1^{++}	1		1,3		3,5
2^{++}			1,3		3,5
2^{--}		1,3		1,3,5	
2^{-+}	2		0,2,4		2,4,6
3^{++}	3		1,3,5		1,3,5,7
3^{--}		3		1,3,5	
3^{+-}		2,4		0,2,4,6	

Table 5.2: Selection rules for the production of the possible $X \rightarrow K^+K^-$ resonances from all initial states up to $J_{\bar{p}p} = 3$.

Initial state $J_{\bar{p}p}^P$	L_{YK} ($J_Y^P = 1^-$) ($K^*(892)$)	L_{YK} ($J_Y^P = 0^+$) ($K_0^*(1430)$)	L_{YK} ($J_Y^P = 2^+$) ($K_2^*(1430)$)
0^{-+}	1	0	2
1^{--}	1		2
1^{+-}	0,2	1	1,3
1^{++}	0,2	1	1,3
2^{++}	2		1,3
2^{--}	1,3	2	0,2,4
2^{-+}	1,3	2	0,2,4
3^{++}	2,4	3	1,3,5
3^{--}	3		2,4
3^{+-}	2,4		1,3,5

Table 5.3: Selection rules for the production of the possible $Y^\pm \rightarrow K^\pm\pi^0$ resonances from all initial states up to $J_{\bar{p}p} = 3$.

5.3 The Canonical Formalism

In the analysis using the "canonical formalism" a sequence of operations acting on the 4-vectors in the $\bar{p}p$ reference system is of fundamental importance. Consider first the process $\bar{p}p \rightarrow A + 1$, $A \rightarrow 2 + 3$ where the particle 1 has no spin, and where the isobar A is produced at an angle (θ, ϕ) with respect to the beam direction (see fig. 5.3). Initially all 4-vectors of the final state in the $\bar{p}p$ rest frame are transformed to new vectors in a new reference frame where the direction of flight of the isobar A is the new z -axis ($\equiv z'$). This is performed by a rotation around the beam axis (angle ϕ) and by a subsequent rotation around the new y -axis (angle θ). After a Lorentz transformation ("boost") to the center of mass system of A the new system is rotated back by $-\phi$, then by $-\theta$. In this way the new 4-vectors are referred to a new z'' that is parallel to the original beam axis. With these operations the amplitudes which are invariant under Lorentz boost can be written in terms of Legendre polynomials which are dependent on the decay angles α rather than α' and the rotation matrices which are needed for the first rotation are cancelled. This procedure, called "Wick rotation" follows a canonical treatment of spin based on the helicity formalism [69].

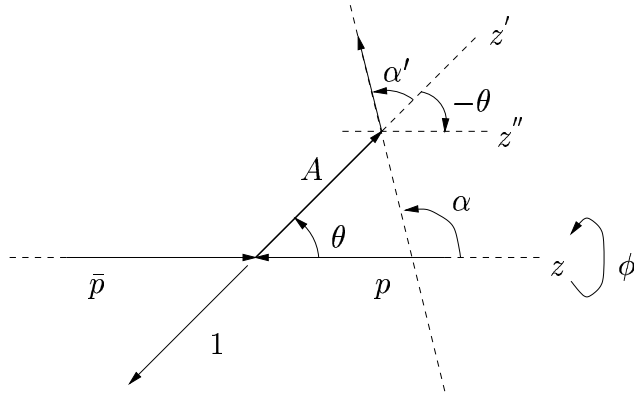


Figure 5.3: Angles used in the canonical formalism: The Wick rotation by the angles θ and ϕ are followed by a Lorentz boost to the rest frame of the isobar and by another rotation with angles $-\phi$ and $-\theta$. α defines the direction of a decay particle from the resonance A in the rest frame of A after the Wick rotation.

The coupling between the initial \bar{p} -state and the state $A + 1$ is given by the Clebsch-Gordan decomposition

$$|J, \lambda_i \rangle = \sum_{\lambda_f, L_z, l} \langle s, \lambda_f, L, L_z | J, \lambda_i \rangle |s, \lambda_f \rangle |L, L_z \rangle \quad (5.14)$$

where

λ_i is the projection in the overall reference system of the total spin J of the $\bar{p}p$ system,

L_z is the projection of the orbital angular momentum L between A and the meson 1 in the overall reference system,

λ_f is the projection of the spin s of the particle A along the z -axis.

The angular dependent part, that is the *eigenstate* of the angular momentum, is represented by the associated Legendre functions

$$|L, L_z \rangle = P_L^{L_z}(\theta, \phi). \quad (5.15)$$

The decay of the resonance A with spin s into spin 0 particles is described simply by

$$|s, \lambda_f \rangle = P_s^{\lambda_f}(\alpha, \beta) \quad (5.16)$$

where α and β define the direction of a decay particle from the resonance A in the rest frame of A after the Wick rotation. The initial state is unpolarized. There is no interference between initial singlet and triplet state, i.e. the amplitudes belonging to different λ_i add up incoherently. The recoiling particle has spin 0 and there is nothing in the channel we can consider to determine the azimuthal angle, hence we have a cylindrical symmetry with respect to the beam direction.

The formalism used here integrates over all possible initial states, with the production angles of every isobar simulated in a simple form. The approximation is to consider the minimal θ dependence which is essential. Because of the cylindrical symmetry there is no dependence on the azimuthal angle. For all neutral final states the differential cross section $\frac{d\sigma}{d\Omega}$ is symmetric about $\theta = 90^\circ$, i.e. $\frac{d\sigma}{d\Omega}$ is even in powers of $\cos\theta$. For a reaction of type A, where the isobar X decays into K^+K^- , the effect on the quality of the fit introducing a parametrization of the type

$$P_L^{L_z}(\theta, \phi) \equiv P_L^{L_z}(\theta) = p_0 + p_2(\cos\theta)^2 + p_4(\cos\theta)^4 + \dots \quad (5.17)$$

is considered separately for every resonance. The dependence on $(\cos\theta)^4$ and on higher orders can be neglected. The parameter p_0 is absorbed in the overall normalization. For a reaction of type B, where the isobar Y decays into $K^\pm\pi^0$, $\frac{d\sigma}{d\Omega}$ is forward-backward asymmetric and a parametrization of the θ dependence of the form

$$P_L^{L_z}(\theta) = p_0 + p_1\cos\theta + p_2(\cos\theta)^2 + \dots \quad (5.18)$$

is considered separately for every positively and negatively charged isobar.

To account for final states with the same λ_f but coming from different initial states in equation 5.14 a free parameter c_{ab}^λ is added to the strengths a and b of the two amplitudes to account for partial coherence, i.e. a mixture of coherent and incoherent amplitudes. The total probability density is written, in analogy to eq 5.5, in the form

$$D(X, Y) = \sum_{\lambda_f} \left\{ a_\lambda^2 |A|^2 + b_\lambda^2 |B|^2 + 2c_{ab}^\lambda a_\lambda b_\lambda [\cos\phi_{ab}^\lambda \Re(AB^*) + \sin\phi_{ab}^\lambda \Im(AB^*)] \right\} \quad (5.19)$$

This expression is only valid for two channels. The general expression including all channels, that is used in the present analysis, is given in appendix A. The coefficients c_{ab}^λ are constrained to lie between 0 for no coherence and to ± 1 for full coherence, corresponding to a unique initial partial wave. Since all reactions

involve one isobar plus one spin 0 particle it is shown [65] that cross sections contain no interference between states of X (or Y) with different λ .

It is instructive to consider, for example, the interference between two resonances that overlap in the Dalitz plot, like

$$\bar{p}p(0^{-+}, 1^{++}, 2^{++}, 2^{-+}, 3^{++}) \rightarrow \pi^0 + [f_0(1500), f'_2(1525)] \quad (5.20)$$

In total we have 4 parameters for the strenghts (a_0 for $f_0(1500)$ and b_0, b_1, b_2 for $f'_2(1525)$), one for the degree of coherence c_{ab}^0 and one for the phase difference between the $f_0(1500)$ and the $f'_2(1525)$. The phase of one channel is set to zero as reference phase. The number of parameters increase to 6+6 if we consider the interference between two tensors (eg. the $f'_2(1525)$ and the $f_j(1710)$ if $j = 2$) because additional parameters $c_{ab}^\lambda, \phi_{ab}^\lambda$ for $\lambda = 0, 1, 2$ for every helicity amplitudes have to be considered.

The advantage of the approximations described above is the reduced number of free variables in the fit. Infact, reducing the number of free parameters is a necessity. However, the software implementation does not allow to handle the masses and the widths as free parameters. They have to be optimized by hand.

An additional approximation reduces the number of parameters and makes a considerable simplification in the analysis. In previous experiments (eg. CERN-Munich experiment [71]) the formation of a resonance with a z -component of the spin $|\lambda| > 1$ is strongly suppressed. This has been confirmed also from the Crystal-Barrel collaboration [64]. The amplitudes with $|\lambda| > 1$ optimize to zero and the corresponding parameters can be set to zero.

5.4 The Fitting Procedure

A correct description of the experimental Dalitz plot is given if the theoretical intensity w_i (eq. 5.5) calculated for an elementary phase-space volume $d\tau_i$ in any point (X, Y) of the D.P. minimizes the χ^2 function

$$\chi^2 = \sum_i \frac{[n_i - w_i(\bar{a})]^2}{\sigma_i^2} \quad (5.21)$$

where the sum extends over all elementary phase-space volumes (i.e. bins of the D.P.),

n_i is the number of events in the same bin i of the D.P.,

\bar{a} is the m -dimensional vector of the m unknown parameters that have to be fitted

σ_i are the standard errors which take into account the experimental and the theoretical errors.

Finding the set of parameters \bar{a} which minimize the χ^2 function is equivalent to finding the set of parameters which maximize the standard likelihood function, that is given by the products of the probability density functions (PDF). For an

unbinned Dalitz plot we have

$$\mathcal{L} = \prod_{i=1}^N w_i(\bar{a}_m) \quad (5.22)$$

where N is the number of events. The integral over all phase space $\int w d\tau$ is not constant if the set of parameters varies, therefore the weight function has to be normalized and the likelihood function is defined as

$$\mathcal{L} = \prod_{i=1}^N \frac{w_i(\tau_i, \bar{a}_m) \epsilon(\tau_i)}{\int w_i(\tau_i, \bar{a}_m) \epsilon(\tau_i) d\tau}. \quad (5.23)$$

The coefficients $\epsilon(\tau_i)$ describe the acceptance and the efficiency of the experimental apparatus. The integral in the denominator is approximated via the summation of the weight function over a sample of Monte Carlo events. The phase-space distributed Monte Carlo events are reconstructed using the same selection criteria as the data and the factor ϵ is implicitly considered in the summation. If N_{MC} is the number of Monte Carlo events the integral can be approximated with

$$\int w \epsilon d\tau = \frac{N}{N_{MC}} \sum_{j=1}^{N_{MC}} w(\tau_j^{MC}, \bar{a}) = \frac{N}{N_{MC}} \Phi. \quad (5.24)$$

The single probabilities have in general small values so that it is useful to minimize the negative logarithmic likelihood (NLL)

$$NLL = -\ln \mathcal{L}. \quad (5.25)$$

Taking into account the approximation 5.24 the NLL is

$$NLL = - \left(\sum_{i=1}^N \ln w_i + \sum_{i=1}^N \epsilon \right) + N \ln \frac{N\Phi}{N_{MC}} \quad (5.26)$$

All constant terms which do not depend on \bar{a} do not affect the optimization procedure. Constant is also the sum of the single efficiencies so that the NLL to be minimized is

$$S = -\ln \mathcal{L} = - \left(\sum_{i=1}^N \ln w_i \right) + N \ln \left(\sum_{j=1}^{N_{MC}} w_j \right) \quad (5.27)$$

With this definition a reduction of S of $0.5 \cdot r$ by extending the hypotheses by r more free variables corresponds to a statistically significant improvement (one standard deviation), which corresponds to a change of 1 in the reduced χ^2 test to r degrees of freedom. Therefore the error of a fitted parameter, like the mass or the width of a resonance, can be estimated scanning the value of parameter in the neighborhood of the optimum and keeping all the other parameters fixed. For

small changes the NLL should behave, if the theoretical assumptions are correct, like a parabola. If additional resonances or interferences are introduced and the number of parameters is increased, the log-likelihood gives the goodness of a fit relative to the previous optimization. To get an absolute reference a χ^2 -test is still required.

5.5 χ^2 Test with Equal Binning Content

In the standard definition of the χ^2 (eq. 5.21) the summation is extended to all bins. The terms of the summation are not defined if no entries are present and are removed with a consequent loss of information. This occurs when the statistics is low and/or when the efficiencies and the acceptance of the detector is low (close to the boundaries of the Dalitz plot). For bins with a low number of contents, the definition 5.21 does not have any statistical meaning. A simple solution to this problem consists in increasing the size of the bins but in this way the definition of the narrow structures is lost.

For this reason a new procedure of creation of bins with equal content of data is being developed [72]. The experimental Dalitz plot is divided in bins with different sizes but with an equal number of contents: 1000 bins with approximately 16 entries for the Dalitz plot at 900 MeV/c and with ~ 4 entries at 1642 MeV/c (see fig. 5.4, 5.5).

As a consequence the sizes of the bins are decreased in the high populated areas and no empty bins are present.

The reduced χ^2 is calculated using an adaptation of the standard Pearson χ^2 (see [73])

$$\chi^2 = \sum_i \frac{(n_i - f_i m_i)^2}{f_i (n_i + m_i)} \quad (5.28)$$

where

n_i is the number of observed events in the i -th bin,

m_i is the number of Monte Carlo events in the i -th bin,

f_i is the average of the theoretical weights f_{ij} of individual Monte Carlo events in the i -th bin

$$f_i = \frac{1}{m_i} \sum_{j=1}^{m_i} f_{ij} \quad (5.29)$$

The expression 5.28 is obtained taking into account only the variance of the observed number of events. A correction that takes into account the variation of the transition amplitude within a bin can also be included, using a complicated expression of the χ^2 [73], but it can be neglected as compared to the variance of n_i .

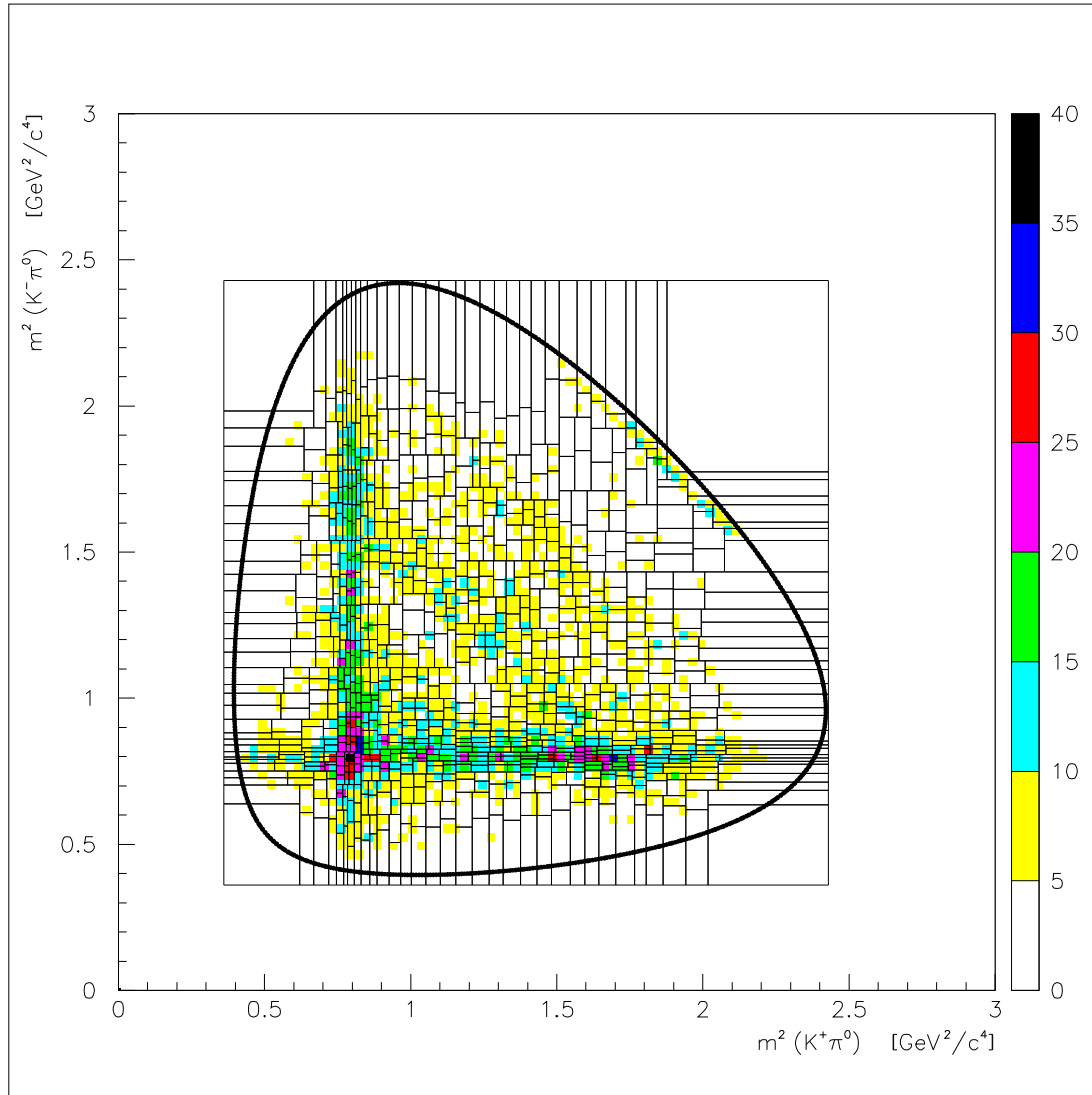


Figure 5.4: Binned Dalitz plot (1000 Bins) at 900 MeV/c with nearly equal content of data (~ 16 events per bin)

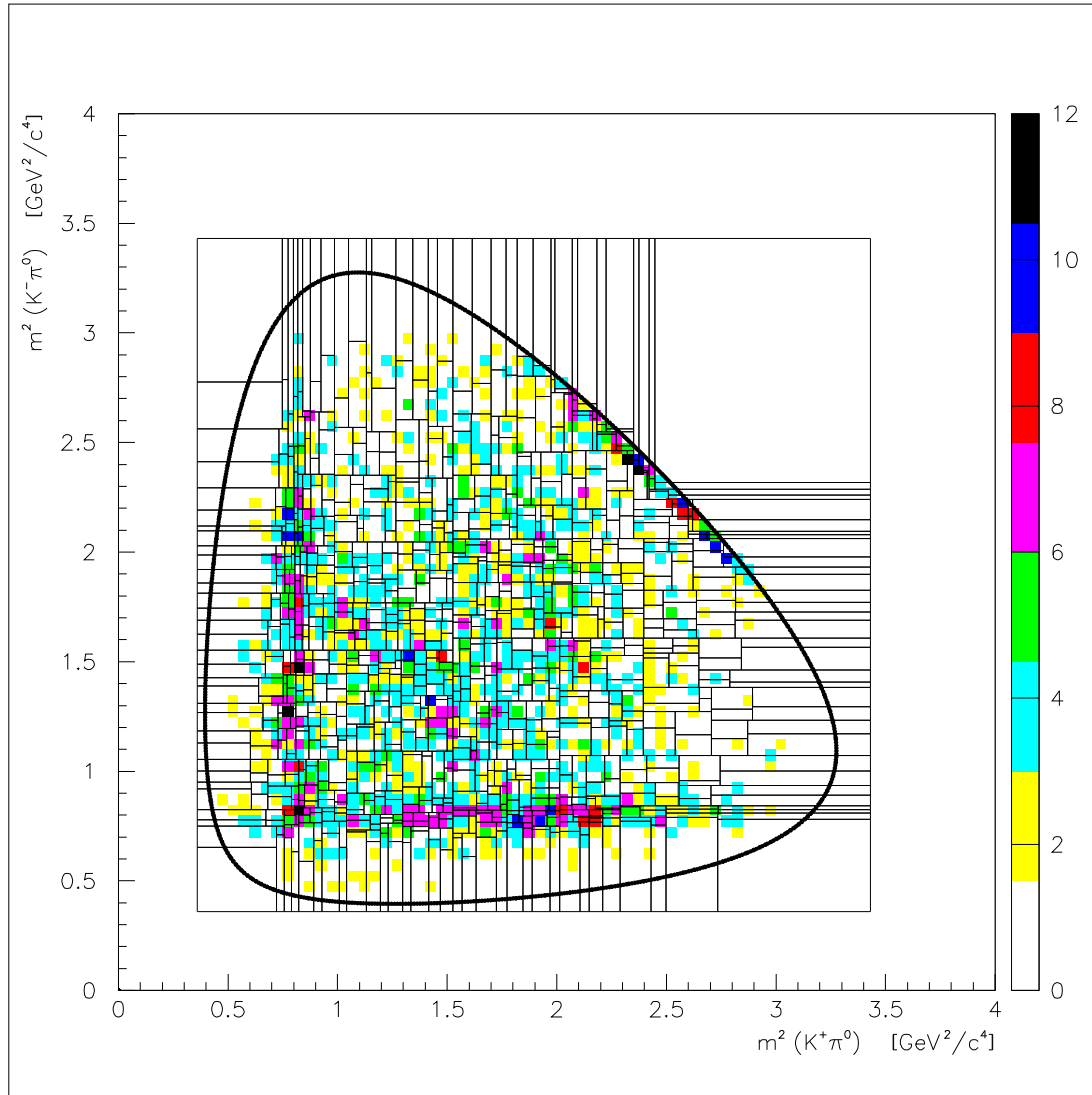


Figure 5.5: Binned Dalitz plot (1000 Bins) at 1642 MeV/c with nearly equal content of data (~ 4 events per bin)

5.6 Description of the Fitting Program

To save CPU time the rotation of the momentum vectors, the Lorentz transformation and the calculation of the Legendre polynomials is done once for each event and for all channel, separately at the beginning.

The main program optimizes the coupling constants $a_\lambda, b_\lambda, \dots$, the partial degrees of coherence c_{ab}^λ , and the phases ϕ_{ab}^λ . The FUMILI [74] minimization program is used for faster convergence. If the masses and widths are handled as fixed parameters the fit is very fast and lasts typically 2s per iteration (on Alpha dec-stations). A full convergence is obtained typically after 10-40 iterations. The masses and widths can also be varied but in this case an intermediate calculation is required. We experience that a manual scan works more efficiently compared to a numerical optimization. Fitting the masses and width "by hand" offers the opportunity to

- watch interactively the improvement or deterioration to the quality of the fit
- interrupt the optimization whenever the distance to the minimum gets steadily smaller without the value of the log-likelihood improving
- control the step lengths

When the optimization has fully converged, the calculation of the reduced χ^2 with equal binning content is performed and the improvement is compared with the log-likelihood change (with respect to a previous fit). As a general rule we experience that a LL change of 0.5 is significant only when the mass or the width of a resonance is varied. If the form of the PDF is different (i.e. additional resonances or different spin of the isobars) a minimum ΔLL change of ~ 10 per number of added parameters, corresponding to a significant change of the χ^2 , is required for a better fit.

Chapter 6

Results of the Analysis

The description of the reaction $\bar{p}p \rightarrow K^+K^-\pi^0$ at an incoming antiproton momentum of 900 MeV and at 1642 MeV/c has been carried out using the canonical formalism. The data at low momentum is well suited to the observation of the K^+K^- resonances with an invariant mass around 1.5 GeV. On the other hand the investigation of the resonances with masses around 1.7 GeV is complicated at 900 MeV/c because of the crossing $K^*(890)$ bands. For this purpose the analysis at 1642 MeV/c is more appropriate even if the statistic is lower: indeed the high number of initial states better justifies the approximation used in the canonical formalism. At both momenta various resonances with different spin combinations have been fitted in this mass range with the objective to

- confirm the $f_0(1500)$ and separate it from the $f'_2(1525)$
- find the $f_J(1710)$
- solve the puzzle of the spin of the $f_J(1710)$
- confirm the $a_2(1660)$

6.1 Basic Fit at 900 MeV/c

As a starting point the following intermediate states have been considered:

$$\bar{p}p \rightarrow \phi(1020)\pi^0 \quad (1)$$

$$\rightarrow f_2(1275)\pi^0 \quad (2)$$

$$\rightarrow f_0(1500)\pi^0 \quad (3)$$

$$\rightarrow K^{*\pm}(892)K^\mp \quad (4)$$

$$\rightarrow K_0^{*\pm}(1430)K^\mp \quad (5)$$

$$\rightarrow K_2^{*\pm}(1430)K^\mp \quad (6)$$

In this fit only one scalar at 1500 MeV is included. Without considering the interferences, only the contributions of every single channel are fitted. With the

masses and widths fixed to the current values given by the Particle Data Group [2] the basic fit requires only the optimization of 12 parameters. All branching ratios are relative to the $K^*(890)$ (helicity 0) so the fit is performed actually with 11 free parameters. We experience that amplitudes with $|\lambda| > 1$ optimize to zero and can be excluded from the fit without a significant change in the log-likelihood.

For the decay of the f_2 resonances to K^+K^- , a centrifugal barrier B_2 is included using the standard Blatt-Weisskopf form

$$B_2 \propto \frac{9k^2 R^2}{\sqrt{1 + 3k^2 R^2(1 + 3k^2 R^2)}} \quad (6.1)$$

where k is the decay momentum and $R = 0.2$ fm is the radius of interaction [75]. The log-likelihood change is 79.6 for the $f_2(1275)$. For other resonances far from threshold the effect of the barrier is negligible.

There is a dominant contribution of the $K^{*\pm}(890)$. The $K^\pm\pi^0$ mass range of 1430 MeV is fitted including the $K_0^{*\pm}(1430)$; the contribution of the channel $K_2^{*\pm}(1430)$ is negligible ($< 0.5\%$).

To simulate in an approximate way the θ dependence of the charged isobar the amplitudes corresponding to K^{*+} and K^{*-} are multiplied by a factor

$$F(\theta) = 1 + p_1 \cos\theta + p_2 \cos^2\theta \quad (6.2)$$

The parameters p_1 , p_2 are fitted separately for each K^{*+} and K^{*-} . The corresponding angular distributions are compared with the data and are shown in fig. 6.1. A large improvement in the log-likelihood is obtained fitting the amplitudes of the $K^*(890)$ with equal and opposite coefficients of the $\cos\theta$ term, describing in an approximate way the forward-backward asymmetries of the charged isobars. The same optimization is repeated for the $K_2^{*\pm}(1430)$ and for the $K_0^{*\pm}(1430)$. The contribution of the $K_2^{*\pm}(1430)$ is still below 0.5% and channel (6) is omitted from the basic fit. We find no need for $K_1(1410)$ which has only a 6.7% branching ratio to $K\pi$ [2].

Next consider the self-interference of the $K^{*+}(890)$ with the $K^{*-}(890)$. No change in the log-likelihood is obtained, while the interference of the $K^{*\pm}(890)$ with the $K_0^{*\mp}(1430)$ is significant (see table 6.1). The fitted Dalitz plot and the relative χ^2 , calculated using the procedure with bins containing equal amount of data are shown in fig. 6.2; the projections of the Dalitz plot are shown in fig. 6.3. The fit looks clearly unsatisfactory in the 1.5 and 1.6 GeV K^+K^- mass range.

Interference	NLL	Par.	$\Delta LL/\Delta P.$	χ^2
$K^{*\pm}(892) \times K^{*\pm}(892)$	-1631.4	9	0.0/2	1.816
$K_0^*(1430) \times K^{*\pm}(892)$	-1665.9	9	34.5/2	1.791

Table 6.1: Log-likelihood changes for crossing interferences.

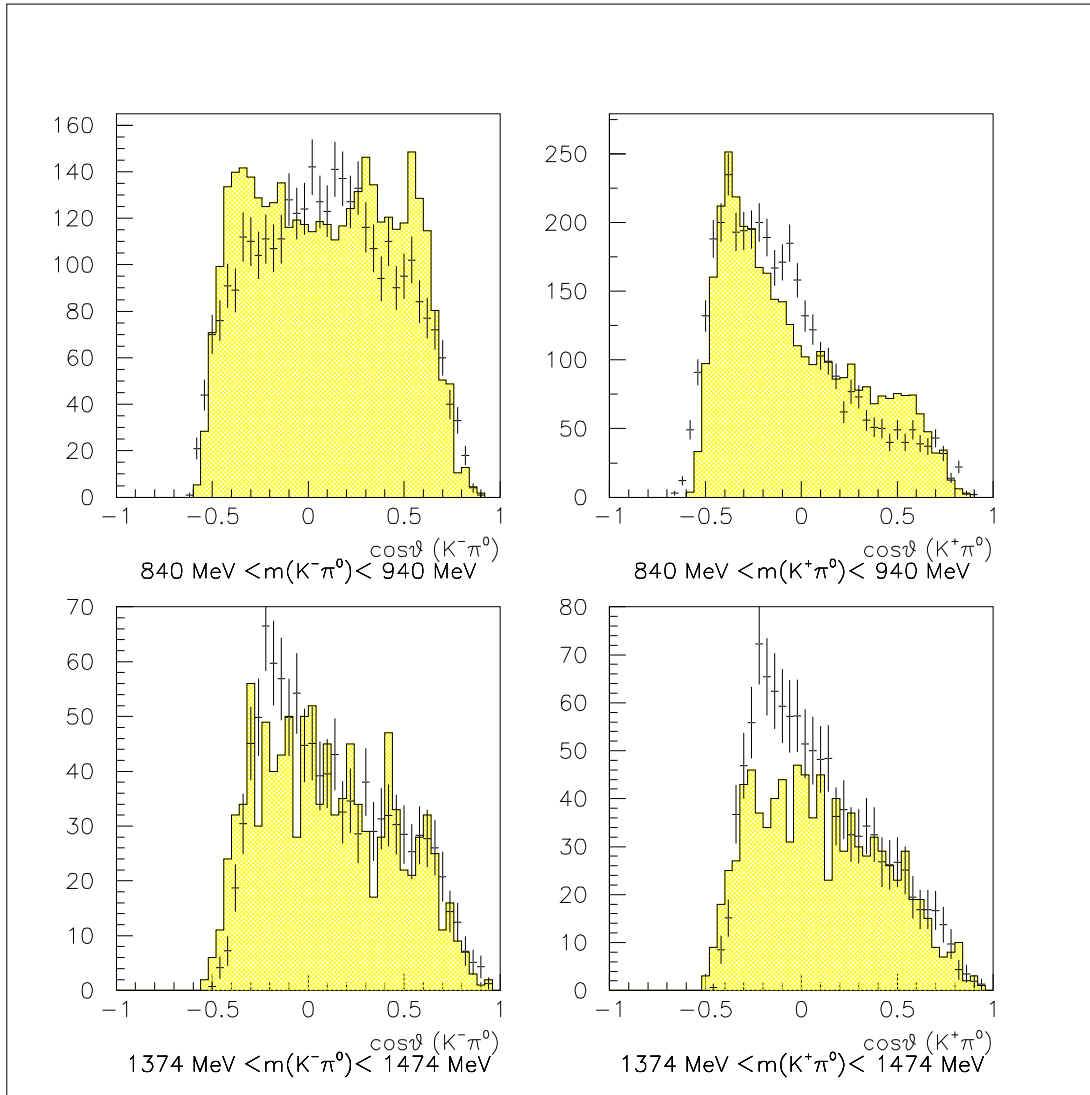


Figure 6.1: Fitted polar production angles of the $K^-\pi^0$ and $K^+\pi^0$ isobars at 900 MeV/c and in different mass range corresponding to the $K^*(890)$ and to the $K_0(1430)$.

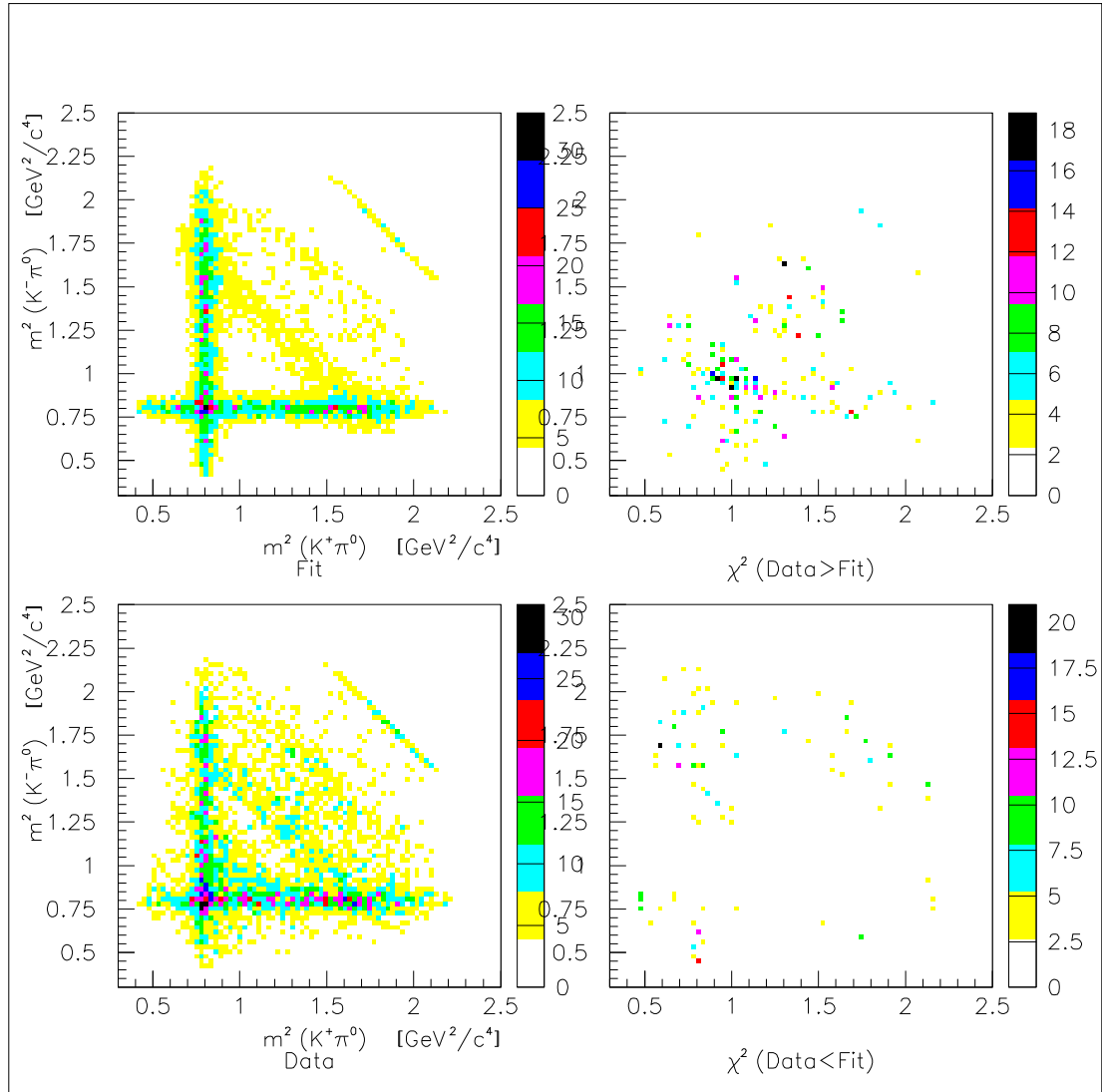


Figure 6.2: Basic fit of the Dalitz plot at 900 MeV/c.

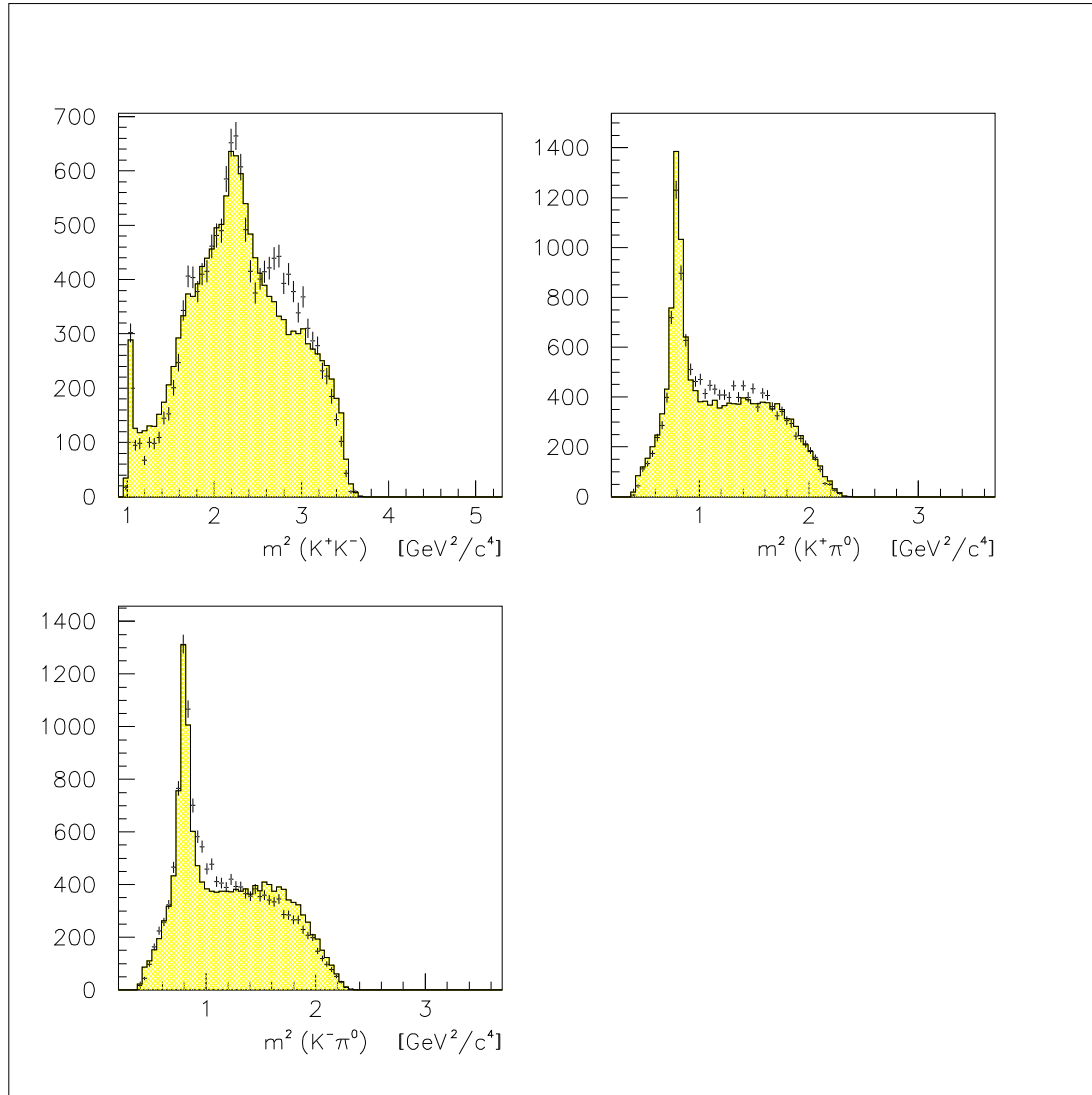


Figure 6.3: Basic fit: projections of the Dalitz plot at 900 MeV/c.

6.2 Improved Fit at 900 MeV/c

In addition to channels (1)-(5) a resonance with a mass of 1650 MeV and width of 150 MeV is considered. The log-likelihood changes for a spin $J=0,1,2,3$ and the effect of its interference with the crossing $K^*(890)$ bands are reported in table 6.2. Obviously a scalar or a $\rho_3(1690)$ is less favoured. The result is ambiguous between

	NLL	Par.	$\Delta LL/\Delta P.$	χ^2
$X_0(1650)$	-1715.1	10	50./1	1.6191
$K^{*\pm}(892) \times X_0(1650)$	-1720.2	12	5.1/2	1.623
$X_1(1650)$	-1856.2	11	190.3/2	1.5430
$K^{*\pm}(892) \times X_1(1650)$	-1862.2	15	6/4	1.541
$X_2(1650)$	-1834.0	11	168.1/2	1.5476
$K^{*\pm}(892) \times X_2(1650)$	-1871.1	15	37.1/4	1.545
$X_3(1690)$	-1747.0	13	81.1/4	1.6288
$K^{*\pm}(892) \times X_3(1690)$	-1766.8	17	19.8/4	1.626

Table 6.2: Log-likelihood changes including $X_J(1650)$ with $J = 0, 1, 2, 3$.

$J=1$ and $J=2$. A slightly better change in the log-likelihood favours a tensor in this mass range as compared to a vector, but this is not confirmed from the χ^2 -test. We include the channel

$$\bar{p}p \rightarrow (a/f)_2(1650)\pi^0. \quad (7)$$

The fit looks still inadequate: in particular neither the peak at ~ 1500 nor the dip at ~ 1525 are correctly described (see fig. 6.4, 6.5). The introduction of the $f'_2(1525)$ in addition to the channels (1)-(5) and (7) shows a significant change of the log-likelihood which is also confirmed by the χ^2 test (see 6.3). The change is clearly visible by eye: the peak and the dip are now adequately fitted (see the K^+K^- projection in fig. 6.6). A modest peak close to ~ 1300 indicates also the presence of the $a_2(1320)$. It interferes with the neighbour $f_2(1275)$. The results of the fit are shown in fig. 6.8. They are in agreement with the data up to 1.6 GeV. We then keep the channels (1)-(5), (7) and

Interference	NLL	Par.	$\Delta LL/\Delta P.$	χ^2
$K^{*\pm}(892) \times f_0(1500)$	-1874.6	17	3.5/2	1.545
$f'_2(1525) \times f_0(1500)$	-1945.2	21	70.6/4	1.478
$f_2(1270) \times a_2(1320)$	-2050.3	29	33.7/8	1.454

Table 6.3: Log-likelihood changes including $f'_2(1525)$ and the $a_2(1320)$

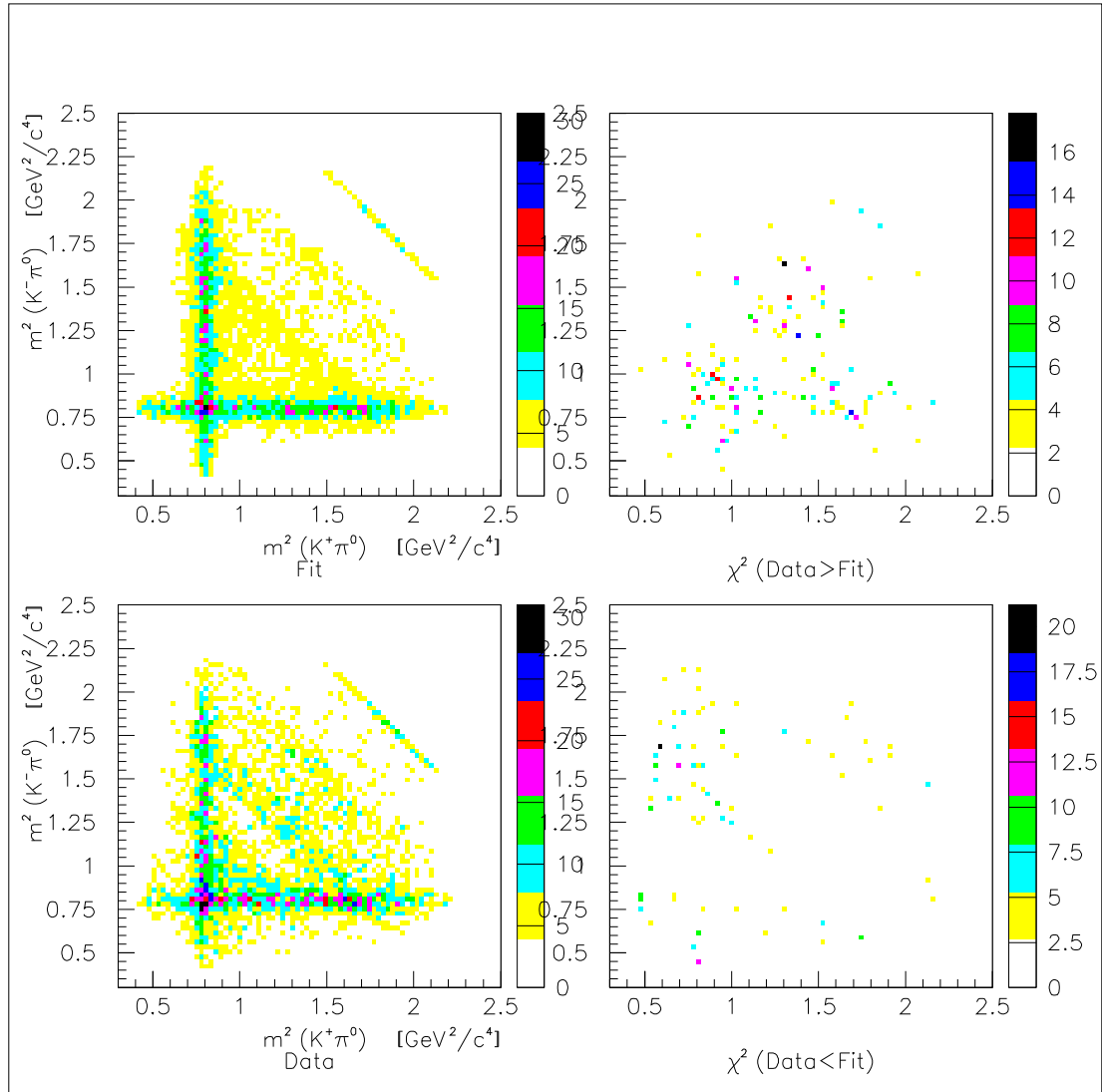


Figure 6.4: Improved fit with a tensor at 1650 MeV

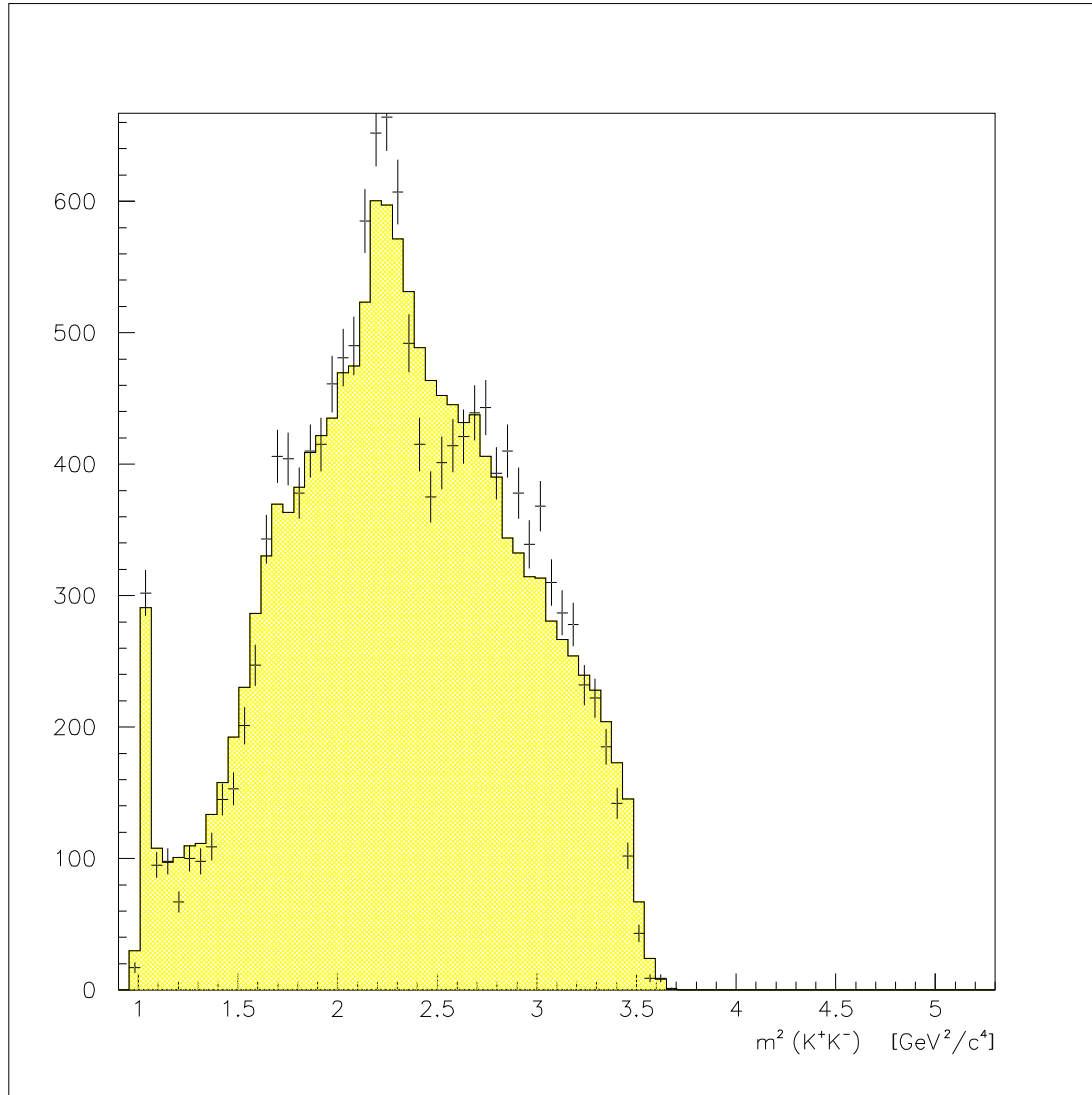


Figure 6.5: Improved fit with a tensor at 1650 MeV (K^+K^- projection).

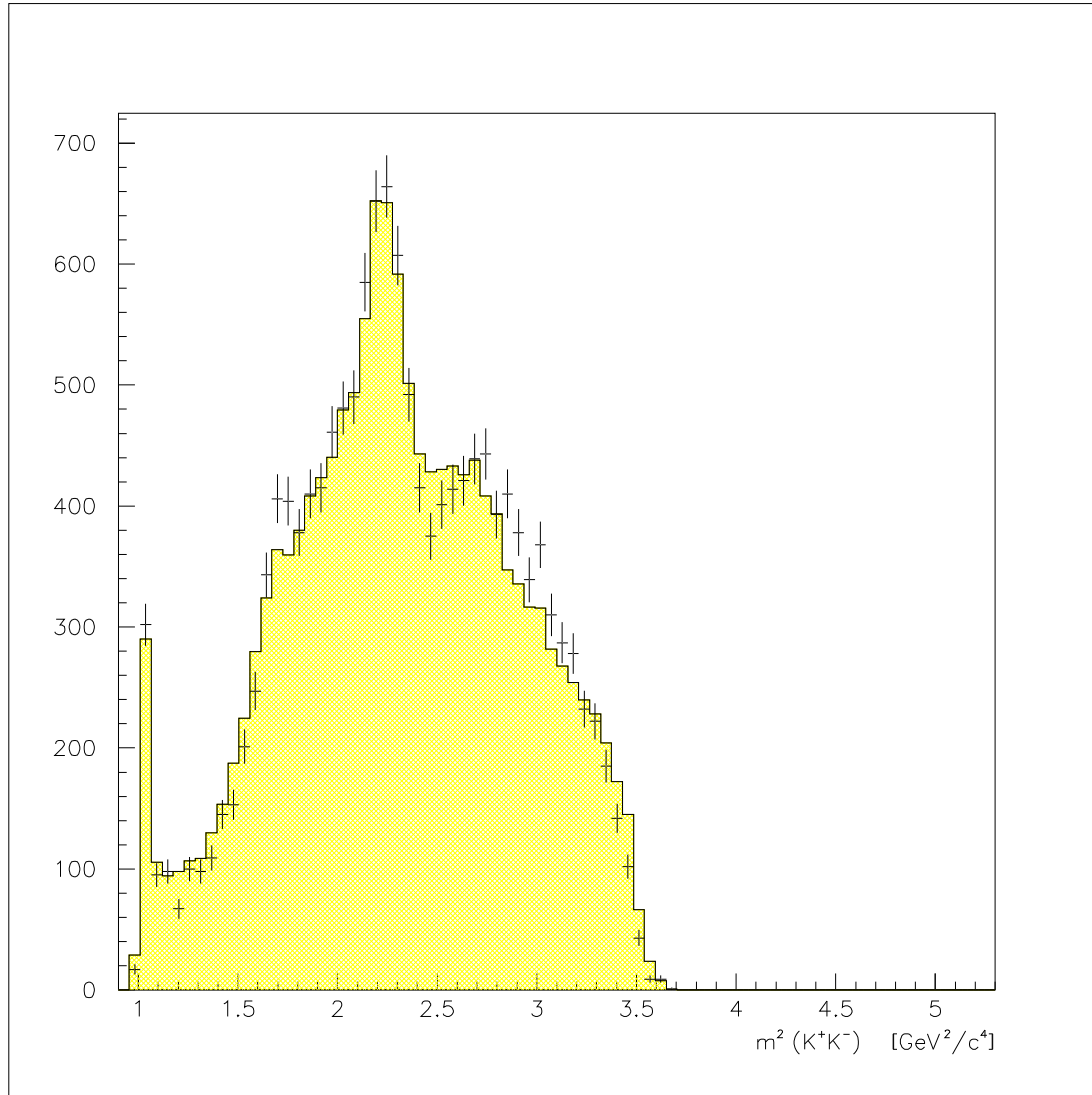


Figure 6.6: Improved fit with a tensor at 1650 MeV and the $f'_2(1525)$ (K^+K^- projection)

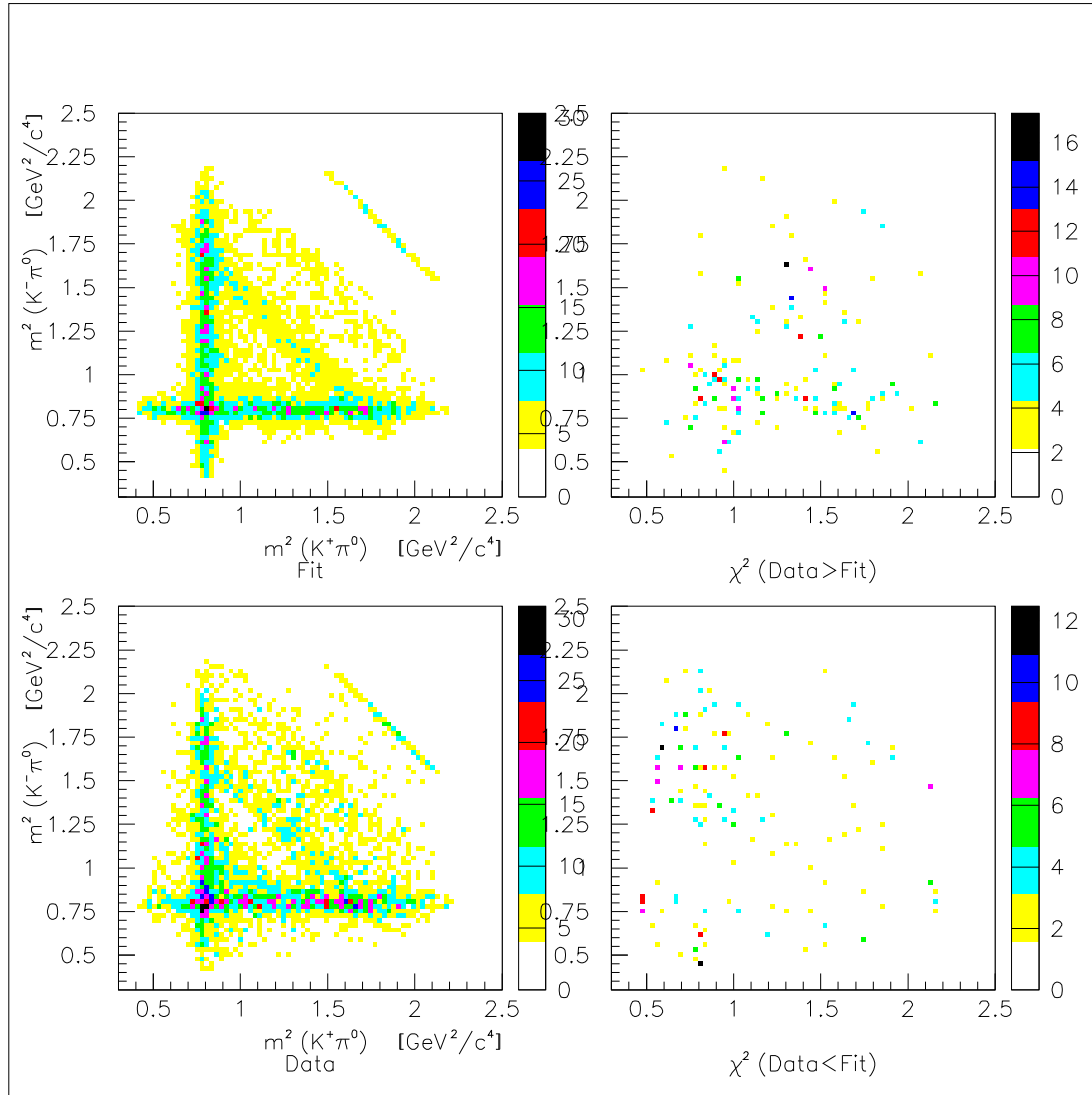


Figure 6.7: Improved fit with a tensor at 1650 MeV, the $f'_2(1525)$ and the $a_2(1320)$.

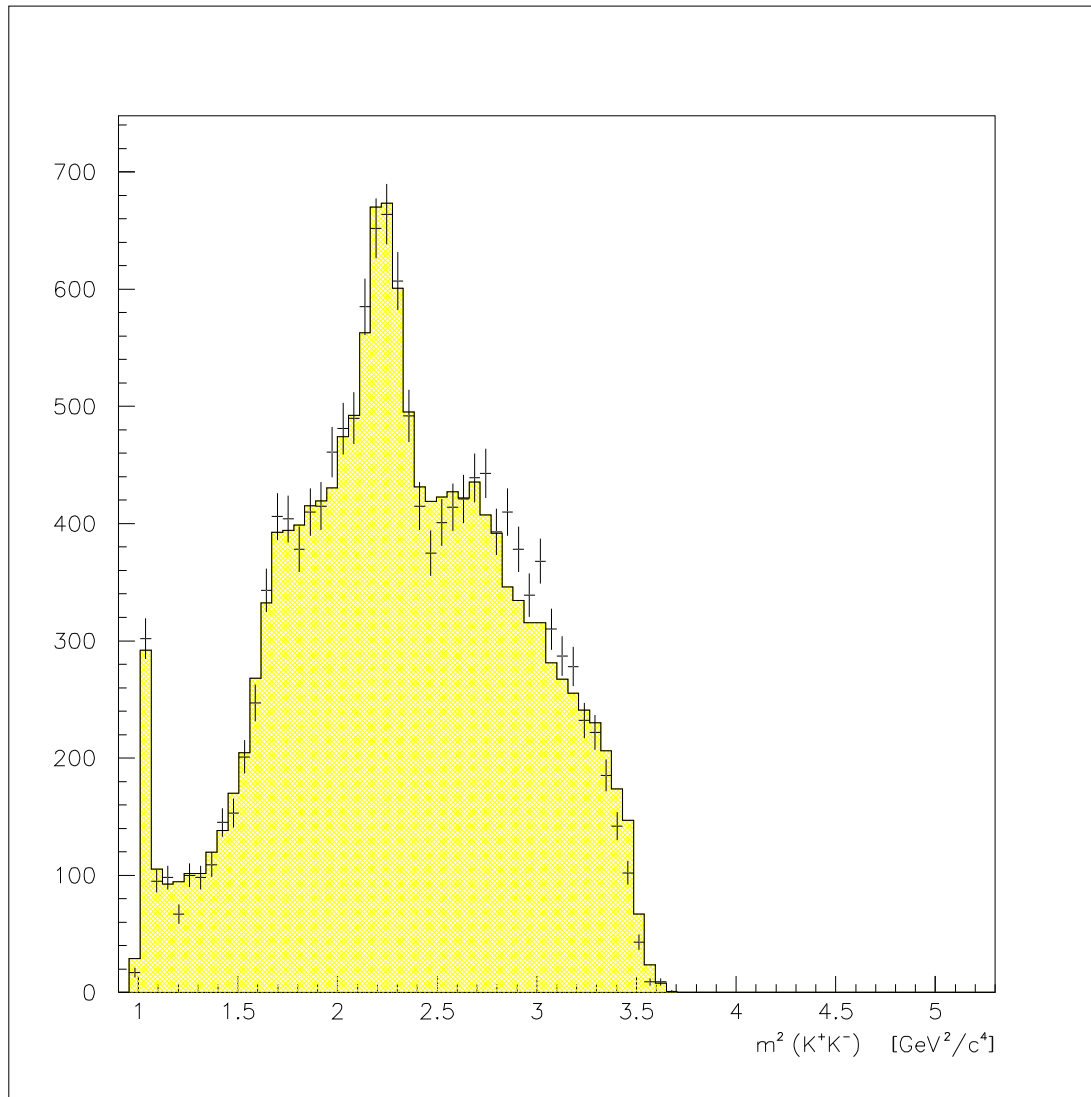


Figure 6.8: Improved fit with a tensor at 1650 MeV, the $f'_2(1525)$ and the $a_2(1320)$ (K^+K^- projection).

$$\bar{p}p \rightarrow f_2'(1525)\pi^0 \quad (8)$$

$$\bar{p}p \rightarrow a_2(1320)\pi^0 \quad (9)$$

The isovector scalar $a_0(1450)$ has been seen by the Crystal Barrel collaboration in other channels and needs confirmation. A tentative to fit in addition to the $f_0(1500)$ a broad scalar ($\Gamma = 200 \div 300$ MeV) in the $1300 \div 1500$ MeV mass range corresponding to the $f_0(1370)/a_0(1450)$ was not successful (contribution less than 1.5%). Due to its broad width its optimization is difficult. It has a negligible contribution and is neglected. Table 6.4 reports the modest log-likelihood changes. To check whether the integration over initial states i.e. the

Interference	NLL	Par.	$\Delta LL/\Delta P.$	χ^2
$a_0(1450)$	-2064.2	30	1.4/1	1.459
$f_2'(1525) \times a_0(1450)$	-2069.0	32	4.8/2	1.445
$f_0(1500) \times a_0(1450)$	-2071.5	33	2.5/1	1.442

Table 6.4: Log-likelihood changes including $a_0(1450)$.

simple parametrization of the production angle has an effect on our previous conclusion (spin 2) for the spin of the $X_J(1650)$, we approximate the dependence on the production angles, multiplying the corresponding amplitudes by a factor

$$F(\theta) = 1 + p_2 \cos^2 \theta, \quad (6.3)$$

where the parameters p_2 are optimized separately for every K^+K^- resonance. The log-likelihood improvement is modest ($LL = -2068.7$) if $J = 2$ compared to the number of additional parameter required. 5 additional parameters for the $\cos^2 \theta$ dependence of the $f_2(1275)$, $a_2(1320)$, $f_2(1500)$, $f_2'(1525)$, $X_J(1680)$ are needed to be optimized and the controversy between spin 1 and spin 2 remains. Spin 0 or spin 3 are still less favoured (see table 6.5). The optimization of the mass and widths for different spin is shown in table 6.6, in fig. 6.15 for $J = 1$ and in fig. 6.16 for $J = 2$.

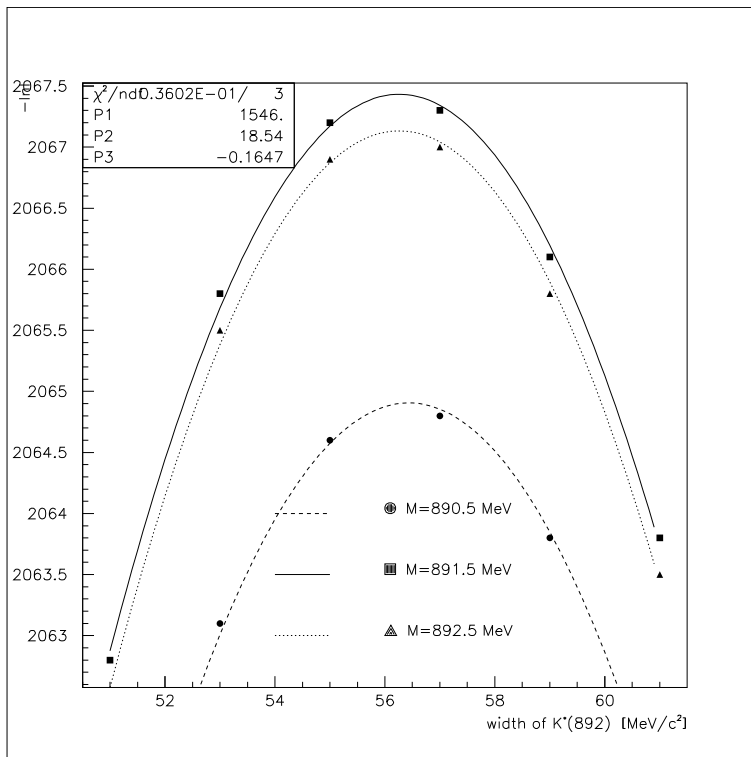
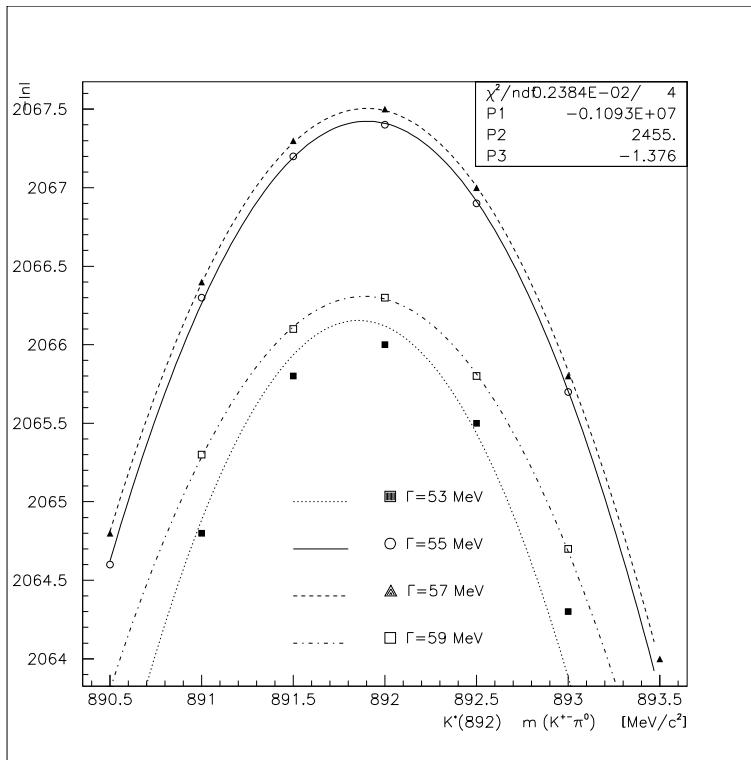
	NLL	Par.	χ^2
$X_0(1650)$	-1972.0	26+5	1.486
$X_1(1650)$	-2066.6	29+5	1.445
$X_2(1650)$	-2068.7	29+5	1.452
$X_3(1670)$	-2042.3	30+5	1.471

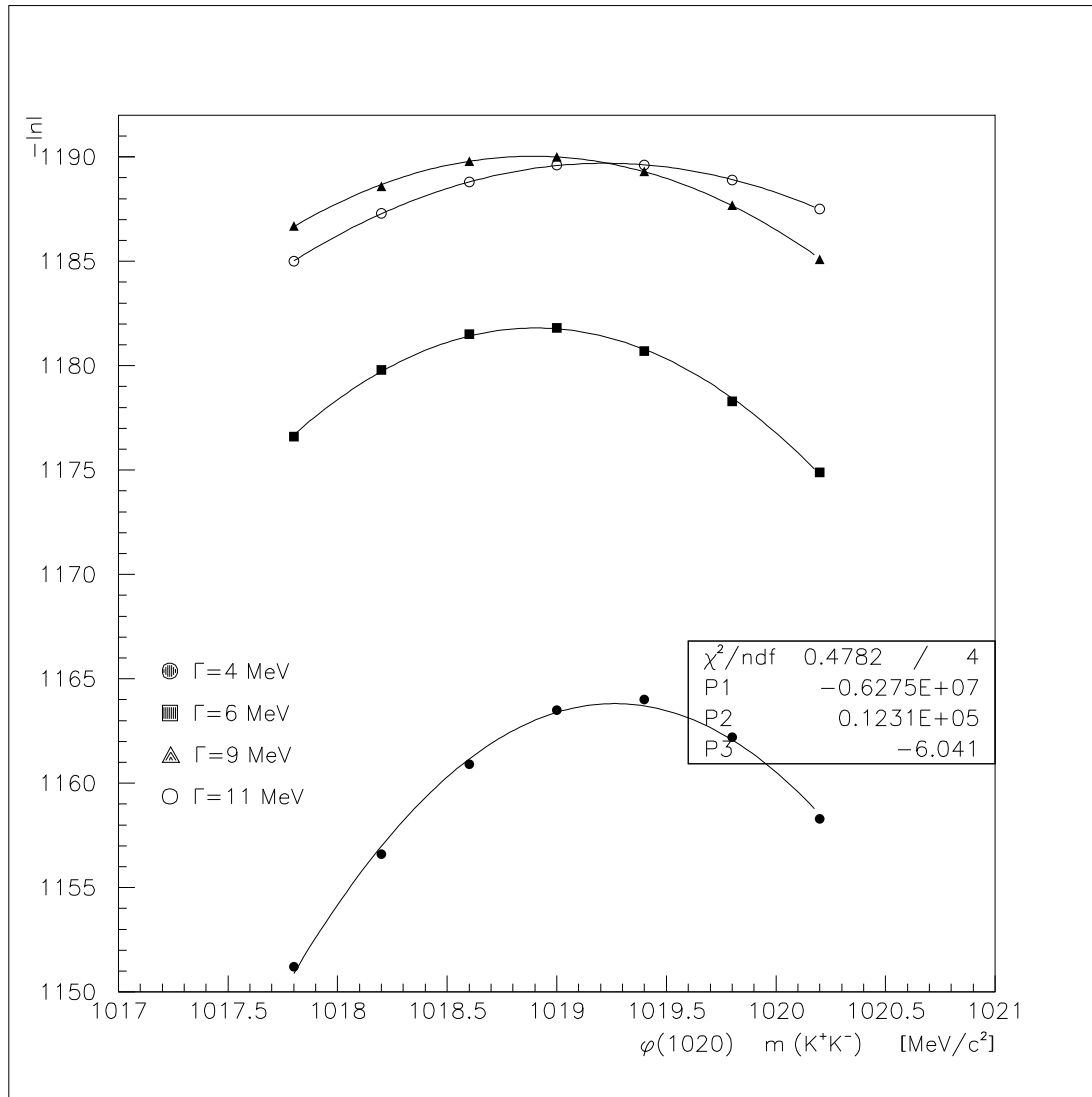
Table 6.5: Log-likelihood changes including $X_J(1650)$ with $J = 0, 1, 2, 3$ after the optimization of the production angles. The controversy is between spin 1 and spin 2.

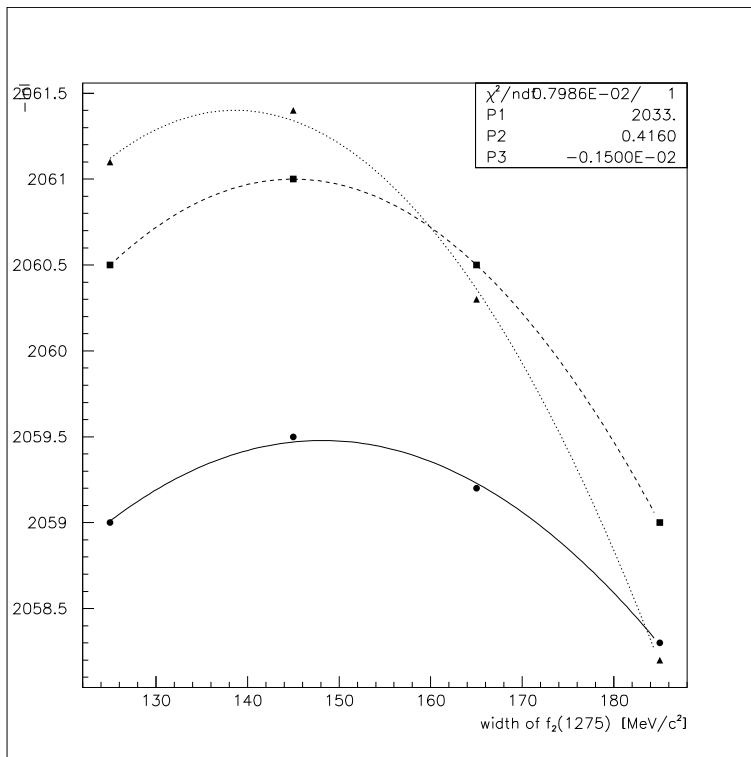
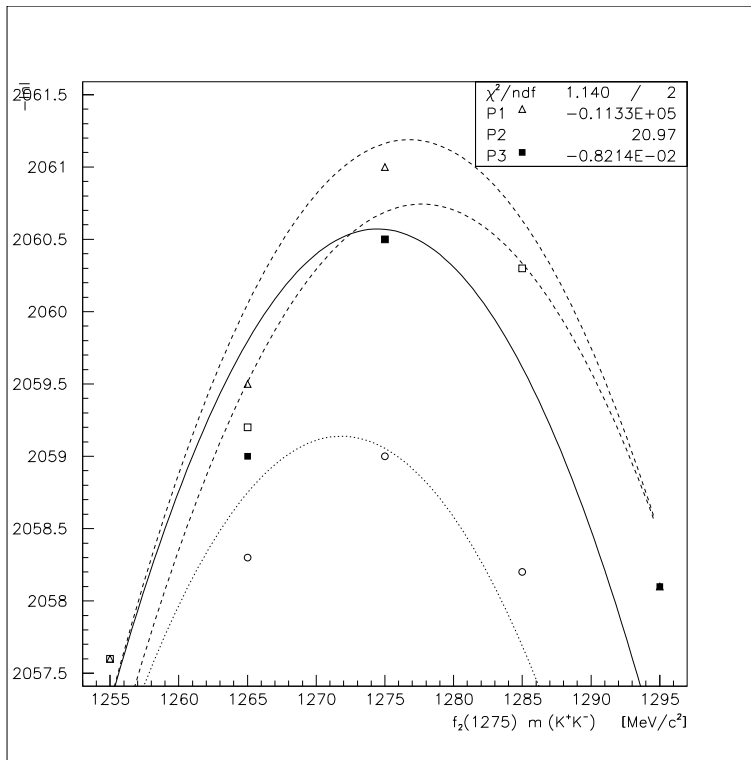
The fitted masses and widths are listed in table 6.6. A very good agreement of the narrow $K^*(890)$ and $\phi(1020)$ (see fig. 6.9, 6.10) with the PDG values are a confirmation of our calibration. However, because of the experimental resolution, the width of the $\phi(1020)$ optimizes at 9 MeV rather than 4 MeV. The $a_2(1320)$ optimizes at 1306 MeV (see fig. 6.12). The modest shift of the mass of the $a_2(1320)$ can be attributed to the interference with the $f_2(1275)$. The $f_0(1500)$, which interferes with the $f'_2(1525)$, optimizes at 1485 MeV (see fig. 6.13). In general, we experience that the interference between two overlapping resonances slightly shifts the mass and/or the width of one or both resonances. The differences with the PDG tables are within approximately three standard deviations. With the exception of the $a_2(1320)$ and the $f_0(1500)$ all other resonances are within one standard deviation ($\Delta LL = 0.5$) in agreement with the PDG values (see also fig. 6.11, 6.14). The broad $K_0(1430)$ lies toward the top end of $K^\pm\pi^0$ phase space and one cannot see an optimum in the invariant mass.

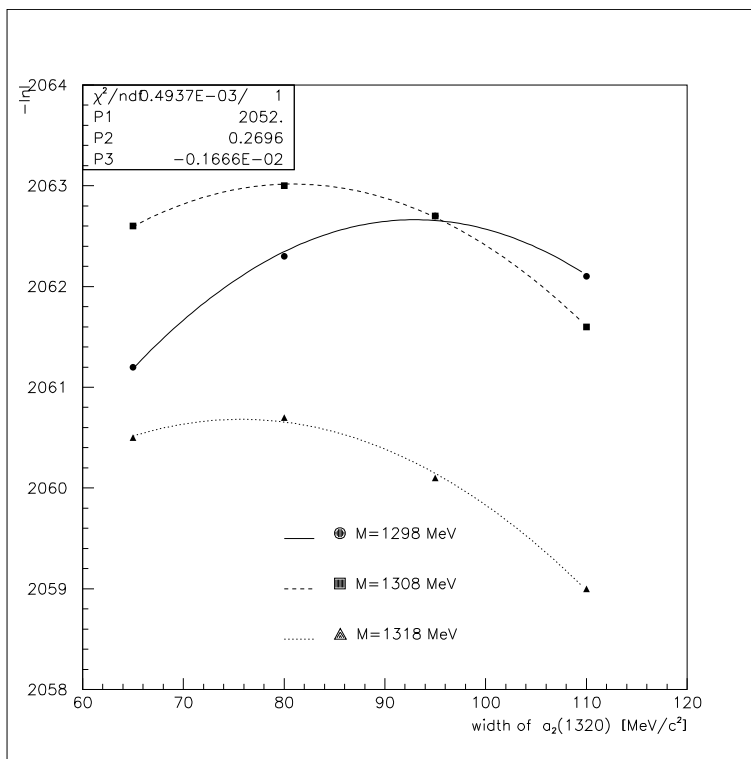
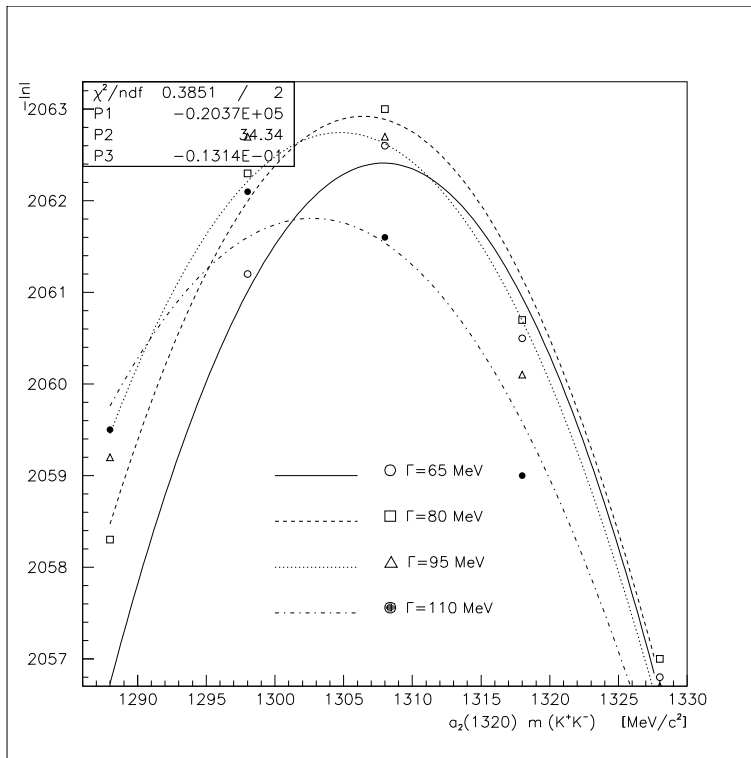
Resonance	Mass	Width
$K^{*\pm}(892)$	891.87 ± 0.62	56.3 ± 1.7
$K^{*\pm}(892)$	(891.66 ± 0.26)	(50.8 ± 0.9)
$K_0^*(1430)$	(1429 ± 5)	(287 ± 21)
$\phi(1020)$	1019.27 ± 0.29	at ~ 4.0
$\phi(1020)$	(1019.413 ± 0.008)	(4.43 ± 0.05)
$f_2(1275)$	1276.8 ± 7.8	145.0 ± 20.0
$f_2(1275)$	(1275.0 ± 1.2)	$(185.5^{+3.8}_{-2.7})$
$a_2(1320)$	1306.4 ± 6.2	80.9 ± 17.3
$a_2(1320)$	(1318.1 ± 0.7)	(107 ± 5)
$f_0(1500)$	1486.4 ± 3.5	118.8 ± 10.1
$f_0(1500)$	(1500 ± 10)	(112 ± 10)
$f'_2(1525)$	1528.5 ± 8.6	76.7 ± 7.1
$f'_2(1525)$	(1525 ± 5)	(76 ± 10)
$(\phi/\rho)_1(1680)$ Fit	1670.0 ± 5.0	127.8 ± 15.4
$\phi_1(1680)$	$(1680. \pm 20.)$	$(150. \pm 50.)$
$\rho_1(1700) \rightarrow \eta\rho^0, \pi^+\pi^-$	$(1700. \pm 20.)$	$(240. \pm 60.)$
$(a/f)_2(1660)$	1667.3 ± 5.7	146.3 ± 19.2
$f_J(1710)$	$(1712. \pm 5.)$	$(133. \pm 14.)$
$a_2(1660)$	$(1660. \pm 40.)$	$(280. \pm 70.)$

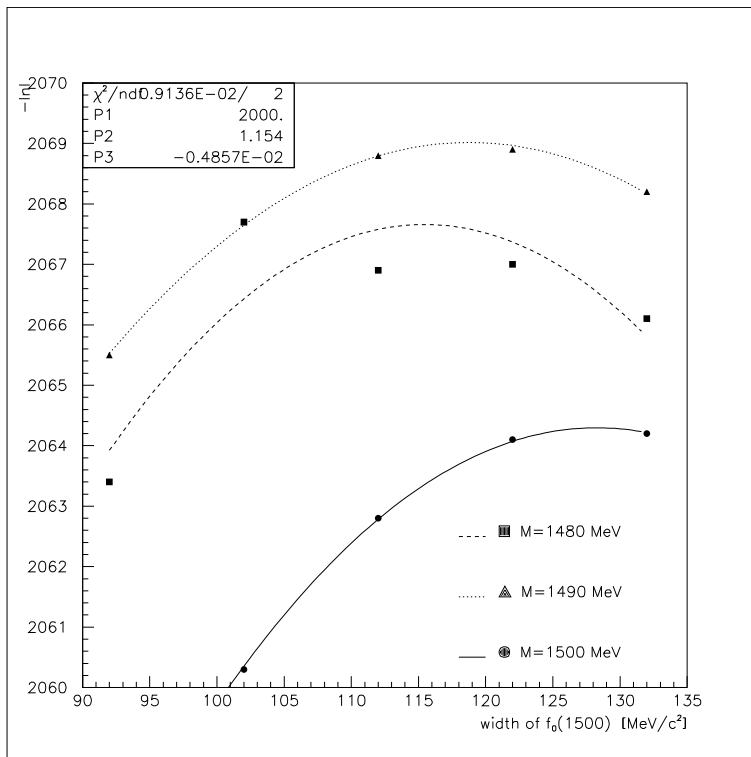
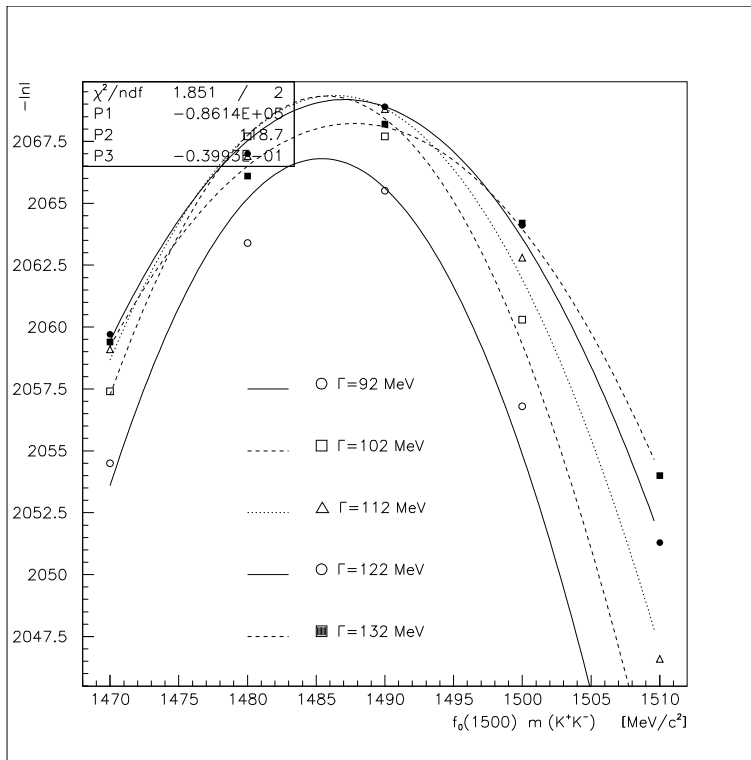
Table 6.6: Improved fit at 900 MeV/c: fitted masses and widths. The values in brackets are taken from the PDG tables [2].

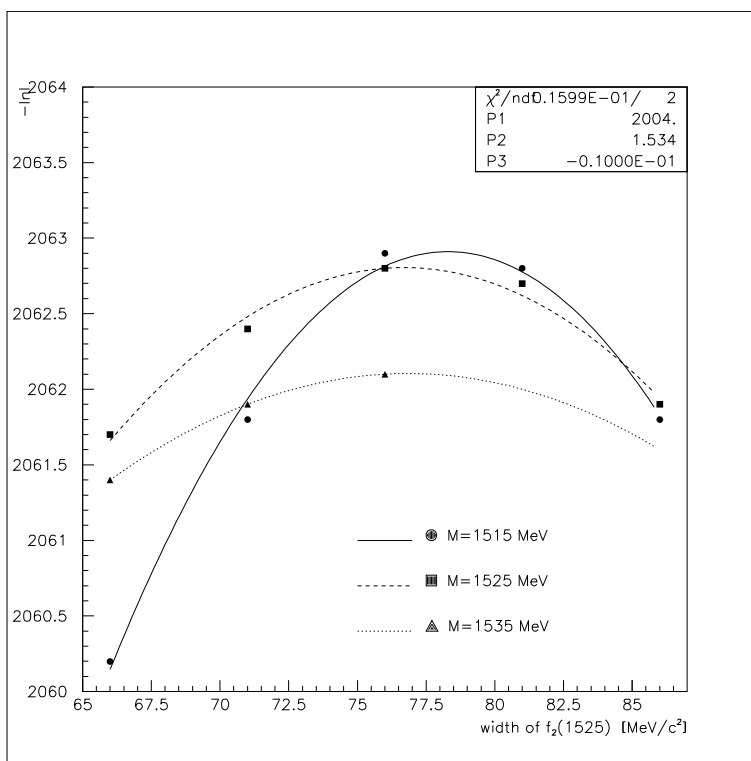
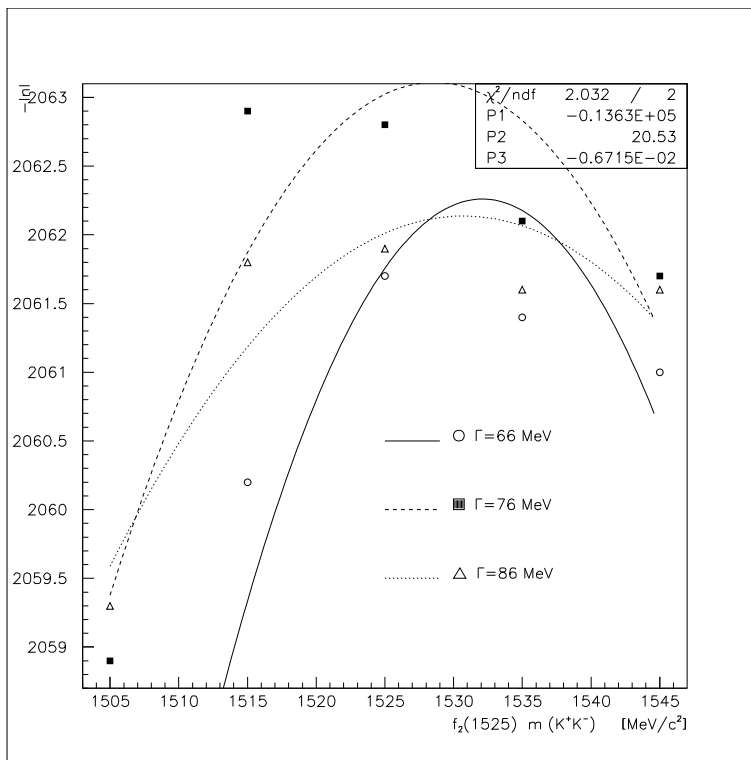
Figure 6.9: Fitted mass and width of the $K^{*\pm}(892)$.

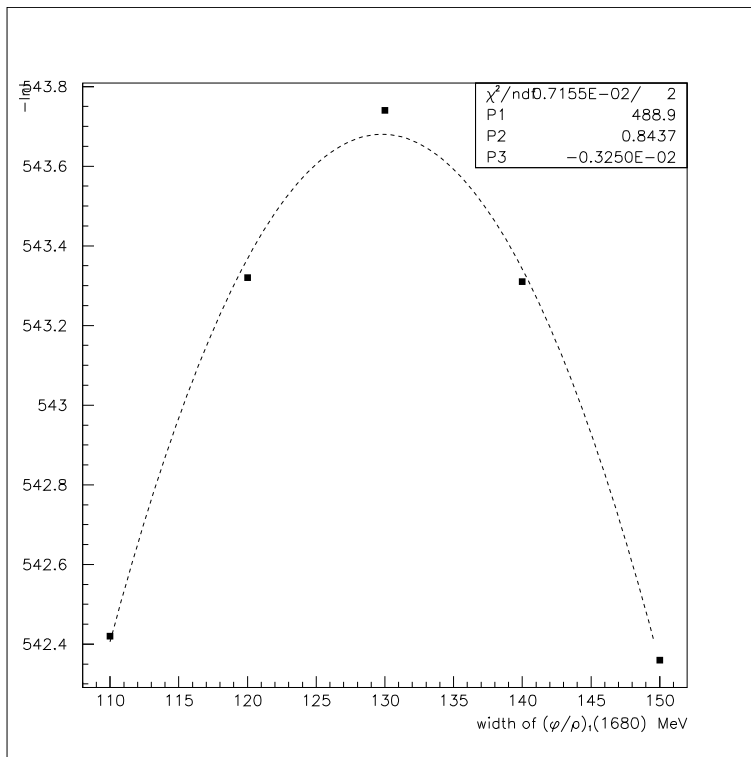
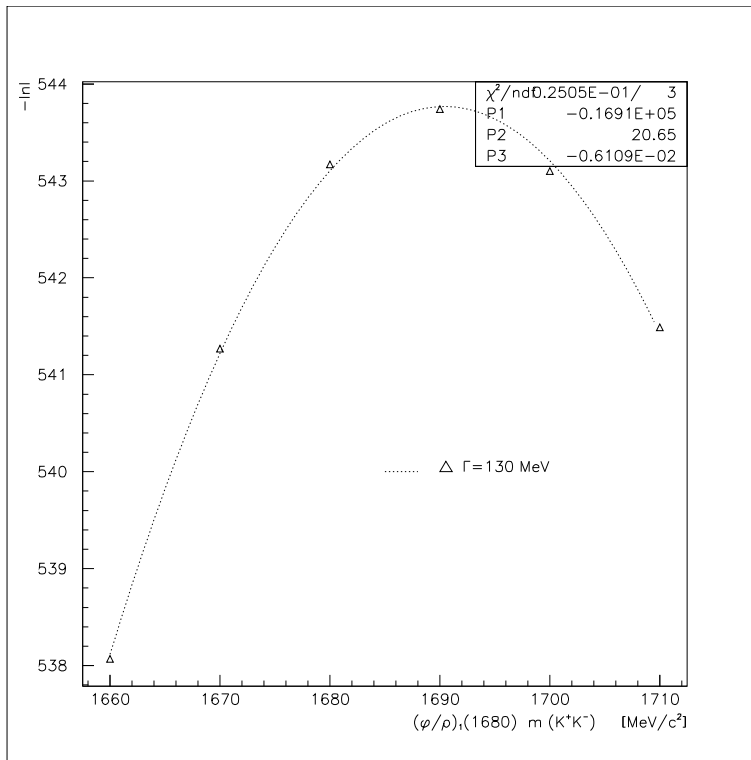
Figure 6.10: Fitted mass of the $\phi(1020)$.

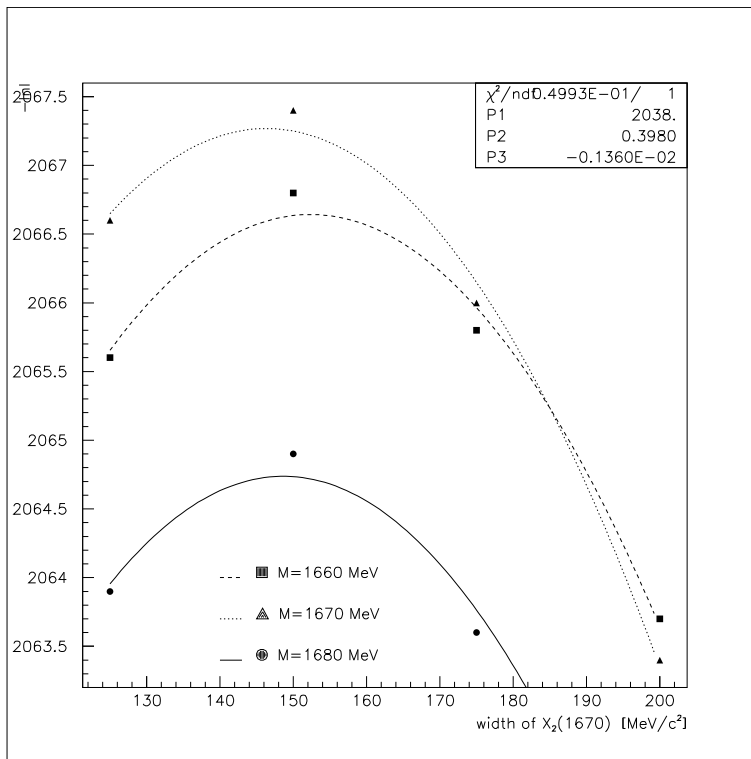
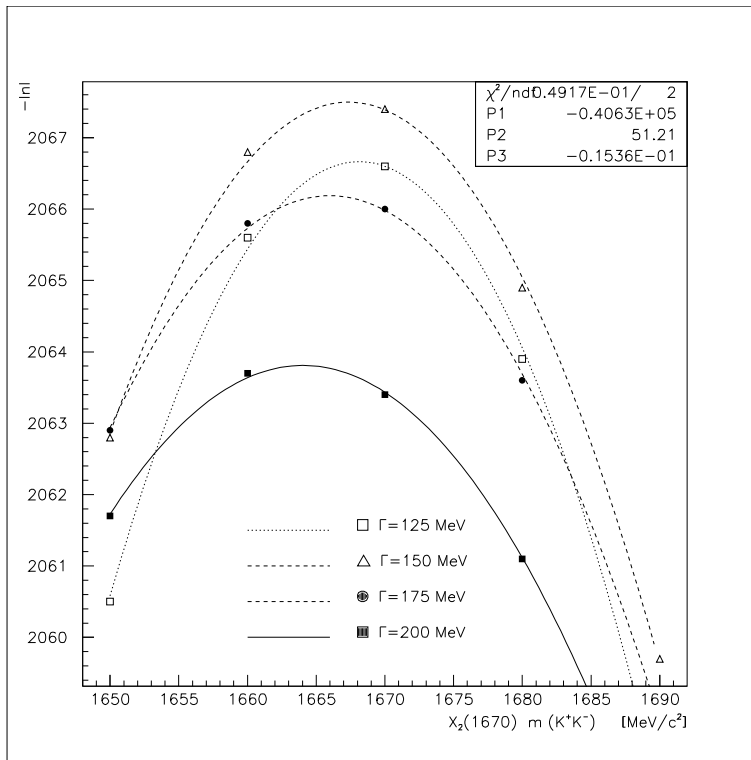
Figure 6.11: Fitted mass and width of the $f_2(1275)$.

Figure 6.12: Fitted mass the width of the $a_2(1320)$.

Figure 6.13: Fitted mass and width of the $f_0(1500)$.

Figure 6.14: Fitted mass and width of the $f_2(1525)$.

Figure 6.15: Improved fit: mass and width of the $X_J(1680)$ if $J = 1$.

Figure 6.16: Improved fit: mass and width of the $X_J(1670)$ if $J = 2$.

6.3 Additional Spin Tests

It is important, at this point, to check if including or not the $f_0(1500)$ has an effect on the conclusion about the spin of the $X_J(1650)$, which we obtain.

We consider the improved fit (1)-(5), (7),(8) and exclude the $f_0(1500)$ i.e. the channel (3). It is interesting to note that repeating the optimization, a scalar which interferes strongly with the $f_2'(1525)$, gives the best fit (see table 6.7) If we identify the resonance at 1640 with the $f_J(1710)$ this can explain the controversy on its spin. Concerning this we remind that chronologically the $f_0(1500)$ was discovered after the $f_J(1710)$ (also called θ) [2]. Earlier analysis considered only the $f_2'(1525)$ in the 1.5 GeV mass region. We can therefore naively think that the $f_J(1710)$ has spin 0. However, re-scanning again the masses, the $f_2'(1525)$ and the $f_0(1710)$ optimize at $m = 1495, \Gamma = 145$ MeV and at $m = 1640, \Gamma = 210$ MeV respectively. In this case the two peaks at ~ 1500 and at ~ 1650 MeV are not correctly described as can be seen from fig.6.17. In addition, the log-likelihood changes and the χ^2 tests confirm the improved fit with the channels (1)-(5), (7) with $J=2$ (or 1) and (8), including also the $f_0(1500)$ as better fits (see table 6.8).

	<i>NLL</i>	Par.	$\Delta LL/\Delta P.$	χ^2
$f_2'(1525), X_0(1650)$	-1665.7	13	-49.4/3	1.789
$f_2'(1525) \times X_0(1650)$	-1813.3	15	147.6/3	1.592
$f_2'(1525), X_1(1650)$	1764.9	16	-91.3/5	1.7395
$f_2'(1525) \times X_1(1650)$	-1789.2	20	24.3/4	1.749
$f_2'(1525), X_2(1650)$	-1776.8	16	-57.2/5	1.7373
$f_2'(1525) \times X_2(1650)$	-1789.2	20	12.4/4	1.749

Table 6.7: Fit at 900 MeV/c without the $f_0(1500)$: fitted masses and width of the $X_J(1650)$ for $J = 0, 1, 2$. The log-likelihood changes are calculated with respect to the improved fit with the $X_J(1650)$ channel (7) (see table 6.2), excluding the channel (3) and including the channel (8); a negative $\Delta LL/\Delta P$ means a worse fit.

	<i>NLL</i>	Par.	χ^2
$f_2'(1495) \times X_0(1640)$	-1913.7	15	1.500
$f_2'(1525) \times f_0(1500) \times X_2(1650)$	-1945.2	21	1.478

Table 6.8: Additional spin tests: the fit at 900 MeV/c excluding the $f_0(1500)$ and with the $X_0(1650)$ is compared to the fit including the $f_0(1500)$ and with the $X_2(1650)$.

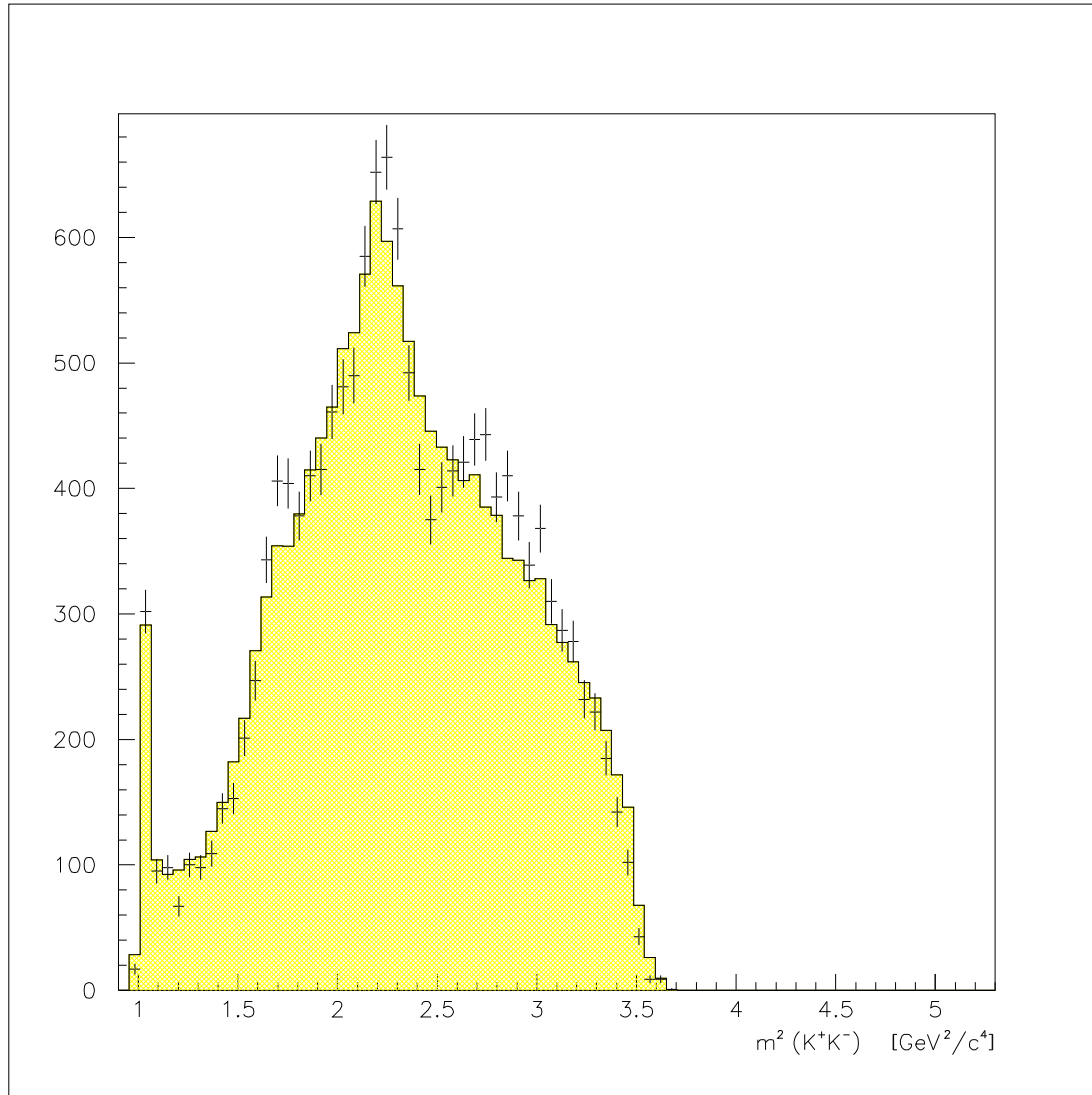


Figure 6.17: Fit with the channels (1)-(5), (7),(8) excluding the $f_0(1500)$. The optimization of the masses and widths of the $f_2'(1525)$ and of the $X_0(1650)$ is repeated.

6.4 Best Fit at 900 MeV/c

Consider again the improved fit including the channels (1)-(5), (7)-(9):

$$\bar{p}p \rightarrow \phi(1020)\pi^0 \quad (1)$$

$$\rightarrow f_2(1275)\pi^0 \quad (2)$$

$$\rightarrow f_0(1500)\pi^0 \quad (3)$$

$$\rightarrow K^{*\pm}(892)K^\mp \quad (4)$$

$$\rightarrow K_0^{*\pm}(1430)K^\mp \quad (5)$$

$$\bar{p}p \rightarrow X_J(1650)\pi^0 \quad (7)$$

$$\bar{p}p \rightarrow f'_2(1525)\pi^0 \quad (8)$$

$$\bar{p}p \rightarrow a_2(1320)\pi^0 \quad (9)$$

We now consider the possibility that more than one resonance is present in the mass range between $1.6 \div 1.7$ GeV. We consider again the improved fit without the optimization of the production angles of the $X_J(1680)$ with $J = 2$. Including two Breit-Wigner amplitudes, the optimization of the masses and widths, taking into account different spin combinations, is repeated again. The best fit on which we have confidence, is obtained with a broad tensor ($\Gamma = 280$ MeV) at a mass of ~ 1620 MeV (see fig. 6.21) and a vector at ~ 1680 MeV ($\Gamma = 145$ MeV) (see fig. 6.22) that can be identified with the $a_2(1660)$ and the $\phi(1680)$ (or the $\rho(1700)$) respectively:

$$\bar{p}p \rightarrow (a/f)_2(1620)\pi^0 \quad (7)$$

$$\bar{p}p \rightarrow (\phi/\rho)_1(1680)\pi^0 \quad (10)$$

The possibility of a scalar or another tensor or the $\rho_3(1690)$ (channel(10) with $J = 0, 2, 3$), instead of a vector at 1680 MeV in addition to the broad tensor at 1620 MeV has been considered as well. The log-likelihood changes, keeping the masses of the first tensor at 1620 MeV, are plotted in fig. 6.23. With a scalar at 1680 MeV the fit is not stable and does not fully converge. Another tensor (instead of a vector) is excluded by a change of 39.6 in the log-likelihood with the same number of parameters, that is definitive. The $\rho_3(1690)$ is also excluded: the log-likelihood is -2019.2 and is out of the scale in the plot 6.23.

We consider also a scalar at 1630 MeV (channel(7) with $J = 0$) instead of a tensor and in addition to the vector at 1680 MeV (channel(10) with $J = 1$): the log-likelihood change is 33 with 3 parameters less, that is significantly worse and confirms the broad tensor at 1620 MeV.

The contributions obtained fitting the channels (1)-(5), (7)-(10) are reported in table 6.11. The helicity 2 amplitudes have always a contribution $\simeq 1\%$ and are neglected. The fitted masses and widths are given in table 6.10. The corresponding best fit is shown in fit 6.20.

Looking at the intensities we can see that the fitted vector is a factor 4 times larger than the $\phi(1020)$. If the vector at 1680 is the $\phi(1680)$ it seems unlikely that the radial excitation will be produced more strongly than $\phi(1020)$. On the other hand the fitted mass and width and its contribution makes it difficult to identify with the $\rho(1700)$ only. This leads to the hypothesis that the signal is likely due to both of these resonances. Another possible interpretation is that there is another structure in the mass range around ~ 1.7 GeV (visible in the Dalitz plot at 1642 MeV/c) that is obscured from the $K^{*\pm}(890)$ bands. In this case fitting the Dalitz plot only with a tensor at 1620 MeV and a vector at 1680 MeV can have the effect of increasing the contribution of the vector. In a further attempt the fit with a scalar at ~ 1740 MeV in addition to a tensor at 1620 MeV and a vector at 1680 MeV failed to converge.

	NLL	Par.	χ^2
Best fit	-2151.1	35	1.393
Best fit without $(a/f)_2(1620)$	-2094.3	29	1.400
Best fit without $(\phi/\rho)_1(1680)$	-2074.7	29	1.462

Table 6.9: Best fit at 900 MeV/c: comparison including and excluding the $(a/f)_2$ or the $(\phi/\rho)_1$.

Resonance	Mass	Width
$(\phi/\rho)_1(1680)$	1680.5 ± 5.0	144.0 ± 5.6
$\phi_1(1680)$	(1680. \pm 20.)	(150. \pm 50.)
$\rho_1(1700) \rightarrow \eta\rho^0, \pi^+\pi^-$	(1700. \pm 20.)	(240. \pm 60.)
$(a/f)_2(1660)$	1623.8 ± 12.1	277.0 ± 23.4
$f_J(1710)$	(1712. \pm 5.)	(133. \pm 14.)
$a_2(1660)$	(1660. \pm 40.)	(280. \pm 70.)

Table 6.10: Best fit at 900 MeV/c: fitted masses and width of the $(a/f)_2(1620)$, $(\phi/\rho)_1(1680)$. For a reference the PDG values (in brackets) of the candidates are also listed with the corresponding decay modes of the $\rho_1(1700)$.

Resonance	Hel. 0	Hel. 1	Hel. 2	Tot. int.	$\Delta LL/\Delta P$
$K^{*\pm}(892)$	11.17	32.68		43.85	
$K_0^*(1430)$	17.71			17.71	
$K_2^*(1430)$	-	-	-	-	
$\phi(1020)$	0.96	0.86		1.82	
$f_2(1275)$	1.96	4.83	-	6.79	
$a_2(1320)$	2.84	0.47	-	3.31	
$f_0(1500)$	32.57			32.57	
$f_2'(1525)$	10.60	0.38	-	10.98	
$(a/f)_2(1630)$	1.97	1.96		2.93	76.4/6
$(\phi/\rho)_1(1680)$	7.20	0.34		7.54	56.8/6

Table 6.11: Best fit: contributions at 900 MeV/c. In evaluating these branching ratios, interferences are omitted. Thus contributions do not add up exactly to 100%. The log-likelihood changes are obtained when the channel is dropped from the fit and the other channels are re-optimised.

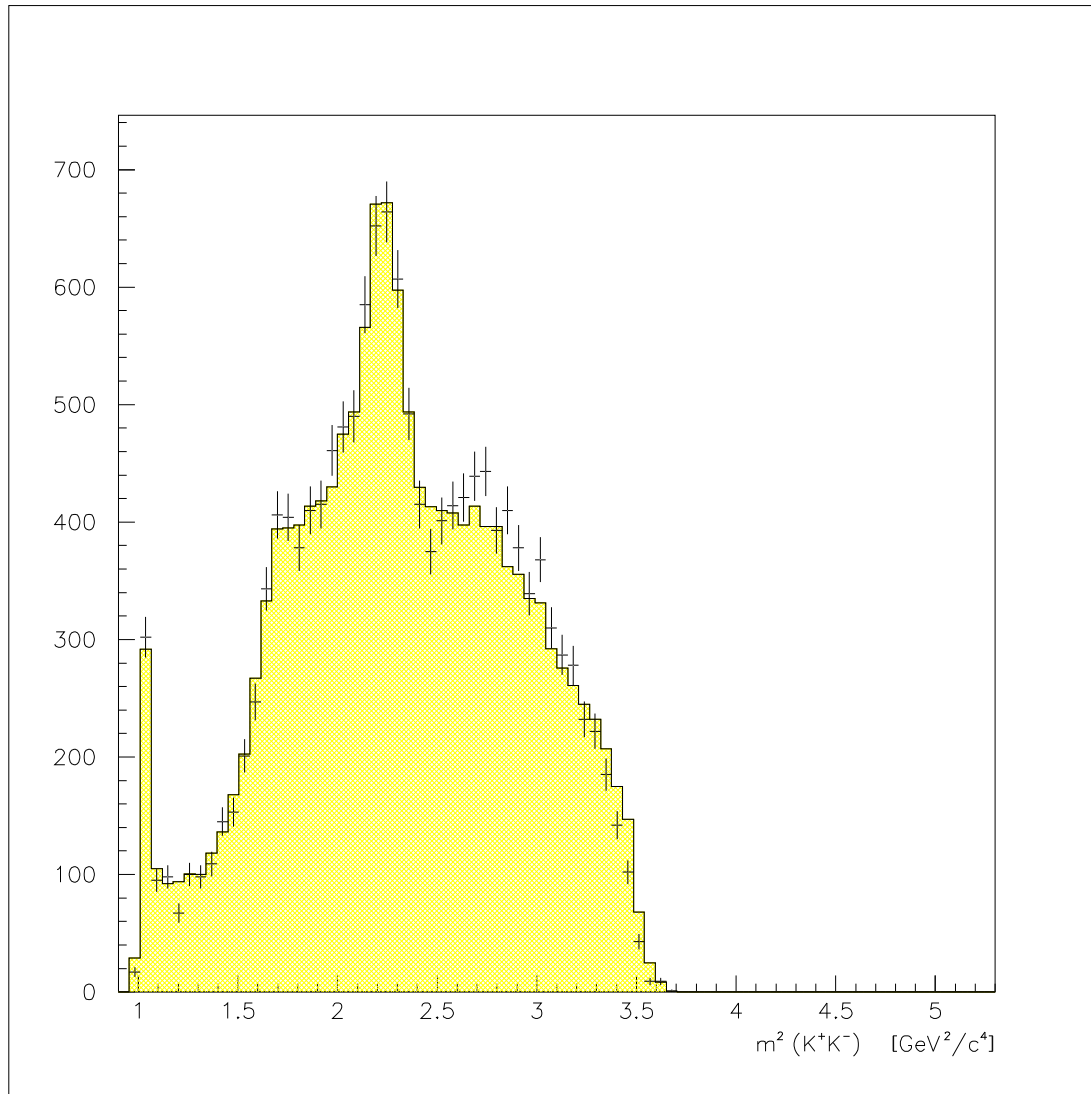


Figure 6.18: Best fit at 900 MeV/c (K^+K^- projection).

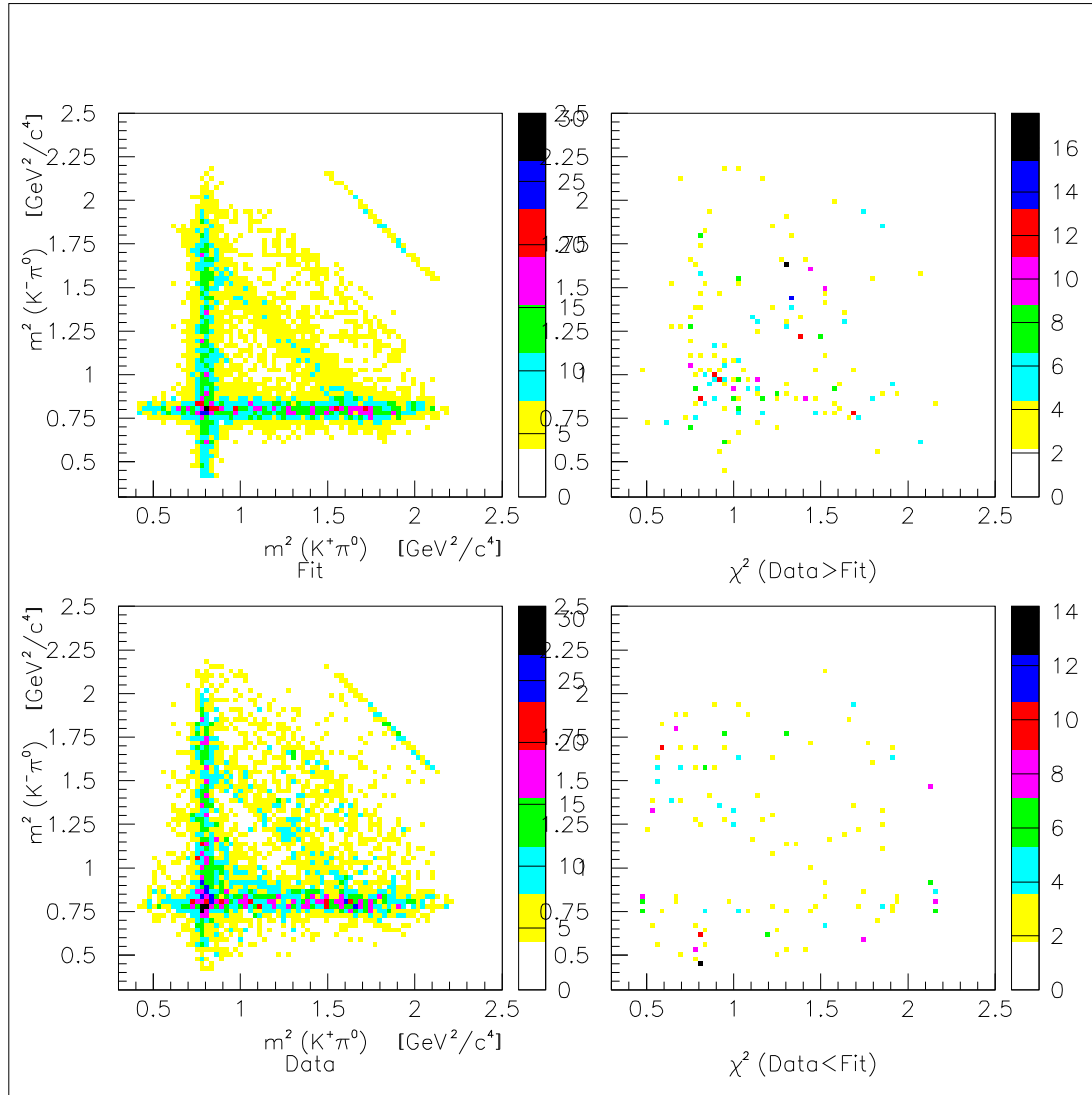


Figure 6.19: Best fit at 900 MeV/c.

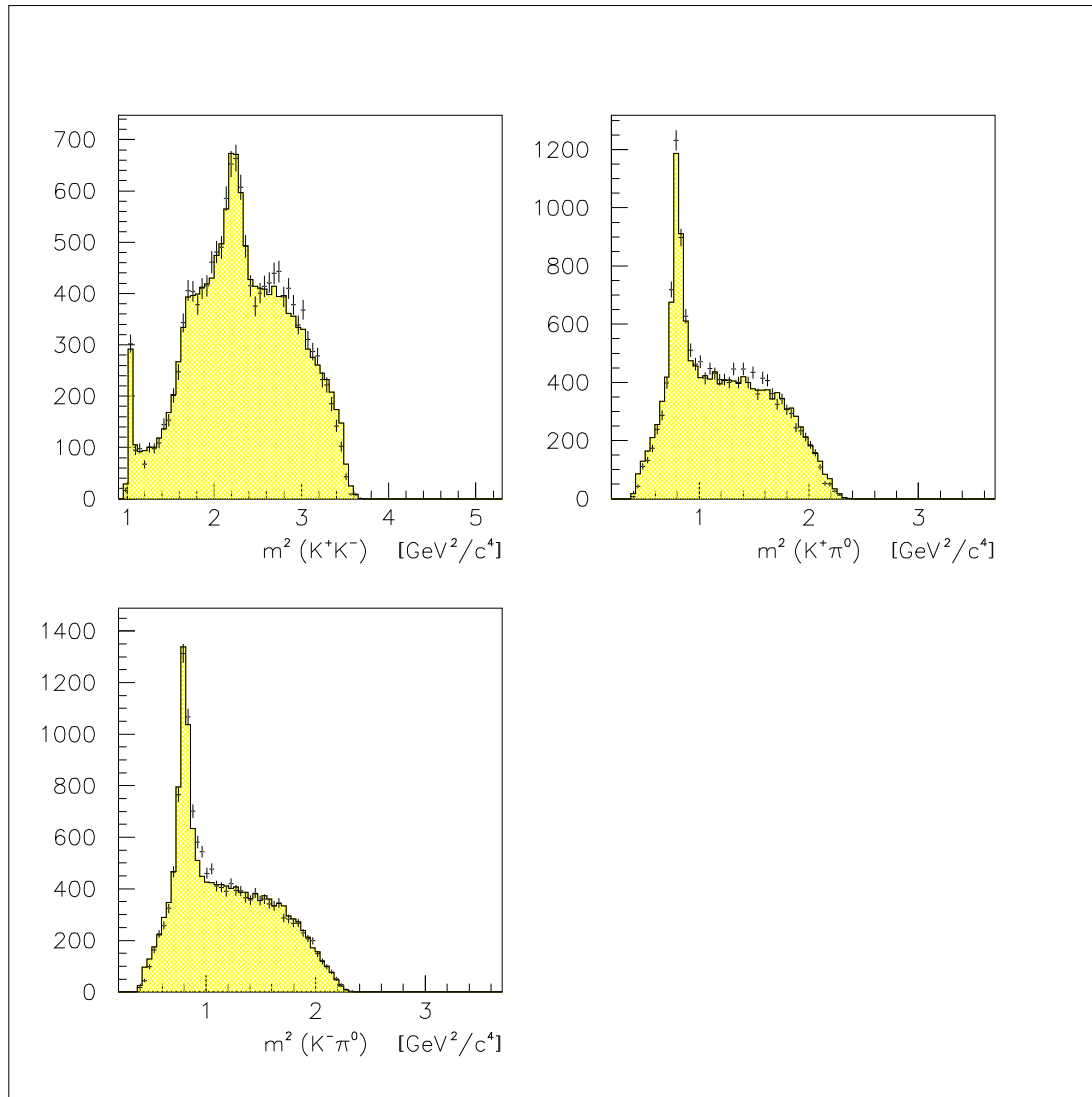


Figure 6.20: Best fit at 900 MeV/c (projections).

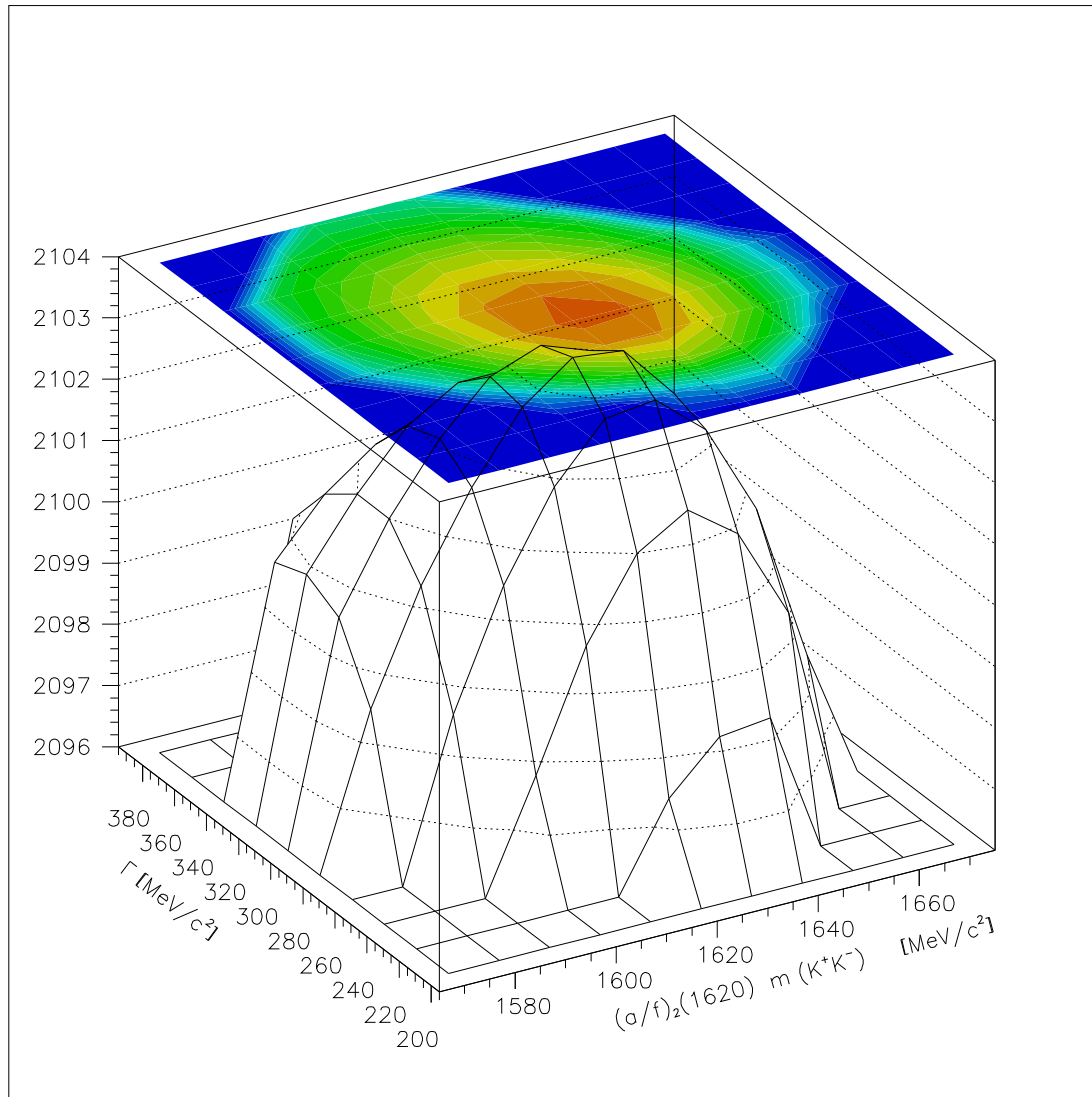


Figure 6.21: Best fit: mass and width of the $(a/f)_2(1620)$ if $J = 2$.

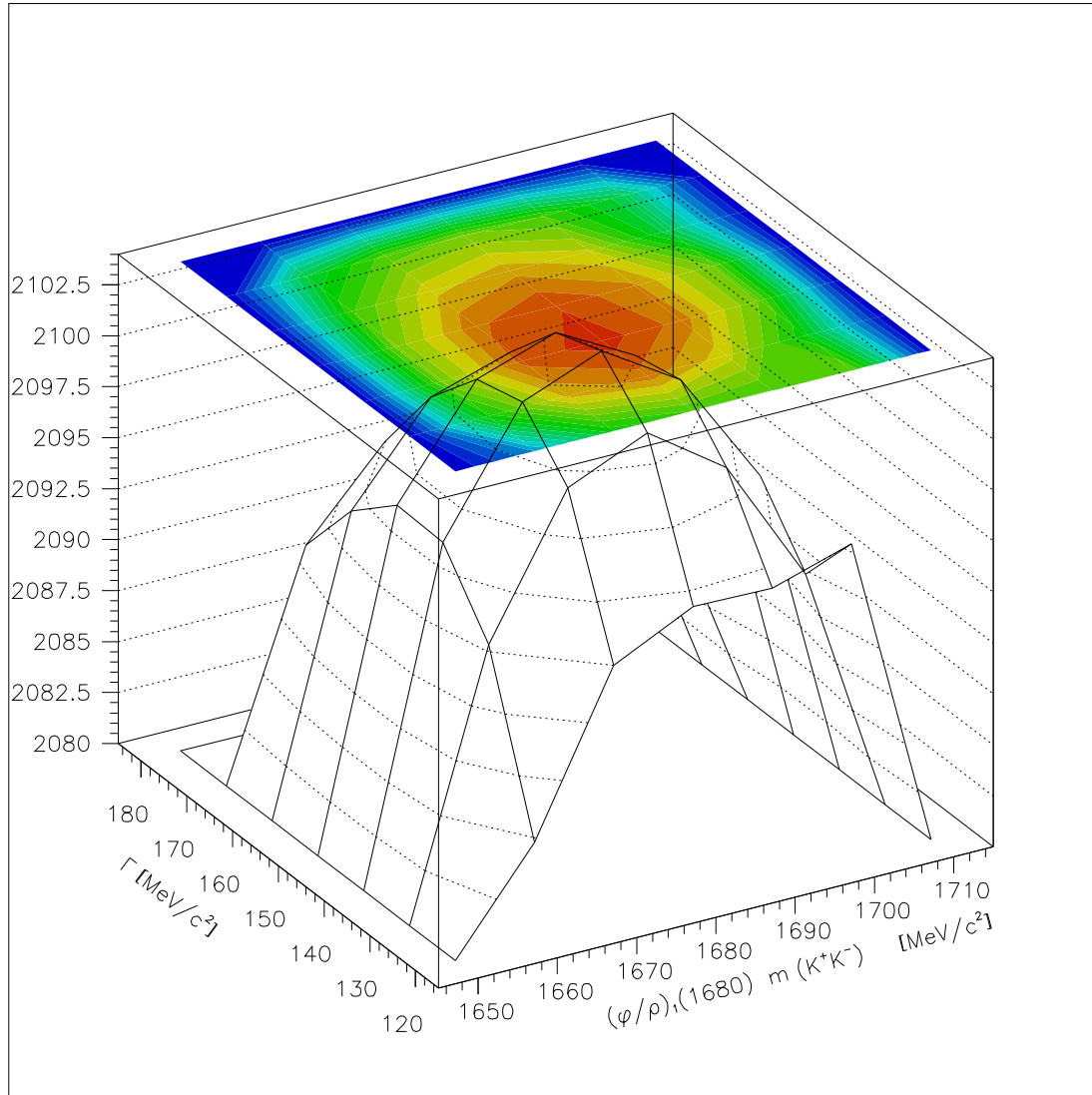


Figure 6.22: Best fit: mass and width of the $(\phi/\rho)_1(1680)$.

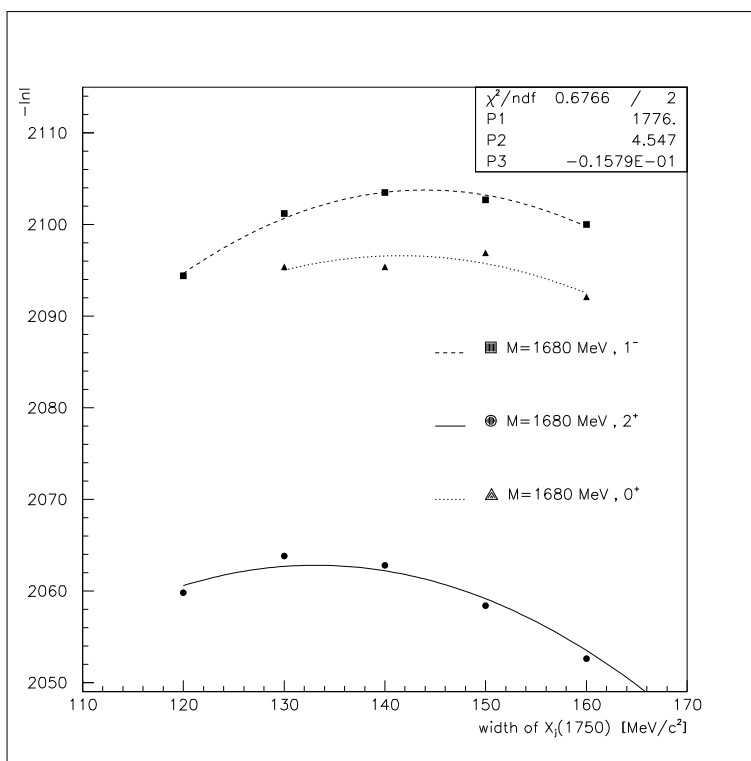
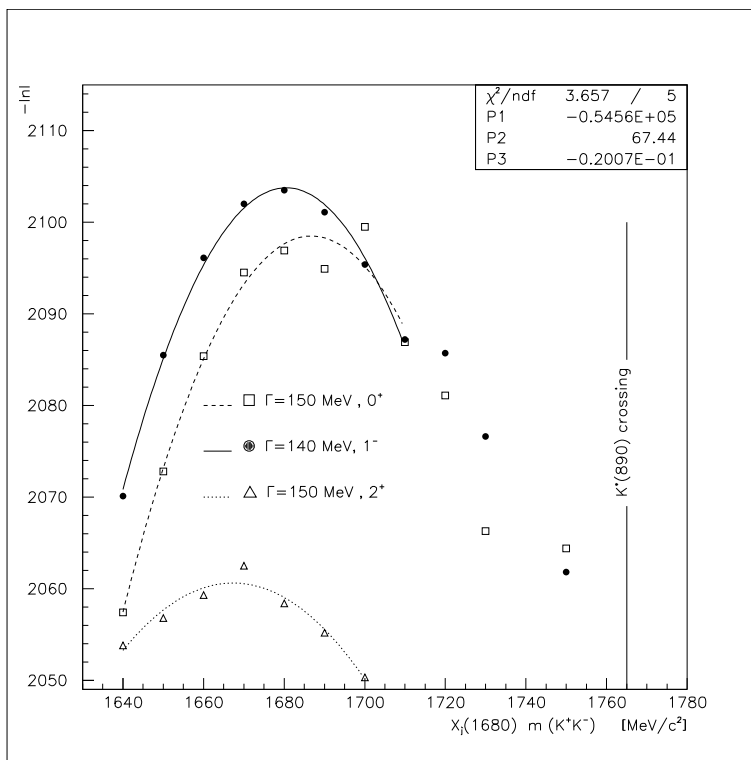


Figure 6.23: Best fit: mass and width of the $X_J(1680)$ if $J = 0, 1, 2$. With $J = 0$ the fit is not stable: the log-likelihood values are only indicative and a full convergence was not reached.

6.5 Basic Fit at 1642 MeV/c

The channels taken into consideration at 1642 MeV/c for a basic fit are:

$$\bar{p}p \rightarrow \phi(1020)\pi^0 \quad (1)$$

$$\rightarrow f_2(1275)\pi^0 \quad (2)$$

$$\rightarrow f_0(1500)\pi^0 \quad (3)$$

$$\rightarrow f_0(1712)\pi^0 \quad (4)$$

$$\rightarrow K^{*\pm}(892)K^\mp \quad (5)$$

$$\rightarrow K_0^{*\pm}(1430)K^\mp \quad (6)$$

The basic fit has a log-likelihood of -416.40 ($\chi^2 = 1.704$) with 8 free parameters. The optimization of the production angles of the $K^{*\pm}(892)$'s and of the $K_0^{*\pm}(1430)$'s with a parametrization of the form $F(\theta) = 1 + p_1 \cos\theta + p_2 \cos^2\theta$ is not significant at 1642 MeV/c ($\Delta LL < 0.1$). The fitted angular distributions of the K^* 's are in better agreement with the data (see fig. 6.24) as compared to the distribution at 900 MeV/c. There is no evidence, with the present statistics, of forward-backward asymmetries which may be due to the high number of initial states at 1642 MeV (up to $J = 5$).

If the channel

$$\bar{p}p \rightarrow K_2^{*\pm}(1430)K^\mp \quad (7)$$

is also considered, its contribution goes to zero as well as at 900 MeV/c. There is instead a significant improvement when the channel

$$\bar{p}p \rightarrow K_1^{*\pm}(1680)K^\mp \quad (8)$$

is included with a log-likelihood of -436.67 ($\chi^2 = 1.689$). The basic fit of the Dalitz plot, including the channels (1)-(6),(8) and the projections are shown in fig. 6.25. and 6.26.

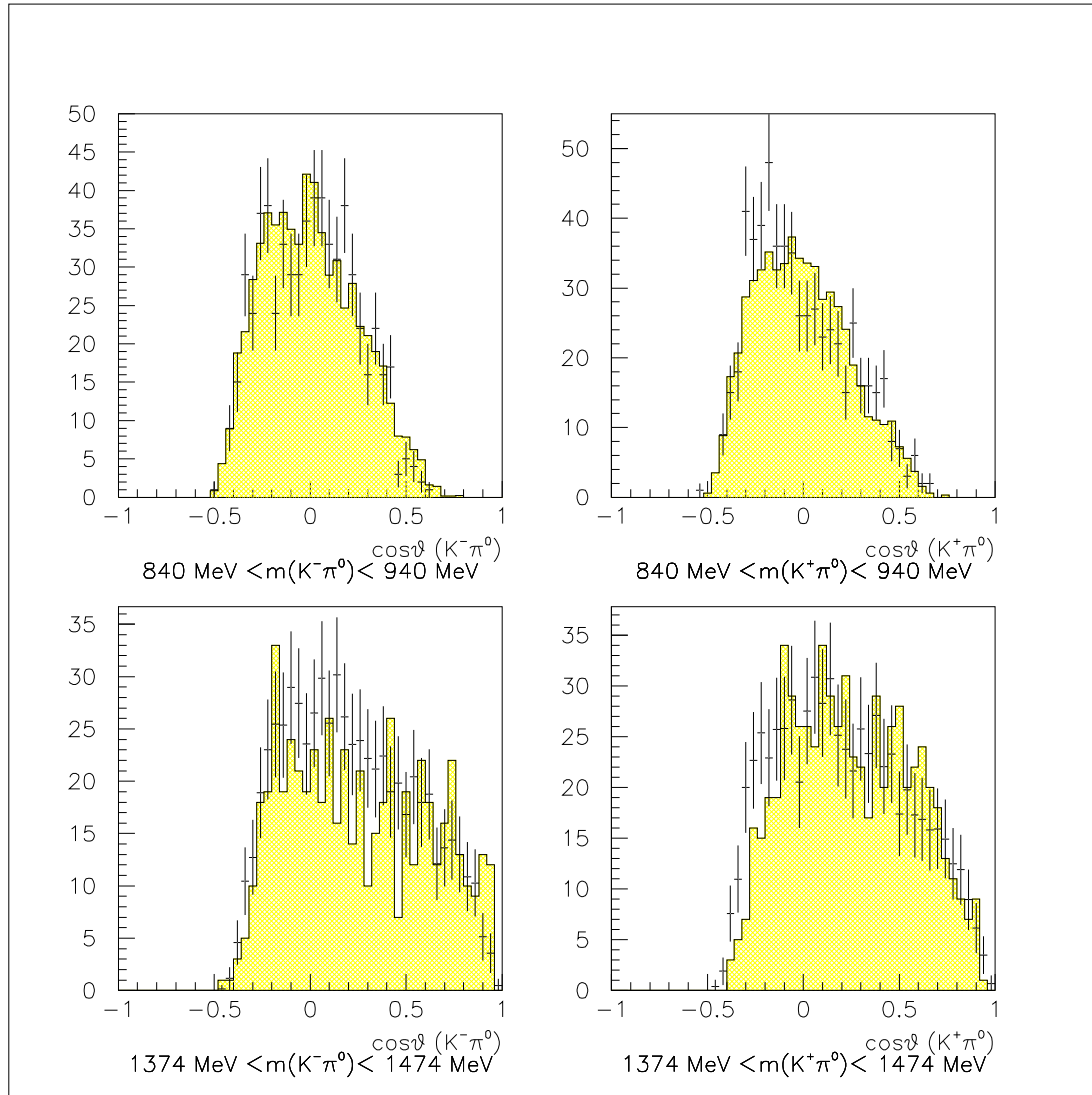


Figure 6.24: Fitted polar production angles of the $K^-\pi^0$ and $K^+\pi^0$ isobars at 1642 MeV/c and in different mass range corresponding to the $K^*(890)$ and to the $K_0(1430)$.

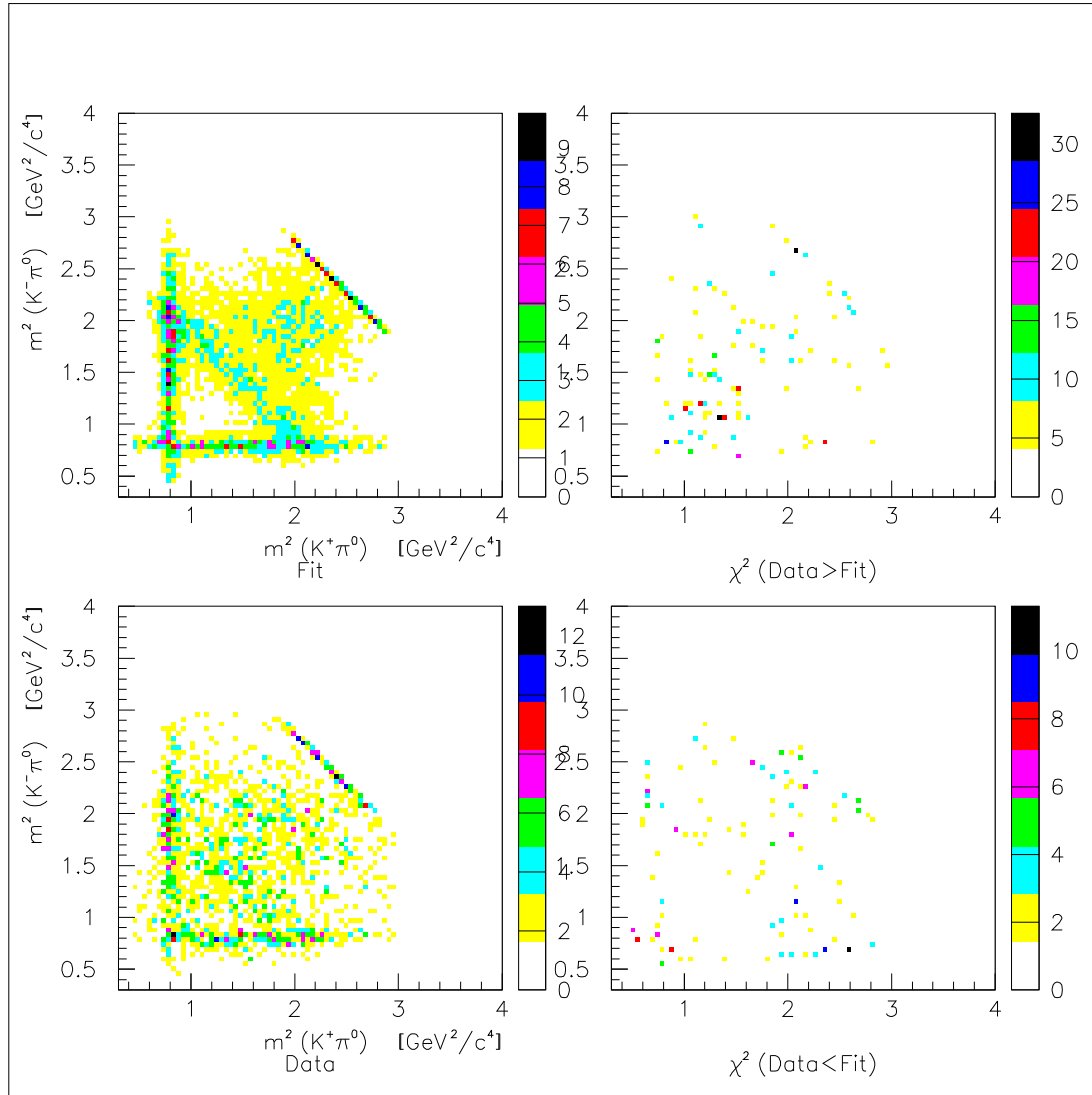


Figure 6.25: Basic fit of the Dalitz plot at 1642 MeV/c.

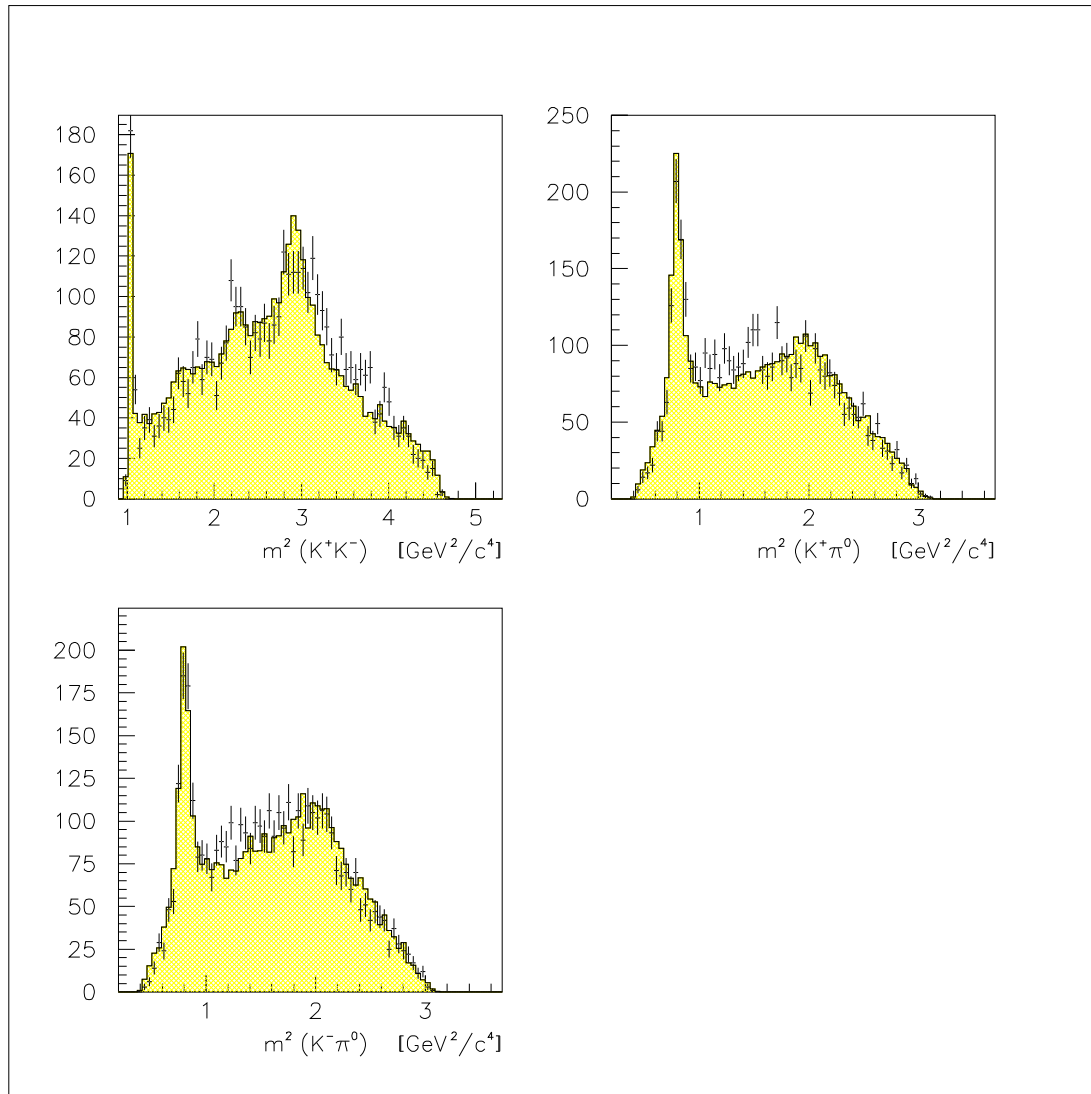


Figure 6.26: Basic fit: projections of the Dalitz plot at 1642 MeV/c.

6.6 Improved Fit at 1642 MeV/c

We consider next, as at 900 MeV/c, the following channels in addition to (1)-(6),(8):

$$\bar{p}p \rightarrow f_2'(1525)\pi^0 \quad (9)$$

$$\bar{p}p \rightarrow a_2(1320)\pi^0 \quad (10)$$

We obtain a better fit when the $f_2'(1525)$ is included, in consistency with the results at lower momenta (see table 6.12). The improvement of the fit when the $a_2(1320)$ is also included is not significant in relation to the number of additional free parameters and the channel (2) ($f_2(1275)$) reproduces adequately the Dalitz plot in this mass range (see fig. 6.27).

Interference	NLL	Par.	$\Delta LL/\Delta P.$	χ^2
$K^{*\pm}(892) \times K^{*\pm}(892)$	-440.15	12	3.75/2	1.677
$f_2'(1525) \times f_0(1500)$	-449.84	17	9.69/5	1.673
$f_2(1275) \times a_2(1320)$	-452.08	25	2.24/8	1.667

Table 6.12: Basic interferences at 1642 MeV/c.

The mass scan of the $f_J(1710)$ with $J = 0$ with a fixed width of $\Gamma = 150$ MeV finds an optimum at ~ 1750 MeV. This is surprising and confirms the fact that this mass range is obscured by the $K^{*\pm}(892)$ bands in the Dalitz plot at 900 MeV/c. Significant changes in the log-likelihood are obtained when the interference of the crossing $K_0^{*\pm}(1430)$ with the $f_2'(1525)$ and the $K^{*\pm}(892)$ are considered (see table 6.13) An additional structure around 1920 MeV is visible

Interference	NLL	Par.	$\Delta LL/\Delta P.$	χ^2
$K_0(1430) \times f_2'(1525)$	-484.71	20	6.11/2	1.579
$K_0(1430) \times K^{*\pm}(892)$	-490.69	21	5.98/1	1.576

Table 6.13: Additional interferences at 1642 MeV/c.

in the Dalitz plot. Therefore, we include the channel

$$\bar{p}p \rightarrow X_0(1920)\pi^0 \quad (11)$$

A resonance in this mass range has been seen in earlier experiments and here is confirmed here with a $\Delta LL = 9.57$ with one more additional parameter (spin 0). It has a significant contribution ($\sim 5\%$). Mass and width scans for different spin combination of the $X_J(1750)$, $X_J(1920)$ lead to the conclusion that spin 2 is

Resonance	Mass	Width	NLL	Par.	χ^2
$X_2(1750)$	1731.5 ± 9.3	193.9 ± 29.6	-501.60	22	1.550
$X_0(1920)$	(1920)	(200)			
$X_2(1750)$	(1731.5)	(193.9)			
$X_0(1920)$	1936.8 ± 28.7	181.9 ± 77.2	-501.77	22	1.550
$X_2(1920)$	1929.9 ± 13.6	106.5 ± 64.7	-503.35	23	1.549
$X_2(1750)$	1733.6 ± 7.4	178.0 ± 20.3	-503.32	23	1.550
$X_0(1750)$	1739.5 ± 7.5	192.0 ± 23.9	-503.61	22	1.547
$X_2(1920)$	(1929.9)	(106.5)			

Table 6.14: Optimization of the $X_J(1750)$, $X_J(1930)$ for $J = 0, 2$. The fitted values, with the preferred spin, obtained in a previous optimization are used in the following fits with fixed values (in brackets).

slightly preferred over spin 0 for the $X_J(1920)$ (see table 6.14). It has an optimum at a mass of 1930 MeV ($\Gamma = 106$) in agreement with earlier determinations by GAMS [76], VES [77], LASS [78] and the Omega group [79]. The log-likelihood change between $J = 0$ and $J = 2$ for the $X_J(1750)$ is not significant (see fig. 6.28). The optimum of the $X_J(1750)$ for $J = 0$ is reached at a mass of 1740 MeV and $\Gamma = 192 \text{ MeV}$. The mass and width optimizations for other resonances are listed in table 6.15. To get the optimum of the $f_2(1275)$ we have also to include another tensor at 1320 MeV, which corresponds presumably to the $a_2(1320)$ if we compare the mass and width with the PDG values. However, to reduce the number of parameters the $a_2(1320)$ will be omitted in further fits. The fitted Dalitz plot and the projections are shown in the fig. 6.29, 6.30.

Resonance	Mass	Width
$K^{*\pm}(892)$	897.1 ± 1.5	50.9 ± 1.7
$K_0^*(1430)$	(1429 \pm 5)	(287 \pm 21)
$\phi(1020)$	1019.1 ± 0.5	9.1 ± 0.5
$f_2(1275)$	1269.4 ± 12.4	191.4 ± 13.3
$a_2(1320)$	$1315. \pm 15.9$	103.9 ± 25.3
$f_0(1500)$	1486.6 ± 10.3	(112.)
$f_2'(1525)$	(1525.)	77.1 ± 12.7

Table 6.15: Improved fit at 1642 MeV/c: fitted masses and widths. The values in brackets are taken from the PDG [2] and are fixed.

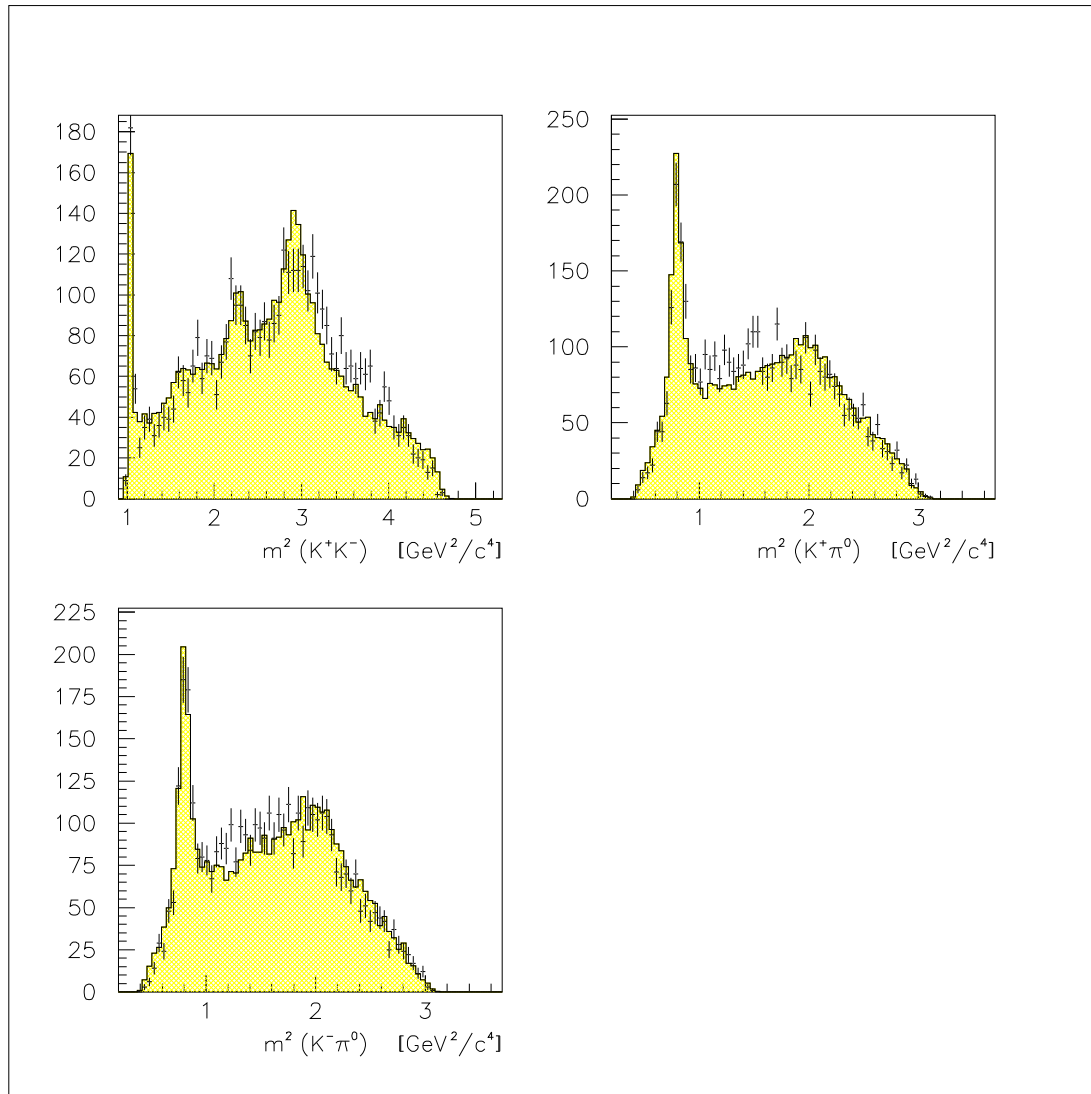
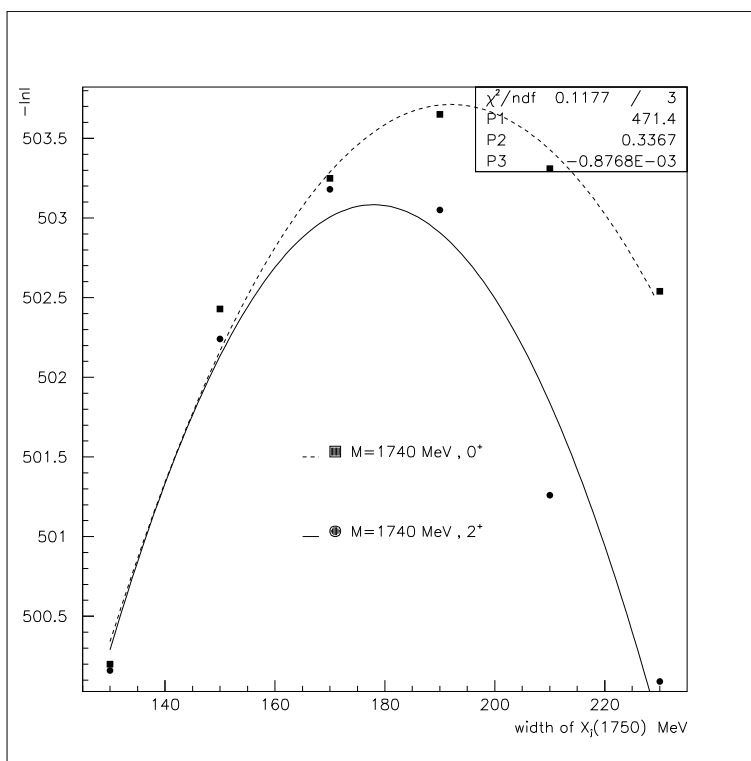
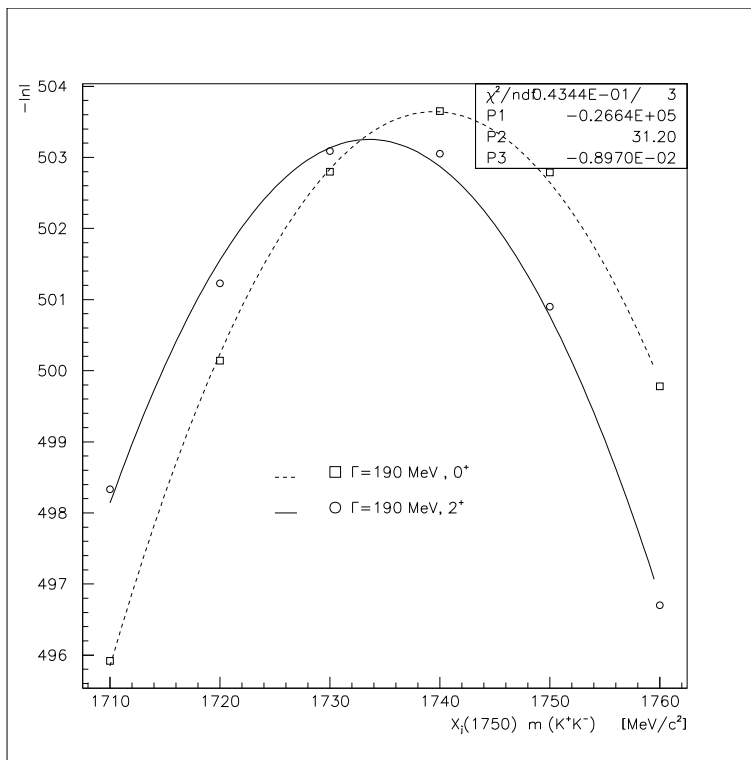


Figure 6.27: Improved fit (projections) including the $f_2'(1525)$.

Figure 6.28: Improved fit: mass and width of the $X_J(1740)$ if $J = 0, 2$.

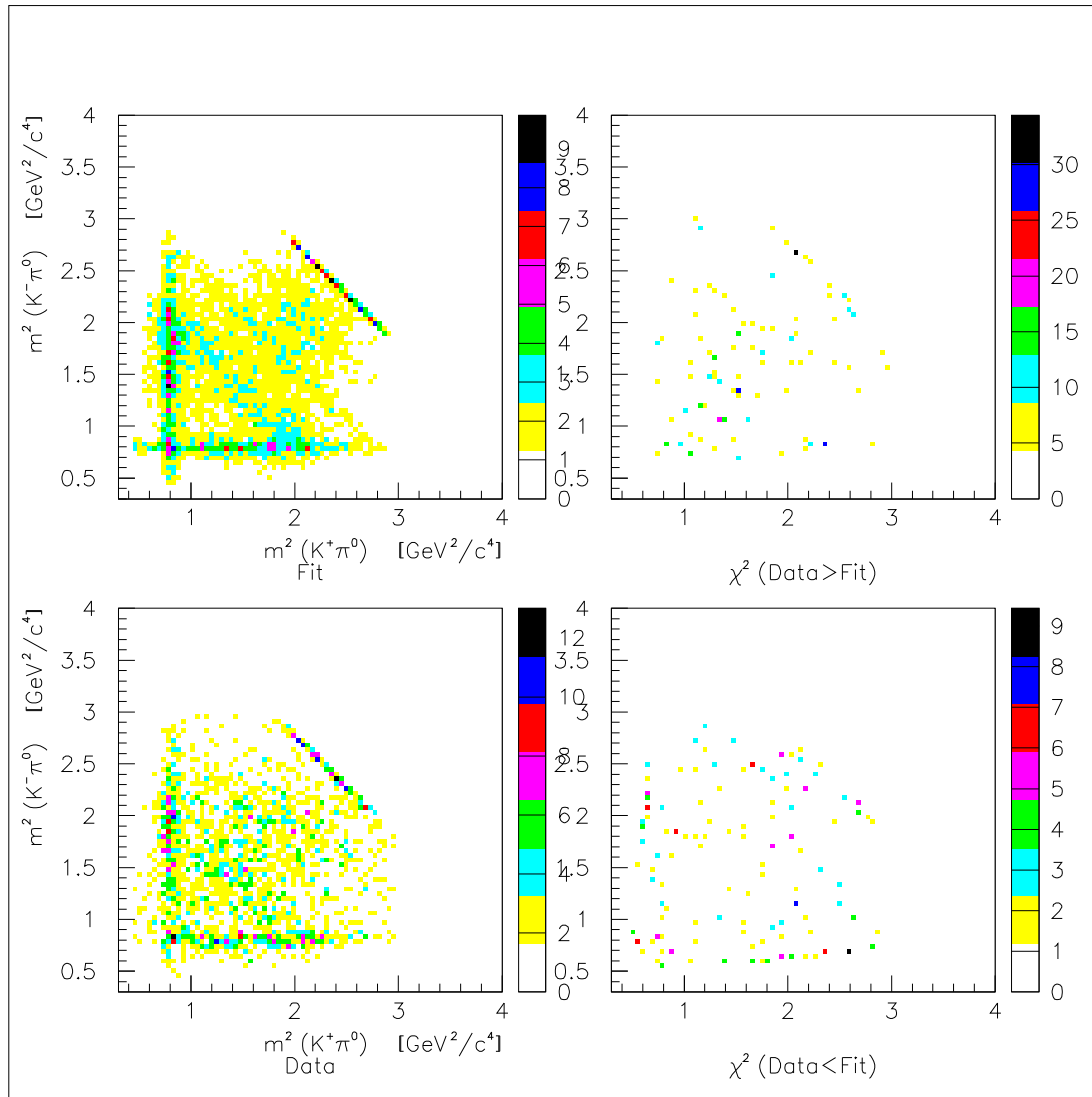


Figure 6.29: Improved fit including the $f'_2(1525)$, $X_0(1740, 190)$ and the $X_2(1930, 110)$.

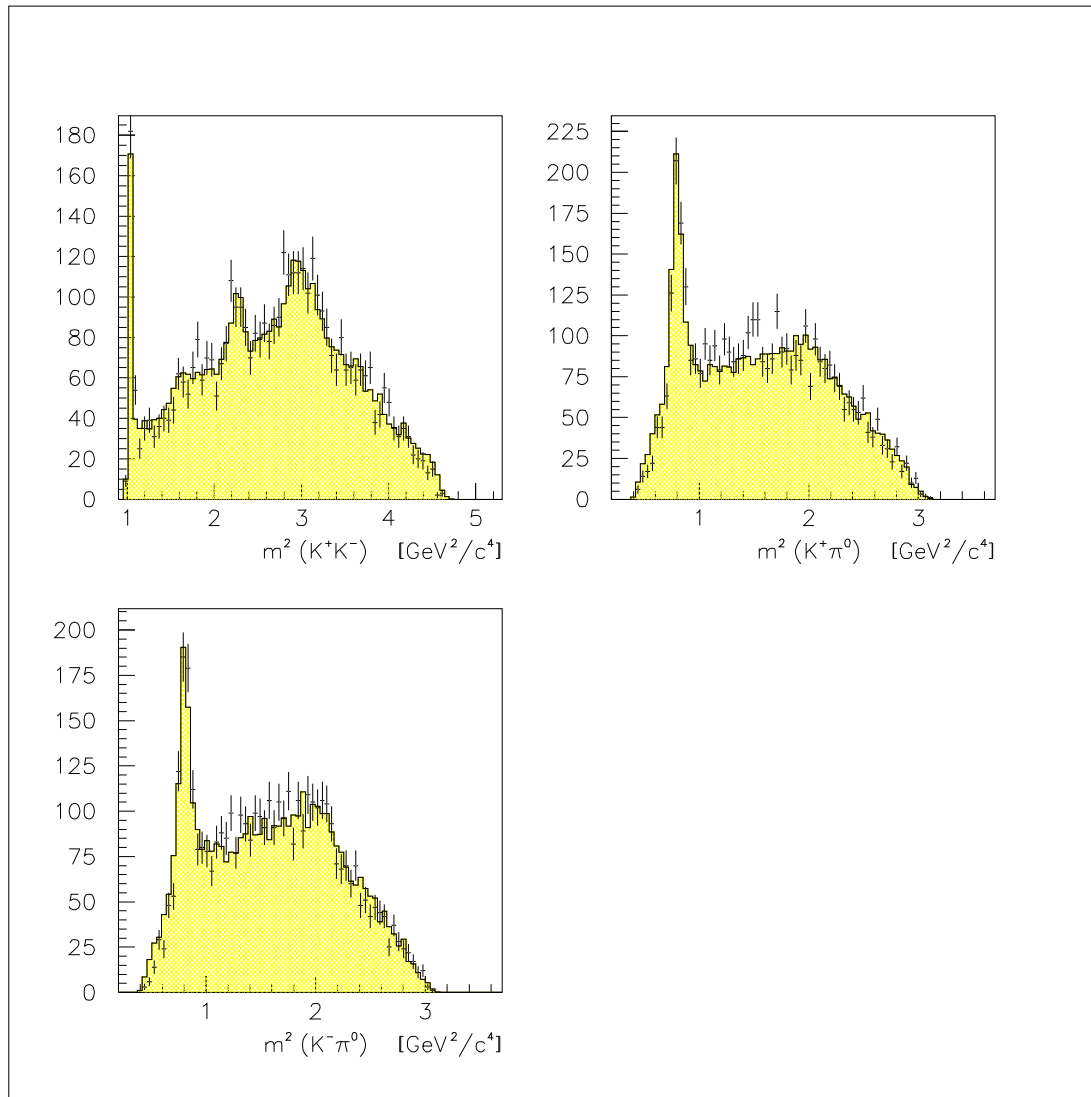


Figure 6.30: Improved fit (projections) including the $f'_2(1525)$, $X_0(1740,190)$ and the $X_2(1930,110)$.

6.7 Best Fit at 1642 MeV/c

Including the additional interference between the $K_1(1680)$ and the $K_0(1430)$ with respect to the improved fit gives a log-likelihood of -539.84 with 24 parameters ($\Delta LL = 36.23/2$) with $\chi^2 = 1.503$. Keeping in mind the results of the analysis at low momentum we include in addition to the channel (1)-(6), (8)-(10) also a tensor at 1620 MeV and a vector at 1680 MeV.

$$\bar{p}p \rightarrow (a/f)_2(1620)\pi^0 \quad (11)$$

$$\bar{p}p \rightarrow \phi(1680)\pi^0 \quad (12)$$

The modest changes of the log-likelihood are not confirmed by a significant improvement of the χ^2 . This effect is presumably due to the present χ^2 definition, where the fluctuations of the probability density function within the same bin are not considered. As a confirmation of the presence of the same resonances

	NLL	Par.	χ^2
Best fit	-543.74	28	1.504
Best fit without $(a/f)_2(1620)$	-541.82	26	1.505
Best fit without $(\phi/\rho)_1(1680)$	-538.47	26	1.513
Best fit without $X_0(1770)$	-505.83	27	1.595

Table 6.16: Best fit at 1642 MeV/c: comparison including and excluding the $(a/f)_2$ or the $(\phi/\rho)_1$ or the X_0 .

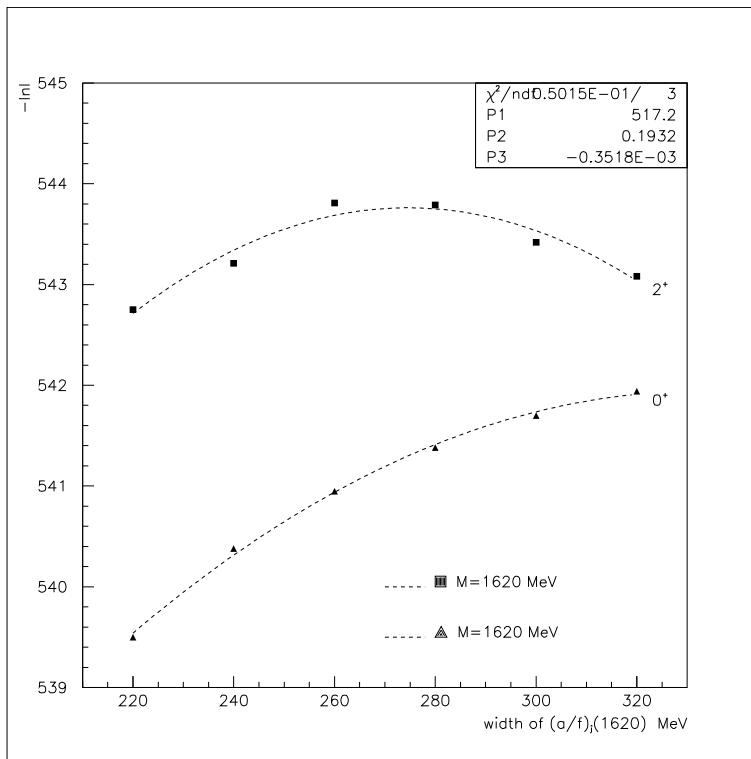
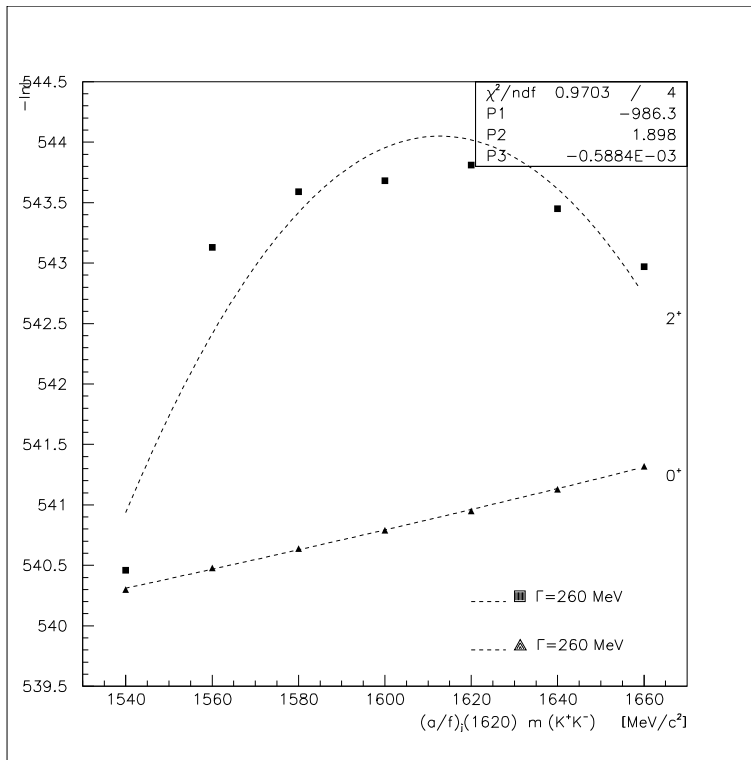
observed at 900 MeV/c, we have to point out that repeating the optimization starting from masses or widths, slightly lower or below the earlier determination, the fit converges, in a very good agreement, to the same values obtained at 900 MeV/c. In addition, the mass of the structure at 1740 MeV is shifted to 1770 MeV. The exact values of the observed resonances are given in table 6.17 and have to be compared to the earlier determination at 900 MeV (table 6.10). The optimization is repeated for different spin combinations. The best fits for different spin combination are shown in the corresponding plots (see figs. 6.31, 6.32, 6.33, 6.33,6.34). Keeping all other channels, attempts to fit another scalar or another tensor around 1680 instead of the vector (channel (11)) were not successful and in fig. 6.32 the optimization is shown for $J = 1$ only. Looking at the fitted contribution it is important to note that with a scalar at 1770 MeV the contribution of the vector at 1680 MeV is now comparable to the $\phi(1020)$, as one expects for the first radial excitation.

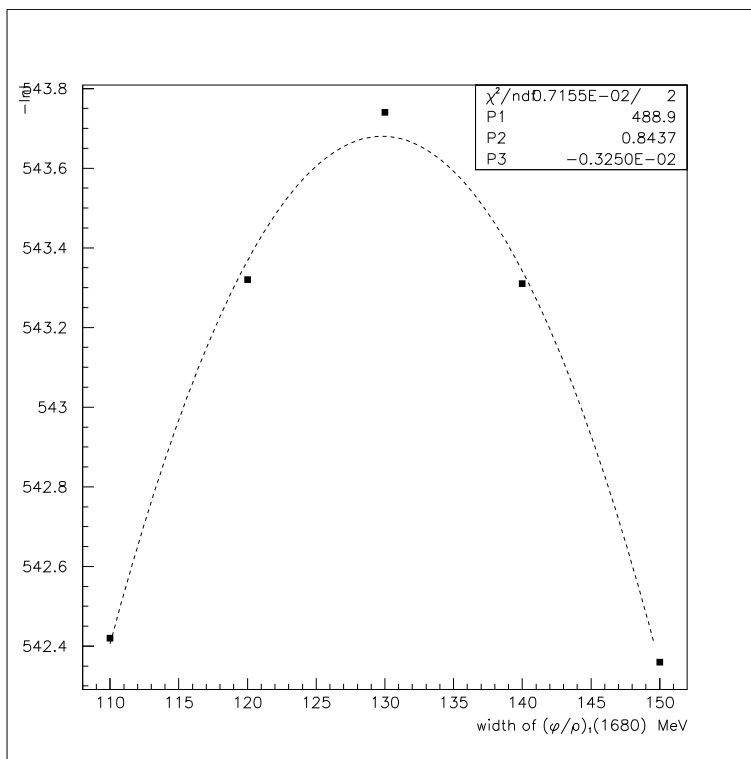
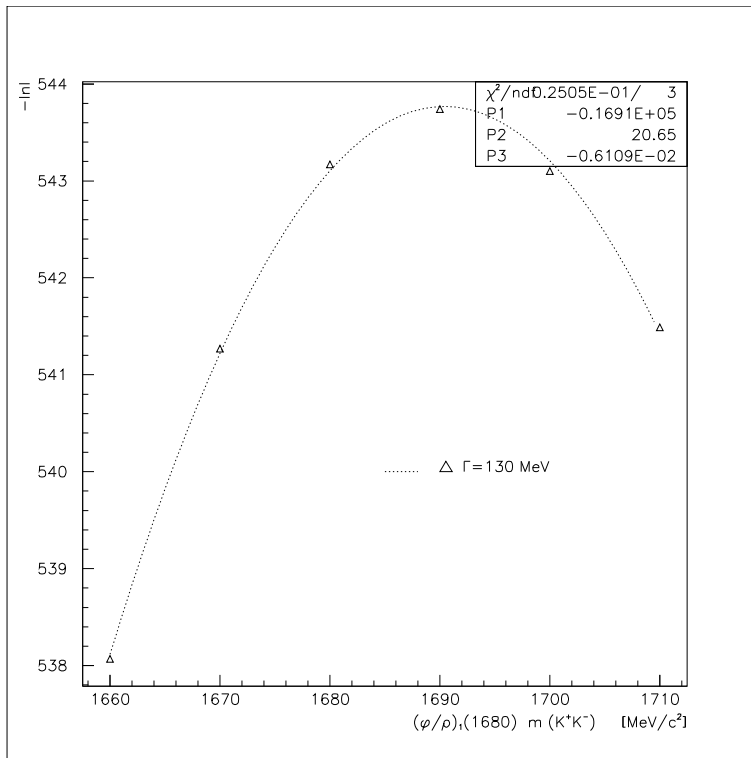
Resonance	Mass	Width	NLL	Par.	χ^2
$(a/f)_2(1620)$	(1620)	(280)			
$(\phi/\rho)_1(1680)$	(1690)	(130)			
$X_0(1750)$	1775.4 ± 7.1	113.3 ± 29.2	-543.99	28	1.503
$X_2(1750)$	1774.7 ± 5.1	90.0 ± 14.6	-541.36	29	1.508
$X_2(1920)$	(1929.9)	(106.5)			
$(a/f)_2(1620)$	1612.7 ± 29.1	274.6 ± 37.7	-543.74	28	1.504
$(a/f)_0(1620)$	~ 1620	~ 280	-541.38	27	1.505
$(\phi/\rho)_1(1680)$	(1690)	(130)			
$X_0(1770)$	(1770)	(110)			
$X_2(1920)$	(1929.89)	(106.55)			
$(a/f)_2(1620)$	(1620)	(280)			
$(\phi/\rho)_1(1680)$	1690.4 ± 12.4	129.9 ± 12.4	-543.74	28	1.504
$(X)_0(1770)$	(1770)	(110)			
$X_2(1920)$	(1929.9)	(106.5)			
$(a/f)_2(1620)$	(1620)	(280)			
$(\phi/\rho)_1(1680)$	(1690)	(130)			
$X_0(1770)$	(1770)	(110)			
$X_0(1920)$	1932.4 ± 13.9	115.4 ± 26.2	-540.22	27	1.503
$X_2(1920)$	1930.9 ± 11.8	91.0 ± 20.2	-542.54	28	1.506
$X_4(1920)$	1932.5 ± 12.6	76.3 ± 24.5	-533.35	29	1.518

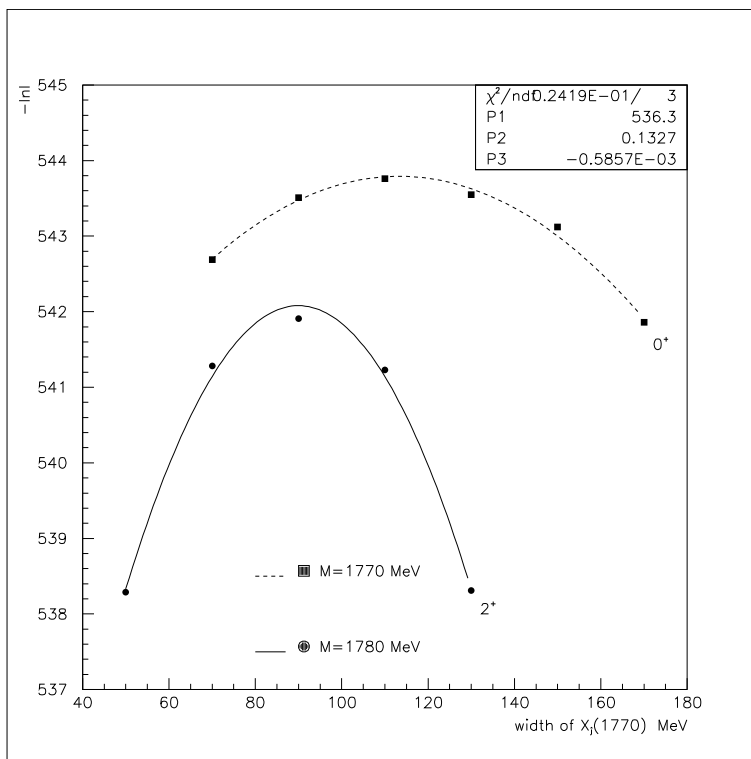
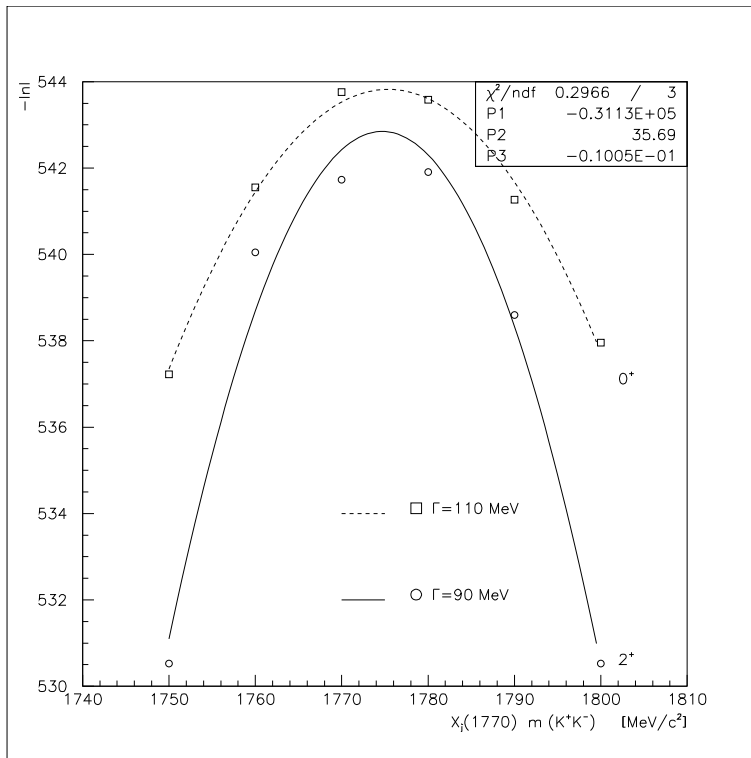
Table 6.17: Spin test and mass/width scanning including all channels at 1642 MeV/c. The fitted values, with the preferred spin, in a previous optimization are used in the following fits with fixed values (in brackets).

Resonance	Hel. 0	Hel. 1	Hel. 2	Tot. int.	$\Delta LL/\Delta P$
$K^{*\pm}(892)$	2.21	21.19		23.4	
$K_0^*(1430)$	19.24			19.24	
$K_1^*(1680)$	2.49	-		2.49	
$\phi(1020)$	1.12	3.21		4.33	
$(a/f)_2(1275)$	7.24	2.32	-	9.56	
$f_0(1500)$	14.69			14.69	
$f_2'(1525)$	12.89	0.65	-	13.54	
$(a/f)_2(1620)$	2.46	-		2.46	1.92/2
$(\phi/\rho)_1(1680)$	0.01	9.05		9.06	5.27/2
$X_0(1770)$	10.71			10.71	37.91/1
$X_2(1920)$	4.64	0.21		4.85	

Table 6.18: Best fit: contributions at 1642 MeV/c including all channels (1)-(6), (8)-(12). In evaluating these branching ratios, interferences are omitted. Thus contributions do not add up exactly to 100%. The log-likelihood changes are obtained when the channel is dropped from the fit and the contributions and the phases of the other channels are re-optimized.

Figure 6.31: Best fit: mass and width of the $X_J(1620)$ if $J = 0, 2$.

Figure 6.32: Best fit: mass and width of the $X_J(1680)$ if $J = 1$.

Figure 6.33: Best fit: mass and width of the $X_J(1770)$ if $J = 0, 2$.

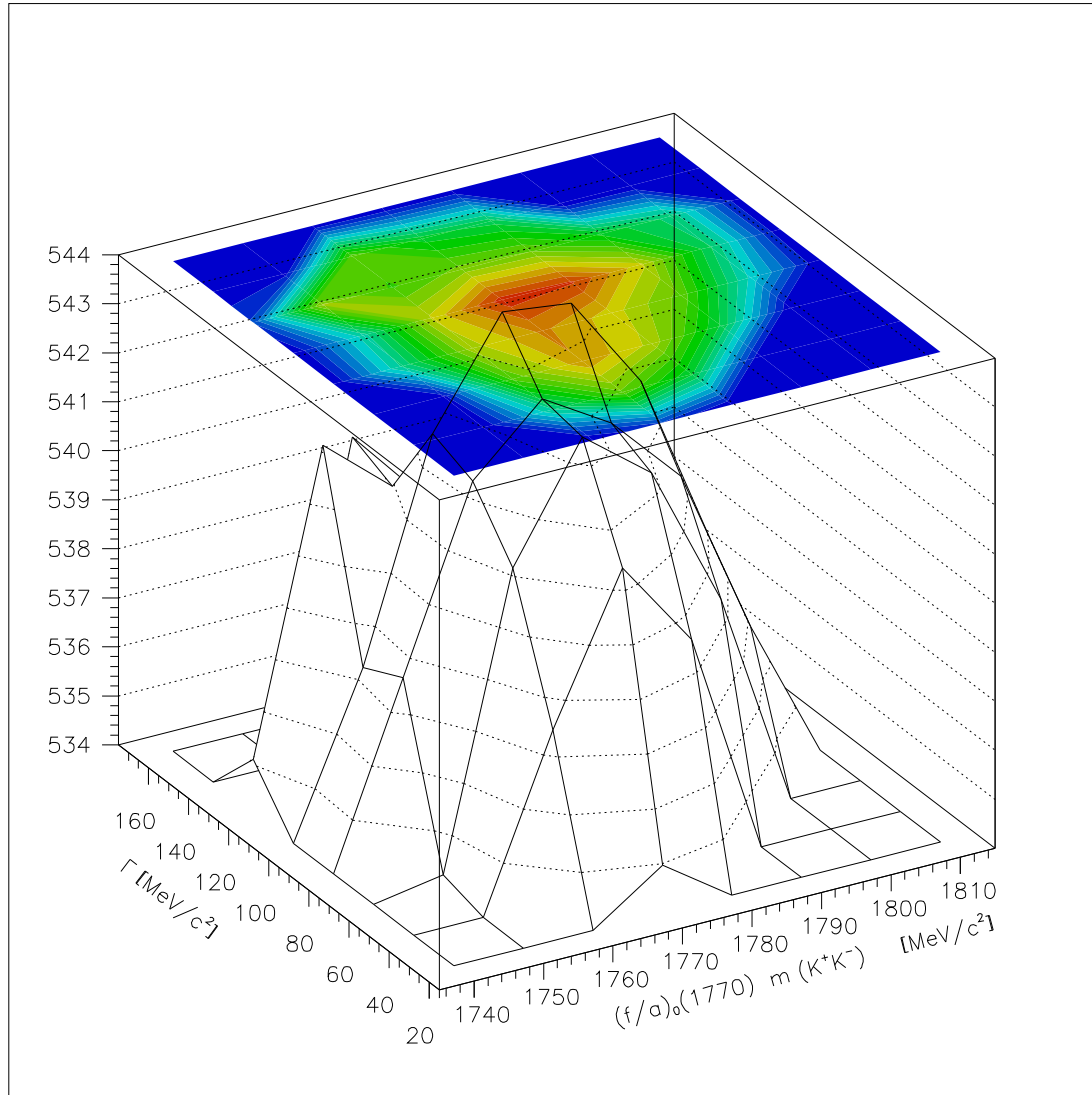
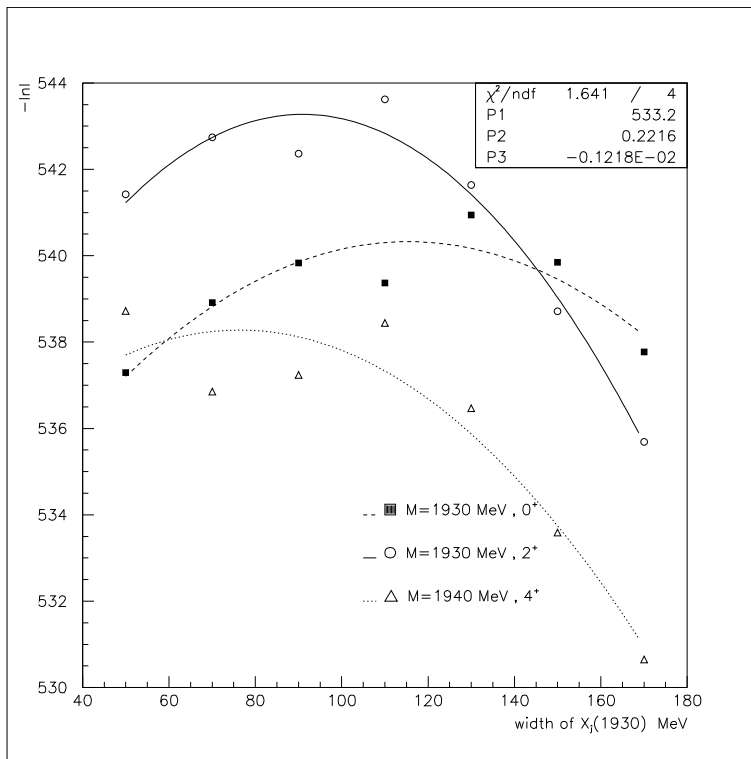
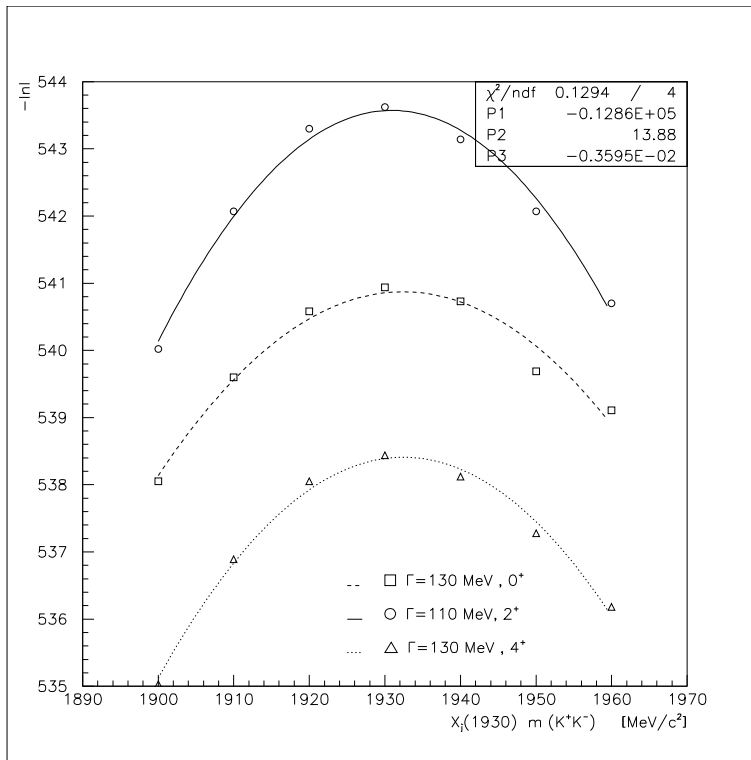


Figure 6.34: Best fit: mass and width of the $(f/a)_0(1770)$.

Figure 6.35: Best fit: mass and width of the $X_J(1930)$ if $J = 0, 2, 4$.

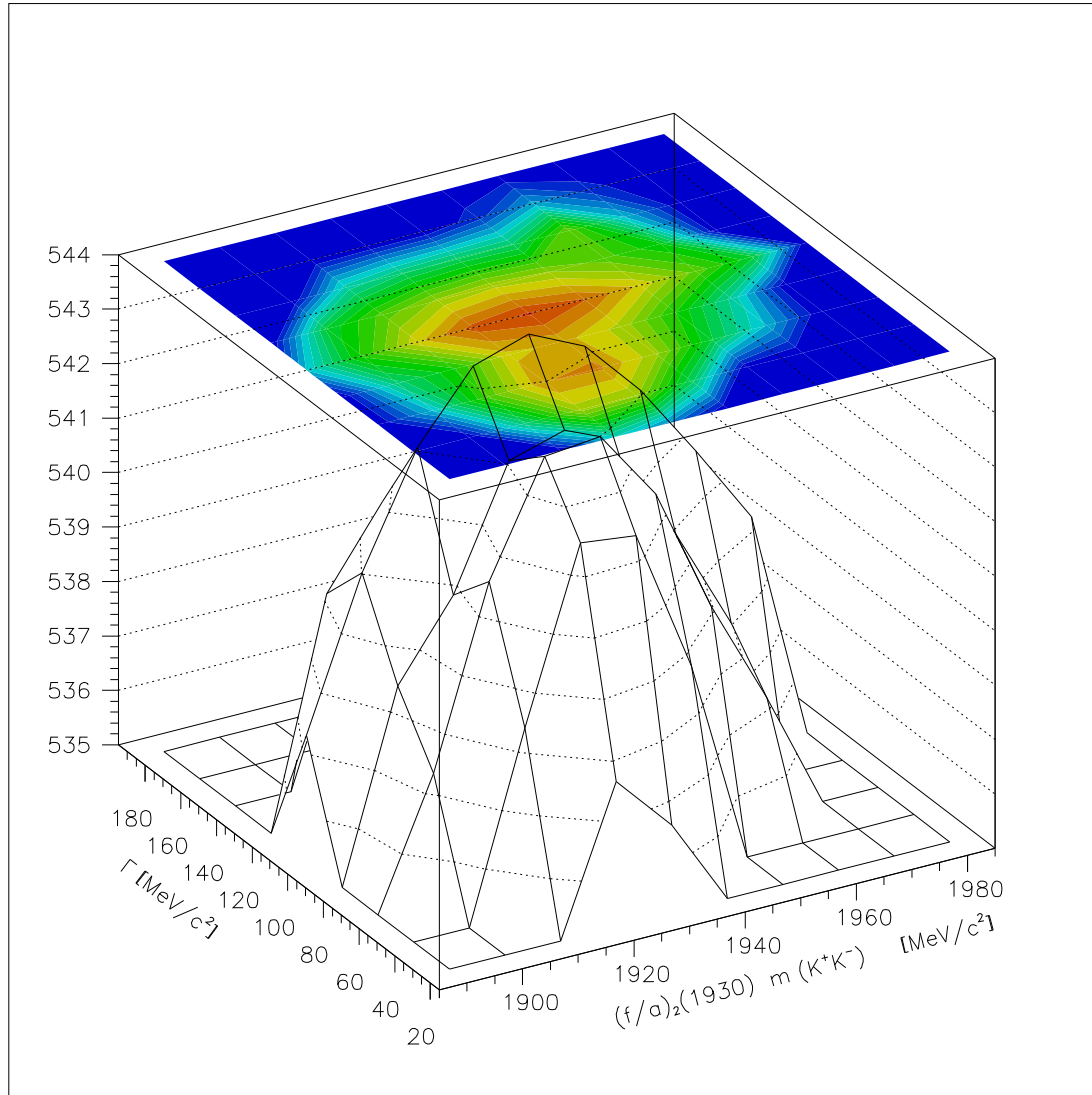


Figure 6.36: Best fit: mass and width of the $(f/a)_2(1930)$.

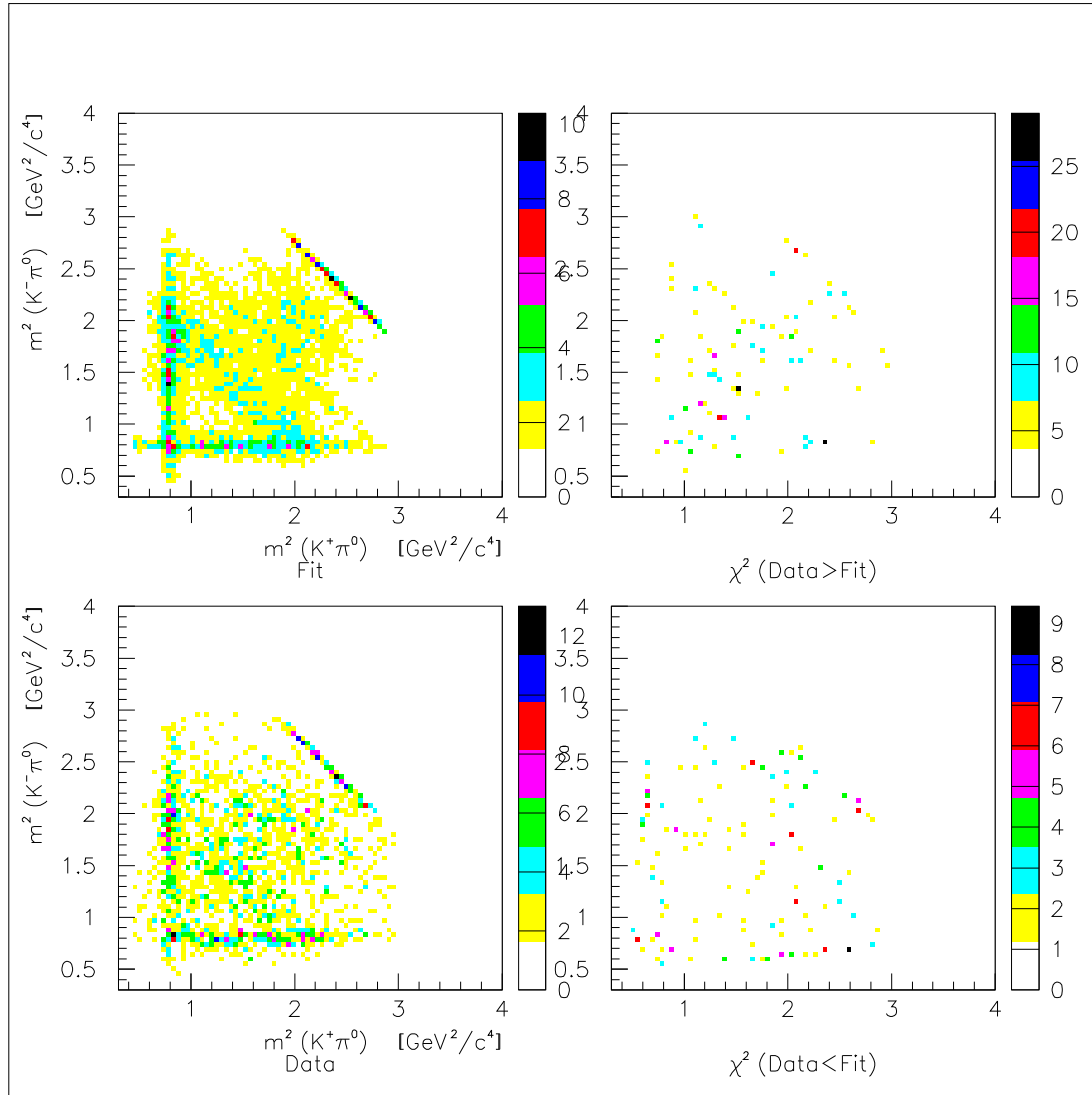


Figure 6.37: Best fit including the channels (1)-(6),(8)-(12).

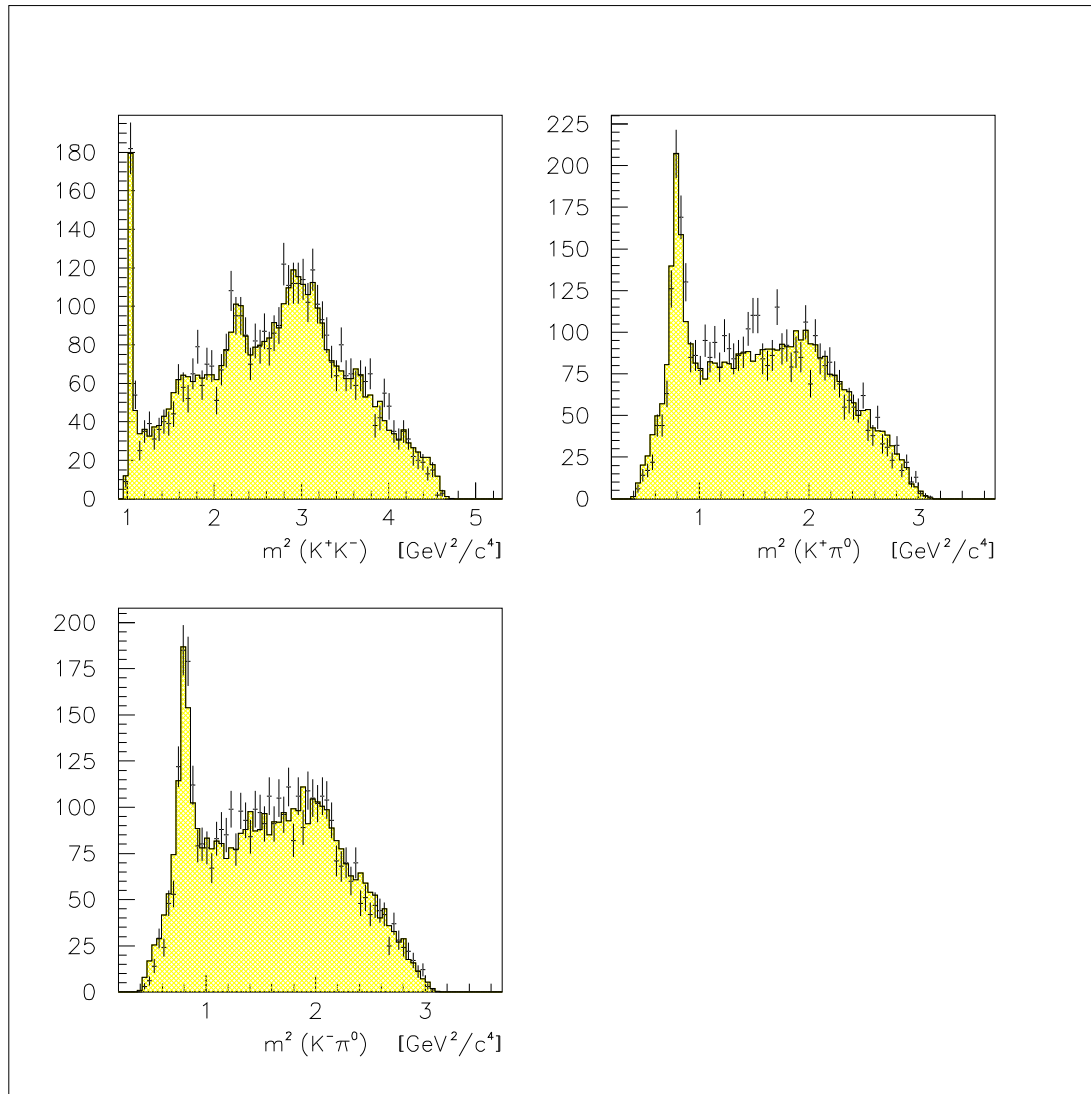


Figure 6.38: Best fit including the channels (1)-(6),(8)-(12) (projections).

Chapter 7

Conclusion

7.1 Observed Resonances

The reaction $\bar{p}p \rightarrow K^+K^-\pi^0$ at an antiproton momentum of 900 MeV/c and at 1642 MeV/c is studied with the Crystal Barrel detector at LEAR. The important result obtained in the analysis at 1642 MeV/c is the clear evidence of a K^+K^- resonance at $1775. \pm 7.$ MeV ($\Gamma = 113. \pm 29.$ MeV) with spin 0 slightly preferred over spin 2. Another structure is observed at an invariant K^+K^- mass of $1931. \pm 12.$ MeV ($\Gamma = 91. \pm 20.$ MeV).

In addition to these two resonances two more K^+K^- resonances in the 1.6-1.7 GeV mass region are observed: a broad tensor at $1624. \pm 12.$ MeV ($\Gamma = 277. \pm 23.$) and a vector at $1680. \pm 5.$ MeV ($\Gamma = 144. \pm 6.$).

Evidence for destructive $f_0(1500)$ - $f'_2(1525)$ interference is observed at both momenta, particularly clear at 900 MeV/c. Because of the moderate statistics at high momentum, the optimization of the masses and widths of the $f_0(1500)$ and $f'_2(1525)$ is only possible at 900 MeV/c, where the statistics is ~ 4 times higher: the $f_0(1500)$ optimizes at a mass of 1486.4 ± 3.5 ($\Gamma = 118.8 \pm 10.1$) and the $f'_2(1525)$ at 1528.5 ± 8.6 ($\Gamma = 76.7 \pm 7.1$) respectively, which is consistent with the PDG.

7.2 Interpretation of the Results

The interpretation of the resonances in the 1.6–1.8 GeV K^+K^- is based, because of the isospin ambiguity, mainly on the comparison of the masses and widths with the PDG tables.

The 2^{++} at ~ 1620 MeV can be identified with the $a_2(1660)$ already observed by the Crystal Barrel collaboration in the analysis of the reaction $\bar{p}p \rightarrow \eta\eta\pi^0$ at 1940 MeV/c, decaying to $\eta\pi^0$ [33]. In the $\eta\pi^0$ channel the fitted mass and width were 1660 ± 40 , $\Gamma = 280 \pm 70$ MeV respectively and are close to the values that are obtained in the present analysis. It is presumably the first radial excitation of the $a_2(1320)$ and sets a mass scale for the tensor nonet.

The vector at 1680 MeV is presumably the first radial excitation of the

$\phi_1(1020)$, the $\phi_1(1680)$, but an eventual mixture with the $\rho_1(1700)$ cannot be excluded.

Next we consider the structure at 1770 MeV. Very recently the PDG lists the $f_J(1710)$ with $J = 0$ at a mass of 1715 ± 7 MeV and a width of 125 ± 12 MeV. Concerning proton-antiproton annihilation the PDG includes in the list for the $f_0(1710)$ also the $f_0(1770)$ observed in an analysis of Crystal Barrel $\eta\eta$ data with a mass of $M = 1770 \pm 12$ MeV [32] but this data is not used for the average.

This value is indeed far removed from 1715 MeV and may indicate that the $f_0(1770)$ is distinct from the θ , $f_J(1710)$. In the present work the structure at 1775 ± 7 MeV can be better interpreted with the $f_0(1770)$ as with the $f_J(1710)$ if the two resonances are distinct, although our width of $\Gamma = 113$ MeV is in a better agreement with the PDG average of the the $f_0(1710)$. A very recent partial wave re-analysis of the BES data on $J/\psi \rightarrow \gamma(\pi^+ \pi^- \pi^+ \pi^-)$ [80] finds a 0^{++} resonance decaying dominantly to $\sigma\sigma$ at 1740 MeV and a 2^{++} resonance decaying dominantly to $\rho\rho$ at 1940 MeV.

With the present statistic and the actual determinations it is hard to conclude whether one or two f_0 are present in the 1.7 GeV region. In proton-antiproton annihilation the E760 collaboration observed significant peaks in the $\eta\eta$ mass spectrum at ~ 1500 , 1748 ± 10 and ~ 2104 MeV but no J^P determination was performed [81].

Recently the L3 collaboration observed an enhancement at 1770 ± 20 MeV in the $K_S K_S$ final state in two-photon collision [82]. In order to be formed by two photons this resonance must have $J^P = (even)^{++}$. The observed angular distribution favoured here the $J = 0$ assignment.

Next we consider the 1.5 GeV mass region. In addition to the $f_0(1500)$ tentatives to fit the $a_0(1450)$ or the $f_0(1370)$ failed to converge and gave negligible contributions. Therefore we assume that the strength of the $f_0(1500)$ of about 14.7% at 1642 MeV/c corresponds entirely to the $f_0(1500)$ and can be compared to the strength of the structure at 1770 MeV (10.7%). If the latter resonance is identified with the $f_J(1710)$ the branching ratio of these two resonances in the $K^- K^+$ channel respect to other decay modes (eg. $\pi\pi$, $\eta\eta$, $\eta\eta'$) in flight, can give us important information about the glueball spectrum and about the quark model assignment of the low-lying scalar nonet. Actual pictures see, if we consider the $f_0(980)$ and the $a_0(980)$ to be multiquark states, the other three scalars listed from the PDG, namely the $f_0(1370)$, the $f_0(1500)$ and the $f_0(1710)$ as mixtures between the 0^{++} glueball with the nearby $n\bar{n}$ and $s\bar{s}$ members of the low-lying scalar nonet (see fig. 7.2). Within this frame the low-lying scalar nonet is made up of the $a_0(1450)$ and the $K^*(1430)$ in addition to the $n\bar{n}$ and $s\bar{s}$ members. The current question about the $f_0(1500)$ and the $f_0(1710)$, which are close in mass to the last predictions for the 0^{++} glueball state (Lattice theories) in the quenched approximation, namely 1.55 ± 0.05 GeV [10] or 1.74 ± 0.07 GeV [11], is not whether it is entirely glue or the $s\bar{s}$ state but which one is more glue or $s\bar{s}$ state. On the other hand if the structure at ~ 1770 MeV is the same as observed from the L3 collaboration we have to assume that it is dominantly $s\bar{s}$, because glueball production is suppressed in $\gamma\gamma$ collision. This strongly support the glue-

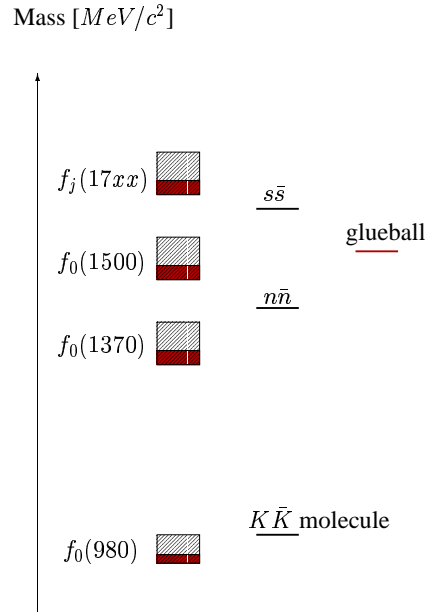


Figure 7.1: Possible mixing scheme for the low-lying scalar isoscalar mesons

ball nature of the $f_0(1500)$. The $f_0(1370)$ it is elusive because has a broad width and decays weakly to $K\bar{K}$. It is not observed in our channel and given that its width is in line with the $a_0(1450)$ and the $K_0(1430)$, we can associate it with the $n\bar{n}$ member of the nonet.

Concerning the structure at 1930 MeV ($\Gamma = 106$) it optimizes at values that are in agreement with earlier determinations by GAMS [76], VES [77], LASS [78] and the Omega group [79]. Recently, four f_2 were identified at 1920, 2020, 2210 and 2300 MeV [83]. Their nature is clarified if we draw the Veneziano plots where the their mass-squared is plotted as a function of the radial quantum number n . They are fitted with parallel straight-line trajectories and can be attributed [84] to $\bar{q}q$ 3P_2 states $f_2(1270)$, $f_2(1565)$, $f_2(1920)$ and $f_2(2210)$ and 3F_2 states $f_2(2020)$ and $f_2(2300)$.

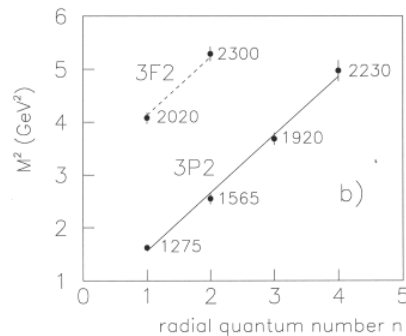


Figure 7.2: Suggested trajectories of M^2 v. radial quantum number for 2^+ states [84]; the given masses are in MeV.

Appendix A

Probability Density Function for the Reaction $\bar{p}p \rightarrow K^+ K^- \pi^0$ at 900 and at 1642 MeV/c

The total probability density w for every helicity λ_f is

$$w_{\lambda_f} = a_{\lambda_f} e^{i\delta_{\lambda_f}} \frac{B_s P_s^{\lambda_f}(\alpha, \beta)}{M_0^2 - m^2 - iM_0\Gamma} = a_{\lambda_f} e^{i\delta_{\lambda_f}} \Delta_{M_0, \Gamma}(m) P_s^{\lambda_f}(\alpha, \beta)$$

where the decay of the isobar with spin s is given by the Legendre polynomials $P_s^{\lambda_f}(\alpha, \beta)$ and Δ is the relativistic Breit-Wigner amplitude with constant width which includes the Blatt-Weisskopf B_s centrifugal barrier factors. a_{λ_f} are the coupling constants and δ_{λ_f} are the relative phases for every helicity amplitude.

The general expression including the channels considered in the present analysis is

$$\begin{aligned} w = & \sum_{\lambda_f=0,1} a_{\phi_1(1020), \lambda_f}^2 |\Delta_{\phi_1}(m_{KK}) P_1^{\lambda_f}(\alpha_{KK}, \beta_{KK})|^2 \\ & + \sum_{\lambda_f=0,1,2} a_{f_2(1275), \lambda_f}^2 |\Delta_{f_2}(m_{KK}) P_2^{\lambda_f}(\alpha_{KK}, \beta_{KK})|^2 \\ & + \sum_{\lambda_f=0,1,2} a_{a_2(1320), \lambda_f}^2 |\Delta_{a_2}(m_{KK}) P_2^{\lambda_f}(\alpha_{KK}, \beta_{KK})|^2 \\ & + a_{f_0(1500)}^2 |\Delta_{f_0}(m_{KK})|^2 \\ & + \sum_{\lambda_f=0,1,2} a_{f_2'(1525), \lambda_f}^2 |\Delta_{f_2'}(m_{KK}) P_2^{\lambda_f}(\alpha_{KK}, \beta_{KK})|^2 \\ & + \sum_{\lambda_f=0,1,2} a_{a_2(1640), \lambda_f}^2 |\Delta_{a_2}(m_{KK}) P_2^{\lambda_f}(\alpha_{KK}, \beta_{KK})|^2 \\ & + \sum_{\lambda_f=0,1} a_{\phi_1(1680), \lambda_f}^2 |\Delta_{\phi_1}(m_{KK}) P_1^{\lambda_f}(\alpha_{KK}, \beta_{KK})|^2 \end{aligned}$$

$$\begin{aligned}
& + a_{f_0(1770)}^2 |\Delta_{f_0}(m_{KK})|^2 \\
& + \sum_{\lambda_f=0,1,2} a_{f_2(1930),\lambda_f}^2 |\Delta_{f_2}(m_{KK}) P_2^{\lambda_f}(\alpha_{KK}, \beta_{KK})|^2 \\
& + \sum_{\lambda_f=0,1} a_{K_1(890),\lambda_f}^2 \times \\
& \left(|\Delta_{K_1}(m_{K+\pi}) P_1^{\lambda_f}(\alpha_{K+\pi}, \beta_{K+\pi})|^2 + |\Delta_{K_1}(m_{K-\pi}) P_1^{\lambda_f}(\alpha_{K-\pi}, \beta_{K-\pi})|^2 \right. \\
& \left. + c_{K_1, K_1, \lambda_f} e^{i\delta_{K_1, K_1, \lambda_f}} \Delta_{K_1}(m_{K+\pi}) \Delta_{K_1}^*(m_{K-\pi}) \times \right. \tag{A.1} \\
& \left. P_1^{\lambda_f}(\alpha_{K+\pi}, \beta_{K+\pi}) P_1^{\lambda_f}(\alpha_{K-\pi}, \beta_{K-\pi}) \right)
\end{aligned}$$

$$\begin{aligned}
& + a_{K_0(1430)}^2 \left(|\Delta_{K_0}(m_{K+\pi})|^2 + |\Delta_{K_0}(m_{K-\pi})|^2 \right. \\
& \left. + c_{K_0, K_0} e^{i\delta_{K_0, K_0}} \Delta_{K_0}(m_{K+\pi}) \Delta_{K_0}^*(m_{K-\pi}) \right) \tag{A.2}
\end{aligned}$$

$$+ a_{K_0(1430)} a_{K_1(890)} c_{K_0, K_1} e^{i\delta_{K_0, K_1}} \Delta_{K_0}(m_{K-\pi}) \Delta_{K_1}^*(m_{K+\pi}) P_1^{*0}(\alpha_{K+\pi}, \beta_{K+\pi}) \tag{A.3}$$

$$+ a_{K_0(1430)} a_{K_1(890)} c_{K_0, K_1} e^{i\delta_{K_0, K_1}} \Delta_{K_0}(m_{K+\pi}) \Delta_{K_1}^*(m_{K-\pi}) P_1^{*0}(\alpha_{K-\pi}, \beta_{K-\pi}) \tag{A.4}$$

$$\begin{aligned}
& + \sum_{\lambda_f=0,1} a_{K_1(1660),\lambda_f}^2 \times \\
& \left(|\Delta_{K_1}(m_{K+\pi}) P_1^{\lambda_f}(\alpha_{K+\pi}, \beta_{K+\pi})|^2 + |\Delta_{K_1}(m_{K-\pi}) P_1^{\lambda_f}(\alpha_{K-\pi}, \beta_{K-\pi})|^2 \right) \\
& + a_{f_0(1500)} a_{K_1(890)} c_{f_0, K_1} e^{i\delta_{f_0, K_1}} \Delta_{f_0}(m_{KK}) \Delta_{K_1}^*(m_{K+\pi}) P_1^{*0}(\alpha_{K+\pi}, \beta_{K+\pi}) \tag{A.5} \\
& + a_{f_0(1500)} a_{K_1(890)} c_{f_0, K_1} e^{i\delta_{f_0, K_1}} \Delta_{f_0}(m_{KK}) \Delta_{K_1}^*(m_{K-\pi}) P_1^{*0}(\alpha_{K-\pi}, \beta_{K-\pi}) \tag{A.6}
\end{aligned}$$

$$\begin{aligned}
& + \sum_{\lambda_f=0,1} a_{f_2'(1525),\lambda_f} a_{K_1(890),\lambda_f} c_{f_2', K_1, \lambda_f} e^{i\delta_{f_2', K_1, \lambda_f}} \times \\
& \times \Delta_{f_2'}(m_{KK}) \Delta_{K_1}^*(m_{K+\pi}) P_2^{\lambda_f}(\alpha_{KK}, \beta_{KK}) P_1^{*\lambda_f}(\alpha_{K+\pi}, \beta_{K+\pi}) \tag{A.7}
\end{aligned}$$

$$\begin{aligned}
& + \sum_{\lambda_f=0,1} a_{f_2'(1525)} a_{K_1(890)} c_{f_2', K_1, \lambda_f} e^{i\delta_{f_2', K_1, \lambda_f}} \times \\
& \times \Delta_{f_2'}(m_{KK}) \Delta_{K_1}^*(m_{K-\pi}) P_2^{\lambda_f}(\alpha_{KK}, \beta_{KK}) P_1^{*\lambda_f}(\alpha_{K-\pi}, \beta_{K-\pi}) \tag{A.8}
\end{aligned}$$

$$+ \sum_{\lambda_f=0,1} a_{\phi_1(1680)} a_{K_1(890)} c_{\phi_1, K_1, \lambda_f} e^{i\delta_{\phi_1, K_1, \lambda_f}} \times$$

$$\Delta_{\phi_1}(m_{KK}) \Delta_{K_1}^*(m_{K+\pi}) P_1^{\lambda_f}(\alpha_{KK}, \beta_{KK}) P_1^{*\lambda_f}(\alpha_{K+\pi}, \beta_{K+\pi}) \tag{A.9}$$

$$+ \sum_{\lambda_f=0,1} a_{\phi_1(1680)} a_{K_1(890)} c_{\phi_1, K_1, \lambda_f} e^{i\delta_{\phi_1, K_1, \lambda_f}} \times \tag{A.10}$$

$$\Delta_{\phi_1}(m_{KK}) \Delta_{K_1}^*(m_{K-\pi}) P_1^{\lambda_f}(\alpha_{KK}, \beta_{KK}) P_1^{*\lambda_f}(\alpha_{K-\pi}, \beta_{K-\pi}) \tag{A.11}$$

$$+ \sum_{\lambda_f=0,1,2} a_{f_2(1275)} a_{a_2(1320)} c_{f_2, a_2, \lambda_f} e^{i\delta_{f_2, a_2, \lambda_f}} \times$$

$$\times \Delta_{f_2}(m_{KK}) \Delta_{a_2}^*(m_{KK}) P_2^{\lambda_f}(\alpha_{KK}, \beta_{KK}) P_2^{*\lambda_f}(\alpha_{KK}, \beta_{KK}) \tag{A.12}$$

$$+ \sum_{\lambda_f=0,1} a_{\phi_1(1680)} a_{a_2(1620)} c_{\phi_1, a_2, \lambda_f} e^{i\delta_{\phi_1, a_2, \lambda_f}} \times$$

$$\times \Delta_{\phi_1}(m_{KK}) \Delta_{a_2}^*(m_{KK}) P_2^{\lambda_f}(\alpha_{KK}, \beta_{KK}) P_2^{*\lambda_f}(\alpha_{KK}, \beta_{KK}) \tag{A.13}$$

The present form includes also the interference terms: the self-interference between the two crossing $K_1^{*\pm}(890)$ is in line A.1 and between the two crossing $K_0^{*\pm}(1430)$ in line A.2, while the interferences between themselves are in lines A.3, A.4. In lines A.5÷ A.11 we consider the interferences of the $K_1^{*\pm}(890)$ with the diagonal bands (K^+K^- resonances). The interferences between two overlapping bands $f_2(1275)$, $a_2(1320)$ and $a_2(1620)$, $\phi_1(1680)$ are also included in lines A.12, A.13.

The fitted parameters are the coupling constants a_{λ_f} , the coherence strenghts c_{λ_f} and the relative phases δ_{λ_f} for every helicity amplitude.

Bibliography

- [1] H. Fritzsche, M. Gell-Mann, *Proc. of the XVI International Conference on High Energy Phys.*, Vol.2 135 Batavia (1972)
- [2] Particle Data Group, *Review Of Particle Physics*, The European Physical Journal C (2000)
- [3] F. E. Close, G. R. Farrar, Zhenping Li, *Determining the gluonic content of isoscalar mesons* , Physical Rev. Lett. 76 4111 (1996)
- [4] S. Godfrey and J. Napolitano, *Light Meson Spectroscopy*, Submitted to Review of Modern Physics, Nov. 12 (1998)
- [5] G. R. Farrar, *Detecting Light-Gluino-Containing Hadrons*, Physical Rev. Lett. 76 4111 (1996)
- [6] F. E. Close, *Gluonic Hadrons*, Rep. Prog. Phys. 51 833-882 (1988)
- [7] Barnes, T. and F. E. Close, Phys. Lett. B123, 89 (1983a)
- [8] Latorre, J.L., *et al.*, Phys. Lett. 147b, 169 (1984)
- [9] N. Isgur and J. Paton, Phys. Lett. B124, 247 (1983)
- [10] G. Bali *et al.*, *A comprehensive lattice study of SU(3) glueballs*, Phys. Lett. 309, 378 (1993)
- [11] H. Chen, J. Sexton, A. Vaccarino and D. Weingarten, *The scalar and the tensor glueball in the valence approximation* , Nucl. Phys. B, Proc. Suppl. 34 (1994)
- [12] J. Sexton, A. Vaccarino and D. Weingarten, *Coupling constants for scalar glueball decay* , Nucl. Phys. B, Proc. Suppl. 47, 128 (1996)
- [13] C. Amsler *et al.*, Crystal Barrel Collaboration, *Observation of a new $I^G(0^{++})$ resonance at 1450 MeV* , Phys. Lett. B 333 277 (1994)
- [14] D. Bugg, V. V. Anisovich, A. Sarantsev, B.S. Zou, *Coupled channel analysis of data on $barpp \rightarrow 3\pi^0$, $\eta\eta\pi^0$, and $\eta\pi^0\pi^0$ at rest, with the N/D method* , Phys. Rev. D 50 4412 (1994)

-
- [15] V. V. Anisovich *et al.*, Crystal Barrel Collaboration, *Observation of two $J^{PC} = 0^{++}$ isoscalar resonance at 1365 and 1520 MeV*, Phys. Lett. B 323 233 (1994)
- [16] C. Edwards *et al.*, *Evidence for a $\eta\eta$ resonance in J/ψ radiative decays*, Phys. Rev. Lett. 48 458 (1982)
- [17] D. Bugg *et al.*, *Further amplitude analysis of $J/\psi \rightarrow \gamma(\pi^+\pi^-\pi^+\pi^-)$* , Phys. Lett. B 353 378 (1995)
- [18] J. Weinstein and N. Isgur *et al.*, *$qq\bar{q}\bar{q}$ system in a potential model*, Phys. Rev. D27 588 (1983)
- [19] C. Amsler *et al.*, Crystal Barrel Collaboration, *Coupled channel analysis of antiproton-proton annihilation into $\pi^0\pi^0\pi^0$, $\pi^0\eta\eta$ and $\pi^0\pi^0\eta$.*, Phys. Lett. B355, 425, (1995).
- [20] A. Abele *et al.*, Crystal Barrel Collaboration, *A Study of $f_0(1500)$ decays into $4\pi^0$'s in proton antiproton annihilation into five π^0 's at rest*, Phys. Lett. B380, 453, (1996).
- [21] C. Amsler *et al.*, Crystal Barrel Collaboration, *$\eta\eta'$ threshold enhancement in antiproton proton annihilations into $\pi^0\eta\eta'$ at rest*, Phys. Lett. B340, 259, (1994).
- [22] A. Abele *et al.*, Crystal Barrel Collaboration, *Antiproton-proton annihilation at rest into $K_L K^{+-}\pi^{-+}$* , Phys. Rev. D57, 3860, (1998)
- [23] A. Abele *et al.*, Crystal Barrel Collaboration, *Observation of $f_0(1500)$ decay into $KL KL$.*, Phys. Lett. B385, 425, (1996).
- [24] C. Amsler and F. Close, *Is $f_0(1500)$ a scalar glueball?*, Phys. Rev. D 53 (1996)
- [25] T.A.Armstrong *et al.*, WA76 Collaboration, *Observation of centrally produced $\theta/f_2(1720)$ in the reaction $pp \rightarrow p_f(K\bar{K})p_s$ at 300 GeV/c*, Phys. Lett. B 227 (1989)
- [26] T.A.Armstrong *et al.*, WA76 Collaboration, Z. Phys. C48 (1991)
- [27] H.Albrecht *et al.*, ARGUS Collaboration, Z. Phys. C48 (1990)
- [28] D.V.Bugg *et al.*, *Further amplitude analysis of $J/\psi \rightarrow \gamma(\pi^+\pi^-\pi^+\pi^-)$* , Phys. Lett. B 353 (1995)
- [29] J.Z.Bai *et al.*, BES Collaboration, *Structure Analysis of the $f_j(1710)$ in the Radiative Decay $J/\psi \rightarrow \gamma K^+ K^-$* , Phys. Rev. Lett. 77 (1996)
- [30] B.R.French *et al.*, WA76/102 Collaboration, *A partial wave analysis of the centrally produced $K^+ K^-$ system in pp reactions at 300 GeV/c*, Phys. Lett. B 460 (1999)

-
- [31] D.Barberis *et al.*, WA102 Collaboration, *A partial wave analysis of the centrally produced K^+K^- and $K_s^0K_s^0$ systems in pp interaction at 450 GeV/c and new information on the spin of the $f_j(1710)$* , Phys. Lett. B453 305(1999)
- [32] A.V. Anisovich *et al.*, *Observation of the $f_0(1770) \rightarrow \eta\eta$ in $\bar{p}p \rightarrow \eta\eta\pi^0$ reactions from 600 to 1200 MeV/c*, Phys. Lett. B449 154 (1999).
- [33] A. Abele *et al.*, Crystal Barrel Collaboration, *Observation of resonances in the reaction antiproton-proton annihilation into $\eta\eta\pi^0$ at 1.94 GeV/c*, Eur. Phys. J. C8, 67, (1999).
- [34] U. Gastaldi and R. Klapish, *The LEAR project and physics with Low-Energy antiprotons*, CERN-EP/81-06 (1981).
- [35] S. van der Meer, *Stochastic Damping of Betatron Oscillations in the ISR*, CERN/ISR-PO/72-31 (1972).
- [36] E. Aker *et al.*, *The Crystal Barrel Spectrometer at LEAR*, Nucl. Instr. and Meth. A321 69 (1992).
- [37] G. Reifenroether and E. Klempt, *Antiprotonic Hydrogen: from atomic capture to annihilation*, Nuclear Physics A503 885 (1989).
- [38] R. Veenhof, *GARFIELD user guide*, CERN Program Library W5050(1989).
- [39] M. Doser *et al.*, *The Crystal Barrel Si-Vertex Detector*, Nucl. Instr. and Meth. A412 70 (1998).
- [40] R. Brun and J. Zoll, *ZEBRA user guide*, CERN Program Library Q100 (1987).
- [41] A. Berdoz, C.A. Meyer, W.Roethel and P. Schmidt, *Report on the last Cb-Runs 8.10-9.12 1996*, CB-Note 313 (1997).
- [42] *CMZ User Guide and Reference Manual*, CERN Program Library (1990).
- [43] F. James and M. Roos, *MINUIT Function Minimization and Error Analysis*, CERN Program Library D506(1989).
- [44] S. Spanier, *Diploma thesis*, Mainz University(1991).
- [45] N. P. Hessey, *Split-off recognition with Dolby-C*, CB-Note 199 (1992).
- [46] M. Benayoun *et al.*, *Split-off recognition in data with charged tracks, The TAXI logic*, CB-Note 280 (1995).
- [47] N. P. Hessey, *Photon energy correction factors derived from response means*, CB-Note 161 (1991).
- [48] M. Lakata, *A new multi-vertex fitter and updated vertex-locator information*, CB-Note 285 (1995).

-
- [49] I. Uman and O. Kortner, *A new photon energy correction function and the JDC z-scaling for inflight data*, CB-Note 341 (1991).
- [50] M. Heinzelmann, *Missing momentum of charged particles at 900 MeV/c and resistive wire length scaling*, CB-Note 328 (1998).
- [51] G. Folger, *Offline reconstruction software V1.22/04*, CB-Note 121 (1993).
- [52] C.A. Meyer, *Chamber reconstruction software*, CB-Note 93 (1988).
- [53] F.H. Heinsius, *Crystal Data-Reconstruction Software V1.43*, CB-Note 92 (1991).
- [54] M. Burchell, *Global Tracking Particle Bank Structure*, CB-Note 118 (1990).
- [55] P. A. Aarnio *et al.*, *FLUKA users guide. Technical Report TIS-RP-190*, CERN (1990).
- [56] A. J. Noble, *A study of Hadronic Interactions in CBGEANT. FLUKA and GHEISHA*, CB-Note 258 (July 1994).
- [57] A. J. Noble, *The Release of CBGEANT 5.00. News and Added Features*, CB-Note 264 (1994).
- [58] R. Bossingham, *LEAR Crystal Barrel Experiment, PS197. Monte Carlo Software CBGEANT 4.06/03*, CB-Note 169 (1992).
- [59] *GEANT 3.21. Detector Description and Simulation Tool*, CERN Program Library W5013 (1994).
- [60] P. Hidas, *LEAR Crystal Barrel Experiment, PS197. Kinematic Fitting Software Ver. 3.11/00*, CB-Note 138 (1997).
- [61] S. Brandt, *Statistische Methoden der Daten-Analyse*, Bibliographisches Institut Mannheim/Wien/Zürich (1964)
- [62] R. H. Dalitz, *Phil. Mag.* 44 1068 (1953)
- [63] E. Fabri, *Nuovo Cimento* 11 479 (1954)
- [64] J. Adomeit *et al* , Crystal Barrel Collaboration, *Evidence for two isospin zero $J^{PC} = 2^{-+}$ mesons at 1645 and 1875 MeV*, *Z. Phys. C* 71, 227-238 (1996).
- [65] D. V. Bugg, CB-Note 272 (1995).
- [66] K. Gottfried and J. D. Jackson, *Nuovo Cimento* 33, 309 (1964), *Phys. Lett.* 8, 144 (1964)
- [67] F. Hippel and C. Quigg, *Phys. Review D.* 5, N.3 624 (1972)

-
- [68] S. Mundigl, M. V. Vacas, W. Weise, *Two meson doorway model of low energy antiproton-proton annihilation*, Nucl. Phys. A523 517 (1991)
- [69] C. Bourrely, E. Leader, J. Soffer, *Polarization phenomena in hadronic reactions*, Phys. Rep. 59 2, 95 (1980)
- [70] W. Weise, *Proceedings of the Second Low Energy Antiproton Physics Conference*, LEAP '92 Courmayeur (1992)
- [71] B. Hyams *et al.*, Nucl. Phys. B64, 134 (1973)
- [72] O. Kortner and C. Zupancic, *An Algorithm to Bin Multidimensional Event Distributions and the Method of Contrast Enhancement*, to be submitted to Nucl. Instr. Met. (2000)
- [73] O. Kortner and C. Zupancic *et al.*, *Fitting simulated random events to experimental histograms by means of parametric models*, to be submitted to Nucl. Instr. Met. (2000)
- [74] I. Silin *D510: Fitting Chisquare and Likelihood Functions*, CERN Program Library D510 (1971).
- [75] K. Peters and E. Klempt, *The suppression of $s\bar{s}$ creation from tensor meson decays*, Phys. Lett. B352 467 (1995)
- [76] D. Alde *et al.*, Phys. Lett. B241 600 (1990)
- [77] G. M. Beladidze *et al.*, Zeit f. Phys. C54 367 (1992)
- [78] D. Aston *et al.*, Nucl. Phys. B21 (suppl.) 5 (1991)
- [79] S. Abatzis *et al.*, Phys. Lett. B324 509 (1994)
- [80] J.Z. Bai *et al.*, Phys. Lett. B472 207 (2000)
- [81] T.A. Armstrong *et al.*, Phys. Lett. B307 399 (1993)
- [82] S. Braccini, for the L3 Collaboration, *The $K_s K_s$ final state in two photon collision and some implications for glueball searches*, Nucl. Phys. A655 143 (1999)
- [83] A. V. Anisovich *et al.*, *Analysis of $\bar{p}p \rightarrow \pi^+\pi^-, \pi^0\pi^0, \eta\eta$ and $\eta\eta'$ from threshold to 2.5 GeV/c*, Phys. Lett. B 323 233 (1994)
- [84] D.V. Bugg *et al.*, *The glueball spectrum*, submitted to Elsevier Preprint (2000)

ACKNOWLEDGMENTS

Firstly I would like to thank all my colleagues in the Crystal Barrel collaboration for producing the beautiful data.

I would like to express in particular my gratitude to Pr. M. A. Faessler, who gave me the opportunity to join the Crystal Barrel group in a friendly atmosphere, for the productive supervision, to Pr. C. Zupancic for the constructive criticism and fruitful collaboration, to Pr. W. Duennweber for the successful assistance to this work and to L. Montanet (CERN) for the extremely important discussions. I would like to express my deep thanks to Pr. D. Bugg (QMC London) for the fruitful collaboration on data analysis.

I wish also to thank O. Kortner, W. Roethel, R. Ouared (CERN), S. Wallis-Plachner and F. Meyer-Wildhagen for many helpful discussions and collaboration to process the data and to M. Dlaboha for the linguistic comments to the draft.

Finally I wish to thank Natascha Schädler, who helped me to relieve the difficult initial periods, for the encouragement to undertake this work.

LEBENS LAUF

Persönliche Daten

Name : Uman
Vorname : Ismail
Geburtsdatum : 23. Februar 1963
Geburtsort : Istanbul (Türkei)
Nationalität : Italienisch
Wohnort : München
Familienstand : ledig
Sprachen : italienisch, englisch, türkisch, deutsch

Studium

11/1981 - 1990 : Studium der Physik an der *Università degli studi* in Perugia.

1990 - 1993 : Anfertigung der Italienischen Doktorarbeit verbunden mit regelmässigen Aufenthalten am LNGS (*Laboratori Nazionali del Gran Sasso*) in L'Aquila unter der Leitung von Prof. G. Mantovani.

11/1993 : Italienische Promotion in Physik an der Universität in Perugia und Dissertation.
Thema : *Simulationstudien des Einfach- und Vielfach-Myonflusses am LVD-Detector.*

5/1996 - 3/2001 : Wiss. Mitarbeiter mit Gelegenheit zur Promotion (2001) an der Ludwig-Maximilians-Universität München im Rahmen des Crystal-Barrel-Experiments am CERN unter der Leitung von Prof. Dr. M. A. Faessler.
Thema : *Antiproton-proton annihilation in flight into $K^+K^-\pi^0$ final states.*